

UNIVERSITY OF OKLAHOMA
GRADUATE COLLEGE

AN EXPERIMENTAL AND NUMERICAL STUDY OF
EVAPORATION ENHANCEMENT AND COMBUSTION
IN POROUS MEDIA

A DISSERTATION
SUBMITTED TO THE GRADUATE FACULTY
in partial fulfillment of the requirements for the
Degree of
DOCTOR OF PHILOSOPHY

By
CHENDHIL PERIASAMY
Norman, Oklahoma
2007

UMI Number: 3261119



UMI Microform 3261119

Copyright 2007 by ProQuest Information and Learning Company.
All rights reserved. This microform edition is protected against
unauthorized copying under Title 17, United States Code.

ProQuest Information and Learning Company
300 North Zeeb Road
P.O. Box 1346
Ann Arbor, MI 48106-1346

AN EXPERIMENTAL AND NUMERICAL STUDY OF
EVAPORATION ENHANCEMENT AND COMBUSTION
IN POROUS MEDIA

A DISSERTATION APPROVED FOR THE
SCHOOL OF AEROSPACE AND MECHANICAL ENGINEERING

BY

Dr. S. R. Gollahalli (Chairman)

Dr. Faruk Civan

Dr. Feng C. Lai

Dr. Wilson E. Merchán-Merchán

Dr. Ramkumar N. Parthasarathy

© Copyright by CHENDHIL PERIASAMY 2007
All Rights Reserved.

ACKNOWLEDGEMENTS

I sincerely thank and express my deep sense of gratitude to my GURUJI Professor S. R. Gollahalli, Lesch Centennial Chair and Director of School of Aerospace and Mechanical Engineering, for his mentoring, and invaluable guidance for the last five years. I am indebted to his constant encouragement and several thought provoking discussions that prepared me into a confident individual. He always believed in my potential and has brought out the best of me in my academic life. I thank Dr. Gollahalli for also sharing his professional and personal life experiences with me. I am proud that I had the opportunity to be his student.

I thank my dissertation committee members Professor R. N. Parthasarathy, Professor F. C. Lai, Professor F. Civan, and Professor W. Merchán-Merchán for their time and constructive comments to improve the quality of my work. I also thank my former dissertation committee member Professor A. K. Agrawal for his useful comments.

I would like to thank the financial assistance provided by the US Army DEPSCoR (Grant No.: DAAD 190210082), Lesch Centennial Chair, and the School of Aerospace and Mechanical Engineering in the form of teaching and research assistantships continuously for the last past five years.

I also thank Mr. Billy Mays and Mr. Greg Williams of AME Machine Shop, and Mr. Sathish Sankara Chinthamony and Dr. Benjamin Baird for their help in the fabrication of my experimental setup.

I thank the present and past members of the Combustion and Flame Dynamics Laboratory: Norman Love, Jaime Erazo, Barry Goepfert, Axzel Marin, Dr. Sien-Fong Goh, Praveen Hariharan, Tracy Smith, Pablo Barajas, and Marin Meas for several fruitful discussions we had, and excellent companionship that made my stay in the laboratory a wonderful experience. I also thank my past roommates, Essex 109 group of friends, and the fluids gang for making my life in Norman enjoyable.

I would like to express my deep sense of gratitude to my mother and father for their support, unconditional love, and care. Mere words do not suffice to thank their dedication and sacrifice to give me the best life. I thank my brother Ramesh who has been a good friend to me and helpful during the course of this work through his constant encouragement. I thank my father-in-law, mother-in-law, and sister-in-law Lavanya for their love, care, blessing, and affection showered on me. I also thank my cousin Suganthi and her family for their help during this work.

Without the unconditional love, support, understanding, and encouraging words of my loving wife Uma, I would not have been able to complete this dissertation. I am very grateful to her for spending several days with me in the lab. She has been a constant source of energy and strength to me. Thank You.

CHENDHIL PERIASAMY

TABLE OF CONTENTS

ACKNOWLEDGEMENTS	iv
TABLE OF CONTENTS	vi
LIST OF TABLES	xii
LIST OF FIGURES	xiii
ABSTRACT	xx

CHAPTER 1 INTRODUCTION AND LITERATURE REVIEW

1.1	Motivation for the Study.....	1
1.2	Excess Enthalpy Flames.....	2
1.3	Typical Porous Media Combustor Setup.....	4
1.4	Literature Survey.....	7
1.4.1	Flow through Porous Media.....	7
1.4.2	Heat Transfer in Porous Media.....	8
1.4.2.1	Characterization of Heat Transfer Properties...8	
1.4.2.2	Conduction and Convection Heat Transfer.....	10
1.4.3	Gaseous Fuel Combustion in Porous Media.....	11
1.4.3.1	Flame Stabilization.....	11
1.4.3.2	Pollutant Emission.....	14
1.4.4	Spray Evaporation and Combustion.....	16
1.4.5	Liquid Fuel Combustion in Porous Media.....	19
1.5	Specific Objectives of the Present Work.....	22
1.6	Methodology.....	23
1.7	Scope of the Present Work.....	24
1.8	Organization of the Dissertation.....	25

CHAPTER 2 EXPERIMENTAL DETAILS

2.1	Introduction.....	26
2.2	Experimental Setup.....	26
2.2.1	Laboratory Combustion Chamber.....	26
2.2.2	Test Porous Media.....	27
2.3	System Components.....	28
2.3.1	Coflow Air Preheater.....	28
2.3.2	Air Settling Chamber.....	28
2.3.3	Fuel Supply System and Injector Arrangement.....	29
2.3.4	Porous Media Housing.....	29
2.3.5	Test Section.....	30
2.3.6	Porous Media Heating Setup.....	31
2.3.7	Pilot Flame.....	31
2.4	Instrumentation.....	32
2.4.1	Phase Doppler Particle Analyzer.....	32
2.4.2	Infrared Camera.....	33
2.4.3	Minimum Heat Feedback Rate Measurements.....	33
2.4.4	Vapor Concentration Analyzer.....	34
2.4.5	Temperature Measurement.....	34
2.4.6	Combustion Gas Analyzers.....	35
2.4.7	Pressure Drop and Velocity Measurements.....	36
2.4.8	Flame Radiation.....	37
2.5	Test Matrix.....	38
2.6	Experimental Procedure.....	38
2.7	Data Management.....	39
2.7.1	Data Acquisition System.....	39
2.7.2	Data Analysis and Integration.....	40
2.8	Chapter Summary.....	41

CHAPTER 3 COMPUTATIONAL MODELING

3.1	Introduction.....	63
3.2	Model Assumptions.....	63

3.3	Governing Equations.....	65
3.3.1	Governing Equations for Gas and Solid Phases.....	65
3.3.1.1	Overall Mass Conservation.....	65
3.3.1.2	Gas-phase Species Conservation.....	66
3.3.1.3	Gas-phase Momentum Conservation.....	67
3.3.1.4	Turbulence Modeling.....	70
3.3.1.5	Energy Conservation Equations.....	71
3.3.2	Governing Equations for Liquid Phase.....	75
3.3.2.1	Droplet Motion.....	75
3.3.2.2	Droplet Heating.....	76
3.3.2.3	Droplet Vaporization.....	77
3.3.2.4	Droplet Boiling.....	78
3.3.2.5	Spray Model.....	79
3.4	Boundary and Initial Conditions.....	80
3.5	Grid Generation.....	81
3.6	Solution Procedure	81
3.7	Model Comparison.....	83
3.8	Grid Sensitivity Analysis.....	85
3.9	Chapter Summary.....	85

CHAPTER 4 EVAPORATION ENHANCEMENT IN POROUS MEDIA

4.1	Introduction.....	93
4.2	Pressure Drop Measurements.....	94
4.2.1	Unheated Coflow Conditions.....	94
4.2.2	Heated Coflow Conditions.....	95
4.2.3	Comparison with Literature.....	95
4.2.4	Calculation of Permeability from Pressure Drop Data.....	98
4.3	Porous Medium Temperature with Simulated Heat Feedback.....	99
4.3.1	Thermocouple Measurements.....	99
4.3.2	Infrared Imaging.....	100

4.3.3	Predicted Temperature Profiles in Porous Media.....	102
4.3.3.1	Axial Temperature Distribution.....	102
4.3.3.2	Surface Temperature Distribution.....	103
4.3.3.3	Effect of Local Thermal Non-equilibrium....	103
4.3.3.4	Comparison with Experimental Data.....	104
4.4	Spray Characteristics.....	105
4.4.1	Characteristics of Kerosene Spray.....	105
4.4.1.1	Measured Sauter Mean Diameter Profiles....	105
4.4.1.2	Comparison with Numerical Model.....	108
4.4.1.3	Measured Droplet Velocity Profiles.....	109
4.4.1.4	Measured Mass Flux.....	109
4.4.2	Characteristics of n-Heptane Spray.....	111
4.4.3	Characteristics of Methanol Spray.....	112
4.5	Minimum Heat Feedback Rate for Complete Vaporization..	113
4.5.1	Definition of Minimum Heat Feedback Rate.....	113
4.5.2	Vaporization with Porous Media.....	114
4.5.3	Vaporization without Porous Media.....	117
4.6	Vapor Concentration Profiles.....	117
4.6.1	Measured Kerosene Vapor Concentration Profiles with no Heat Feedback Rate.....	118
4.6.2	Vapor Concentration Measurements with Simulated Heat Feedback Rate.....	120
4.6.3	Comparison with Model Predictions.....	121
4.6.4	Computational Parametric Study.....	121
4.6.4.1	Effects of Porous Medium Heat Feedback Rate.....	122
4.6.4.2	Effects of Porous Medium Structure.....	122
4.6.4.3	Effects of Fuel Flowrate.....	123
4.6.4.4	Effects of Flame Temperature.....	125
4.7	Chapter Summary.....	126

CHAPTER 5 COMBUSTION OF LIQUID SPRAY IN POROUS MEDIA

5.1	Introduction.....	183
5.2	Flame Appearance.....	183
5.2.1	Interior Flames.....	184
5.2.2	Surface Flames.....	185

5.3	Lean Extinction Limits.....	186
5.3.1	Definition of Flame Extinction in Porous Media.....	186
5.3.2	Measurement of Flame Extinction in Porous Media.....	187
5.4	Damköhler Number Analysis at Flame Extinction.....	188
5.5	Temperature Characteristics near Extinction.....	193
5.5.1	Porous Medium Interior Temperature.....	193
5.5.2	Adiabatic Flame Temperature.....	195
5.5.3	Comparison with Literature.....	196
5.5.4	Surface Temperature Uniformity.....	197
5.6	Flame Radiation.....	197
5.7	Pollutant Emissions.....	198
5.7.1	Equilibrium Composition.....	199
5.7.2	Emission Indices of Carbon Monoxide (EI _{CO}).....	200
5.7.3	Emission Indices of Nitric oxide (EI _{NO}).....	202
5.7.4	Exit Concentration Levels of Carbon Dioxide (CO ₂).....	204
5.7.5	Exit Concentration Levels of Oxygen (O ₂).....	205
5.8	Chapter Summary.....	205

CHAPTER 6 OVERALL DISCUSSION, CONCLUSIONS AND RECOMMENDATIONS

6.1	Overall Discussion.....	223
6.1.1	Porous Medium Characteristics.....	223
6.1.2	Spray Characteristics.....	224
6.1.3	Evaporation Enhancement.....	225
6.1.4	Combustion of Fuel Spray in Porous Media.....	227
6.2	Conclusions.....	229
6.3	Practical Impacts.....	230
6.4	Recommendations for Further Work.....	231

REFERENCES.....	234
APPENDIX A CALIBRATION CHARTS.....	243
APPENDIX B SAMPLE CALCULATIONS.....	249
APPENDIX C UNCERTAINTY CALCULATIONS.....	255
APPENDIX D NOMENCLATURE.....	259
APPENDIX E COMPUTATIONAL RESULTS OF EVAPORATION ENHANCEMENT WITH A POINT SOURCE MODEL.....	266
APPENDIX F COMPUTATIONAL RESULTS OF EVAPORATION ENHANCEMENT WITH AN AIR-BLAST ATOMIZER MODEL.....	277
APPENDIX G COMPUTATIONAL RESULTS OF EVAPORATION ENHANCEMENT WITH A TWO-ENERGY EQUATION MODEL AND AN UNSTEADY INJECTOR MODEL.....	286
APPENDIX H EFFECT OF COFLOW AIR TURBULENCE ON SPRAY CALCULATIONS.....	296
APPENDIX I LIST OF PUBLICATIONS BASED ON THIS WORK.....	299

LIST OF TABLES

Table 2.1	Combustion chamber dimensions and nominal ambient conditions...	43
Table 2.2	Typical properties of porous medium.....	44
Table 2.3	Important properties of the fuels used in the study.....	44
Table 2.4	Uses of different test sections in the experiment.....	45
Table 2.5	Properties of Borosilicate and Vycor® glass.....	45
Table 2.6	List of instruments and their purposes.....	46
Table 2.7	Major specifications of PDPA instrument.....	47
Table 2.8	Major specifications of infrared camera.....	47
Table 2.9	Test matrix.....	48
Table 3.1	Boundary conditions at flow inlet, side walls, and flow exit.....	86
Table 3.2	Initial conditions for droplet stream.....	87
Table 3.3	Important physical properties of porous medium used in modeling...87	87
Table 3.4	Computational parameters used in the modeling.....	88
Table 4.1	Computational parameters used in two-energy equation modeling...127	127
Table 4.2	Comparison of droplet characteristics of kerosene, n-heptane, and methanol sprays upstream of evaporation porous medium.....	127
Table 4.3	Results of vaporization experiments without porous media.....	128

LIST OF FIGURES

Chapter 1	Introduction and Literature Review	
Figure 1.1	Typical experimental arrangement of liquid fuel combustion in porous media.....	5
Figure 1.2	Interactions among different heat transfer modes and combustion in porous media.....	6
Chapter 2	Experimental Details	
Figure 2.1a	Schematic diagram of experimental setup.....	49
Figure 2.1b	Photograph of the experimental setup.....	50
Figure 2.2	Photographs of the porous media used in experiments.....	51
Figure 2.3	Coflow air supply and heater setup.....	51
Figure 2.4	Schematic diagram of settling chamber and injector setup.....	52
Figure 2.5a	Schematic diagram of fuel supply system.....	53
Figure 2.5b	Exploded view and the diagram of the DELAVAN air-blast atomizer.....	54
Figure 2.6	Schematic diagram of porous medium housing.....	55
Figure 2.7	Velocity profile at the exit of the upstream test section.....	55
Figure 2.8	Experimental arrangement for porous medium heating setup.....	56
Figure 2.9	Pilot flame setup.....	56
Figure 2.10	Schematic diagram of the PDPA system.....	57
Figure 2.11	Experimental setup for surface temperature imaging with IR camera.....	58
Figure 2.12	Experimental setup for vapor concentration measurement	59
Figure 2.13	Schematic diagram of combustion gas composition analysis setup...	60
Figure 2.14	Pressure drop measurement setup.....	61
Figure 2.15	Typical setup of the data acquisition system.....	62
Chapter 3	Computational Modeling	
Figure 3.1	Physical domain considered for the present analysis.....	89
Figure 3.2	Computational grid generated for the present analysis.....	89
Figure 3.3	Solution flow diagram and FLUENT TM interactions with UDF solver.....	90
Figure 3.4	Comparison of predicted droplet lifetime with the experimental and numerical results of Runge et al. (1998).....	91

Figure 3.5	Comparison of transverse temperature profiles of the present model with the analytical solutions of Vafai and Kim (1989).....	91
Figure 3.6	Effects of grid size on vapor concentration ($x = 12.7$ cm, $HS = 200$ W).....	92
Chapter 4	Evaporation Enhancement in Porous Media	
Figure 4.1	Measured pressure drop across porous media of different pores per centimeter at various coflow air velocities (unheated).....	129
Figure 4.2	Measured pressure drop across porous media of different pores per centimeter at various coflow air velocities (Coflow air temperature = 350 K).....	129
Figure 4.3	Measured pressure drop across porous media of different pores per centimeter at various coflow air velocities (Coflow air temperature = 400 K).....	130
Figure 4.4	Measured pressure drop across porous media of different pores per centimeter at various coflow air velocities (Coflow air temperature = 450 K).....	130
Figure 4.5	Effect of coflow air temperature on the pressure drop across 18 PPCM porous media at a coflow air flow rate of 195 l/min.....	131
Figure 4.6	Comparison of measured pressure drop across porous media with Ergun equation (unheated coflow air).....	132
Figure 4.7	Calculation of permeability of porous media from the measured pressure drop data (PPCM = 18).....	132
Figure 4.8	Measured surface temperature distribution in 25 and 31 PPCM porous media with different heat feedback.....	133
Figure 4.9	Qualitative IR images of surface temperature of 25 PPCM porous media with a simulated heat feed back of 1% (No kerosene fuel was supplied; Air inlet temperature = 400 K; Volume flow rate = 195 l/min).....	134
Figure 4.10	Qualitative IR images of surface temperature of 31 PPCM porous media with a simulated heat feed back of 1 % (No kerosene fuel was supplied; Air inlet temperature = 400 K; Volume flow rate = 195 l/min).....	134
Figure 4.11	Surface temperature distribution of 25 PPCM porous medium with assumed emissivities (Heat feedback = 1 %; No kerosene fuel was supplied; Air inlet temperature = 400 K; Volume flow rate = 195 l/min).....	135
Figure 4.12	Axial variation of porous medium and gas-phase temperature in the computational domain (Heat feedback rate = 1%; no fuel spray).....	136

Figure 4.13	Effect of heat feedback rate on the axial variation of porous medium centerline temperature ($T_i = 450$ K; No fuel spray was considered; Air flowrate = 190 l/min).....	136
Figure 4.14	Predicted porous medium surface temperature for different heat feedback rates ($R =$ radius of the computational domain, 2.15 cm).....	137
Figure 4.15	Comparison of porous medium axial temperature predicted by local thermal equilibrium and non-equilibrium models (heat feedback rate = 1%; no fuel spray).....	138
Figure 4.16	Comparison of measured and predicted porous medium temperature at the exit surface for 1% combustion heat feedback rate.....	138
Figure 4.17	Transverse Sauter mean diameter profiles of kerosene spray at 2.5 cm upstream of porous Coflow temperature – 423 K).....	139
Figure 4.18	Transverse Sauter mean diameter profiles of kerosene spray at 2.5 cm upstream of porous Coflow temperature – 450 K).....	140
Figure 4.19	Transverse Sauter mean diameter profiles of kerosene spray at 2.5 cm upstream of porous Coflow temperature – 490 K).....	141
Figure 4.20	Transverse Sauter mean diameter profiles of kerosene spray at 2.0 cm upstream of porous Coflow temperature – 423 K).....	142
Figure 4.21	Transverse Sauter mean diameter profiles of kerosene spray at 2.0 cm upstream of porous Coflow temperature – 450 K).....	143
Figure 4.22	Transverse Sauter mean diameter profiles of kerosene spray at 2.0 cm upstream of porous Coflow temperature – 490 K).....	144
Figure 4.23	Transverse Sauter mean diameter profiles of kerosene spray at 1.5 cm upstream of porous Coflow temperature – 423 K).....	145
Figure 4.24	Transverse Sauter mean diameter profiles of kerosene spray at 1.5 cm upstream of porous Coflow temperature – 450 K).....	146
Figure 4.25	Transverse Sauter mean diameter profiles of kerosene spray at 1.5 cm upstream of porous Coflow temperature – 490 K).....	147
Figure 4.26	Comparison of measured and predicted droplet diameter at 1.5 cm upstream of the leading edge of the porous medium ($R =$ radius of the computational domain, 2.15 cm; $\phi = 0.5$; $T_i = 450$ K).....	148
Figure 4.27	Transverse droplet axial velocity profiles of kerosene spray at 2.5 cm upstream of porous media (Coflow temperature – 423 K)...	149
Figure 4.28	Transverse droplet axial velocity profiles of kerosene spray at 2.5 cm upstream of porous media (Coflow temperature – 450 K)...	150
Figure 4.29	Transverse droplet axial velocity profiles of kerosene spray at 2.5 cm upstream of porous media (Coflow temperature – 490 K)...	151
Figure 4.30	Transverse droplet axial velocity profiles of kerosene spray at 2.0 cm upstream of porous media (Coflow temperature – 423 K)...	152
Figure 4.31	Transverse droplet axial velocity profiles of kerosene spray at 2.0 cm upstream of porous media (Coflow temperature – 450 K)...	153

Figure 4.32	Transverse droplet axial velocity profiles of kerosene spray at 2.0 cm upstream of porous media (Coflow temperature – 490 K)...	154
Figure 4.33	Transverse droplet axial velocity profiles of kerosene spray at 1.5 cm upstream of porous media (Coflow temperature – 423 K)...	155
Figure 4.34	Transverse droplet axial velocity profiles of kerosene spray at 1.5 cm upstream of porous media (Coflow temperature – 450 K)...	156
Figure 4.35	Transverse droplet axial velocity profiles of kerosene spray at 1.5 cm upstream of porous media (Coflow temperature – 490 K)...	157
Figure 4.36	Transverse liquid mass flux profiles of kerosene spray at 2.5 cm upstream of porous media (Coflow temperature – 423 K).....	158
Figure 4.37	Transverse liquid mass flux profiles of kerosene spray at 2.5 cm upstream of porous media (Coflow temperature – 450 K).....	159
Figure 4.38	Transverse liquid mass flux profiles of kerosene spray at 2.5 cm upstream of porous media (Coflow temperature – 490 K).....	160
Figure 4.39	Transverse liquid mass flux profiles of kerosene spray at 2.0 cm upstream of porous media (Coflow temperature – 423 K).....	161
Figure 4.40	Transverse liquid mass flux profiles of kerosene spray at 2.0 cm upstream of porous media (Coflow temperature – 450 K).....	162
Figure 4.41	Transverse liquid mass flux profiles of kerosene spray at 2.0 cm upstream of porous media (Coflow temperature – 490 K).....	163
Figure 4.42	Transverse liquid mass flux profiles of kerosene spray at 1.5 cm upstream of porous media (Coflow temperature – 423 K).....	164
Figure 4.43	Transverse liquid mass flux profiles of kerosene spray at 1.5 cm upstream of porous media (Coflow temperature – 450 K).....	165
Figure 4.44	Transverse liquid mass flux profiles of kerosene spray at 1.5 cm upstream of porous media (Coflow temperature – 490 K).....	166
Figure 4.45	Transverse Sauter mean diameter profiles of n-heptane spray at different axial locations upstream of porous media (Unheated coflow).....	167
Figure 4.46	Transverse Sauter mean diameter profiles of n-heptane spray at different axial locations upstream of porous media ($T_i = 323$ K)....	168
Figure 4.47	Transverse droplet axial velocity profiles of n-heptane spray at different axial locations upstream of porous media (Unheated coflow).....	169
Figure 4.48	Transverse droplet axial velocity profiles of n-heptane spray at different axial locations upstream of porous media ($T_i = 323$ K)....	170
Figure 4.49	Transverse Sauter mean diameter profiles of methanol spray at different axial locations upstream of porous media (Unheated coflow).....	171
Figure 4.50	Transverse Sauter mean diameter profiles of methanol spray at different axial locations upstream of porous media ($T_i = 323$ K)....	172
Figure 4.51	Transverse droplet axial velocity profiles of methanol spray at different axial locations upstream of porous media (Unheated coflow).....	173

Figure 4.52	Transverse droplet axial velocity profiles of methanol spray at different axial locations upstream of porous media ($T_i = 323 \text{ K}$)....	174
Figure 4.53	Variation of minimum heat feedback requirement with the distance between the injector and porous medium for 25 and 31 PPCM porous media (Coflow air flowrate = 195 l/min; Coflow air temperature = 450 K).....	175
Figure 4.54	Measured transverse kerosene vapor concentration profiles at 5 cm downstream of the porous medium for 25 and 31 PPCM porous media with different equivalence ratios (No combustion heat feedback; Coflow air flowrate = 195 l/min; Coflow air temperature = 450 K).....	176
Figure 4.55	Liquid mass flux distribution (MF) and vapor concentration profiles (VC) with 25 PPCM porous medium at 0.3 and 0.6 equivalence ratios (No combustion heat feedback; Coflow air flowrate = 195 l/min; Coflow air temperature = 450 K).....	177
Figure 4.56	Measured transverse n-heptane vapor concentration profiles at 5 cm downstream of the porous medium for 25 PPCM porous media with different equivalence ratios (No combustion heat feedback; Unheated coflow).....	178
Figure 4.57	Vapor concentration profiles with 31 PPCM porous medium at 0.3 and 0.6 equivalence ratios with and without combustion heat feedback (Coflow air flowrate = 195 l/min; Coflow air temperature = 450 K).....	179
Figure 4.58	Comparison of predicted and measured kerosene vapor concentration profile at 5 cm downstream of porous medium ($R =$ radius of the computational domain, 2.15 cm; $\phi = 0.3$; heat feedback rate = 1%).....	179
Figure 4.59	Effect of combustion heat feedback rate on predicted transverse distribution of kerosene vapor concentration ($\phi = 0.3$; $T_i = 450 \text{ K}$; $\epsilon = 0.87$).....	180
Figure 4.60	Effect of porosity on axial temperature profiles in porous media (No liquid fuel supplied; $T_i = 450 \text{ K}$; Heat feedback rate = 1.0%)...	181
Figure 4.61	Effect of porosity on transverse kerosene vapor concentration profiles at 5 cm downstream of porous media ($\phi = 0.3$; $T_i = 450 \text{ K}$; Heat feedback rate = 1.0%).....	181
Figure 4.62	Effect of fuel flowrate on transverse kerosene vapor concentration profiles at 5 cm downstream of porous media ($T_i = 450 \text{ K}$; $\epsilon = 0.87$; Heat feedback rate = 1.0%).....	182
Figure 4.63	Effect of flame temperature on predicted axial porous medium and fluid temperature profiles for different assumed flame temperatures ($T_i = 450 \text{ K}$; $\epsilon = 0.87$).....	182

Chapter 5 Combustion of Liquid Spray in Porous Media

Figure 5.1	Experimental arrangement of evaporation and combustion porous media.....	207
Figure 5.2	Photograph of typical interior combustion flame in porous media.....	208
Figure 5.3	Photograph of typical surface combustion flame in porous media.....	208
Figure 5.4	Effect of effective gas velocity on extinction equivalence ratio.....	209
Figure 5.5	Effect of preheating residence time on extinction equivalence ratio.....	209
Figure 5.6	Effect of Damköhler number on extinction equivalence ratio.....	210
Figure 5.7	Locations of temperature measurement in combustion porous media.....	211
Figure 5.8	Axial variation of porous medium temperature in evaporation and combustion porous media ($d_{ip} = 6$ cm; Coflow air velocity = 126 cm/s; Equivalence ratio = 0.35; Damköhler number = 5.38).....	212
Figure 5.9	Effect of equivalence ratio on the axial variation of porous medium temperature in evaporation and combustion porous media during flame extinction ($d_{ip} = 6$ cm; Coflow air velocity = 126 cm/s).....	212
Figure 5.10	Temperature in combustion porous medium prior to flame extinction ($d_{ip} = 4$ cm; Coflow air velocity = 111 cm/s).....	213
Figure 5.11	Temperature in combustion porous medium prior to flame extinction ($d_{ip} = 5$ cm; Coflow air velocity = 126 cm/s).....	213
Figure 5.12	Temperature in combustion porous medium prior to flame extinction ($d_{ip} = 5$ cm; Coflow air velocity = 111cm/s).....	214
Figure 5.13	Decay of porous medium surface temperature of interior flames prior to extinction ($Da = 5.0$).....	214
Figure 5.14	Effect of equivalence ratio on adiabatic flame temperature of pre-vaporized, premixed combustion kerosene-air with no porous medium.....	215
Figure 5.15	Contours of difference between maximum and minimum temperatures on the porous medium surface during interior combustion visualized by infrared imaging (Conditions: $d_{ip} = 4$ cm; Coflow air velocity = 96 cm/s).....	216
Figure 5.16	Contours of difference between maximum and minimum temperatures on the porous medium surface during interior combustion visualized by infrared imaging (Conditions: $d_{ip} = 5$ cm; Coflow air velocity = 96 cm/s).....	217
Figure 5.17	Contours of difference between maximum and minimum temperatures on the porous medium surface during interior combustion visualized by infrared imaging (Conditions: $d_{ip} = 5$ cm; Coflow air velocity = 96 cm/s).....	218

Figure 5.18	Radiation from porous medium surface during the extinction interior combustion (Coflow air velocity = 96 cm/s).....	219
Figure 5.19	Equilibrium compositions of combustion products at different equivalence ratios for pre-vaporized premixed kerosene-air combustion (with no porous medium).....	219
Figure 5.20	Measured emission indices of carbon monoxide (CO) at four equivalence ratios prior to extinction for two injector locations (Coflow air velocity = 96 cm/s).....	220
Figure 5.21	Measured emissions of CO (corrected to 3% oxygen) at four equivalence ratios prior to extinction for two injector locations (Coflow air velocity = 96 cm/s).....	220
Figure 5.22	Measured emission indices of nitric oxide (NO) at four equivalence ratios prior to extinction for two injector locations (Coflow air velocity = 96 cm/s).....	221
Figure 5.23	Measured emissions of NO (corrected to 3% oxygen) at four equivalence ratios prior to extinction for two injector locations (Coflow air velocity = 96 cm/s).....	221
Figure 5.24	Measured exit concentration levels of carbon dioxide (CO ₂) at four equivalence ratios prior to extinction for two injector locations (Coflow air velocity = 96 cm/s).....	222
Figure 5.25	Measured exit concentration levels of oxygen O ₂ at four equivalence ratios prior to extinction for two injector locations (Coflow air velocity = 96 cm/s).....	222

ABSTRACT

Combustion of gaseous fuels in porous media improves combustion performance and reduces pollutant emissions by transferring combustion heat upstream via conduction and radiation to preheat reactants. Such heat feedback may be beneficially exploited to enhance vaporization of a liquid sprayed upstream of the porous medium, in addition to improving combustion performance. This dissertation presents an experimental and computational study of evaporation enhancement and combustion of liquid spray aided by porous media.

Blocks of open-cell, silicon carbide coated, carbon-carbon ceramic foam of bulk cross section 4 x 4 cm and thickness of 2.5 cm were used as porous medium sections for liquid evaporation and subsequent combustion. Liquid fuel (kerosene, n-heptane, and methanol) was sprayed into a co-flowing, preheated (350 - 490 K) air environment using an air-blast atomizer, and the spray subsequently entered the porous medium. In controlled evaporation studies, combustion heat feedback to evaporation porous medium was simulated with a resistive heating mechanism. The minimum heat feedback rate required for complete vaporization of liquid and the vapor concentration profiles downstream of evaporation porous medium were measured. The stable operating regimes of spray flames in the combustion porous medium were determined and a general understanding of flame extinction in porous media was developed using a Damköhler number analysis.

A two-energy equation model was developed to study the evaporation enhancement of liquid spray in the porous media. Combustion in the porous media was simulated by using a uniform volumetric heat source in the porous region. The solid and gas phase equations were coupled using a volumetric heat transfer coefficient. The computer simulations were performed with a commercial code, FluentTM 6.0.

The results showed that the pressure drop across the porous media increased as the coflow air velocity, temperature, and linear pore density of the medium were increased. The measured and predicted surface temperatures of evaporation and combustion porous media showed that the temperature distribution was uniform within ± 25 K and 50 K, respectively. The droplet Sauter mean diameter data revealed that the spray core region contained droplets with lower diameter, and the droplet diameter increased radially outward. A heat feedback rate to the evaporation porous medium section of about 1% of the average heat release in the combustion section was needed to completely vaporize the kerosene fuel. The vapor concentration level downstream of evaporation porous medium with 1% combustion heat release feedback was 63% higher than that with no heat feedback.

Stable spray flames were established both inside (referred to as interior flames) and on the downstream exit surface (surface flames) of the combustion porous medium. The equivalence ratio at flame extinction in each mode was determined. The extinction equivalence ratio decreased with a decrease in coflow air velocity. A nominal value of Damköhler number of 5.0 was required to initiate the interior

combustion mode. As Damköhler number was increased, the extinction equivalence ratio decreased (i.e., extending the fuel lean operation). The axial temperature profiles in evaporation and combustion porous media were measured. Also measured were the radiative heat release from porous medium downstream exit surface, and pollutant emissions of carbon monoxide and nitric oxide. The results demonstrate the benefits of porous medium in making NO emission somewhat insensitive to operating parameters such as equivalence ratio and location of injector.

Our results also suggest that the use of porous media in combustors allows operation at a lower coflow air temperature or with a shorter evaporation section. The porous-medium-burner concepts developed in this dissertation can be employed in many practical liquid combustion systems such as gas turbine combustors, air-heating systems, industrial burners, porous chemical reactors, heat recovery systems, and hybrid burners for bio-fuels.

Chapter 1

Introduction and Literature Review

1.1 Motivation for the Study

Many practical devices such as gas turbines, furnaces, diesel engines and rocket engines are powered by the combustion of liquid fuels. The combustion research community around the world has always been focusing on increasing combustion efficiency and reducing pollutant emissions of such combustion systems. Exhaust gas recirculation, selective catalytic reduction, use of non-circular burners, and lean premixed combustion are some of the techniques that have been explored in the past to achieve these goals.

Exhaust gas recirculation is employed in gasoline and diesel engines to reduce nitric oxide (NO_x) emission by mixing some of the exhaust gases with engine intake charges (Abd-Alla, 2002). Selective catalytic reduction employs a reductant and catalyst to reduce NO_x emission (Ma et al., 2000), and is primarily used in power plants. Non-circular burners also reduce certain pollutant emission from diffusion flames (Gollahalli et al., 1992; Smith et al., 2006). Lean premixed combustion has been gaining more attention recently for reducing NO_x in gas turbine engines (Huang et al., 2006; Bell et al., 2006).

Combustion in porous media is a relatively newer technique, which could potentially reduce the emissions of nitric oxide (NO_x) and carbon monoxide (CO) while

improving the combustion efficiency. In this method, the heat from combustion is fed back to preheat reactants without actually recirculating the combustion products. It offers several advantages, such as extension of lean flammable limits, stable burner operation over a wide range of loads, delivery of homogeneous fuel/air mixture, and capability to burn low-grade fuels.

Significant amount of research has been done in the past to understand the combustion of *gaseous fuels* in porous media. On the other hand, the application of porous media for liquid combustion is limited. Implementation of porous media combustion concepts to *liquid fuels* would lead to the development of more efficient engines with lower pollution emissions. In liquid-fueled combustion systems, the pre-combustion events (fuel evaporation and fuel-air mixing) are very crucial and understanding them helps simplifying the complexities involved in the combustion processes. Porous media could be used to both enhance the liquid fuel evaporation and improve the combustion characteristics. This dissertation deals with an experimental and numerical study of *liquid spray* evaporation and combustion in porous media.

1.2 Excess Enthalpy Flames

Combustion in porous media is based on the excess enthalpy flame concept. According to this concept, the thermal energy of the combustion products can be recirculated from the reaction zone to the upstream preflame zone by inserting a

porous medium in the former zone. This recirculated heat energy is then used to preheat the fresh reactants. Further, the heat feedback augments the initial enthalpy of reactants. Such combustion produces local peak temperatures higher than the adiabatic flame temperature at a given equivalence ratio. These flames are referred to as excess enthalpy flames or superadiabatic flames.

Excess enthalpy concepts and different methods of recirculation of heat energy are described in Weinberg (1971) and Hardesty and Weinberg (1974). Inserting a porous solid in the flame zone to recirculate the combustion heat was proposed by Takeno and his coworkers (Takeno and Sato, 1979; and Kotani and Takeno, 1982). Using one-dimensional flame theory, Takeno and Sato (1979) showed that the flame could be sustained for higher mass flowrates by employing porous solids in the flame region. They also showed that low heat content mixtures could be burned with increased combustion rate. The study revealed that the flame structure could be controlled by the heat transfer coefficient between the solid and the gas. The experimental investigations by Kotani and Takeno (1982) reported a leanest flammable equivalence ratio limit of 0.32 for methane flames and confirmed the theoretical findings of Takeno and Sato (1979). Subsequently, considerable amount of research has been conducted and burners, primarily employing *gaseous fuels*, have been designed and tested. However, implementation of porous media for *liquid-fueled systems* has not yet been studied in detail.

1.3 Typical Porous Media Combustor Setup

In porous media combustion experiments, generally two porous media are placed in the combustion chamber: one (combustion porous media, CPM) in the reaction zone, and the other (evaporation porous media, EPM) in the upstream region of the reaction zone. A typical porous media setup is shown in Fig. 1.1. CPM is heated during combustion and establishes a heat feedback to EPM by solid conduction and radiation. The EPM is heated due to this heat feedback. The heated EPM enhances the evaporation of liquid spray injected onto it by conduction and convection. Intricate flow path and complex structure, which are inherent to the porous media, improve the mixing of fuel vapors and air. The heated EPM also preheats the vapor-air mixture and hence prepares a homogeneous, flammable mixture for combustion. The various heat transfer modes in porous media and their interactions with combustion are presented in Fig. 1.2 (Viskanta, 1995; Barra and Ellzey, 2004).

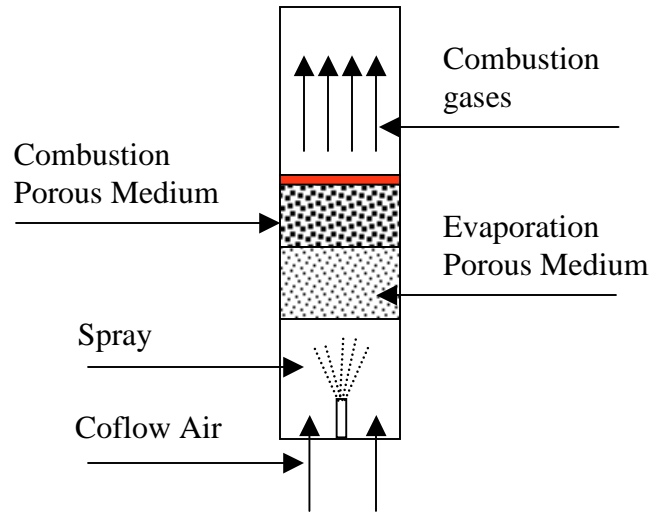


Figure 1.1 Typical experimental arrangement of liquid fuel combustion in porous media

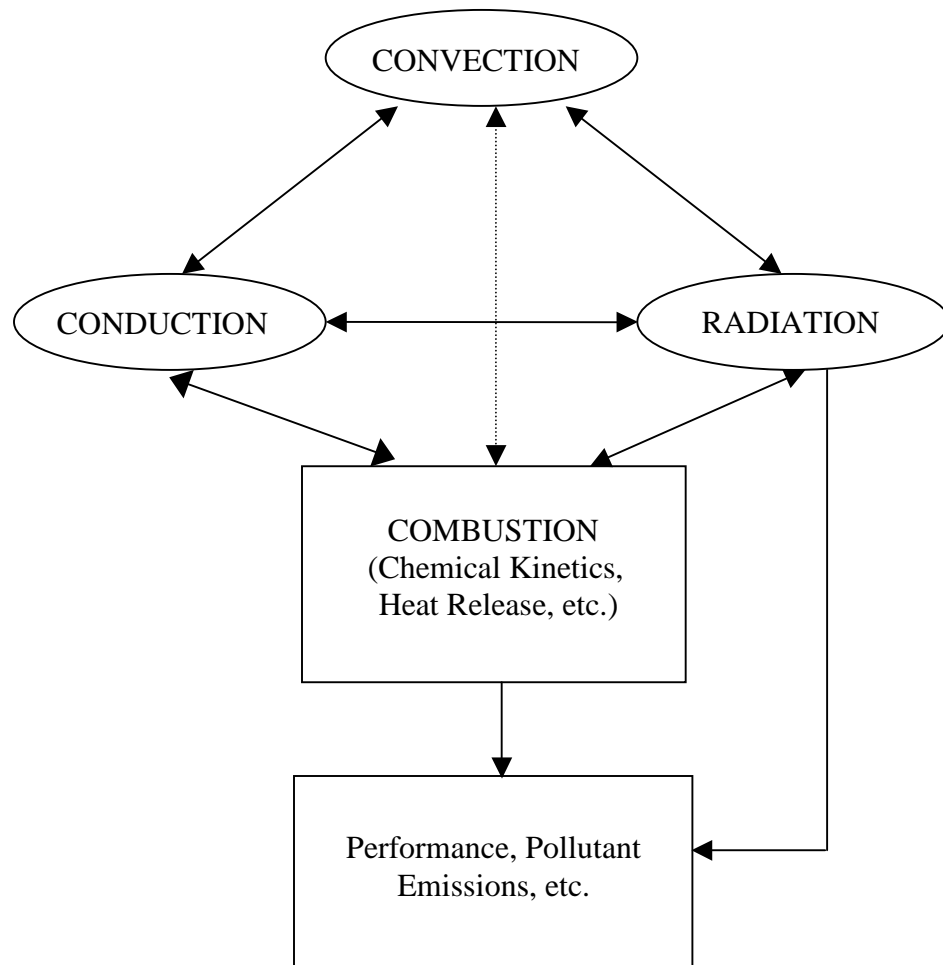


Figure 1.2 Interactions among different heat transfer modes and combustion in porous media

1.4 Literature Survey

1.4.1 Flow through Porous Media

Ergun (1952) studied the following factors that affect the pressure drop across a packed bed: (i) flow rate of the fluid, (ii) viscosity and density of the fluid, (iii) closeness (porosity) and orientation of packing, and (iv) size, shape, and surface area of the particles. Based on the experimental data, an empirical correlation for pressure drop in packed beds was formulated. The correlation could be used for a porous medium, if appropriate values were chosen for porosity and pore diameter.

Macdonald et al. (1979) evaluated the applicability of eight different pressure drop correlations for porous media. The results showed that the modified Ergun equation is applicable for a wide range of porosities 0.36 to 0.92. From their study, a correlation for friction factor was also proposed. Fand et al. (1987) experimentally studied different flow regimes in porous media of uniformly and randomly packed spheres. Reynolds numbers that characterized the flow transition were determined.

Civan and Evans (1996) determined permeability and the non-Darcy flow coefficient by solving a differential form of Forchheimer equation. The effect of core length of porous media was also studied. Civan and Evans (1998) compared the accuracy of pressure-squared and pseudopressure formulations of the Forchheimer equation.

Zeng and Grigg (2006) presented a revised Forchheimer number as a criterion for identifying the beginning of non-Darcy flow in porous media. The number

represented the ratio of pressure drop due to liquid-solid interactions to that by viscous resistance. Using the measured data on permeability and non-Darcy coefficient, the revised Forchheimer number was formulated.

1.4.2 Heat Transfer in Porous Media

Numerous investigations have been performed to understand heat transport in porous media. This section presents only a brief review of literature that are relevant to the current work. A more complete description of heat and mass transfer in porous media can be found in Wakao and Kaguei (1982), Kaviany (1995) and Vafai (2005).

1.4.2.1 Characterization of Heat Transfer Properties

Howell et al. (1996) reviewed correlations for estimating thermal conductivity, radiative coefficient, phase function, and convective heat transfer coefficient for partially stabilized zirconia (PSZ) based porous media. Viskanta and coworkers (Younis and Viskanta, 1993; Fu et al., 1997; Fu et al., 1998; Mital et al., 1998) developed methods to characterize the heat transfer properties of porous media.

Younis and Viskanta (1993) experimentally measured the volumetric heat transfer coefficients between air and highly porous ceramic foams of alumina and cordierite for different mean pore diameters. They presented Nusselt number correlations over a range of Reynolds numbers and sample thickness-to-mean-pore-diameter ratios.

Fu et al. (1997) presented a theoretical model to predict volumetric radiative properties. Results of extinction coefficients were compared with available experimental data. Porosity, reflectivity of the porous solid and the number of pores per inch were the three main factors affected the radiation properties. The extinction coefficient was found to decrease with an increase in reflectivity and/or porosity and increase with an increase in mean pore diameter.

Fu et al. (1998) developed theoretical models based on unit cell method to predict stagnant effective thermal conductivity of cellular ceramics. Results showed that the effective thermal conductivity was found to decrease with porosity. Model predictions were also compared with the available experimental data. Mital et al. (1998) described a procedure to measure the radiation efficiency (defined as the ratio between total radiative power emitted by the burner and the energy release rate) in radiant burners. The authors reported that radiative efficiencies were in the range of 20-35 %. They also showed that efficiencies above 45 % were not realistic.

Kamiuto and Yee (2005) developed a correlation for volumetric heat transfer coefficient between air and open-cell porous materials by compiling the experimental data of several researchers. The authors also presented a Nusselt vs Reynolds number heat transfer correlation.

1.4.2.2 Conduction and Convection Heat Transfer

Lee and Howell (1991) performed experimental and numerical studies on heat and mass transfer in highly porous media. Permeability was measured experimentally and the overall heat transfer coefficient was calculated numerically. Based on their experiments, they presented different correlations for Sherwood and Nusselt numbers.

Alazmi and Vafai (2000) presented a comprehensive analysis of various models used for studying the transport processes through porous media. Models with constant porosity, variable porosity, thermal dispersion, local thermal non-equilibrium were analyzed. Results showed that the differences between constant porosity and variable porosity models were negligible. Differences among the local thermal non-equilibrium models were significant only in the entry region. However, the models employing the dispersion effects showed different results depending on the inertia parameter.

Local thermal non-equilibrium models have been investigated by Nakayama and coworkers (Kuwahara et al., 2001; and Nakayama et al., 2001). Using a volume-averaged form of energy equation for solid and gas phases, the authors reported a correlation for the interfacial convective heat transfer coefficient to couple the equations. For one-dimensional problems, the equations were simplified to a fourth order ordinary differential equation. Using the model, fluid and solid temperature distributions were predicted.

Oliveira and Kaviany (2001) summarized the processes leading to thermal and chemical nonequilibrium in gaseous fuel combustion in porous media. Governing equations for phase change in porous media assuming local thermal non-equilibrium were derived by Dual et al. (2004) using volumetric averaging procedure. Three closed form energy equations (solid, liquid, and vapor) were developed in their study. The effective transport properties were related to the pore-scale physics.

1.4.3 Gaseous Fuel Combustion in Porous Media

During the past two decades, several investigations on the interactions between the heat transfer and combustion in porous media have been conducted. Viskanta (1995), Howell et al. (1996), and Kamal and Mohamad (2006a) presented comprehensive reviews on this topic. The authors reviewed the correlations for estimating the heat transfer properties of porous media as applied to combustion conditions. CO and NO_x emissions and radiant thermal efficiency were presented as functions of flame speed (Howell et al., 1996). This section presents a summary of some important investigations of gaseous combustion in porous media.

1.4.3.1 Flame Stabilization

Flame stabilization phenomenon in gas-fired porous burners has been studied by several investigators (Sathe et al., 1990a; and Sathe et al., 1990b; Lammers and de Goey, 2003; Barra et al., 2003; Mathis and Ellzey, 2003). Tong and coworkers (Sathe et al., 1990a; and Sathe et al., 1990b) studied the flame stabilization and multimode heat transfer in porous radiant burners. From their study, they concluded

that flame could be stabilized in the upstream half or near the downstream edge of the porous medium where the velocity profile exhibited positive slopes. Both radiative properties and thermal conductivity of the solid influenced the flame speed and burner stability.

Hsu et al. (1993) conducted experimental and numerical investigations on premixed gas (methane/air) combustion within porous media with different pore sizes. Results demonstrated that the flame speed and burning rates were much higher than those of an adiabatic laminar free flame. 2-D direct numerical simulations and volume-averaged simulations were carried out by Sahraoui and Kaviany (1994) for methane/air porous burners. Discrete solid-phase simulations showed that for $k_s/k_g = 1$, where k_s and k_g are the thermal conductivities of solid and gas, respectively the flame speed decreased as the porosity decreased. When k_s/k_g was increased, the flame speed also increased with a decrease in porosity. Continuous solid-phase simulations showed a higher flame speed than that of discrete solid-phase simulations.

Lammers and de Goey (2003) have conducted a numerical study on the flash back of the premixed flames stabilized on the surface of a ceramic burner. Stability diagrams and flash-back regimes were presented for flames stabilized inside and outside the burner in cold and hot environments. Results indicated that the volumetric heat transfer coefficient and effective material conductivity influenced the flash-back limits.

Barra et al. (2003) presented a one-dimensional numerical study in a two-section porous burner to understand the effects of materials properties on flame stabilization. The flame was stabilized at the interface between the two sections. Results showed that materials with low conductivity, small heat transfer coefficients, and large radiative extinction coefficients were desired for upstream section. For downstream section of the burner, high conductivity and large heat transfer coefficients were necessary to enhance the heat transfer. Mathis and Ellzey (2003) conducted an experimental study to measure the flame stabilization, operating range, and CO/NO_x emissions for two different methane-fueled porous burners. Though the CO/NO emission level was almost the same for both burners, the stable flame ranges were different.

Barra and Ellzey (2004) numerically studied the heat recirculation and heat transfer processes in methane-fired porous burners. They defined nondimensional numbers such as flame speed ratio, heat recirculation efficiency, preheat conduction efficiency, preheat radiation efficiency, and output radiant efficiency in order to quantify the recirculation processes. For each inlet condition, a stable velocity range was obtained (48 cm/s – 74 cm/s at an equivalence ratio of 0.65, for instance). Flame speed ratio increased with an increase in equivalence ratio. This enhancement in flame speed was due to both solid-to-solid radiation and solid conduction within the porous medium. At a low equivalence ratio of 0.55, conduction effects were dominant and radiation effects were negligible. Radiation effects became important at a higher equivalence ratio of 0.9 where the conduction effects became less important.

1.4.3.2 Pollutant Emission

Khanna et al. (1994) measured the emissions and radiation from a methane-fueled porous burner for different equivalence ratios and flow rates. With an increase in equivalence ratio ($\phi = 0.6$ to 0.87), NO_x concentration increased from 5 ppm to 30 ppm, CO emissions increased from 5 ppm to 120 ppm, and radiant thermal efficiency of the burner decreased. However, at a given equivalence ratio, NO_x emissions remained almost constant and CO emissions were strongly dependent on the flame location.

Ellzey and Goel (1995) presented the CO and NO emissions from a two-stage porous media burner with different methane-air mixture strengths. By appropriately choosing the equivalence ratios for the two stages, typical values of NO and CO emissions ranged from 17-30 ppm and 10-75 ppm, respectively. Results were also compared with single-stage burners and the authors concluded that the two-stage burners produced lower emissions than that of single-stage burners. Bouma et al. (1995) conducted experimental and numerical investigations of the NO emissions from ceramic foam surface burners. Computations included 25 reactions and 16 species for methane oxidation and 52 reactions and 28 species for nitrogen chemistry. The slopes of NO emission profiles were higher in the flame zone and became almost constant thereafter. NO emissions increased axially (above the surface of the burner) with an increase in thermal load. The NO profiles were found to depend on the type of chemical mechanism used.

Henneke and Ellzey (1995) modeled the filtration combustion of methane in packed beds with detailed chemical kinetics. Transient simulations were performed and the variations of solid and gas temperatures and mass fractions of methane (CH₄), carbon monoxide (CO), and carbon dioxide (CO₂) were presented along the axial direction of the burner. Simulation results showed that the wave propagation was affected by gas-phase dispersion at equivalence ratios above 0.6. Rumminger et al. (1996) predicted the gas temperatures above a porous burner and compared them with experimental values. Temperature measurements were obtained using an uncoated type-K thermocouple, OH-LIF, and laser absorption techniques. Results indicated that all of methane was consumed within the porous medium at a firing rate of 315 kW/m² and at an equivalence ratio of 0.9.

Zhou and Pereira (1997) numerically studied the combustion and pollutant formation of methane/air flames with detailed chemical kinetics. Effects of solid radiation, excess air ratio, and solid conductivity on NO and CO formation were analyzed. Results showed that the NO emissions decreased with an increase in solid conductivity. Because of the radiative heat feedback, the flame could be stabilized at the interface between two ceramic blocks with different porosity. Trimis et al. (1997) developed a combined porous media combustor and heat exchanger system with low emission and high energy density. The new system occupied only 1/20 of the existing burners and had a power modulation of 1 to 20. NO_x emissions were significantly affected by excess air ratio and less affected by heat load.

Bouma and de Goey (1999) reported an experimental and numerical study on premixed combustion on ceramic foam burners. Solid and gas temperatures, and CO and NO emissions were predicted and compared with experiments. CO and NO concentrations were found to increase with an increase in thermal load. Leonardi et al. (2003) performed theoretical and experimental investigations of interior combustion of methane and air in metal fiber burners/heaters. Results showed that the exit gas temperature and radiation efficiency of the burner increased when the firing rate and equivalence ratio were increased.

Kamal and Mohamad (2006b) studied burner stability, pollutant emission, and radiation intensity of swirling methane-air gaseous combustion in porous media. The burner sustained a lean equivalence ratio of 0.507 and yielded NO_x and CO emissions of 0-1 and 50 ppm, respectively. The swirl further increased the radiation intensity by 50%.

1.4.4 Spray Evaporation and Combustion

Spray combustion has been an active field of research over the past half-century with a pioneering contribution by Spalding (1952). Extensive reviews on spray evaporation and combustion are presented by Williams (1973), Law (1982), Faeth (1983), and Sirignano (1983). Recently, advanced models for droplet heating and evaporation (Sazhin, 2005) and drop evaporation in turbulent flows (Birouk and Gökalp, 2006) are reviewed.

Rao and Lefebvre (1976) derived an empirical relationship for kerosene evaporation by considering the effects of air temperature and velocity, axial distance from the injector, fuel injection pressure, and atomizer flow number. Banhawy and Whitelaw (1980) predicted the flow properties of a confined Kerosene-spray flame and compared with experimental measurements. Radial profiles of temperature and axial velocities were plotted at different axial locations.

Reitz and Bracco (1982) examined various atomization theories and reported experimental data obtained from fourteen different nozzles using five different liquids. Roles of several phenomena such as cavitation, liquid viscosity, injection velocity, velocity profile rearrangement, aerodynamic surface wave growth, and liquid turbulence were analyzed. Of these, the aerodynamic surface wave growth mechanism was able to explain the experimental results well. Aggarwal et al. (1984) studied the vaporization behavior of single-component isolated droplets using different liquid-phase (D^2 law, infinite conductivity, diffusion limit, and internal vortex circulation) and gas-phase models. The authors recommended the simplified vortex model when the droplet Reynolds number based on relative velocity is high compared to unity.

Presser et al. (1990) have analyzed the effects of physical and chemical effects of four different fuels on the structure of spray flames. Droplet size and velocity distribution were presented. The results showed that viscosity of the fuel had the largest influence in droplet mean size and velocity.

Card and Williams (1992) have presented two four-step reduced mechanisms (propane route and ethane route) for n-Heptane combustion from 22 starting mechanisms. With these reduced mechanisms, the flame structure and extinction were studied using rate-ratio asymptotics.

Runge et al. (1998) measured the diameter and temperature of decane, n-heptane, water, JP-4 and JP-8 droplets during evaporation. JP-4 and JP-8 droplets showed an initial rapid vaporization as lighter fractions vaporized, followed by slower vaporization due to the vaporization of heavier components. Schmidt et al. (1999) described an atomization model, based on linearized instability analysis for pressure-swirl injectors. This model primarily employed the knowledge on external spray characteristics. Applicability of the model to predict Sauter mean diameter and spray penetration was demonstrated.

Benaissa et al. (2002) modeled the evaporation of multi-component fuel blends such as JP-4 and Jet-A1. Droplet diameter and temperature during evaporation were predicted. It was found that during the initial phase of droplet evaporation forced convection caused the evaporation of lighter fractions. After this short period, the droplet evaporation followed the classical D^2 -Law. Widmann and Presser (2002) presented reference experimental data on methanol spray flames. Spray characteristics such as droplet size, velocity, volume flux, and species concentration were presented for validating computational models.

Gomez and Russo (2006) reported the physical characterization of the structure of ethanol/argon/oxygen coflow laminar spray diffusion flames. The authors reported the droplet size and axial and radial velocity components of the droplets. Scaling and self-similar analysis of the flames revealed a momentum-controlled cold core and a buoyancy-controlled high temperature boundary layer.

1.4.5 Liquid Fuel Combustion in Porous Media

Haack (1993) numerically studied the evaporation and combustion of single Decane droplets in porous media. Evaporation enhancement due to radiative heat transfer from combustion porous media was studied. Radiation from porous medium increased the vaporization rate and droplets deviated from the standard D^2 -Law. Flame speeds of premixed Decane flames in porous media were found to be at least twice higher than that of the free flames.

Kaplan and Hall (1995) conducted an experimental study using liquid fuels in porous media. Four different designs of heptane-fueled radiant burners were tested to analyze the stable operating ranges and measure the emission characteristics. An air-blast atomizer with a full cone spray pattern (spray angle of 60°) was used to inject the fuel. Stable combustion was achieved over the equivalence ratio range of 0.57-0.67. The study reported that burner stability was primarily affected by the droplet size and the distance between the porous medium and nozzle. The study did not show any evidence for plugging of the porous medium by liquid fuels. Emission

measurements indicated that combustion was complete and the emissions were found to be as low as 3-7 ppm and 15-20 ppm for CO and NO_x, respectively.

Tseng and Howell (1996) investigated liquid fuel combustion in porous media numerically and experimentally. Multi-step chemical kinetics for n-heptane was included in the numerical code. The initial droplet size did not affect the burning rate, since all the droplets were completely vaporized before the flame front. Flame stabilization was achieved as low as an equivalence ratio of 0.3. They reported CO and NO_x emissions of less than 10 ppm and 15-20 ppm, respectively.

Martynenko et al. (1998) mathematically analyzed the one-dimensional, self-sustaining combustion in inert porous media with all modes of heat transfer. Droplet collisions with porous medium were modeled using a collision probability, which depended on particle Stokes number. Predicted axial profiles of solid, gas, and liquid temperatures, and mass fractions of liquid and vapor were presented.

Jugjai et al. (2002) studied the evaporation and combustion characteristics of a kerosene-fueled, atomizer-free burner. The fuel was supplied drop-wise using a syringe. Flame stabilization was achieved by inducting a stream of swirling air. Combustion characteristics were obtained by measuring the temperature profile. Complete vaporization with effective vapor preheating was reported. Stable combustion was achieved at an equivalence ratio range of 0.37-0.55 at a thermal input

range of 2.62-3.49 kW. The effects of equivalence ratio, optical thickness of the porous medium and thermal input on combustion characteristics were also elucidated.

Park and Kaviany (2002) mathematically analyzed the characteristics of a diesel engine equipped with an in-cylinder porous regenerator. Droplet evaporation and interactions with regenerator were included in the model. Droplet-Regenerator interactions and air preheating due to upstream radiation enhanced the fuel evaporation. Increased superadiabatic temperature further enhanced the evaporation and increased the peak pressure, which corresponded to an increase in efficiency. A thermal efficiency of 53% was reported, while the efficiency of conventional Diesel engine was 43%.

Jugjai and Polmart (2003) described a novel down-flow, atomizer-free porous burner. Axial temperature profile in the porous burner and emitter was measured. Effects of heat input, equivalence ratio, porous bed height, and the distance between porous burner and emitter on combustion characteristics were analyzed. Stable combustion was achieved as low as an equivalence ratio of 0.2. NO_x emissions were lower than 160 ppm and CO emissions found to be dependent on the operating conditions and porous bed emitter height.

1.5 Specific Objectives of the Present Work

The aforementioned literature survey suggests that the amount of research that has been done on the combustion of liquid fuels, especially on the characterization of evaporation enhancement and its interactions with combustion is limited. This dissertation seeks to advance the understanding of evaporation and combustion processes in porous media. Both fundamental and applied studies have been conducted. The following are the specific objectives of this research:

- To quantify evaporation enhancement rate due to combustion in porous media
- To measure minimum heat feedback rate required for complete vaporization
- To delineate the effects of different fuels on evaporation enhancement
- To develop a local thermal non-equilibrium computational model to predict evaporation characteristics of liquid spray in porous media
- To predict vapor concentration distribution downstream of porous media
- To conduct a detailed parametric study to understand the effects of heat feedback rate, porous medium structure, coflow air inlet temperature, and fuel flowrate on evaporation characteristics
- To establish regimes of operation of surface and interior combustion spray flames
- To study interactions between evaporation and combustion
- To measure pollutant emission characteristics of interior combustion flames

1.6 Methodology

A series of experimental and computational studies has been devised to meet the objectives stated in Section 1.5. Evaporation experiments were first performed by simulating the combustion heat feedback rate using an electric resistive heating. Next, combustion experiments were performed to study the interactions between evaporation and combustion. Computational simulations of evaporation enhancement have also been performed and compared with experimental measurements. The methodology adopted in the study is outlined below:

Evaporation Experiments in Simulated Combustion Environment:

1. To measure droplet characteristics such as diameter, axial velocity, and mass flux upstream of the porous medium
2. To measure vapor concentration profiles downstream of the porous medium
3. To measure minimum heat feedback rate required for complete vaporization
4. To study the effects of different fuels on the evaporation enhancement in porous media

Combustion Experiments:

1. To determine stable operating regimes of surface and interior combustion of liquid fuels in porous media
2. To study the interactions between evaporation and porous media
3. To measure global emissions of CO and NO

Computational Work:

1. To computationally investigate the evaporation and combustion of liquid spray in porous media with a local thermal non-equilibrium model

1.7 Scope of the Present Work

The present work is motivated by the need of a detailed study of evaporation enhancement and its interactions with combustion in porous media. Three fuels and five porous media were chosen for this purpose. In conjunction, a computational model was also employed. Using measured and/or predicted data, a general understanding of evaporation and combustion has been developed.

Evaporation enhancement was experimentally studied in a simulated combustion environment. This simulated heat feedback was later replaced with direct burning of liquid fuels inside porous media. Computational model solved for gas and solid phase temperatures in porous media. Combustion heat feedback rate was modeled as a uniform volumetric heat source in the porous medium. Further assumptions and restrictions of the computational model are given in Chapter 3.

A physical model has been developed for the combustion of liquid fuels in porous media. Using the model, the interactions between combustion and evaporation were explained. Regimes of burner operation and emission characteristics were also determined.

1.8 Organization of the Dissertation

This chapter presented an overview of evaporation enhancement and combustion in porous media. A comprehensive literature review and specific objectives of the present work are also presented in this chapter. Chapter 2 presents the experimental setup, procedure and instrumentation used in this study. Description of the computational model is given in Chapter 3. Experimental and computational results on evaporation enhancement in porous media are discussed in Chapter 4. Combustion of liquid fuels and its subsequent interactions with evaporation are presented in Chapter 5. Conclusions and recommendations for further study are given in Chapter 6.

Chapter 2

Experimental Details

2.1 Introduction

This chapter presents various experimental techniques employed to study evaporation enhancement and combustion in porous media. The porous media burner setup and the different components of the experimental setup are discussed in detail. The experimental arrangement for measuring various quantities is described. The experimental procedure is outlined. A brief description of the data acquisition system is also included in this chapter.

2.2 Experimental Setup

2.2.1 *Laboratory Combustion Chamber*

All the experiments were conducted at the University of Oklahoma Combustion and Flame Dynamics Laboratory. A vertical steel test chamber of 76×76 cm cross section and 163 cm height was used to house the experimental setup. The setup consisted of housing for evaporation and combustion porous media, rectangular glass test sections, fuel supply system, and coflow air preheating system. A schematic of the combustion chamber and experimental setup is shown in Fig. 2.1a. Three walls of the test chamber were fitted with Pyrex plate glass windows (25×135 cm) and the fourth wall was fitted with a slotted metal sheet to provide the access to the measurement probes. A base plate with a square opening of side 11 cm was fitted at the bottom of the test

chamber. The porous medium housing sections were mounted on the base plate and the air settling chamber was located immediately below the base plate. The top of the test chamber was open to atmosphere through an exhaust duct. The ambient pressure inside the lab was maintained slightly above atmospheric pressure to ensure the presence of a positive draft inside the test chamber. This prevented the leaking of products of combustion into the main laboratory facility. The dimensions of the test chamber, porous media, and nominal operating conditions are listed in Table 2.1. A photograph of the experimental setup is shown in Figure 2.1b.

2.2.2 Test Porous Media

Open-cell silicon carbide coated carbon-carbon matrix porous media of cross section 4.3×4.3 cm and a height of 2.5 cm were used in this study. Porous media with different pores per centimeter (PPCM) were used. All porous media had a porosity of about 87%. Figure 2.2 shows the photographs of 8 and 31 PPCM porous media used in the experiments. Typical properties of porous media are listed in Table 2.2. Porous media with larger PPCM such as 25 and 31 were used as evaporation porous media (EPM) and the ones with smaller PPCM such as 8 and 12 were used as combustion porous media (CPM). The EPM also acted as a flame arrestor during combustion experiments.

2.3 System Components

2.3.1 Coflow Air Preheater

The coflow air was obtained from a university-wide compressed air source. It was filtered using a 0.1-micron filter and metered using a calibrated rotameter. The calibration chart for the rotameter is presented in Appendix A. Figure 2.3 shows the coflow air supply and heater setup. The air was dried by passing it through a packed bed of calcium sulphate (desiccant). A high throughput electrical heater (Model: Sylvania SUREHEAT 36,000) connected to a variable power supply unit and temperature controller was used to preheat and deliver high temperature air to the test section. The heater allowed us to set the desired temperatures (up to 1000 K) of the output air. The flow lines were wrapped with pipe insulation material to minimize the heat loss.

2.3.2 Air Settling Chamber

From the preheater, the hot air was admitted to an insulated aluminum settling chamber from its sides. The settling chamber measured 10x10 cm cross section and 10 cm height. The chamber was filled with glass marbles of 5 cm diameter to attain a uniform flow at the exit. Figure 2.4 shows the schematic diagram of the settling chamber. Also shown in this figure is the fuel injector setup. The injector setup is described in detail in the following section (Section 2.3.3). To the bottom of the chamber, the fuel supply pipe was attached using a hub and boss arrangement and setscrew. The injector protruded into the test section. Further, it could be moved up and down inside the chamber and locked in position using the setscrew.

2.3.3 Fuel Supply System and Injector Arrangement

Three fuels were used in the experiments: aviation-grade kerosene, n-heptane, and methanol. Important properties of these fuels are listed in Table 2.3. Figure 2.5a shows a schematic diagram of fuel supply system. Each fuel was stored in a nitrogen-pressurized tank, and was then drawn from the tank, metered using a calibrated rotameter (see Appendix A for calibration chart), and supplied to the injector. A solid cone air-blast type injector was procured (Delavan Model No. 3060-1) and modified to fit into the present experimental setup. Figure 2.5b shows a schematic diagram of the injector. The injector was attached to one end of a cylindrical pipe. The Figure 2.4 shows the injector setup with the cylindrical pipe and air settling chamber. The fuel and atomizing air were brought in as separate streams and admitted to the cylindrical pipe at its bottom using a Tee-connection. While the fuel was supplied to the injector using a stainless steel tube located inside the cylindrical pipe, the atomizing air was supplied through the annulus region between the cylindrical pipe and stainless steel tube.

2.3.4 Porous Media Housing

The evaporation porous medium (EPM) was housed in an aluminum block of cross section 10x10 cm and a height of 2.5 cm. A schematic diagram of the porous medium housing is shown in Fig. 2.6. The aluminum block had a provision to introduce the electrical wires to the electrodes attached to the EPM. The porous medium was insulated from its housing using electrically non-conductive insulating material.

2.3.5 Test Section

The following three test sections were used in the study.

- (i) Borosilicate glass test section
- (ii) Stainless steel test section
- (iii) High temperature glass test section

Table 2.4 lists the location and purpose of these test sections in the experimental setup. The test sections were of 5 x 5 cm inside cross-section and 25 cm height. The thickness of borosilicate glass used in the test section was 4 mm. Two test sections were installed on each side of the porous medium housing (upstream and downstream). The injector protruded into the upstream test section. This upstream test section also provided optical access to the spray-diagnostic instruments. Figure 2.7 presents the velocity profile, measured using pitot static tube, at the exit of the upstream test section. The figure suggests that the flow at the exit of the test section is uniform within $\pm 4\%$ of average velocity. The small drop in the velocity at the center of the test section is due to the presence of the injector. The downstream stainless steel test section provided access to sampling probes during vapor concentration measurements. The evaporated fuel vapors were flared using a pilot flame at the exit of the downstream test section. Stainless steel, porous disk flame arrestors were installed to prevent the propagation of the flame into the evaporation test section. During the combustion experiments, the downstream glass test section was made up of a high-temperature Vycor[®] glass test section. The properties of borosilicate and Vycor[®] glasses are presented in Table 2.5.

2.3.6 Porous Media Heating Setup

For evaporation experiments, a resistive heating mechanism was installed to simulate heat feedback rate from combustion zone. This enabled us to vary the heat feedback rate in a controlled manner. Figure 2.8 shows a schematic diagram of porous medium heating setup. Two copper plates were placed flush on opposite sides of the porous medium using an electrically-conductive high-temperature cement. A DC power source was used to supply the required electric field across the copper plates i.e., transverse to the flow direction inside the porous medium. The porous medium itself was used as the resistive element owing to its high electrical resistance. Depending upon the desired heat feedback rate, the wattage output of the power source could be set. An electrically non-conductive high temperature gasket sheet was wound around the porous medium to insulate it from the housing.

2.3.7 Pilot Flame

A pilot flame was used for two purposes: (i) to flare the vapors during the evaporation experiments, and (ii) to initiate the combustion in the porous medium. Figure 2.9 shows a schematic diagram of the pilot flame setup. A stainless steel tube of internal diameter of 2 mm was used as the burner and commercial quality liquefied petroleum gas was used as the fuel. A needle valve was used to control the flowrate of the fuel.

2.4 Instrumentation

Several conventional and optical instruments were used to study the evaporation and combustion in porous media. A comprehensive list of the instruments and their purposes is given in Table 2.6. A brief description of each instrument and operating procedure is presented below.

2.4.1 *Phase Doppler Particle Analyzer*

The droplet characteristics, upstream of the evaporation porous medium, were obtained in situ using a single-component Phase Doppler Particle Analyzer (PDPA). PDPA measures the droplet characteristics such as the Sauter mean diameter (SMD), liquid mass flux, particle number density and mean axial velocity. In PDPA, two collimated laser beams are focused at the measurement location. The droplets passing through this intersection scatter light and produce a far-field fringe pattern that moves past a set of three detectors at the Doppler-shifted frequency. By measuring the spatial and temporal frequency of the fringe pattern, the droplet diameter and velocity can be measured. Detailed information about the theory of operation of PDA instrument can be found in Goldstein (1996).

A schematic diagram of the PDPA system is shown in Fig. 2.10. The instrument had two major sets of optics (a) transmitting optics; (b) receiving optics. These were mounted on separate three-dimensional traversing tables and placed on either side of the test section. A helium-neon laser beam (wavelength = 632.8 nm) was used as the light source. A manufacturer-supplied software (PDPA v3) was used to control the

beam spacing, set velocity offset, and collect Doppler signals. The instrument was configured for forward scattering mode to acquire the scattered signals from droplets. Major specifications of the instrument are provided in Table 2.7.

2.4.2 Infrared Camera

An infrared camera was used to obtain the image of the porous medium surface temperature during evaporation and combustion. The instrument uses mercury-cadmium-telluride detectors in a sealed, evacuated enclosure. The detector is maintained at 77 K by liquid nitrogen for maximum thermal sensitivity and high spatial resolution. A two-dimensional image of the surface temperature is achieved by horizontal and vertical scanning. Specifications of the instrument are given in Table 2.8. A gold plated mirror (96 % reflectivity in the wavelength range of 750 nm - 1500 nm) was placed above the glass test section containing the porous medium at an angle of 45° to the chamber axis to deflect the infrared radiation to the camera (Fig. 2.11).

2.4.3 Minimum Heat Feedback Rate Measurements

A helium-neon laser beam was expanded as a laser sheet using a cylindrical glass rod. The laser sheet was shined at a location downstream of the evaporation porous medium. If the evaporation was not complete, some droplets would be present and scatter light. In that case, the porous medium was externally heated till the vaporization was complete. The external heating simulated the heat feedback rate during combustion. The minimum heat feedback rate required for complete

vaporization could then be determined. The definition and detailed measurement procedure of minimum heat feedback rate are presented in Section 4.5.

2.4.4 Vapor Concentration Analyzer

Vaporized fuel concentration downstream of the evaporation porous medium was measured using an organic vapor analyzer with a catalytic oxidation sensor. A schematic diagram of the vapor concentration measurement setup is shown in Fig. 2.12. Vapor samples from the test section were drawn using a stainless steel probe with an internal diameter of 0.5 mm. The probe and flow lines were heated using electrical heating tape to prevent any potential condensation of vapor. The reaction chamber of the organic vapor analyzer was separated from the instrument and also held under heated environment.

2.4.5 Temperature Measurement

Temperature measurements were taken at the following locations in this study:

- (i) Coflow air temperature measurement and feedback control
- (ii) Temperature along the wall of the porous media
- (iii) Temperature inside the combustion porous medium
- (iv) Combustion gas temperature above the porous medium

All temperature measurements were taken using K-type (Chromel-Alumel) and R-type (Platinum-Platinum 13% Rhodium) thermocouples. Two sets of thermocouples were made in-house. Thermocouples with wire and bead diameters of 0.5 mm and

150 μm , respectively were used for coflow air temperature and combustion gas temperature measurements. Porous media temperature measurements were taken with thermocouples of wire and bead diameters of 0.4 mm and 450 μm , respectively. The data collection procedure is explained in Section 2.6.

2.4.6 Combustion Gas Analyzers

The global emissions of CO, NO, and concentrations of CO₂ and O₂ were measured with a series of gas analyzers. A schematic diagram of the combustion gas analysis setup is shown in Fig. 2.13. Gas samples were collected using a Pyrex cone placed above porous medium. The use of a cone ensures that the total combustion products are collected and well-mixed. An uncooled quartz sampling probe with an internal diameter of 2 mm was placed at the top end of the cone. Solid particulates and other sooty substances in the gas sample were filtered using a coarse (glass wool) and 0.1-micron particulate filters. The sample was also passed through a glass condenser placed in an ice bath. A vacuum pump was used to draw the sample and the flowrate of the sample gas was monitored with a rotameter.

Concentrations of CO and CO₂ were measured using a non-dispersive infrared analyzer. NO concentrations were measured using a Chemiluminescence NO-NO₂-NO_x Analyzer. Oxygen concentrations were measured with a Polarographic sensor. From the measurements, the global emission index was calculated as follows (Turns, 2000, p. 554):

$$\text{Emission index of species } i, EI_i = \frac{X_i}{X_{CO} + X_{CO_2}} \cdot \frac{x MW_i}{MW_{fuel}} \quad (2.1)$$

where,

X_i - mole of fraction of the species of interest

X_{CO} - CO mole fraction

X_{CO_2} - CO₂ mole fraction

x - number of carbon atoms per mole of fuel

MW_i - molecular weight of the species of interest

MW_{fuel} - molecular weight of the fuel

2.4.7 Pressure Drop and Velocity Measurements

Pressure taps were made at two locations in the test section: 30 cm from upstream surface on each side of the evaporation porous medium. The pressure drop across the porous medium was measured using a water-column U-tube manometer (Fig. 2.14). The velocity of coflow air was measured with a pitot static tube. The pitot static tube was connected to an electronic manometer to measure the local dynamic pressure. From the knowledge of local density, the local gas velocity was calculated using Bernoulli's equation, as follows:

$$\text{Local velocity, } v = \sqrt{\frac{2(P_2 - P_1)}{\rho}} \quad (2.2)$$

where,

P_1 - static pressure

P_2 - stagnation pressure

ρ - local density

2.4.8 Flame Radiation

The radiation emission from flames was measured using a pyrhelimeter. The instrument has a sensitivity value of 28.4 W/m²/mV. Data were averaged and corrected for background radiation. The analog voltage output was converted into radiative heat flux using a calibration chart provided by the manufacturer. From the radiative flux, the radiant heat fraction was calculated as follows (Brzustowski et al., 1975):

$$\text{Radiant heat fraction, } F = \frac{4\pi l^2 R}{\dot{m} \text{LHV}_f} \quad (2.3)$$

where,

l - distance between the flame and pyrhelimeter

R - radiative heat flux

\dot{m} - mass flowrate of fuel

LHV_f - lower heating value of fuel

The instrument was located at a distance sufficient enough to treat the flame as a point source [inverse square law, Brzustowski et al. (1975)].

2.5 Test Matrix

Table 2.9 describes the various experiments performed. All the experiments could be categorized as follows:

- (i) Evaporation experiments in porous media
- (ii) Combustion experiments in porous media

2.6 Experimental Procedure

The procedure adopted depends on the type of experiment and the specific parameters of interest. While a detailed measurement procedure is presented later in the appropriate sections, a general procedure followed during the measurements is given below:

Start up:

- First, the coflow air preheater was turned on.
- It took an average of 1½ hour to reach a steady temperature of 450 K in the test section.
- The supply pressure of air was maintained constant throughout the experiments.
- The flow rate of air was set to produce the desired velocity in the test section using a calibrated rotameter.
- The liquid fuel tank was pressurized using compressed nitrogen.

- The propane pilot flame was ignited downstream of the porous medium.
- The flow rate of liquid fuel was set at the desired value.
- The flow rate of atomizing air was set to attain a steady spray.
- Once the fuel was continuously supplied and the vapors started to burn, the propane pilot flame was turned off.

Shutdown:

- The propane pilot flame was again ignited downstream of the porous medium.
- The liquid fuel flow was shut down.
- The pilot flame was turned off after it completely burned off all the fuel vapors.
- The fuel tank was depressurized.
- The coflow air preheater was turned off and the air flow rate was continued until the heating elements were brought to room temperature.

2.7 Data Management

2.7.1 Data Acquisition System

The data acquisition system consisted of National Instruments' LabVIEW 7.1 data acquisition software, signal-conditioning device SCB-100 and a PC interface card PCI 3122-E. SCB-100 both accepts and generates analog and digital signals. The output data from the instruments were directly fed to this device, which were then transferred to a desktop computer via the PCI 3122-E interface card. Figure 2.15

describes a typical setup of the data acquisition system. The thermocouples (set up in the porous medium to study the temperature variation during combustion) were connected to SCB-100. The analog voltage signals from the instruments, such as the electronic manometer and radiometer, were also connected to SCB-100. Further, the SCB-100 device generated digital signals for controlling stepper motor.

For spray diagnostics, a manufacturer-supplied software, PDPA v3 was used. This software acquires and conditions the data. Data were acquired for the entire conditions given in the test matrix. The data were stored in a personal computer with appropriate naming conventions.

2.7.2 Data Analysis and Integration

The test matrix presents an overview of the experiments performed in this study. The pressure drop measurements are used to obtain fluid mechanic characteristics such as viscous resistance and inertial coefficient of the porous medium. Such results are useful in modeling of flow through porous media. The temperature characteristics with simulated heat feedback rate (measured with thermocouple and IR camera) are essential to understand the temperature uniformity of the porous medium during combustion process.

The spray diagnostic data such as velocity, droplet size, and mass flux of liquid fuel are used to establish initial conditions of the spray before entering the porous medium. These data are used to determine the role of droplet size distribution during

evaporation and combustion in porous media. The evaporation enhancement in porous medium could be understood with the knowledge of vapor concentration data and droplet characteristics upstream of the porous medium.

The stability experiments provide the operating limits of combustion in porous media. Global emission measurements explain the pollution characteristics and the effectiveness of combustion in porous burners. Numerical simulations are useful to predict evaporation and combustion processes in porous medium. Such computational models are used to conduct parametric studies, which could provide immediate results over a range of test conditions. Thus, the experimental and numerical results were used to understand the role of porous medium in the evaporation enhancement and combustion of liquid fuels.

Appendix B shows a sample calculation of parameters involved in the evaporation enhancement and combustion in porous medium from measured data. Uncertainties in experimental measurements were computed using statistical theory. Appendix C presents a description of the uncertainty analysis and a sample uncertainty calculation procedure.

2.8 Chapter Summary

This chapter described the experimental setup used in studying the evaporation and combustion of liquid sprayed upstream of porous media. Various instrumentation

used and procedure followed to collect the data were explained. A brief description of data collection, analysis, and integration were also presented in this chapter.

Table 2.1 Combustion chamber dimensions and nominal ambient conditions

Parameter	Value
<i>Test chamber:</i>	
Test chamber dimensions	Cross section: 76×76 cm Height: 163 cm
Pyrex glass plate window	25×135 cm
Porous medium housing	Cross section: 5×5 cm Height: 25 cm
<i>Porous media: (Manufacturer – Ultramet[®])</i>	
Pores per centimeter	31, 25, 18, 12, and 8
Cross-section	4×4 cm
Thickness	2.5 cm
Porosity	87 %
<i>Ambient conditions (on a typical winter day):</i>	
Ambient pressure	102 kPa
Ambient temperature	21 °C
Humidity	42 %
<i>Operating conditions:</i>	
Fuels	Kerosene, n-Heptane; Methanol
Fuel tank pressure	0.34 atm (gauge)
Injector type (Delavan Model 3060-1)	Solid cone
Spray angle	40°
Atomizing air flow rate	4-8 l/min
Coflow air flow rate	75-195 l/min
Coflow air velocity	1-3 m/s
Fuel tank pressure	0.34 atm (gauge)
Temperature of the secondary co-flow	Cold-450 K
Reynolds number (based on test section dimensions and coflow air velocity at 450 K)	5600

Table 2.2 Typical properties of porous medium

Property	Value	Units
Bulk density	0.1-1.45	g/cm ³
Ligament density	3.2	g/cm ³
Surface area	0.08	m ² /cm ³
Specific heat	0.34	cal/g/°C
Maximum use temperature	1700	°C
Thermal conductivity	1-3	W/m-K
Porosity	87	%
Number of pores per centimeter	8-31	-

Table 2.3 Important properties of the fuels used in the study

Property	Kerosene (Jet A)	n-Heptane	Methanol
Type	Multi-component	Paraffin	Alcohol
Chemical formula	C ₁₂ H ₂₃	C ₇ H ₁₆	CH ₃ OH
Number of carbon atoms	12	7	1
C/H	0.52	0.44	0.25
Molecular weight	167	100.20	32.04
Specific gravity	0.81	0.684	0.792
Boiling temperature, K	477	371	338
Const. pressure heating value (Higher), MJ/kg	43.4	48	22.7
Const. pressure heating value (Lower), MJ/kg	42.8	44.6	20.1
Latent heat, kJ/kg	350	316	1170
Stoichiometric air-fuel ratio	14.7	15.2	6.4

Table 2.4 Uses of different test sections in the experiment

Experiment	Upstream	Downstream
Spray diagnostics	Borosilicate glass test section	Borosilicate glass test section
Minimum heat feedback	Borosilicate glass test section	Borosilicate glass test section
Vapor concentration	Borosilicate glass test section	Stainless steel test section
Combustion	Borosilicate glass test section	High temperature glass test section

Table 2.5 Properties of Borosilicate and Vycor[®] glasses *

Property	Borosilicate	Vycor[®]
Density	2.23	2.18 g/cm ³
Strain point	~510 °C	890 °C
Annealing point	560 °C	1020 °C
Softening point	815 °C	1530 °C
Thermal expansion (0-300° C)	3.3 x10 ⁻⁶ /°C	7.5 x 10 ⁻⁷ / °C
Refractive index	1.474	1.458
Continuous operating temperature	230 °C	900 °C

*Supplied by the manufacturer

Table 2.6 List of instruments and their purposes

Instrument	Type	Manufacturer	Model	Range	Purpose
Camera	Digital SLR	Canon	EOS Digital Rebel XT EF-S 18-55	Shutter speed: 1/4000 – 30 s	Flame imaging
PDPA	Light scattering	Aerometrics (Now TSI Inc)	XMT-1100-5 RCV-2100-2 MCB-7100-5 DMS-4000-5 PDPA v3.57	Overall size range: 0.5 – 3000 μm	Velocity and diameter of droplets
Infrared camera	Infrared	Inframetrics	600	-20 – 1000 $^{\circ}\text{C}$ [Extended]	Surface temperature
Vapor concentration analyzer	Catalytic oxidation	Bacharach	0023-7350	0 – 10,000 ppm	Vapor concentration
Thermocouple	K	Omega			Temperature
NO Analyzer	Chemiluminescence	Thermo Environmental	42H	0-5000 ppm	NO concentration
CO Analyzer	NDIR	Rosemont Analytical	880 A		CO concentration
CO ₂ Analyzer	NDIR	Rosemont Analytical	880 A		CO ₂ concentration
O ₂ Analyzer	Polarographic	MSA	MiniOX I	0-22%	Oxygen concentration
Manometer	Electronic	Datametrics	Model 1174		Pressure
Radiometer	Pyroheliumeter	Hy-Cal		Wide angle (150 $^{\circ}$)	Radiation
Data-acquisition Hardware		National Instruments	SCB-100		Data acquisition interface
Data acquisition Software		LabVIEW	Version 7.0		Data acquisition Software
Computers	Pentium IV	Dell			Computer
Other instruments/devices: Pitot static tube, U-tube manometer, rotameters, traverse mechanism, sampling probes, and oscilloscope					

Table 2.7 Major specifications of PDPA instrument

Parameter	Value	Units
<i>Overall Settings:</i>		
Collimating lens	300	mm
Transmission lens	500	mm
Receiver aperture	100	μm
Collection angle	30° reflecting particles	
Photomultiplier tube voltage	450 – 550	V
<i>Specific Settings:</i>		
Velocity Offset	0.0	m/s
Velocity Range	7.39 – 98.98	m/s
Velocity Minimum	0	m/s
Velocity Maximum	97	m/s
Measurement Range	7.39-97	m/s
Diameter Range	0.8 – 103.3	μm
Diameter Maximum	100	μm
Measurement Range	2.9 – 100.0	μm

Table 2.8 Major specifications of infrared camera

Parameter	Value	Units
Distance between detector and mirror	54	cm
Filter	Open – Extended	-
Background temperature	25	°C
Emissivity	1.0	-
Image averaging	16 Frames	

Table 2.9 Test matrix

Fuel	PM Type	T_{coflow}	Injector location	Stabil-ity	Temper-ature	Emissi-on	Radia-tion	Veloci-ty
Kerosene	65-30	450 K	2 cm	✓				
			3-6 cm	✓	✓	✓	✓	✓
Kerosene	80-20	450 K	2 cm	✓				
			3-6 cm	✓	✓	✓	✓	✓
n-Heptane	65-30		2 cm	✓				
			3-6	✓	✓	✓	✓	✓
n-Heptane	80-20		2 cm	✓	✓	✓	✓	✓
			3-6	✓	✓	✓	✓	✓
Methanol	65-30		2 cm	✓	✓	✓	✓	✓
			3-6	✓	✓	✓	✓	✓
Methanol	80-20		2 cm	✓	✓	✓	✓	✓
			3-6	✓	✓	✓	✓	✓

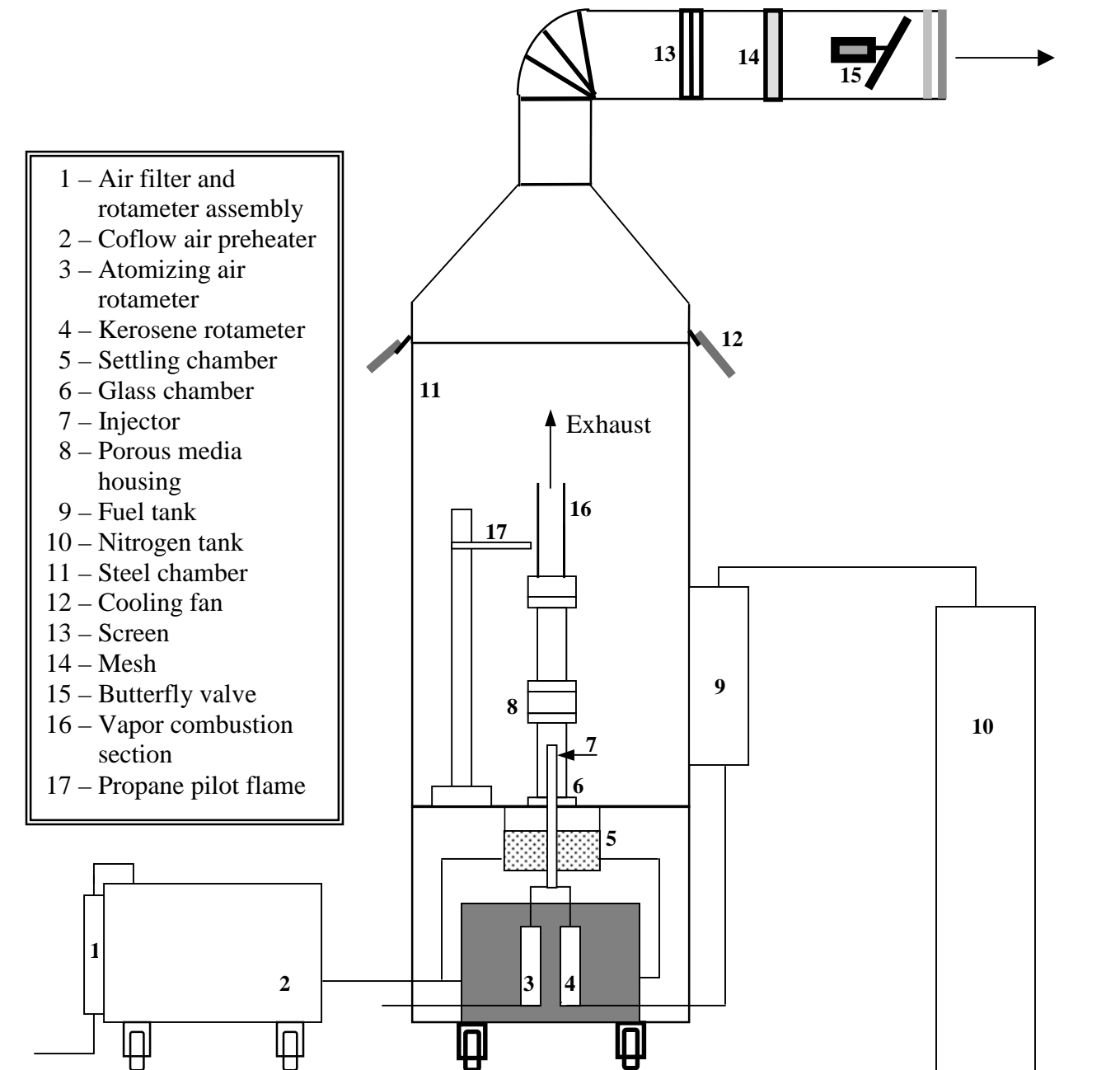


Figure 2.1a Schematic diagram of experimental setup



Figure 2.1b Photograph of the experimental setup (Shown here is a typical minimum heat feedback measurement experiment)

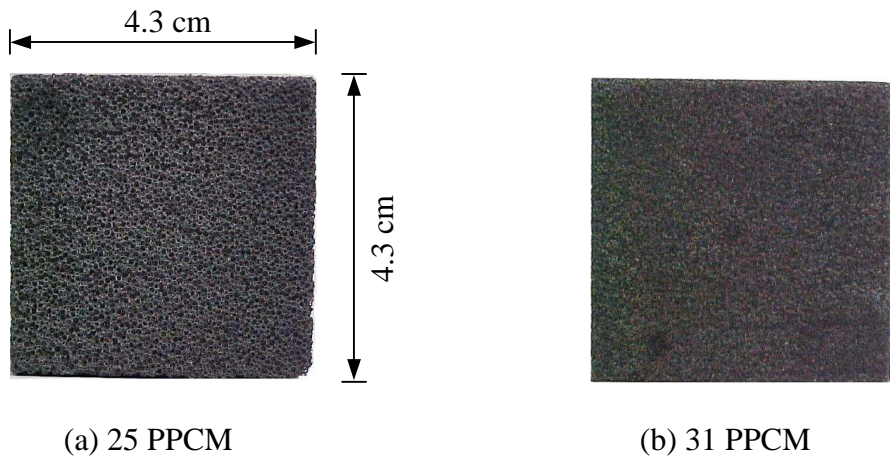


Figure 2.2 Photographs of the porous media used in experiments

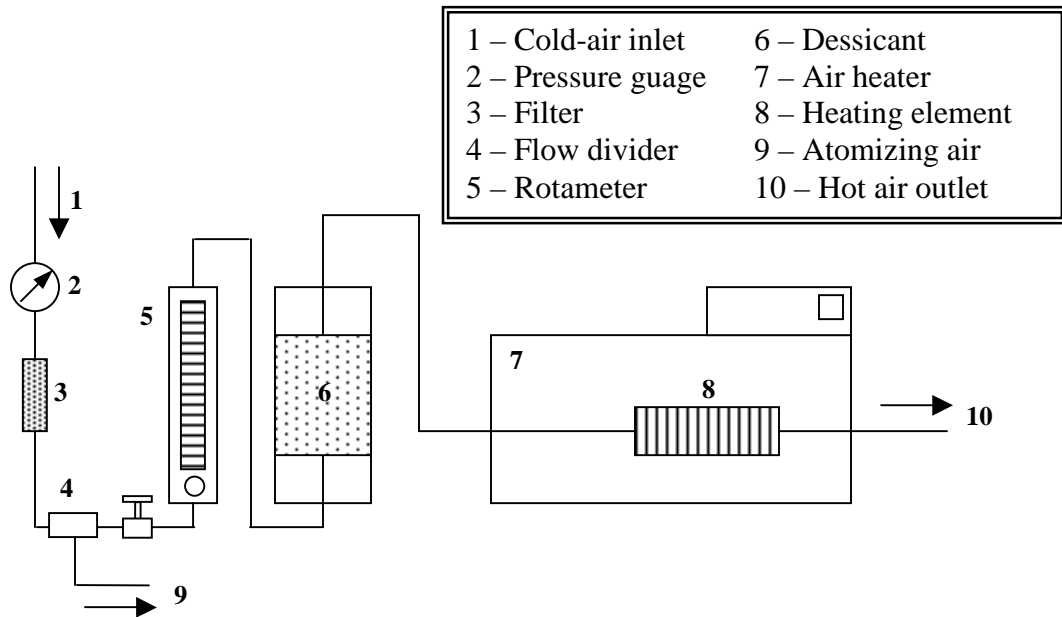


Figure 2.3 Coflow air supply and heater setup

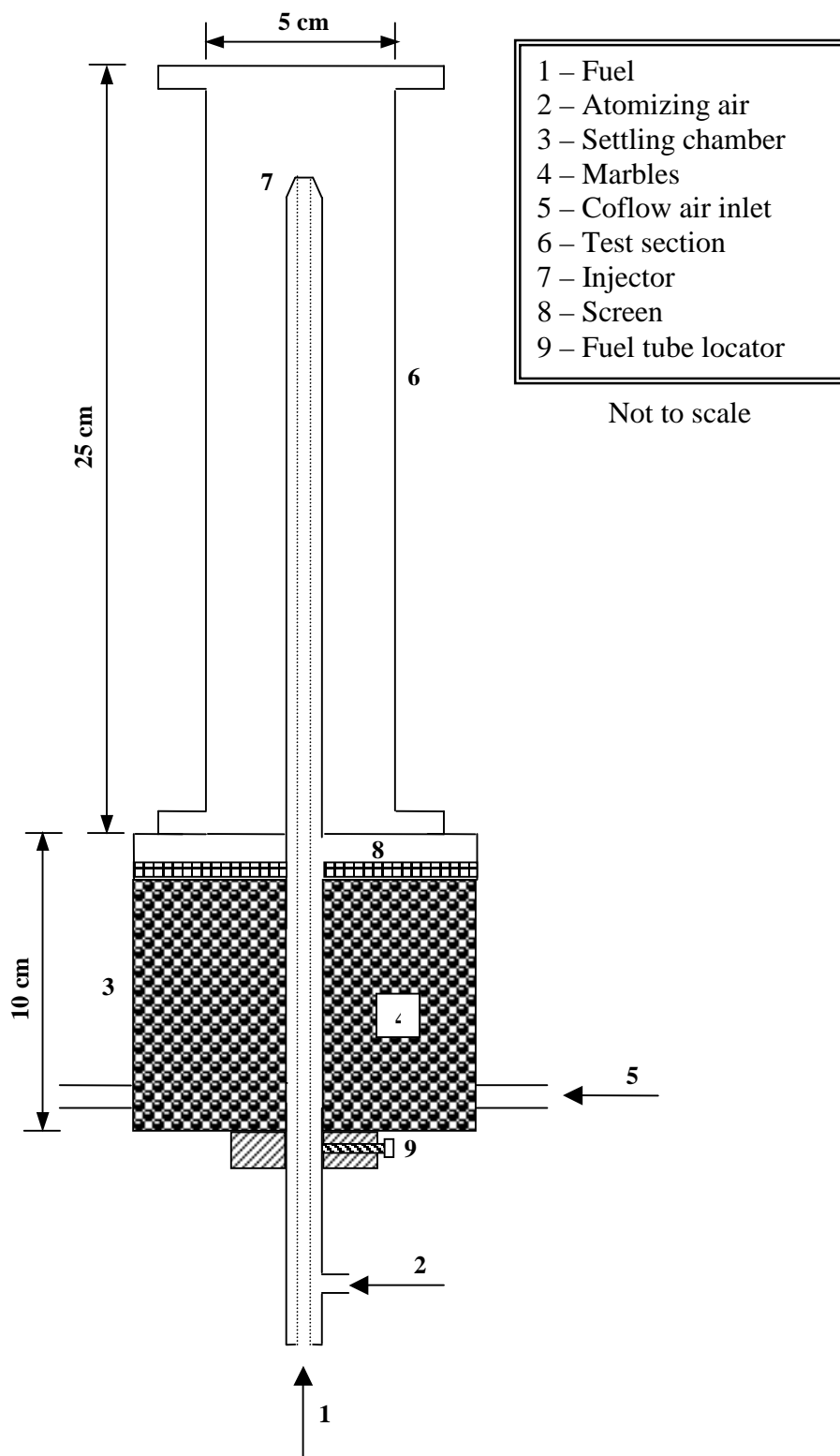


Figure 2.4 Schematic diagram of settling chamber and injector setup

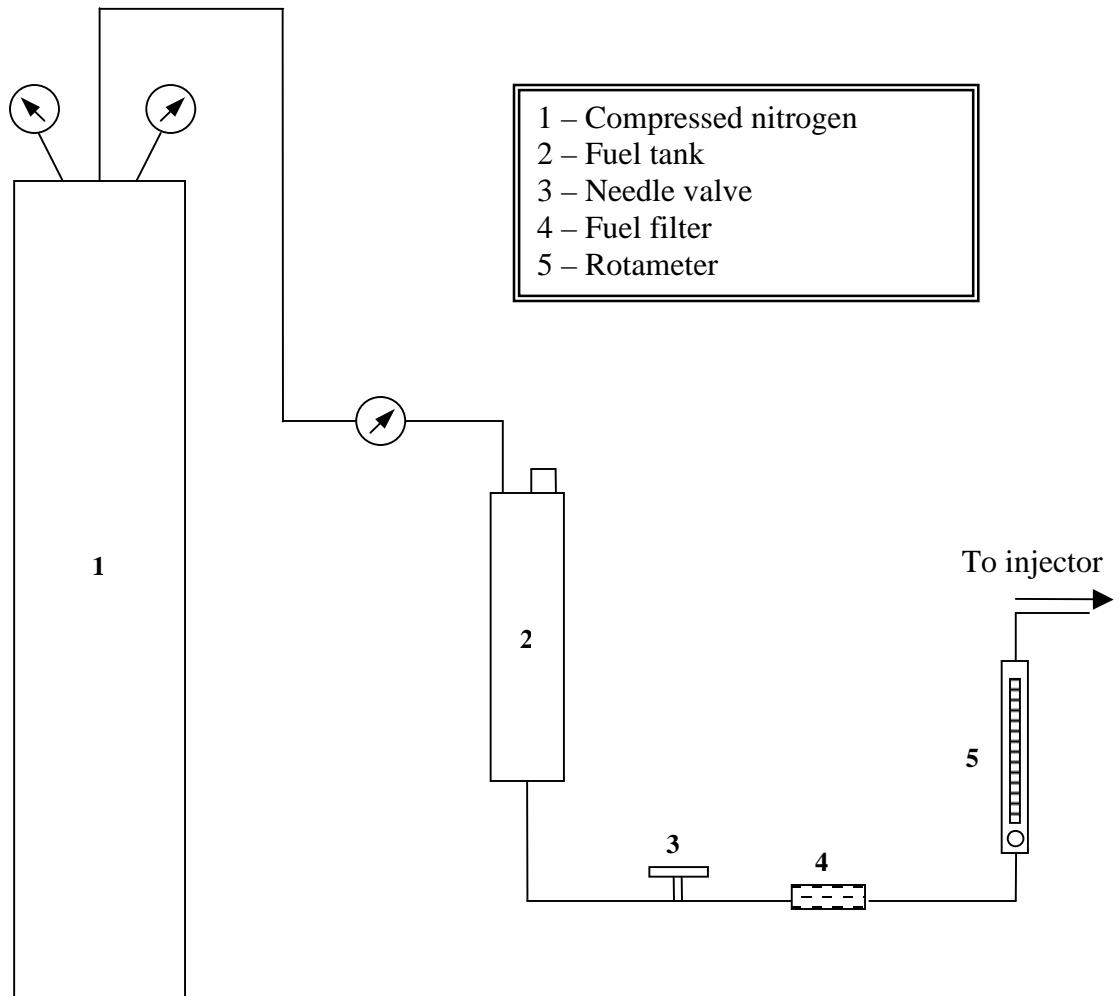
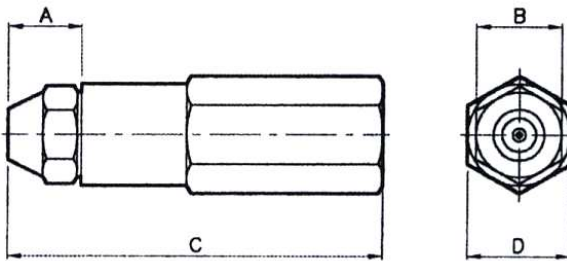
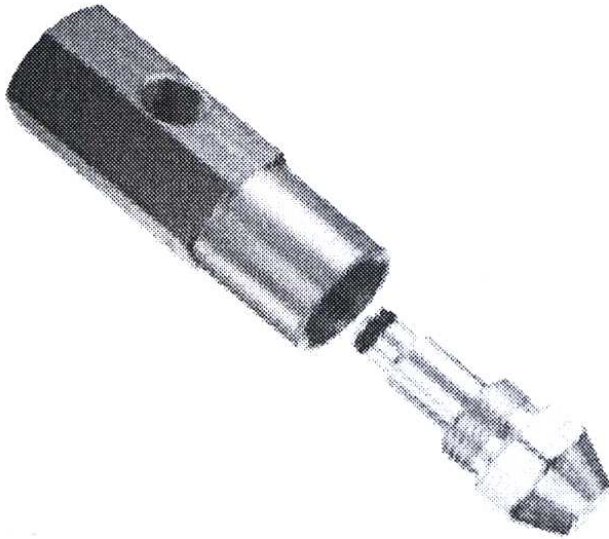


Figure 2.5a Schematic diagram of fuel supply system



Dimensions:
A = 12.7 mm; B (Hex) = 15.9 mm
C = 68.3 mm; D (Hex) = 19 mm
Inlet Sizes: Air – 1/4" NPT
Liquid – 1/8" NPT

Figure 2.5b Exploded view and the diagram of the DELAVAN air-blast atomizer

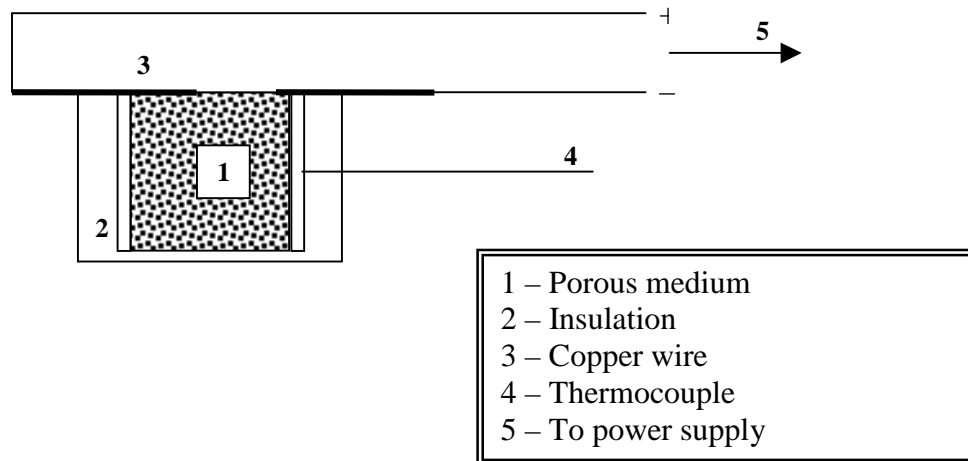


Figure 2.6 Schematic diagram of porous medium housing

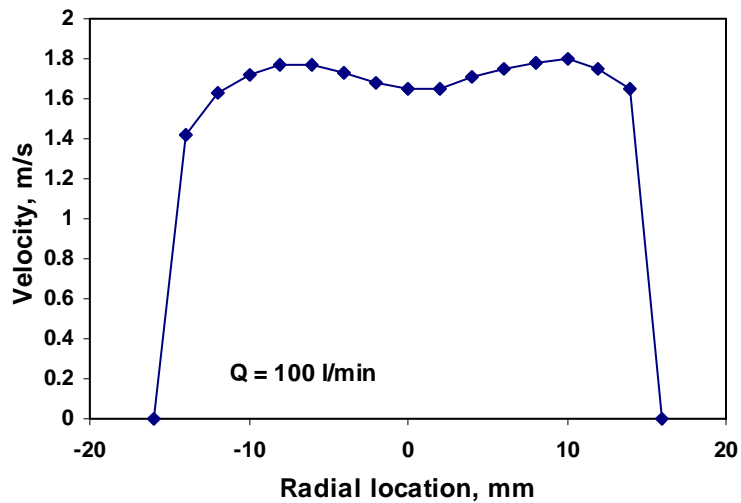


Figure 2.7 Velocity profile at the exit of the upstream test section

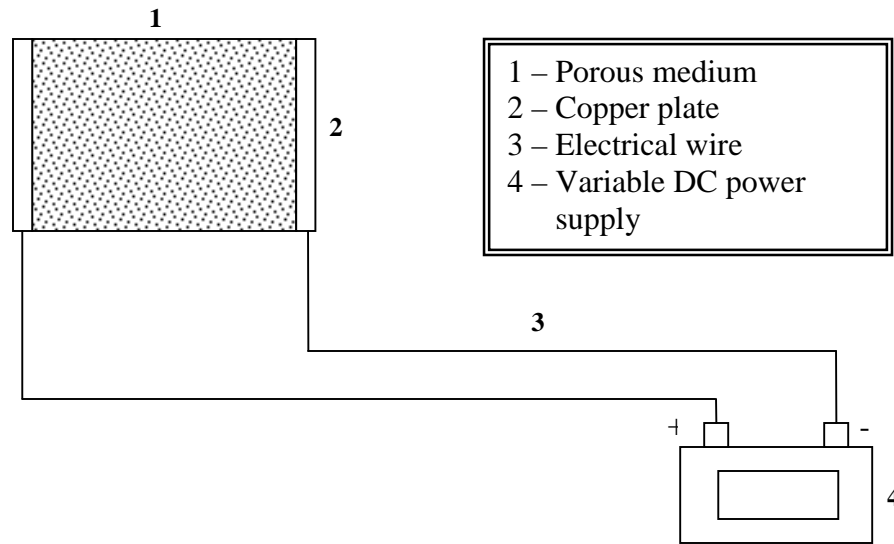


Figure 2.8 Experimental arrangement for porous medium heating setup

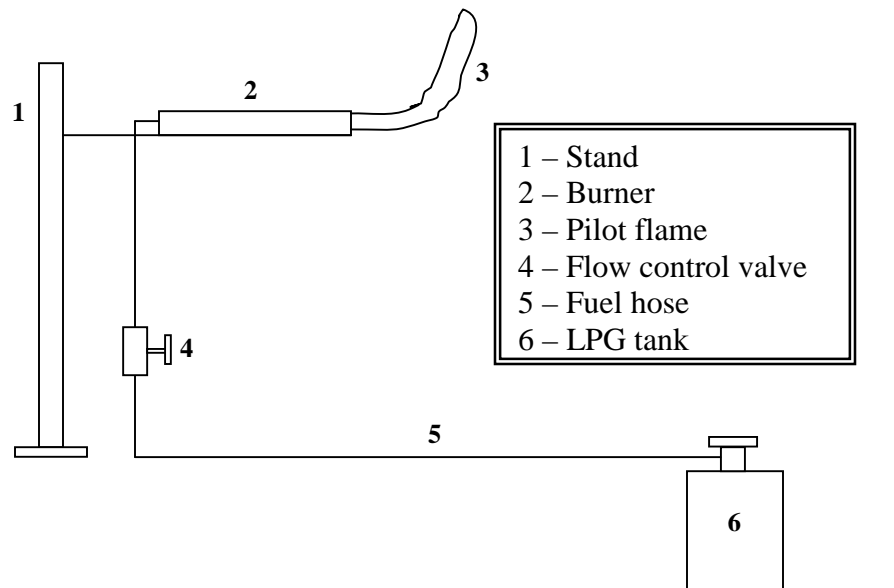


Figure 2.9 Pilot flame setup

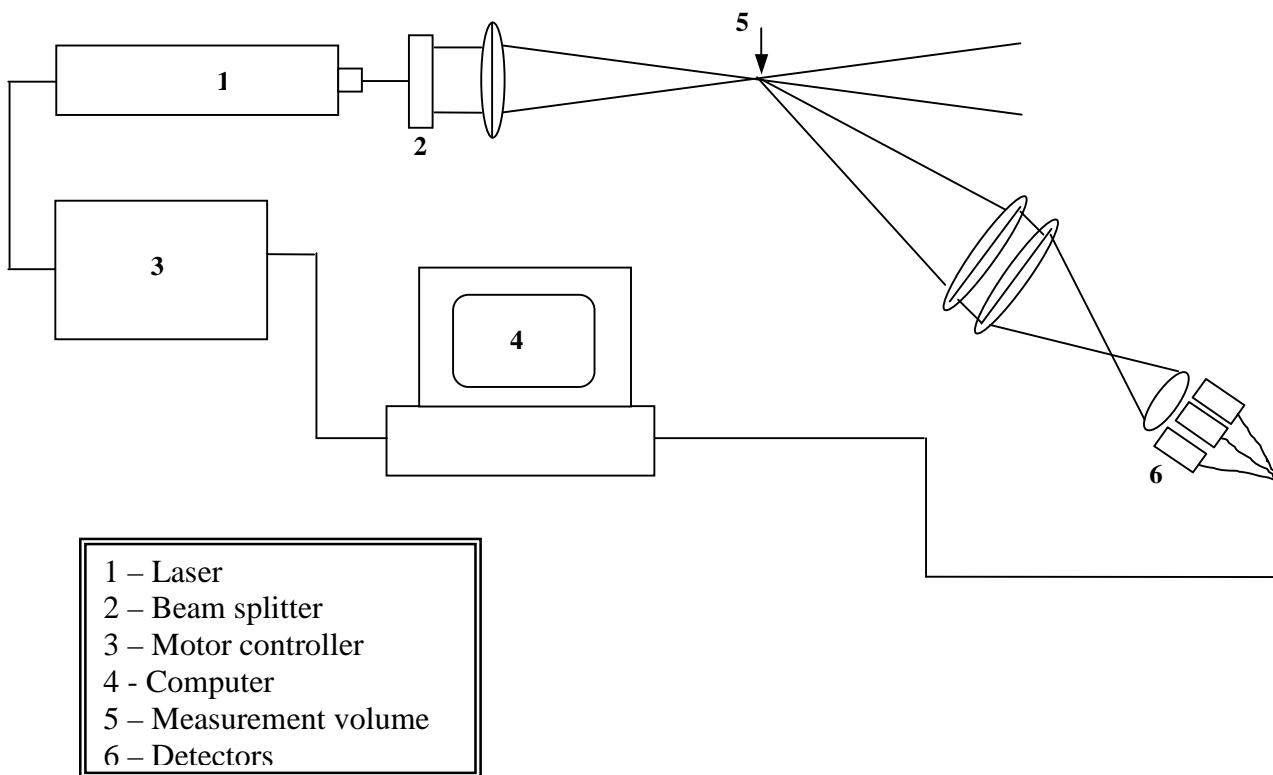


Figure 2.10 Schematic diagram of the PDPA system

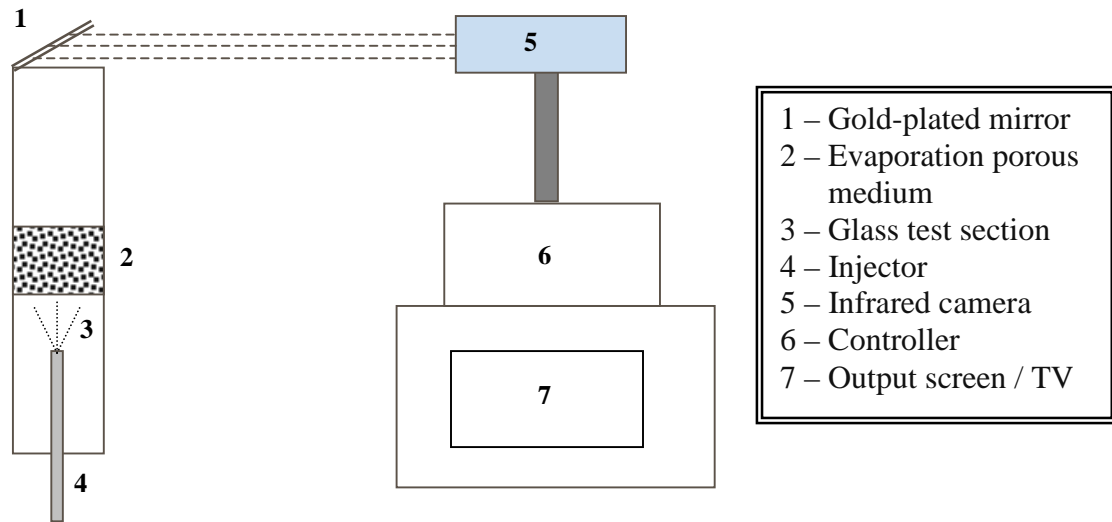


Figure 2.11 Experimental setup for surface temperature imaging with IR camera

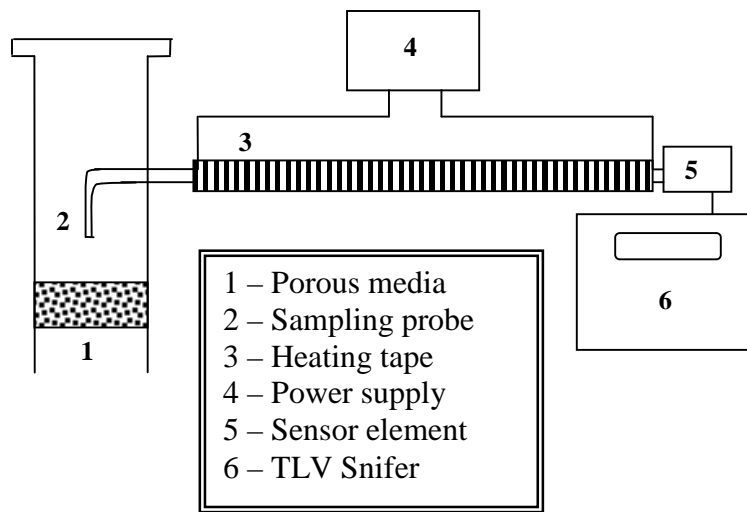


Figure 2.12 Experimental setup for vapor concentration measurement

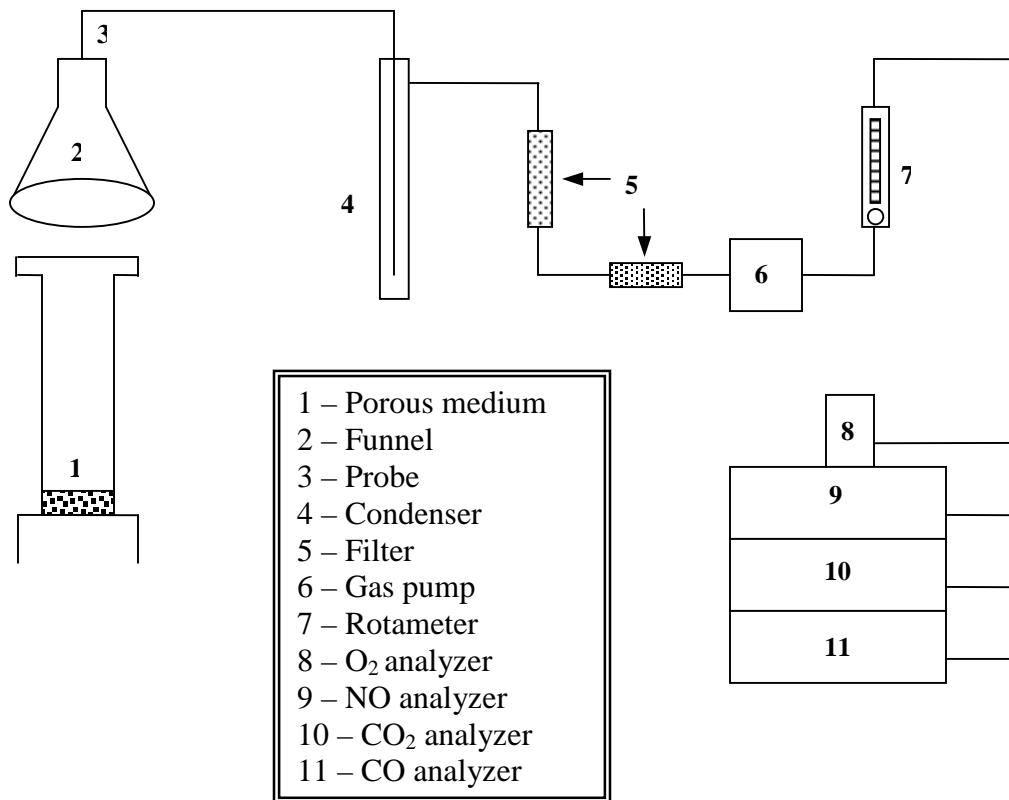


Figure 2.13 Schematic diagram of combustion gas composition analysis setup

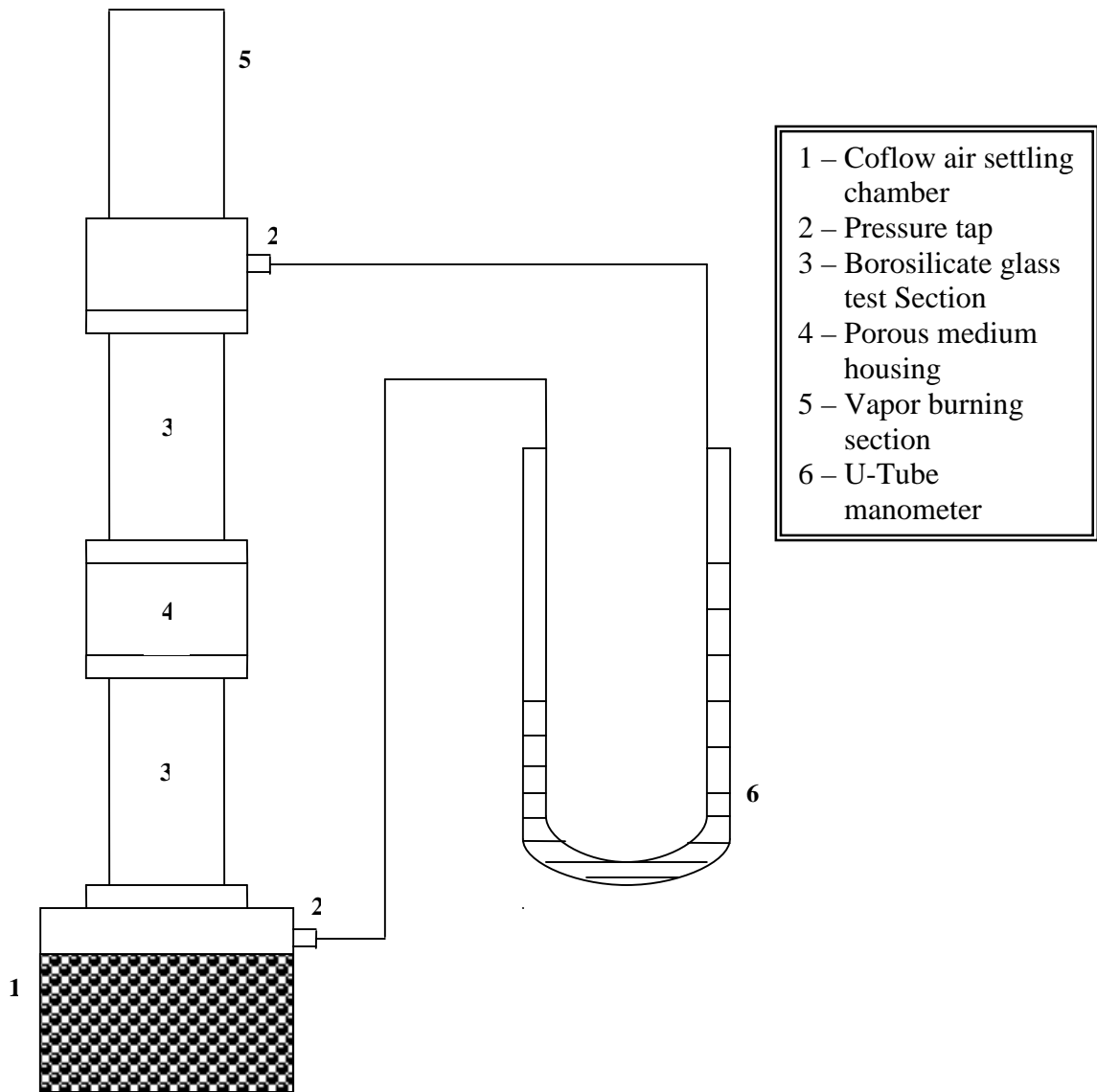
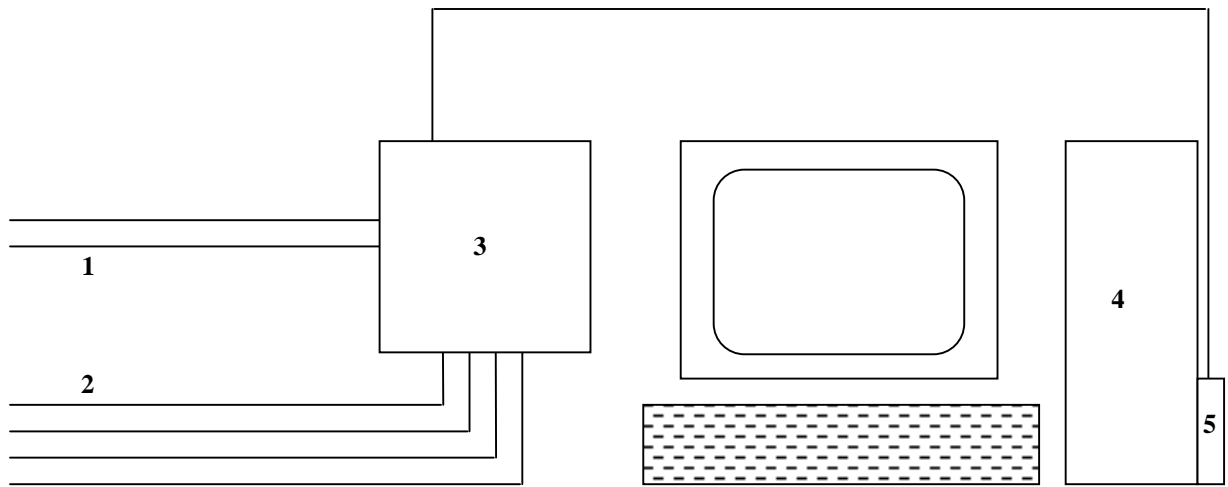


Figure 2.14 Pressure drop measurement setup



- | |
|---|
| <p>1 – Thermocouple or any voltage input
 2 – Stepper motor control
 3 – SCB-100
 4 – Computer
 5 – PCI-3021E</p> |
|---|

Figure 2.15 Typical setup of the data acquisition system

Chapter 3

Computational Modeling

3.1 Introduction

This chapter presents computational models used in this study for the simulation of evaporation enhancement in porous media. Governing equations and solution procedure are described. Grid generation and boundary condition setup are also explained. A comparison of model predictions with published data validating the model and solution scheme is also presented.

3.2 Model Assumptions

Modeling liquid fuel spray evaporation in porous media involves the phase change of a liquid under complex heat transfer and the subsequent mixing of vapors inside a solid medium. The following assumptions are made in order to reduce the complexities involved in the problem:

1. The computational domain is assumed to be symmetric about the injector axis.
2. The heat feedback from the combustion zone is simulated by a volumetric heat source in the porous region (i.e., solid phase energy equation). This allows us to simulate the combustion heat feedback in a controlled uncoupled manner.
3. A single-component fuel ($C_{12}H_{23}$) was assumed for kerosene. Multi-component effects are primarily dominant when the vaporization takes place

at a low temperature. The temperatures considered in this study are in the range of end boiling point temperatures of Kerosene. At this temperature, the single component fuel assumption suffices for analyzing the vapor concentration.

4. The porous medium is treated as inert, homogeneous, and isotropic and is assumed to have a constant porosity. The simulations with an isotropic porous medium would serve as a baseline study for the anisotropic case. Since the porous medium employed in our study has a random pore matrix, this assumption is reasonable. Further, modeling an anisotropic porous medium is computationally expensive.
5. The flow effects of porous media are included as sink terms in the appropriate momentum conservation equations.
6. The effects of the porous medium on turbulence generation or dissipation in the gas phase are neglected. The porous medium does not render unimpeded eddies of arbitrary size to the fluid flow (as in the case of conventional turbulent flows), and hence, this assumption is justified (Nakayama, 1995).
7. The direct interactions of droplets with porous media are neglected. However, these interactions are included via the interactions of droplets with the coflow air stream, which interacts with porous medium.
8. The hydrodynamic and thermal dispersion effects are not included. These effects account for the spreading caused by the porous media in addition to the molecular and turbulent transport.

9. The effects like film formation and fuel pyrolysis inside the porous medium are neglected and further the fuel is assumed to be thermally stable. Since the focus of the present study is on the evaporation characteristics, film formation and pyrolysis effects are neglected.

3.3 Governing Equations

The present study involves three phases: gas (air), liquid (fuel), and solid (porous medium). The gas and solid phases are considered to be continuous and the governing equations are written in the Eulerian frame. The liquid spray is assumed to be discrete and the governing equations are presented in a Lagrangian frame of reference. For steady, 2D axisymmetric, variable-density, non-isothermal, non-reacting, turbulent flows, the governing equations are given below (Kuo, 1986; Bird et al. 2002):

3.3.1 Governing Equations for Gas and Solid Phases

3.3.1.1 Overall Mass Conservation

Overall mass conservation is given by,

$$\frac{\partial \bar{u}}{\partial x} + \frac{1}{r} \frac{\partial}{\partial r} (r\bar{v}) = S_m \quad (3.1a)$$

where S_m is the mass addition due to droplet vaporization. All the symbols are identified in the Nomenclature presented in Appendix D. The mass addition source

term is computed by examining the change in mass of each droplet as it passes through the control volume, as follows:

$$S_m = \frac{\Delta m_d}{m_{d,0}} \dot{m}_{d,0} \quad (3.1b)$$

where Δm_d is the change in mass of the droplet in the control volume (kg), $m_{d,0}$ is the initial mass of the droplet (kg), and $\dot{m}_{d,0}$ is the initial mass flowrate of the droplet injection traced (kg/s).

3.3.1.2 Gas-phase Species Conservation

Individual species mass conservation in the gas phase is given as

$$\rho \left[\bar{u} \frac{\partial \bar{Y}_i}{\partial x} + \bar{v} \frac{\partial \bar{Y}_i}{\partial r} + \frac{\partial}{\partial x} (\bar{u}' Y_i') + \frac{1}{r} \frac{\partial}{\partial r} (r \bar{v}' Y_i') \right] = \text{for } i = 1 \dots N \quad (3.2)$$

$$- \rho D_{i,m} \left[\frac{\partial}{\partial x} \left(\frac{\partial \bar{Y}_i}{\partial x} \right) + \frac{1}{r} \frac{\partial}{\partial r} \left(r \frac{\partial \bar{Y}_i}{\partial r} \right) \right] + S_i$$

where S_i is the source term of the i^{th} species arising from droplet vaporization. For fuel vapors, this term is obtained from the discrete phase calculation of droplets (Equation 3.1b). In this study, a constant value of $2.88 \times 10^{-5} \text{ m}^2/\text{s}$ was used as the diffusion coefficient in Equation 3.2. Note that by replacing the diffusion coefficient ($D_{i,m}$) with proper dispersion tensor one could study dispersion of fuel vapors inside the porous media.

3.3.1.3 Gas-phase Momentum Conservation

Gas-phase axial and radial momentum conservation equations are given below:

Axial Momentum:

$$\rho \left[\bar{u} \frac{\partial \bar{u}}{\partial x} + \bar{v} \frac{\partial \bar{u}}{\partial r} + \frac{\partial}{\partial x} (\overline{u'^2}) + \frac{1}{r} \frac{\partial}{\partial r} (\overline{r u' v'}) \right] = - \frac{\partial \bar{p}}{\partial x} + \mu \left[\frac{\partial}{\partial x} \left(\frac{\partial \bar{u}}{\partial x} \right) + \frac{1}{r} \frac{\partial}{\partial r} \left(r \frac{\partial \bar{u}}{\partial r} \right) \right] + S_{fd} \quad (3.3a)$$

where S_{fd} is the source terms arising from pressure drop due to droplet momentum interactions with continuous flow field. The momentum exchange is computed by examining the change in momentum of a droplet as it passes through each control volume. Hence S_{fd} is given by:

$$S_{fd} = \sum (F_D (u_d - U)) \dot{m}_d \Delta t \quad (3.3b)$$

where F_D is drag force acting on the droplet, u_d is the droplet velocity, and U is the gas phase velocity. This is elaborated further in Section 3.3.2.

Radial Momentum:

$$\rho \left[\bar{u} \frac{\partial \bar{v}}{\partial x} + \bar{v} \frac{\partial \bar{v}}{\partial r} + \frac{\partial}{\partial x} (\overline{v'^2}) + \frac{1}{r} \frac{\partial}{\partial r} (\overline{r u' v'}) \right] = - \frac{\partial \bar{p}}{\partial r} + \mu \left[\frac{\partial}{\partial x} \left(\frac{\partial \bar{v}}{\partial x} \right) + \frac{1}{r} \frac{\partial}{\partial r} \left(r \frac{\partial \bar{v}}{\partial r} \right) \right] + S_{fd} \quad (3.4)$$

The source term S_{fd} is also calculated using the Equation 3.3b.

Velocity Formulation in Porous Medium Model:

Equations 3.3a and 3.4a represent the momentum conservation for the entire computational domain. In this study, the porous medium occupies only a portion of the domain. The gas velocity inside the porous medium is called the interstitial velocity. The interstitial velocity is calculated by multiplying the bulk velocity by the reciprocal of the porosity of the medium. Momentum equations outside the porous medium are based on the bulk velocity, and inside the porous medium, the momentum equations are applied to the interstitial velocity, which is calculated using the porosity. Further, the effects of the porous medium are considered by including an additional pressure drop term (S_{fp}) in the gas-phase momentum equations.

Calculation of Additional Pressure Drop due to Porous Medium:

The additional pressure drops due to the presence of porous medium are modeled using a quadratic form of Forchheimer equation by considering the non-Darcy flow in porous media. The following source term is added to the axial and radial momentum equations *only in the porous region*.

$$S_{fp} = -\left(\frac{\mu}{\alpha} U + C_2 \frac{1}{2} \rho \|U\| U\right) \quad (3.5)$$

If the Equation 3.5 is averaged over the entire porous medium region, the negative sign disappears. Then, the permeability (α) and inertial coefficient (C_2) in the

equation can be calculated using a modified form of Ergun equation (Ergun, 1952; Macdonald et al. 1979), which is shown below:

$$\frac{\Delta p}{l} = \frac{K_1(1-\varepsilon)^2 \mu}{d_p^2 \varepsilon^3} U + \frac{K_2 \rho (1-\varepsilon)}{d_p \varepsilon^3} U^2 \quad (3.6a)$$

Comparing the right-hand-side terms of Equations 3.5 and 3.6a, expressions for the permeability and inertial coefficient are obtained in terms of permeability and pore diameter, as follows:

$$\alpha = \frac{d_p^2 \varepsilon^3}{K_1 (1-\varepsilon)^2} \quad (3.6b)$$

$$C_2 = \frac{2K_2(1-\varepsilon)}{d_p \varepsilon^3} \quad (3.6c)$$

From the knowledge of pore diameter and porosity, the permeability and inertial coefficient of the porous medium can be calculated using the Equations 3.6b and 3.6c. The values of pore diameter and porosity are obtained from Ultramet[®]. Note that in Equations 3.6a-c, the K_1 and K_2 are Ergun constants. Macdonald et al. (1979) presents the following range for these constants: K_1 – 150 to 180 and K_2 – 1.5 to 4.0. In the present study, K_1 and K_2 values of 180 and 4, respectively corresponding to the packed beds with roughest particles, are chosen. With the Equations 3.6b and 3.6c, the additional pressure drop due to porous medium is calculated using Equation 3.4

and substituted in the appropriate gas-phase momentum conservation equation. For a pore diameter of 490 μm and a porosity of 87%, the permeability (α) and inertial coefficient (C_2) of the porous medium were calculated as $4.38 \times 10^{-8} \text{ m}^2$ and 3510 m^{-1} , respectively.

3.3.1.4 Turbulence Modeling

Turbulent quantities arising from the averaging of instantaneous variables are modeled using the Reynolds Stress Model (RSM). This model closes the Reynolds stress by solving five additional transport equations. The RSM accounts for streamline curvature, swirl, rotation, and rapid changes in strain rate. The transport equations for Reynolds stresses, $\overline{\rho v_i' v_j'}$ are given below:

$$\begin{aligned} \frac{\partial}{\partial x_k} (\rho v_k \overline{v_i' v_j'}) = & -\frac{\partial}{\partial x_k} \left[\frac{\mu_t}{\sigma_k} \frac{\partial \overline{v_i' v_j'}}{\partial x_k} \right] + \frac{\partial}{\partial x_k} \left[\mu \frac{\partial}{\partial x_k} (\overline{v_i' v_j'}) \right] \\ & - \rho \left(\overline{v_i' v_k} \frac{\partial v_j}{\partial x_k} + \overline{v_j' v_k} \frac{\partial v_i}{\partial x_k} \right) - G_{ij} + \phi_{ij} - 2\mu \frac{\partial v_i'}{\partial x_k} \frac{\partial v_j'}{\partial x_k} - F_{ij} \end{aligned} \quad (3.7)$$

where

$$\sigma_k = 0.82$$

$$G_{ij} = \beta \frac{\mu_t}{\text{Pr}_t} \left(g_i \frac{\partial T}{\partial x_j} + g_j \frac{\partial T}{\partial x_i} \right) \quad (\text{Buoyancy production}) \quad (3.8a)$$

$$\phi_{ij} = \phi_{ij,1} + \phi_{ij,2} + \phi_{ij,w} \quad (\text{Pressure strain}) \quad (3.8b)$$

Here, $\phi_{ij,1}$ is the slow pressure-strain term, $\phi_{ij,2}$ is the rapid pressure-strain term, and $\phi_{ij,w}$ is the wall-reflection term.

$$F_{ij} = 2\rho\Omega_k \left(\overline{u'_j u'_m} \varepsilon_{ikm} + \overline{u'_i u'_m} \varepsilon_{jkm} \right) \quad (3.8c)$$

(Production by system rotation)

Detailed information on the RSM is available in Launder and Spalding (1974). Note that the turbulence effects in the porous media are not considered directly. The above equations model the turbulence in the continuous flow field, which, in turn, affect the droplet.

3.3.1.5 Energy Conservation Equations

Situations such as rapid vaporization, heat generation, and convective heat transfer in porous media can often lead to local thermal non-equilibrium (Dual et al. 2004). The present problem considers an air stream flowing at a different temperature than that of porous medium (where significant heat generation takes place due to combustion heat feedback). In order to accurately model the evaporation process, one needs to account for local thermal non-equilibrium. This is achieved by solving separate energy equations for the gas phase and the solid phase and coupling them with a volumetric heat transfer coefficient (Viskanta 1995; Howell et al. 1996; Barra et al. 2003; Periasamy et al. 2004). The gas phase and solid phase energy conservation equations are given as follows:

Gas-phase Energy Conservation:

$$\rho c_p \left[\bar{u} \frac{\partial \bar{T}_g}{\partial x} + \bar{v} \frac{\partial \bar{T}_g}{\partial r} \right] = k_{\text{eff}} \left[\frac{\partial}{\partial x} \left(\frac{\partial \bar{T}_g}{\partial x} - \overline{u' T_g'} \right) + \frac{1}{r} \frac{\partial}{\partial r} \left(r \left(\frac{\partial \bar{T}_g}{\partial r} - \overline{v' T_g'} \right) \right) \right] + h_v (T_s - \bar{T}_g) / \varepsilon \quad (3.9a)$$

In the above equation, k_{eff} is the effective thermal conductivity as follows:

$$k_{\text{eff}} = k_f + \frac{c_p \mu_t}{Pr_t} \quad (3.9b)$$

where μ_t and Pr_t are the turbulent viscosity and turbulent Prandtl number, respectively. The turbulent Prandtl number is set at 0.85, and the turbulent viscosity is calculated as shown below:

$$\mu_t = \rho C_\mu \frac{k^2}{\varepsilon} \quad (3.9c)$$

Note that in the above equation C_μ is set at 0.09, k is the turbulent kinetic energy, and ε is the turbulent kinetic energy dissipation rate.

Solid-phase Energy Conservation:

$$k_s \left[\frac{\partial}{\partial x} \left(\frac{\partial T_s}{\partial x} \right) + \frac{1}{r} \frac{\partial}{\partial r} \left(r \frac{\partial T_s}{\partial r} \right) \right] + [Q_{\text{in}} - h_v (T_s - T_g)] = 0 \quad (3.10)$$

where Q_{in} is the volumetric heat input rate (W/m^3) to the porous media to simulate combustion heat feedback rate from the flame zone, and h_v is the volumetric heat transfer coefficient ($W/m^3 K$) between the porous medium and the coflow air. Note that in the above equations, the term $h_v(T_s-T_g)$ appears as sink in solid phase equation and source in gas phase equation and h_v is used to couple the two equations. The interfacial volumetric convective heat transfer coefficient is calculated using the Nusselt number correlations, *proposed for packed beds*, as follows (Wakao and Kaguei, 1982, p. 293):

$$Nu = 2 + 1.1 Re_p^{0.6} Pr^{0.3} \quad (3.11a)$$

where Re_p is the Reynolds number based on the mean pore diameter of the porous medium (490 μm). Once the Nusselt number is known, it is converted into a volumetric Nusselt number, as follows:

$$Nu_v = A_{sf} d_p Nu \quad (3.11b)$$

where A_{sf} is the specific surface area (π/d_p). The volumetric heat transfer coefficient is then calculated as shown below (Henneke and Ellzey, 1995):

$$h_v = \frac{Nu_v k_{eff}}{d_p^2} \quad (3.12)$$

Evaporation enhancement in porous media was also studied using a local thermal equilibrium model with a point-wise injection scheme (See Appendix E).

Radiative Transfer Equation:

The radiative transfer equation for an absorbing, emitting, and scattering medium at position \vec{r} in the direction \vec{s} is

$$\frac{dI(\vec{r}, \vec{s})}{ds} + (a + \sigma_s)I(\vec{r}, \vec{s}) = a n^2 \frac{\sigma T^4}{\pi} + \frac{\sigma_s}{4\pi} \int_{\Omega'} I(\vec{r}, \vec{s}') \Phi(\vec{s} \cdot \vec{s}') d\Omega' \quad (3.13)$$

Equation 3.13 is solved using the P-1 radiation model (Siegel and Howell, 2002). In this model, the radiative transfer equation is transformed into a set of partial differential equations by using the method of spherical harmonics (Modest, 2003).

The transport equation for incident radiation, G, is given below:

$$\nabla \cdot (\Gamma \nabla G) - aG + 4a\sigma T^4 = S^G \quad (3.14)$$

where the parameter Γ is

$$\Gamma = \frac{1}{(3(a + \sigma_s) - C\sigma_s)} \quad (3.15)$$

Equation 3.14 is of type conserved scalar equation and can be solved by defining additional scalar in FLUENT™ to represent the incident radiation, G. Once the incident radiation is computed, the radiative heat flux is calculated as follows:

$$q_r = -\Gamma \nabla G \quad (3.16)$$

The term $-\nabla q_r$ is then included in the energy equation to account for the radiation.

3.3.2 Governing Equations for Liquid Phase

Governing equations for motion, heat transfer, and mass transfer of liquid phase are written in Lagrangian frame of reference. Droplet trajectory is predicted by integrating the force balance on the droplet. Droplet is allowed to begin vaporization upon reaching a preset vaporization temperature (a numerical property to trigger the vaporization process) and to completely vaporize at the boiling point.

3.3.2.1 Droplet Motion

The force balance on a moving droplet particle yields (Kuo, 1986, p. 578):

$$\frac{du_d}{dt} = F_D(U - u_d) + \frac{g_x(\rho_d - \rho)}{\rho_d} \quad (3.17)$$

Here, U is the fluid phase velocity, u_d is the droplet velocity, ρ is the fluid density, ρ_d is the density of the droplet, and the term $F_D(U-u_d)$ represents the drag force per unit mass of the droplet. Since the droplets are moving at high velocities, the gravitational effects i.e., the second term in the right-hand-side of Equation 3.17 can be neglected.

The drag force is calculated as follows:

$$F_D = \frac{3\mu C_D \text{Re}_d}{4d_d^2 \rho_d} \quad (3.18a)$$

where d_d is the droplet diameter, Re_d is the relative Reynolds number, and C_D is the drag coefficient, as given below:

$$\text{Re}_d = \frac{\rho d_d |u_d - U|}{\mu} \quad (3.18b)$$

$$C_D = a_1 + \frac{a_2}{\text{Re}_d} + \frac{a_3}{\text{Re}_d^2} \quad (3.18c)$$

In Equation 3.18c, a_1 , a_2 , and a_3 are constants that apply for smooth particles over several ranges of Reynolds numbers (Morsi and Alexander, 1972).

3.3.2.2 Droplet Heating

When the droplet temperature is lower than the vaporization temperature, heat transferred to the droplet is merely used to increase the droplet temperature, according to the following equation. No mass is transferred from the droplet.

$$m_d c_{p,d} \frac{dT_d}{dt} = hA_d (T_\infty - T_d) \quad (3.19a)$$

The heat transfer coefficient (h) in Eq. 3.19 is evaluated from the Nusselt number correlations of Ranz and Marshall (1952a; 1952b).

$$\text{Nu} = \frac{hd_d}{k_\infty} = 2 + 0.6\text{Re}_d^{0.5} \text{Pr}^{0.33} \quad (3.19b)$$

3.3.2.3 Droplet Vaporization

If the droplet reaches the vaporization temperature, mass transfer occurs and the droplet size starts to decrease. This process continues to occur until it reaches its boiling point or the volatile fraction is completely liberated. The energy balance for a vaporizing droplet is given below:

$$m_d c_{p,d} \frac{dT_d}{dt} = hA_d (T_\infty - T_d) + \frac{dm_d}{dt} h_{fg} \quad (3.20)$$

The molar flux of droplet vapor into the continuous phase (N_i) is evaluated as follows:

$$N_i = k_c (C_{i,s} - C_{i,\infty}) \quad (3.21a)$$

The concentration of vapor at the droplet surface ($C_{i,s}$) is calculated by assuming the partial pressure of vapor at the interface between droplet and continuous phase is equal to the saturated vapor pressure (p_{sat}). $C_{i,\infty}$ is the vapor concentration in the bulk gas. The terms $C_{i,s}$ and $C_{i,\infty}$ are evaluated as shown below:

$$C_{i,s} = \frac{p_{\text{sat}}(T_d)}{RT_d} \quad (3.21b)$$

$$C_{i,\infty} = X_i \frac{P_{\text{op}}}{RT_d} \quad (3.21c)$$

where R is the universal gas constant, X_i is the local bulk mole fraction of species i , and p_{op} is the operating pressure.

The mass transfer coefficient, k_c , is evaluated from the Nusselt number correlation of Ranz and Marshall (1952a; 1952b), which is given below:

$$Nu = 2.0 + 0.6 Re_d^{1/2} Sc^{1/3} = \frac{k_c d_d}{D_{i,m}} \quad (3.22)$$

In this study, a constant value of $2.88 \times 10^{-5} \text{ m}^2/\text{s}$ was used as the diffusion coefficient in Equation 3.22. The reduction in mass is then computed according to the following equation:

$$m_d(t + \Delta t) = m_d(t) - N_i A_d M_{w,i} \Delta t \quad (3.23)$$

This mass is then added to the appropriate species conservation equation (Eq. 3.2) and also the overall mass conservation (continuity) equation (Eq. 3.1a).

3.3.2.4 Droplet Boiling

Once the boiling point of the droplets is reached, the droplets are allowed to undergo boiling, according to the following convective boiling rate equation (Kuo, 1986):

$$\frac{d(d_d)}{dt} = \frac{4k_\infty}{\rho_d c_{p,\infty} d_d} \left[1 + 0.23 \sqrt{Re_d} \right] \ln \left[1 + \frac{c_{p,\infty} (T_\infty - T_d)}{h_{fg}} \right] \quad (3.24)$$

The boiling condition requires that the continuous phase temperature be greater than the droplet temperature. The droplet temperature also remains fixed during boiling.

3.3.2.5 Spray Model

An air-blast atomizer model available in FLUENTTM is used to inject fuel into the computational domain. The air-blast atomizer model is based on the Linearized Instability Sheet Atomization model of Schmidt et al. (1999).

In this model, the fuel is injected through an orifice of known geometry. A swirling air stream is also supplied along with the liquid. The physical processes that convert the liquid into fully developed droplets occur in three stages:

- (i) Film formation
- (ii) Sheet breakup
- (iii) Atomization

A centrifugal motion is imparted to the liquid fuel inside the injector. This creates an air core surrounded by a liquid film. The thickness of the film is supplied as input. Additional air supplied past the liquid sheet causes it to disintegrate and form ligaments. The breakup of liquid sheet and formation of ligaments are due to the growth of short waves. Further breakup of ligaments results in droplets. The maximum relative velocity between the sheet and air can also be specified to enable finer control of droplet size. Additional input to this model are the spray half-angle, sheet constant and ligament constants.

The most probable diameter (d_o) is related to ligament diameter (d_l) as follows:

$$d_o = d_l [1 + 3(\text{Oh})]^{1/6} \quad (3.25)$$

In Eq. 3.25, the Ohnesorge number (Oh) is defined as $\sqrt{\text{We}/\text{Re}}$, where We and Re are the liquid Weber and Reynolds numbers, respectively.

Spray model was also been used in conjunction with a local thermal equilibrium model to study evaporation enhancement (See Appendix F). Evaporation enhancement using a *local thermal non-equilibrium model* with an *unsteady fuel spray* is presented in Appendix G.

3.4 Boundary and Initial Conditions

Following are different boundaries that are considered in the study:

- (i) Coflow air inlet
- (ii) Side walls
- (iii) Symmetric axis
- (iv) Flow outlet
- (v) Atomizing air inlet
- (vi) Conditions for porous medium

Boundary conditions for flow, heat transfer, and species transport at all the boundaries are given in Table 3.1. Droplet particles are injected through the air blast atomizer located at (0,0). The initial conditions for droplets are listed in Table 3.2. Important physical properties of the porous medium are presented in Table 3.3. These properties were obtained from the manufacturer, Ultramet[®].

3.5 Grid Generation

The physical geometry considered for the computational study is of 2D axisymmetric type. A domain size of 2.5 cm x 20.3 cm in the r and x direction respectively, is considered. Figure 3.1 presents such a physical geometry. Cartesian type, uniform grid of quadrilateral mesh elements with 10 points per centimeter is generated using a commercial grid generation code GAMBIT. Shown in Fig. 3.2 is a typical computational grid employed in this study.

3.6 Solution Procedure

The governing equations are discretized using a finite-volume based approach and converted into a set of algebraic equations, which are then solved by matrix methods. Unknown pressure field in the momentum equations is determined by solving the continuity equation iteratively, using a pressure-correction algorithm. The entire process follows the standard SIMPLE algorithm (Patankar and Spalding, 1972).

Convective terms in the governing equations are discretized by Power law scheme. Interactions of porous media with gas-phase are programmed in C++ through a set of user-defined functions. Solutions are obtained using a commercial code FLUENT™. Various computational parameters employed in the study are presented in Table 3.4.

The solution procedure adopted in the study is presented in Fig. 3.3 in the form of a flowchart. The gas-phase with swirling air stream for atomization was first solved under steady state conditions. Porous medium heat source was also activated during this stage. This was done for the following reason: The flow had swirling air stream and porous media source terms. Before starting the droplet injection, it was necessary to establish a stable flow field in order to minimize the convergence difficulties. Once a converged steady-state flow field was obtained, the injection was turned on; computations were carried out and coupled with continuous phase calculations. For every injection, the continuous flow calculations were performed a number of times. For assessing the convergence of the solution, a scaled residual (R^ϕ), for a general variable, ϕ is defined by summing the imbalance in the discretization equation over all the computational cells P, as shown below:

$$R^\phi = \frac{\sum_{\text{cells } P} \left| \sum_{\text{nb}} a_{\text{nb}} \phi_{\text{nb}} + b - a_p \phi_p \right|}{\sum_{\text{cells } p} \left| a_p \phi_p \right|} \quad (3.26)$$

where a_p is the center coefficient, a_{nb} are the influence coefficients for the neighboring cells, and b is the contribution of the constant part of the source term S_c in $S = S_c +$

$S_p\phi$ and of the boundary conditions. In this study, the computations are performed until the residuals attained values of 1×10^{-4} or lower. This process was then repeated until the end of injection period.

3.7 Model Comparison

Two benchmark cases were simulated and the results were compared with that available in literature to assess the predictions of the present model. First, the evaporation of single droplet of n-heptane fuel in quiescent environment (without porous media) was considered. Variation of droplet diameter as a function of time i.e., the droplet life time was captured and compared with the experimental and numerical data obtained by Runge et al. (1998). A non-dimensional time (τ) was calculated as follows:

$$\text{Non-dimensional time, } \tau = \frac{t\nu}{R_0^2} \quad (3.27)$$

where, t is the droplet life time, ν is the gas kinematic viscosity, and R_0 is the initial radius of the droplet. Figure 3.4 presents the decay of the square of the non-dimensional diameter $(D/D_0)^2$ of the droplet with the non-dimensional time. Here, D is the diameter of the droplet at any given time, t and D_0 is the initial diameter of the droplet. Results show a reasonably good agreement between the present model's predictions and literature. Such a variation of the square of droplet diameter with

respect to time is commonly referred to as the D^2 Law. The study, thus, demonstrates that the predictions of droplet parameters are reliable and consistent.

Next, the predictions of porous medium model were compared with the results obtained by Vafai and Kim (1989). They derived an exact solution for forced convection in a channel filled with porous medium for an applied wall heat flux. For a given Darcy number of 0.01 and porosity of 87%, the permeability was calculated and supplied as input to the present model. A heat flux of 1 W/m^2 was applied and the transverse temperature profiles were obtained at different axial locations. Porous medium temperature in each profile was normalized, as shown below:

$$\text{Normalized temperature} = \frac{T_w - \langle T \rangle}{q_w / h} \quad (3.28)$$

where T_w is the wall temperature, q_w is the heat flux applied at the wall, and h is the convective heat transfer coefficient. When the porous medium temperature was normalized according to Equation 3.28, the transverse temperature profiles collapse into a single curve. The results are shown in Fig. 3.5 for an h/k value of 10.27. The figure demonstrates that the predictions of our porous medium model are in excellent agreement with the analytical results of Vafai and Kim (1989).

3.8 Grid Sensitivity Analysis

Different grids of sizes 80x10, 160x20, 200x25, 240x30, 320x40, and 400x50 were used to investigate the effects of grid size on model's predictions. Vapor concentration profiles for each grid at $x = 12.7$ cm were obtained for comparison purposes. The results from this study are shown in Fig. 3.6. The vapor concentration profiles predicted by the grids other than 80x10 showed no dependency on the grid size. Hence, any grid size above 80x10 could be used without sacrificing the accuracy much. Considering the computational time, accuracy and memory size of the computer used, a grid size of 200x25 was selected for further analysis.

Effect of coflow air turbulence on the heat and mass transfer calculations of droplet evaporation is described in Appendix G.

3.9 Chapter Summary

This chapter presented the computational models employed in this study. Governing equations for gaseous, liquid and solid phases were given. Boundary conditions for the continuous flow field and initial conditions for discrete phase were tabulated. Grid generation and solution procedure were also explained. Furthermore, a comparison of model predictions with literature and grid sensitivity analysis was also presented.

Table 3.1 Boundary conditions at flow inlet, side walls, and flow exit

Parameter	Value	Units
<i>Axial and Radial Momentum Equation:</i>		
Boundary type	Mass flow inlet	
Coflow air mass flowrate	3.8	mg/s
No slip at the wall	-	-
Normal gradient for flow variables at flow exit	0	-
<i>Swirl Momentum Equation:</i>		
Boundary type	Velocity inlet	
Swirl velocity magnitude	50	m/s
Axial component of flow direction	0	-
Radial component of flow direction	0.7	-
Tangential component of flow direction	0.7	-
<i>Species Conservation Equation:</i>		
Inlet O ₂ mass fraction	0.232	-
<i>Turbulence Transport Equation:</i>		
Turbulence intensity at flow inlet	5	%
Turbulent viscosity ratio at flow inlet	5	%
<i>Gas-phase Energy Equation:</i>		
Coflow air inlet temperature	300, 350, 400, 450	K
Heat flux applied at side wall	0	W/m ²
<i>Solid-phase Energy Equation:</i>		
Initial guess temperature in the porous region	300	K
Gradient of solid temperature	0	K/m ²
<i>Liquid-phase Equation:</i>		
Overall equivalence ratio	0.3, 0.42, 0.5, 0.6, 0.7	-

Table 3.2 Initial conditions for droplet stream

Input Parameter	Value	Units
Atomizer type	Air-blast	-
Number of particle streams	60	-
Starting location	(0,0)	-
Initial temperature	300	K
Fuel flowrate	0.1	mg/s
Injector inlet diameter	0.001	m
Injector outlet diameter	0.005	m
Spray half angle	20	degrees
Adjusted Parameter*	Value	Units
Relative velocity	80	m/s
Sheet constant	5	-
Ligament constant	0.2	-

*FLUENT™ recommends a range of values for these parameters. However, the specific values depend on the problem under consideration. In the present study, extensive simulations were conducted by comparing the numerical results with the experimental data, and appropriate values were obtained for relative velocity, sheet constant, and ligament constant. These values were used in the subsequent simulations of the evaporation enhancement in porous media.

Table 3.3 Important physical properties of porous medium used in modeling *

Parameter	Value	Units
Bulk density	320	kg/m ³
Thermal conductivity	1	W/m-K
Specific heat	1422.6	J/kg-K
Pores per centimeter	18, 25, and 31	-
Mean pore diameter	190, 270, and 450	micron
Overall effective porosity	87	%
Porous region volume	36.3	cm ³
Heat input range	0.8-1.1	% of average heat input

*Supplied by Ultramet®, Pacoima, CA

Table 3.4 Computational parameters used in the modeling

Technique	Method Adopted
Solution method	Control volume based finite difference method
Discretization of convective terms	Power Law
Pressure-Velocity coupling	SIMPLE
Discretization of pressure term	PRESTO
Solution Parameter	Value Set by the Author
Under-Relaxation parameter	0.2-1.0
Convergence criterion	1×10^{-4}
Number of data points used in radial profiles for increased accuracy	50

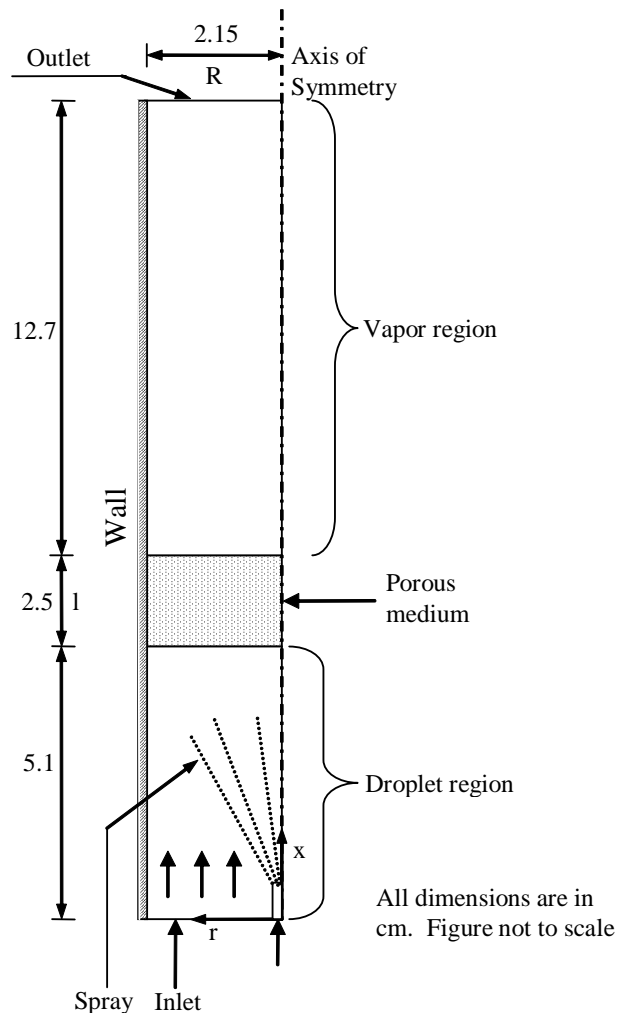


Figure 3.1 Physical domain considered for the present analysis



Figure 3.2 Computational grid generated for the present analysis

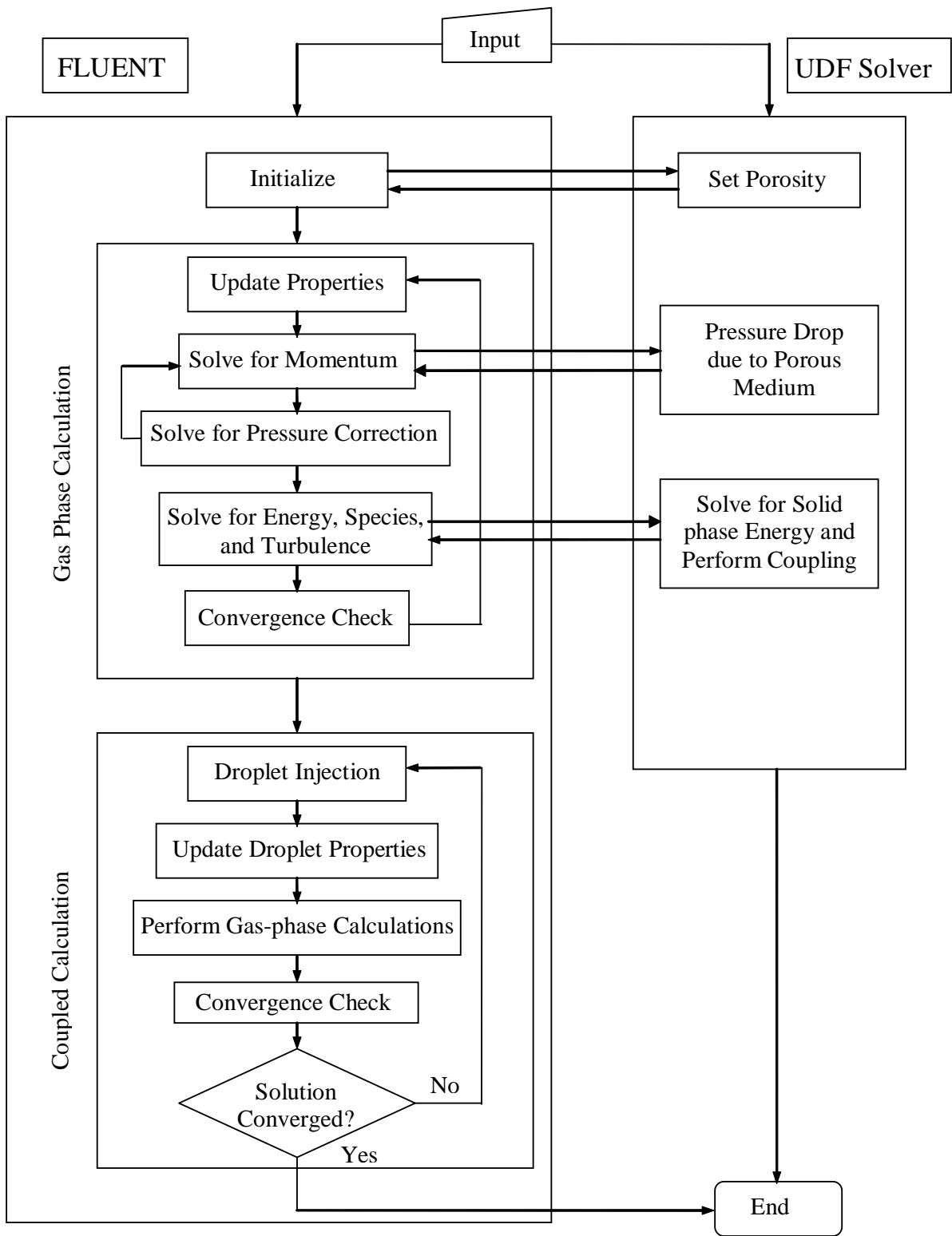


Figure 3.3 Solution flow diagram and FLUENT™ interactions with UDF solver

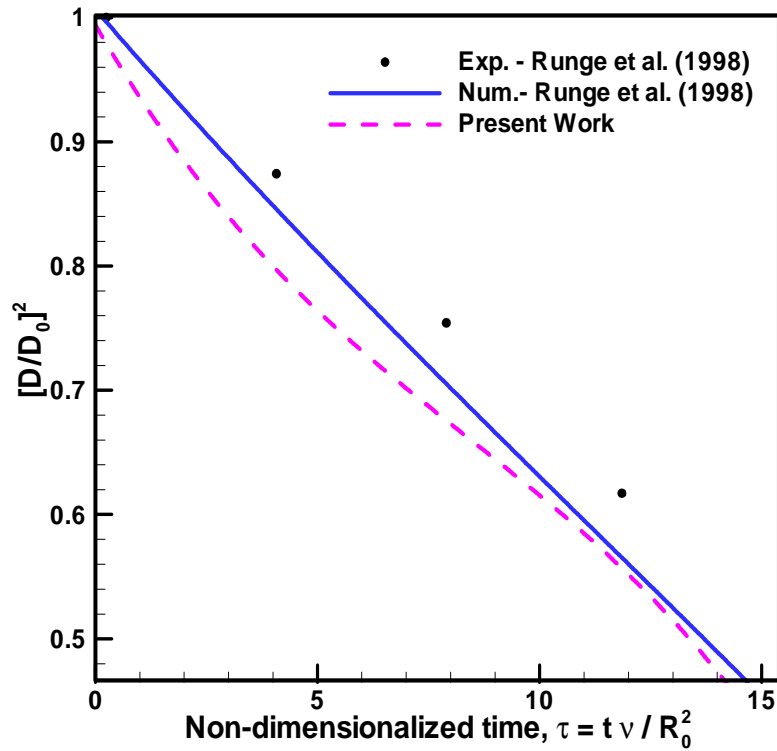


Figure 3.4 Comparison of predicted droplet life time with the experimental and numerical results of Runge et al. (1998)

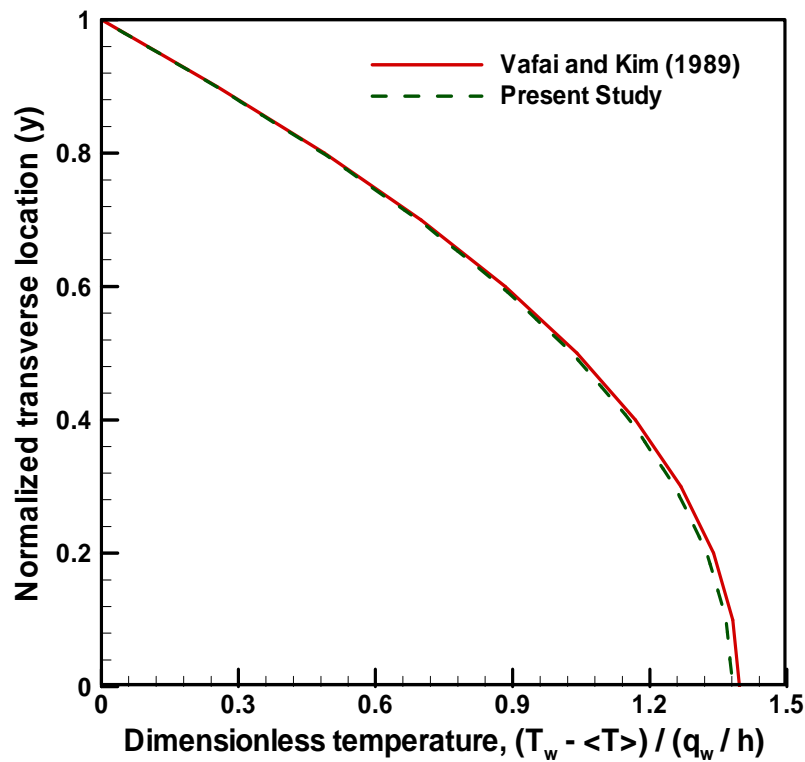


Figure 3.5 Comparison of transverse temperature profiles of the present model with the analytical solutions of Vafai and Kim (1989)

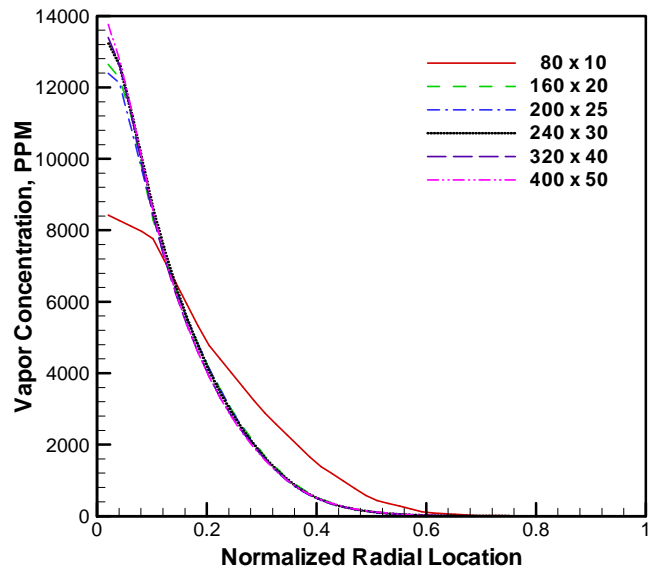


Figure 3.6 Effects of grid size on vapor concentration (x = 12.7 cm, HS = 200 W)

Chapter 4

Evaporation Enhancement in Porous Media

4.1 Introduction

A porous medium placed in the combustion zone establishes a heat feedback upstream due to thermal conduction and radiation. The heat feedback, in turn, may be beneficially exploited to enhance vaporization of a liquid sprayed upstream of the porous medium and to improve the mixing of fuel vapors and air. Enhancement of fuel vaporization depends on the following:

- (i) Strength of heat feedback
- (ii) Droplet characteristics
- (iii) Porous medium properties
- (iv) Coflow conditions
- (v) Injector location

This chapter presents experimental and numerical results on evaporation enhancement of a liquid sprayed on the porous medium with simulated heat feedback rate. First, experimental results on the pressure drop through porous media and the uniformity of surface temperature are discussed. The spray characteristics such as mean axial velocity, droplet diameter, and liquid mass flux are presented. Next, the minimum heat feedback required for complete vaporization and vapor concentration profiles at downstream of the porous medium are presented. This chapter also

discusses the development and results of a computational model to predict spray evaporation rate in porous media using a two-energy equation model.

4.2 Pressure Drop Measurements

The pressure drop measurements were taken from two pressure taps located at 30 cm from upstream surface on each side of the porous medium. Figure 2.14 shows the experimental setup for these measurements. Difference in pressure was measured using a standard U-tube water column manometer. Pressure drop was first measured without porous medium to find out the pressure drop in the channel only. Measurements were taken at unheated coflow conditions (~ 294 K) and heated conditions (350, 400, and 450 K) with different porous media.

4.2.1 Unheated Coflow Conditions

Figure 4.1 shows the pressure drop measured across 25 and 31 PPCM porous media at unheated coflow conditions (~ 294 K) for different coflow velocities. The figure shows that the pressure drop increased as the velocity was increased like in a regular channel flow. This increase was initially linear corresponding to the Darcy flow regime, where the pressure drop was proportional to the viscous resistance. At higher velocities the pressure drop varied as the square of the velocity corresponding to Forchheimer flow regime, where the pressure drop depended on the viscous and inertial resistance of the porous medium. Also, the pressure drop increased as the linear pore density (defined as the number of pores per centimeter) was increased.

The porous medium structure became finer with larger linear pore densities, and hence, offered more resistance to flow. The increase in pressure drop with PPCM also followed a somewhat linear relationship.

4.2.2 Heated Coflow Conditions

The end boiling point of the kerosene used in the present study is ~ 510 K. Hence, the coflow air was preheated up to 450 K. To understand the effect of coflow temperature on the pressure drop across the evaporation porous medium, measurements were taken at 350, 400, and 450 K, and the results are presented in Figs. 4.2 to 4.4, respectively. Figure 4.5 shows the effect of coflow air temperature on the pressure drop across the 18 PPCM porous medium for a coflow air flowrate of 195 l/min. The overall increasing trend of the pressure drop with coflow air velocity was similar to that at ambient flow conditions. When the coflow air temperature was increased, the pressure drop across the porous medium also increased. Due to the decrease in air density, the velocity of air increases (since mass flowrate was constant) when the coflow temperature is increased. At higher flowrates, the pressure drop is proportional to the square of velocity, and hence, higher pressure drops were recorded at higher temperatures.

4.2.3 Comparison with Literature

The pressure drop in porous media has been studied by several researchers (Darcy, 1856; Forchheimer, 1901; Ergun, 1952; Macdonald et al., 1979; Fand et al. 1987; Civan and Evans, 1996; Liu and Masliyah, 1996). For flow through porous media,

the pressure drop (Δp) over a length L is expressed by the following relationship (Howell et al. 1996):

$$\frac{\Delta p}{L} = \frac{\mu}{\alpha} U + \rho C_2 U^2 \quad (4.1)$$

where α is the permeability and C_2 is the inertial coefficient. The above expression includes the viscous and inertial resistances due to fluid flow through porous medium.

Figure 4.6 compares the pressure drop measured in this study with that obtained by Ergun (1952) for unheated coflow conditions. As shown by Figs. 4.1 and 4.2, the pressure drop increased with an increase in velocity. The trend in general agrees with Ergun equation. However, our measured data is about twice that predicted by Ergun's equation for 25 PPCM porous media. This is attributed to the difference in the structure of porous medium. In the present experiments, randomly-structured consolidated fibrous porous medium was used. On the other hand, Ergun's equation was developed from experiments with unconsolidated uniform packed beds.

Another comparison of our results with Macdonald et al. (1979) is given below. The following equation was proposed by Macdonald et al. (1979) for the non-dimensional pressure drop through porous media:

$$F'_k \frac{\varepsilon^3}{1-\varepsilon} = 180(1-\varepsilon)/N'_{Re} + 4.0 \quad (4.2a)$$

where

$$F'_k = -\frac{\text{grad } P}{\rho U^2} D_{eq} \quad (4.2b)$$

and

$$N'_{Re} = \frac{\rho U D_{eq}}{\mu} \quad (4.2c)$$

where grad P is pressure gradient across porous media, D_{eq} is the equivalent diameter in packed beds (or average pore diameter in porous media).

For our experimental conditions (air density = 1.2 kg/m³; velocity = 1.65 m/s; viscosity = 1.85 × 10⁻⁵ Ns/m²; average pore diameter = 490 μm), pressure gradient across the porous medium is calculated to be 15300 (N/m²)/m. The measured pressure data for this case shows a gradient of 10768 (N/m²)/m, which is about 42% lower than that predicted by the Equation 4.2. It should be noted that the Equation 4.2 was developed for the unconsolidated packed bed porous media. The authors also cautioned that any measured data would likely to lie within ± 50% of Equation 4.2. From the above comparisons, our experimental results seem to be in good agreement with literature values.

4.2.4 Calculation of Permeability from Pressure Drop Data

Using Equation 4.1, if a graph is plotted between $(\Delta p/L)/u$ and u , the Y- intercept would give us μ/α . From the knowledge of viscosity of the fluid, we could calculate the permeability of the medium. Figure 4.7 shows such a relationship between $(\Delta p/L)/u$ and u for a porous medium with 18 PPCM. Using a viscosity of 1.85×10^{-5} Ns/m², the permeability of the porous media is calculated to be 17 to 53 md for the coflow temperature range (unheated to 450 K) considered in this study. Note that the permeability is measured in milli Darcy (1 Darcy = 9.87×10^{-13} m²). Thus, the pressure drop data could be used to estimate the permeability of porous media.

In another approach, Civan and Evans (1996) solved the differential form of Forchheimer equation and determined the permeability and non-Darcy flow coefficients. The effect of core length on non-Darcy flow coefficient was studied. Furthermore, Civan and Evans (1998) compared the accuracy of pressure-squared and pseudopressure formulations of the Forchheimer equation. For tight and coarse formation porous media, Civan and Evans (1996) employed permeability values in the range of 0.02 to 645 md. In our study, using the measured pressure drop across porous media and Ergun equation, the permeability values were calculated to be in the range of 3 to 500 md.

4.3 Porous Medium Temperature with Simulated Heat Feedback

Heat energy released in the combustion porous media is recirculated upstream and the evaporation porous medium is heated up. One way to systematically study the effect of this heat feedback is to uncouple the combustion process and simulate the heat feedback by an external method. In this study, the combustion heat feedback was simulated with resistive heating of evaporation porous medium. The electric input supplied to the porous medium for resistive heating is represented as a fraction of heat feedback from the combustion zone. The temperature attained by the porous medium, thus, depends on the strength of the heat source and the effectiveness of convective heat transfer between porous medium and coflow air. The porous medium surface temperature was measured by thermocouples embedded in the porous media and an infrared imaging camera. Porous medium temperature distribution was also predicted by using a local thermal non-equilibrium model.

4.3.1 Thermocouple Measurements

Figure 4.8 shows the measured surface temperature profiles in 25 and 31 PPCM porous media. The measurements were made using a K-type thermocouple under quiescent ambient conditions for different heat feedback rates. The measurements were taken on the centerline of the porous medium surface. The surface temperature was nearly uniform (within 50 K) in all the profiles. When the heat feedback rates were made stronger, higher peak temperatures were obtained, which is in accordance with the energy conservation in porous media. The figure further shows that the peak temperatures in the 25 and 31 PPCM porous media were about the same, indicating

their similar electrical resistance. Uncertainties estimated in the temperature measurements were less than $\pm 1\%$ of the mean value at 95% confidence level.

The lower temperatures recorded near the edges were caused by an increased heat loss from the copper plates to the chamber walls, and also due to the difference in contact resistance between the conductive glue and the porous media. Inside the porous medium, however, the electric power supplied served as heat source and caused an increase in temperature. This demonstrates that the porous medium we have employed has uniform thermo-electric properties.

4.3.2 Infrared Imaging

Note that a thermocouple embedded in a porous medium measures an average of gas and solid temperatures as it is in contact with both solid and fluid media. Hence, it does not indicate the true porous medium temperature. The distribution of temperature in the porous medium could be measured using an infrared technique. This study employed an infrared camera for such measurements. The measurements show the temperature distribution accurately, however, the values are only qualitative since the emissivity of the porous medium was not known accurately. The measurements were taken at different heat feedback rate conditions with and without the presence of preheated coflow air to determine the effects of those parameters.

Figures 4.9 and 4.10 show the surface temperature contours for 25 and 31 PPCM, respectively. The figures show the difference between the maximum and minimum

temperature in each case in order to examine the uniformity of temperature. It can be seen from the IR images that the temperature distribution in porous media was uniform within ± 5 K at 1 % heat feedback. The temperature distribution in 25 PPCM porous medium showed a double peak structure, while it was absent in the 31 PPCM porous medium. The surface temperature distribution was affected by the flow pattern of air inside the porous medium. Due to the difference in pore structure and fiber orientation between the two porous media, the flow pattern of air would be different, and in turn, changed the temperature distribution. The difference in the average temperature of the two porous media was, however, less than 10 K. The surface temperature measured using thermocouple showed that the porous medium temperature was uniform within 50 K. IR imaging indicated a maximum temperature difference of 10 K. This suggests that the temperature of porous medium (solid portion temperature measured by thermocouple) is uniform within measurement uncertainties.

Figures 4.9 and 4.10 present results of the porous medium temperature distribution. Semi-quantitative results could, however, be obtained by assuming a range of emissivities and using temperature measurements obtained by thermocouple. Results of such an analysis is presented in Fig. 4.11 for 25 PPCM porous medium with a simulated heat feedback of 1 % and a coflow air inlet temperature and flow rate of 400 K and 195 l/min, respectively. Comparison of Figs. 4.8 and 4.11 suggests that the emissivity of the porous medium falls between 0.7-0.9.

4.3.3 Predicted Temperature Profiles in Porous Media

4.3.3.1 Axial Temperature Distribution

Figure 4.12 shows the axial distribution of solid and gas phase temperatures in the computational domain with only gas flow for a heat feedback rate of 1%. The flowrate and temperature of the coflow air were held constant at 190 l/min and 450 K, respectively. It can be seen from the figure that the temperature of the gas phase increased in the porous region due to convective heat transfer. The gas phase temperature followed the porous medium temperature very closely. Figure 4.13 presents the predicted steady state axial variation of the porous medium centerline temperature for different heat feedback rates with only gas flow. The heat feedback rate was varied from 0.8 to 1.1% of the average heat input. The results indicate that the porous medium temperature increased linearly along the centerline and attained a peak value closer to the exit of the porous medium at all heat feedback rate conditions. This increase is due to the cumulative energy transfer from the coflow. The peak temperature attained by the porous medium also increased with stronger heat feedback rates. The peak temperature corresponding to the lowest and highest feedback rates considered in this study were 462 and 475 K, respectively.

The combustion heat energy fed upstream via conduction and radiation causes the porous medium temperature to increase. As the coflow air flows through the preheated porous medium, its temperature increases primarily due to convective heat transfer from the porous medium. Thus, the porous medium simultaneously behaves as source and sink in energy transfer. This process leads to a local thermal non-

equilibrium between the solid and gas phases. The effectiveness of heat transfer to the coflow depends on the convective heat transfer coefficient, which in turn, depends on the properties of fluid and porous medium. Recall that the coflow air velocity considered in this study ranged from 1 to 2 m/s. In this range, for the computational geometry considered, the convective effects in the calculation of porous medium temperature could be dominant. Under such situations, one could neglect the conduction term in the energy equation without sacrificing the solution accuracy.

4.3.3.2 Surface Temperature Distribution

Figure 4.14 shows the transverse temperature distribution at the exit surface of the porous medium for different heat feedback rates. These profiles were normalized by the half-width of the test section used in the experiments (w), for comparison. The figure shows that the surface temperature was uniform within 5% of the mean value at all conditions. The peak surface temperature increased with heat feedback rate which is in accordance with energy conservation in porous media.

4.3.3.3 Effect of Local Thermal Non-equilibrium

A study assuming local thermal equilibrium between the porous medium and coflow air was conducted to assess the equilibrium and non-equilibrium models. Figure 4.15 compares the porous medium temperature predicted by equilibrium and non-equilibrium models. Also shown in the figure is the experimental data of the porous medium surface temperature. The results show that the axial temperature profile predicted by the non-equilibrium model agrees with experimental data (infrared

imaging) better than that by equilibrium model. This indicates the existence of non-equilibrium heat transfer in the porous medium.

The difference would become significant when the study is coupled with combustion. In order to accurately predict the temperature distribution under rapid vaporization conditions (as in the present case), one should use local thermal non-equilibrium models (Dual et al., 2004). For local thermal non-equilibrium models, however, the proper selection of the interfacial heat transfer coefficient is essential as it affects the effectiveness of the heat transfer (Alazmi and Vafai, 2000). In this study, the interfacial heat transfer coefficient was calculated using a correlation proposed by Henneke and Ellzey (1995), as explained in Section 3.3.1.5.

4.3.3.4 Comparison with Experimental Data

Using the two-energy equation model (see Chapter 3 Section 3.3.1), computer simulations were performed to predict the surface temperature of porous medium. The computational parameters used for this simulation are given in Table 4.1. Figure 4.16 shows a comparison of model predictions and experimental measurements of porous medium surface temperature for heat feedback rate of 1%. The model predictions agree well with the infrared imaging data. Note that a thermocouple embedded in a porous medium measures an average of gas and solid temperatures as it is in contact with both the pure solid and fluid. On the other hand, infrared imaging measures the temperature of the solid portion directly. Thermal effects are crucial to the completeness of vaporization of liquid fuels. Surface temperature is an indirect

measure of vapor quality downstream of the porous medium. Uniform surface temperature distribution, thus, would lead to homogeneous fuel-air mixture downstream of evaporation porous medium.

4.4 Spray Characteristics

This section presents characteristics of the kerosene, n-heptane, and methanol fuel sprays. Characteristics such as droplet Sauter mean diameter (SMD), axial velocity, and liquid mass flux were measured simultaneously using phase Doppler particle analyzer. The experiments were conducted in unheated and heated coflow air conditions. The atomizing air flowrate was fixed at 8 l/min in all the experiments. This information provides the fuel spray conditions upstream of the evaporation porous medium which are needed to determine the effects of porous medium itself.

4.4.1 Characteristics of Kerosene Spray

4.4.1.1 Measured Sauter Mean Diameter Profiles

The fuel flowrate was varied between 6–14 ml/min. A positive pressure of 0.34 atm was applied to the fuel tank. In all experiments, the secondary air flowrate and temperature were varied from 130-195 l/min and 423-490 K, respectively.

There are several approaches to represent droplet diameter in a spray. In combustion calculations, generally Sauter mean diameter is used. This represents the ratio between total volume and surface area of droplets. Figures 4.17 to 4.19 show the

measured transverse profiles of Sauter mean diameter at 2.5 cm upstream of the leading edge of the evaporation porous medium. Figures 4.20 to 4.22 and Figures 4.23 to 4.25 show the transverse profiles of Sauter mean diameter at 2.0 and 1.5 cm upstream of the porous medium, respectively. In general, the droplet diameters varied from 15 to 35 μm . Lower droplet diameters were recorded in the spray core and the droplet diameter increased radially outward. Further, the droplet diameter increased with an increase in equivalence ratio. In most cases, the temperature increase from 423 K to 450 K did not change the SMD distribution significantly. However, increasing the coflow temperature to 490 K caused significant evaporation (end boiling point \sim 510 K), and hence, reduced the SMD distribution. Uncertainties in the SMD measurements were estimated using Student's t-distribution at 95% confidence level. The estimated uncertainty in SMD close to the spray edge was less than $\pm 2.6\%$ of the mean value. Uncertainties estimated at other locations inside the spray were lower than that measured at the spray edges due to the presence of large number of droplets.

Yule et al. (1982, 1983) noted similar observations with kerosene spray using laser tomographic light scattering technique. Air-blast atomizers are provided with a swirling flow to promote atomization and impart an outward radial momentum to the spray. The swirl, subsequently, converts the tangential velocity into radial velocity and makes the spray spread more radially. The swirl number (S) of the atomizer is calculated as:

$$S = \frac{G/2}{1-G/2} \quad (4.3)$$

where G is the ratio between tangential and axial velocity of fluid in the atomizer. In this case, the radial velocity was assumed to be 25% of axial velocity. The swirl number was calculated as 0.14. An alternative explanation for spray widening given by Presser et al. (1993) is as follows: A toroidal recirculation zone is created within the spray, due to the swirling motion of the primary air. This, in turn, convects the small droplets towards the core and also widens the spray radially. The experimental observations from the present study support these arguments well.

At lower coflow temperatures, a specific pattern was not followed with equivalence ratio or coflow velocity. Kerosene is a multicomponent fuel and it has a range of boiling points. The maximum residence time of fuel spray (t_{res}) in coflow air before impinging on the porous medium could be calculated as:

$$t_{res} = \frac{\text{Maximum distance between the porous medium and injector}}{\text{Minimum droplet axial velocity}} \quad (4.4)$$

In this case, t_{res} was estimated as 6 ms. Due to this residence time spray spent in coflow, some evaporation of lighter fractions could have occurred, and hence, altered the droplet diameter. Such evaporation does not usually follow a systematic trend,

since the local conditions and fuel composition vary. At higher coflow temperatures, droplet diameter showed a distinct variation with equivalence ratio; it increased with an increase in equivalence ratio. At these temperatures, lighter fractions would have already evaporated. With an increase in fuel equivalence ratio, fuel flowrate was increased, which in turn, increased the droplet diameter.

Note that the overall equivalence ratio (actual fuel-air ratio/stoichiometric fuel-air ratio) was based on the sum of atomizing and coflow air flowrates. During the experiments, the atomizing air flowrate was held constant, while the fuel flowrate was increased, and hence, drop size distribution varied with the fuel flow rate.

4.4.1.2 Comparison with Numerical Model

The spray characteristics upstream of the evaporation porous media were predicted by using an air-blast atomizer model (see Section 3.3.2.5). The spray model uses several empirical parameters. These parameters were first determined by conducting a number of simulations and comparing the results with experimental data. Table 3.2 presents the values of empirical constants used in the model. Figure 4.26 presents a comparison of droplet diameter predicted by the numerical model and the measured experimental data. The figure shows that the model predictions agree well with experimental data. As observed from the experimental measurements, smaller droplet diameter was noted in the spray core and its diameter increased radially outward.

4.4.1.3 Measured Droplet Velocity Profiles

Droplet velocity measurements were taken simultaneously with Sauter mean diameter at similar conditions. The secondary air flowrate and temperature were varied from 130-195 l/min and 423-490 K, respectively. Figures 4.27 to 4.29 show the measured transverse profiles of droplet axial velocity at 2.5 cm upstream of the leading edge of the evaporation porous medium. Figures 4.30 to 4.32 and Figures 4.33 to 4.35 show the transverse profiles of droplet axial velocity at 2.0 and 1.5 cm upstream of the porous medium, respectively.

The results show that higher droplet velocities were recorded at the spray core and the droplet velocities decreased radially. The peak axial velocity in each profile varied from 7 to 23 m/s. Since the droplets present in this region were smaller, they moved at higher velocities. Due to the swirl imparted to fuel spray, large particles were thrown away from the spray core, which moved at lower velocities. Also, a large number of particles were thrown away from the spray core. The transverse profiles measured at different location also exhibited similar trends. The peak axial velocity of the droplets decreased axially.

4.4.1.4 Measured Mass Flux

Measurement of liquid fuel mass flux distribution upstream of porous medium is important to understand the vapor concentration downstream of the porous medium. In the measurements, the secondary air flowrate and temperature were varied from

130-195 l/min and 423-490 K, respectively. The liquid mass flux (MF_l) at each measurement point was calculated as follows:

$$MF_l = \frac{\rho_l V_{tot}}{A_{probe} t} \quad (4.5)$$

where,

- ρ_l Density of droplet particles
- V_{tot} Total volume of droplets
- A_{probe} Probe area of PDPA at measurement location
- t Total measurement time

Figures 4.36 to 4.38 show the measured transverse profile of droplet mass flux at 2.5 cm upstream of the leading edge of the evaporation porous medium. Figures 4.39 to 4.41 and Figures 4.42 to 4.44 show the transverse profiles of droplet mass flux at 2.0 and 1.5 cm upstream of the porous medium, respectively.

The reduced data reveal that the mass flux profiles follow the trend of SMD profiles at the corresponding equivalence ratios. The mass flux is higher away from the core due to the presence of higher number of droplets with larger diameter. Mass flux at a given transverse location also increased with increase in equivalence ratio.

When there is no porous medium employed, the vapor concentration profiles should follow the liquid mass flux profiles, if uniform vaporization takes place. *The presence of the porous medium, however, modifies the effects of mass flux profiles, and the heat feedback to the porous medium enhances evaporation. As a result, a uniform vapor concentration distribution could be obtained at the exit, depending on the structure of the porous medium.* The relationships between the mass flux distribution and the vapor concentration are explained in Section 4.6.

4.4.2 Characteristics of n-Heptane Spray

The role of porous medium in the evaporation enhancement of different fuels was also studied with n-heptane and methanol. In the kerosene experiments, a wide range of flowrate and coflow temperatures were used. For the n-heptane spray study, the fuel flowrate was held constant at 6 ml/min and the coflow air flowrate was varied from 77 to 178 l/min. Here the fuel flowrate was held constant and the coflow air flowrate was varied to achieve different equivalence ratios. This was done to keep the firing rate of the burner constant. Particularly, the fuel flowrate of 6 ml/min corresponds to a firing rate of 3 kW typically encountered in industrial burners. Measurements were taken at 2.5, 2.0 and 1.5 cm upstream of the leading edge of the evaporation porous medium.

Figures 4.45 and 4.46 present the measured Sauter mean diameter of n-Heptane spray under unheated and heated coflow conditions, respectively at three axial locations.

Figures 4.47 and 4.48 present the measured droplet axial velocity of n-Heptane spray under unheated and heated coflow conditions, respectively at three axial locations.

Overall, the droplet Sauter mean diameter varied from 50 to 80 μm in most cases. The n-heptane droplet diameter distribution showed that the small particles were present in spray core and larger particles were thrown away from the core. However, this variation was not as pronounced in the n-heptane spray as in the kerosene spray. This is due to the lower boiling point and molecular weight of n-heptane. Also note that n-heptane is a single component liquid with a unique boiling point. The peak droplet diameter occurred at or close to the middle of the spray. The droplet diameter variation with equivalence ratio showed more fluctuations in cold conditions than that in heated conditions. The peak droplet velocity varied from 10 to 40 m/s. The droplet axial velocity generally decreased along the transverse direction. In some cases, due to non-uniform vaporization, droplets with higher velocities were also recorded. With an increase in equivalence ratio, the droplet velocity showed a decreasing trend.

4.4.3 Characteristics of Methanol Spray

In the methanol spray experiments, the fuel flowrate was held constant at 12 ml/min and the coflow air flowrate was varied from 77 to 178 l/min. Measurements were taken at 2.5, 2.0 and 1.5 cm upstream of the leading edge of the evaporation porous medium. Figures 4.49 and 4.50 present the measured Sauter mean diameter of the methanol spray under unheated and heated coflow conditions, respectively at three

axial locations. Figures 4.51 and 4.52 present the measured droplet axial velocity of n-Heptane spray under unheated and heated coflow conditions, respectively at three axial locations.

Table 4.2 shows a comparison of the kerosene, n-heptane, and methanol spray characteristics. Overall, the peak droplet diameter varied from 60 to 85 μm in most cases. The peak droplet diameter occurred at or close to the spray core. Farther away from the porous medium (i.e., closer to injector), the droplet diameter profiles showed a decreasing trend along the transverse direction. This variation became more uniform as the distance to the porous medium from the injector (d_{ip}) was reduced. Similar observations were noted in heated conditions also. The droplet velocity profiles show that the particles at the core had lower velocity and the velocity increased in the transverse direction. Heated coflow air reduced this variation with equivalence ratio. The increasing trend along the transverse direction was also observed in heated conditions.

4.5 Minimum Heat Feedback Rate for Complete Vaporization

4.5.1 Definition of Minimum Heat Feedback Rate

A horizontal laser sheet was passed through the test section at 5 cm downstream of the porous medium. The scattering of light was visible whenever there were droplets leaving the porous media. The liquid fuel spray was considered to be fully vaporized if the scattered incident laser light was not visible. For a given injector location, a

large amount of heat feedback rate (through resistive heating) was supplied initially, and the complete vaporization was ensured by making the laser beam invisible. Then, the heat feedback rate was slowly reduced in steps. Sufficient time was given between each step for the porous medium to attain a thermal steady state. At every step, the appearance of scattered light was checked. This procedure was continued until the scattered light became visible and droplets were seen. The heat feedback rate (electric power supplied to the resistive heater), required just to avoid the escape of droplets from the porous medium, was termed the minimum heat feedback rate required for complete vaporization at that injector location. Then, the injector was moved to the next location and the entire experimental sequence was repeated. In the present experimental setup, the distance between the porous medium and injector had to be at least 3 cm to avoid the spray impinging on the wall.

4.5.2 Vaporization with Porous Media

Figure 4.53 shows the variation of minimum heat feedback rate required for complete vaporization as a percentage of heat input for 25 PPCM and 31 PPCM porous media with the distance between the injector and the porous media. During the experiments, the coflow air flowrate was held constant at 195 l/min, and the temperature was maintained at 400 K. At equivalence ratios (ϕ) of 0.3 and 0.4, no heat feedback was required to achieve complete vaporization for both type of porous media. The preheated coflow air itself was sufficient to vaporize the fuel completely at all injector locations (3-15 cm upstream of the porous medium) studied. At higher equivalence ratios, however, some amount of heat feedback was needed to

completely vaporize the fuel. This heat feedback rate increased as the injector was moved closer to the porous medium. When the injector was moved closer to the porous medium, the residence time of fuel spray in hot air was lower and the fuel spray was not able to vaporize completely, and hence needed a larger heat feedback rate for complete vaporization.

For the 25 PPCM porous medium, the required minimum heat feedback rate increased almost linearly with decreasing distance between the injector and porous medium (Fig. 4.53a). The heat feedback requirements at $\phi = 0.5$ and 0.6 remained close to each other. About 1 % of the average heat input rate between an equivalence ratio of 0.3 and 0.6 (1.5 times of the heat of vaporization) was needed as heat feedback rate to achieve liquid heating and complete evaporation in this case. With 31 PPCM porous medium, no heat feedback was required when the injector was placed at 7 cm or farther from the base of the porous medium. At other injector locations, the heat feedback rate required was lower than that of 25 PPCM porous medium. Under the present conditions, with 1 % heat feedback rate, complete vaporization could be achieved with an upstream injector location of 3 cm. Estimated uncertainty in the minimum heat feedback rate was less than $\pm 10\%$ of the mean value at 95% confidence level. Note that a visual inspection of the laser sheet was followed to determine the scattered light. The uncertainty in the measurements could be caused by the errors associated with the visual inspection, and due to the uncertainties in resistive heating. When no porous medium was employed, this would translate to

the use of a coflow air temperature of at least 500 K or an upstream distance between injector and porous medium of more than 15 cm.

Porous media with high PPCM are suitable for evaporation applications since they could also act as flame arrestors. The porous media with 25 PPCM and 31 PPCM are suitable for such applications, and hence, were employed in this study. The factors such as spurious scattering from the test section, and non-uniformity in the porous medium heating could lead to errors in the heat feedback measurements. It was ensured that the test section was free of droplets sticking to the wall, downstream of the porous medium. Furthermore, the scattering was observed at a fixed location throughout the experiments. Errors due to non-uniformity in the porous medium heating were minimized by waiting for a fixed amount of time between every step. This time interval was enough for the porous medium to attain steady state.

Experiments were conducted to determine the minimum heat feedback required for complete vaporization for n-heptane and methanol sprays. It was found that at both unheated and heated coflow air conditions (50 °C), there was no need for any additional heat input. There are two important factors to achieve complete vaporization: (i) coflow air temperature and (ii) residence time in porous medium. Since the boiling point of these fuels is low, given sufficient residence time in porous media, complete vaporization could be achieved even at low coflow air temperatures. The presence of porous medium increases the residence time, and hence, enhances evaporation.

4.5.3 Vaporization without Porous Media

The spray vaporization characteristics in the absence of porous media were measured for comparison purposes. The laser beam was passed transversely at various axial locations of the spray emanating from the injector at different coflow air temperatures. The light scattering from the droplets was observed. The results are presented in Table 4.3. Results showed that at a coflow air temperature of 500 K or above, fuel droplets were completely vaporized within 3 cm from the injector exit. When the coflow temperature was reduced to 477 K, a minimum distance of 9 cm between injector and porous medium was needed for complete vaporization. With a further reduction in coflow temperature to 450 K and below, a distance of more than 15 cm was needed for complete vaporization. However, results obtained with both the porous media showed that at a coflow temperature of 400 K with combustion heat feedback, the minimum distance required for complete vaporization was 3 cm. Employing porous media, thus, enhances evaporation considerably. The porous medium also permits the operation at a lower coflow air temperature with a shorter section to locate the injector upstream of the porous medium.

4.6 Vapor Concentration Profiles

This section presents the measured and predicted vapor concentration profiles downstream of the evaporation porous media with and without simulated combustion heat feedback. A comparison of the vapor concentration profiles downstream of the

porous medium and liquid mass flux upstream of porous medium is also made to demonstrate the role of porous medium in evaporation enhancement.

4.6.1 Measured Kerosene Vapor Concentration Profiles with no Heat Feedback Rate

Figure 4.54 shows the measured transverse kerosene vapor concentration profiles at 5 cm downstream of 25 and 31 PPCM porous media for different overall equivalence ratios with no combustion heat feedback. The temperature of the coflow air was held constant at 450 K. The vapor concentration ranged from 1500 to 3500 PPM. For 25 PPCM porous media, the vapor concentration decreased radially towards the edges whereas for the 31 PPCM porous media, it fluctuated. With an increase in the equivalence ratio from 0.3 to 0.7, while average vapor concentration showed a maximum variation of 20% from the mean value, the transverse profiles followed no systematic trend. Overall, the average vapor concentration in transverse locations of up to 50% on either side from the centerline of the test section was uniform within $\pm 20\%$ (maximum). The edge effects, such as conduction and radiation losses to the walls, are responsible for the sharp changes near the chamber walls. This demonstrates that the porous medium is uniformly distributing the fuel vapor.

Figure 4.55 shows the transverse distribution of liquid mass flux upstream and vapor concentration downstream of 25 PPCM porous medium at equivalence ratios of 0.3 and 0.6. The vapor concentration distribution in Fig. 4.55 follows the liquid mass flux distribution upstream of the porous media. From the SMD profiles of the

kerosene spray (Figs. 4.17 to 4.25), the droplet diameter ranged from 15 to 35 μm with a variation of 35% of the mean value. Due to the presence of porous media, the vapor concentration distribution was relatively more uniform, although a scattered mass flux pattern was observed upstream of the porous medium. The porous medium establishes a more uniform profile, a benefit derived from its random matrix structure. In addition, due to the complex flow path imposed on the liquid droplets, the droplets' residence time increases, which further improves the evaporation rate. While the operating conditions and upstream spray distribution pattern remain same, the evaporation rate would increase with an increase in the thickness of the porous medium.

During measurements, the vapor samples drawn from the test section quickly condensed outside, since the boiling point of kerosene was ~ 510 K. This problem was minimized by heating the entire sample line using an electrical heating tape. In addition, the reaction chamber of the vapor concentration analyzer was isolated from the instrument and electrically heated. Even with this arrangement of heating, some vapor condensation was observed in the flow line. This led to an uncertainty of 13% of the mean value in measurements at 95% confidence. Figure 4.54 shows a maximum variation of 20% in vapor concentration measurement and the estimated uncertainties were 13%. This indicates that the vapor concentration downstream of the porous medium is fairly uniform.

Figure 4.56 presents the measured transverse n-heptane vapor concentration profile at 5 cm downstream of the porous medium exit surface for $\phi = 0.5$ and 0.6 with unheated coflow air. Recall that no combustion heat feedback is required for complete vaporization of n-heptane spray; just the presence of the porous medium is sufficient. Results indicate that the vapor concentration profiles showed a maximum variation of 14% of the mean value at $\phi = 0.6$. The average vapor concentration decreased by 22% when the equivalence ratio was increased from 0.5 to 0.6. However, the vapor concentration distribution remained somewhat uniform.

4.6.2 Vapor Concentration Measurements with Simulated Heat Feedback Rate

Figure 4.57 shows the transverse profiles of the vapor concentration for a 31 PPCM porous medium and at equivalence ratios of 0.3 and 0.6 with a combustion heat feedback rate of 1 % of heat input rate. The vapor concentration profiles taken without the heat feedback are also shown for comparison. The vapor concentration obtained with heat feedback was higher than that with no heat feedback conditions. With heat feedback, the average vapor concentration increased by 63% and 43% for 0.3 and 0.6 equivalence ratios, respectively. The evaporation enhancement decreased with increase in fuel flowrate. This is because of the fact that the heat feedback rate was held constant and was not sufficient to maintain the complete vaporization at higher fuel flowrates. Similar observations were noted in the computational simulations also.

The above results clearly demonstrate that the porous medium enhances the evaporation. However, the extent of enhancement depends on the combustion heat feedback rate and the porous medium structure. The heat feedback rate, in turn, depends on the combustion chamber stoichiometry and the effectiveness of heat transfer between the downstream flame and the porous medium (Kaplan and Hall, 1995 and Mital et al., 1997).

4.6.3 Comparison with Model Predictions

The transverse vapor concentration profile at 5 cm downstream of the porous medium exit surface for 1% heat feedback rate and $\phi = 0.3$ was predicted using the two-energy equation model. Figure 4.58 compares the numerical predictions and corresponding experimental data. Note that only half-profile of the measured vapor concentration data were compared with numerical model. The figure indicates that model predictions agree well with experimental data. The vapor concentration distribution showed a dip of less than 5% of the mean value in the core region and an increasing trend in the middle of spray. This demonstrates that the present numerical model is effective to predict the evaporation characteristics in porous medium.

4.6.4 Computational Parametric Study

This section presents a parametric study of the effects of the heat feedback rate, porous medium structure and fuel flow rate on spray evaporation characteristics using the numerical model which was validated with vapor concentration measurements.

4.6.4.1 Effects of Porous Medium Heat Feedback Rate

Several simulations with different strengths of heat feedback rates (0.8 to 1.1% of average heat input) were conducted to understand the effects of heat feedback from the combustion porous medium. During the study, air flowrate and overall equivalence ratio were held constant at 190 l/min and 0.3, respectively and the vapor concentration profiles were taken at 5 cm downstream of porous medium. The results are presented in Fig. 4.59. It is evident from Fig. 4.59 that the peak vapor concentration increased when the heat feedback rate was made stronger. The peak concentration obtained with a heat source of 1.1% was 40% times higher than that of the case with 0.8% heat feedback rate. As the heat feedback rate was made stronger, the peak temperature achieved by the porous medium also increased which, in turn, enhanced the evaporation. This shows that the thermal effects of the porous medium play an important role in evaporation enhancement.

4.6.4.2 Effects of Porous Medium Structure

The effects of the porous medium structure were studied by varying the porosity of the medium. Simulations were performed for a range of porosities (0.5–0.8). During the calculations, the porous medium heat feedback rate, air inlet temperature, and overall equivalence ratio were held constant at 1%, 450 K and 0.3, respectively. First, the steady-state axial temperature profiles for the solid medium were obtained and the results are presented in Fig. 4.60. Figure 4.60 suggests that at any given axial location, the solid temperature decreases with increase in porosity. This is in qualitative agreement with the definition of porosity. Recall that porosity is the ratio

between the void volume and total volume of a material. If the porosity is increased and total volume is held constant, the solid surface area decreases. Under constant heat input conditions, if the solid surface area decreases, the heat taken away by the fluid phase increases, which in turn, lowers the temperature attained by the solid medium.

Predicted transverse vapor concentration profiles at 5 cm downstream of the porous medium for different porosities are shown in Fig. 4.61. The figure indicates that the predicted vapor concentration profiles exhibited similar trends. The peak vapor concentration remained constant or decreased by 8% as the porosity was increased from 0.5 to 0.8. This suggests that the porosity of the medium had negligible effects on vapor concentration distribution. Note that these simulations were conducted at 1% combustion heat feedback rate. Our previous simulations (Periasamy and Gollahalli, 2006) show that at higher combustion feedback rates such as 3.6%, the peak vapor concentration decreased by 42% as the porosity was increased from 0.5 to 0.87. At 1% combustion feedback rate, the raise in porous medium temperature was lower than that at 3.6%. This led to lower porous medium temperature, and hence, produced a smaller difference in peak vapor concentration.

4.6.4.3 Effects of Fuel Flowrate

In typical combustion systems, depending on the load, the fuel stoichiometry changes; this affects the peak temperature in the flame zone, and in turn the heat feedback to the evaporation porous media (EPM). Unless the heat feedback is

measured experimentally or known by modeling combustion, a coupled solution to this problem is very difficult. Hence, the problem was solved in an uncoupled manner; first, the effects of different heat feedback strengths were studied by holding the equivalence ratio constant. Then, the equivalence ratio was varied by holding the strength of heat source constant. Results of the former study are discussed in Section 4.6.4.1 and that of the latter study are presented in this section.

Figure 4.62 shows the effect of fuel flowrate (or overall equivalence ratio, since air flowrate is constant) on transverse vapor concentration distribution at 5 cm downstream of porous medium for a heat feedback rate of 1%. The air flowrate was fixed at 190 l/min and fuel flowrate was varied.

Results showed that the vapor concentration profiles followed a near-flat profile in the center region at the exit of the porous medium. With an increase in equivalence ratio from 0.3 to 0.4, the peak vapor concentration increased by 50%. Further increase to 0.7 caused the peak vapor concentration to decrease. Since the air flowrate was held constant, fuel flowrate was increased to achieve richer equivalence ratios. Increase in fuel flowrate beyond a critical value flooded the porous medium. This decreased the evaporation enhancement. Further, the heat feedback rate (and hence, the peak temperature attained by the porous medium) was held constant for all these simulations. In liquid-fueled combustors, increased fuel flowrate means an increase in firing rate. This would, in turn, increase the rate of energy that has been fed back to the evaporation porous media. Hence, the peak temperature attained by

the porous medium would also increase. This, in turn, would lead to higher vapor concentration downstream of the porous medium.

4.6.4.4 Effects of Flame Temperature

In previous sections, a volumetric heat source as a fraction of average heat input was specified in the solid phase energy equation to simulate combustion heat feedback. In this section, instead of adding a heat source, a flame with a specified temperature was set at the exit of the porous medium. The heat transfer from the flame zone to the porous medium was predicted by solving the radiative transfer equation. The radiative heat flux was computed using a P-1 radiation model (see Section 3.3.1.5) and substituted as a source term in the solid phase energy equation. The convective heat transfer to the gas phase was computed using Equations 3.9 and 3.10. Figure 4.63 shows the axial temperature distribution in the porous medium for two flame temperatures. The peak temperatures attained at the leading edge of porous medium were 1245 and 1475 K for flame temperatures of 1400 and 2100 K, respectively. This indicates that under burning conditions the porous medium attains much higher temperatures than that are needed for complete vaporization. This means that additional porous media could be installed upstream for evaporation enhancement. This would, in turn, shorten the evaporation regime.

4.7 Chapter Summary

This chapter presented evaporation characteristics of liquid spray in porous media with simulated combustion heat feedback rate. Both experimental and numerical results were discussed. Measured pressure drop increased with linear pore density, as the porous medium structure became finer with larger linear pore densities. Surface temperature distribution obtained by infrared imaging revealed that the temperature of porous medium was uniform within measurement uncertainties. Predicted axial and surface temperature of the porous medium showed that the peak temperature increased with an increase in heat feedback rate. Model predictions agree well with experimental measurements. Droplet results showed that higher droplet velocities were recorded at spray core and the droplet velocities decreased radially. Peak vapor concentration with combustion heat feedback showed 63% higher than that with no heat feedback. The presence of porous medium increases the residence time, modifies the radial non-uniformity of mass flux profiles, and prepares uniform vapor concentration downstream of porous medium. Combustion heat feedback to the porous medium increases its temperature, improves the heat transfer to droplets, and enhances evaporation.

Table 4.1 Computational parameters used in two-energy equation modeling

Parameter	Value	Units
Porosity	0.87	-
Pore diameter	490	μm
Ergun constant 1	180	-
Ergun constant 2	4.0	-
Porous region volume	36	cm^3

Table 4.2 Comparison of droplet characteristics of kerosene, n-heptane, and methanol sprays upstream of evaporation porous medium

Parameter	Kerosene	n-Heptane	Methanol	Units
Fuel flowrate	6-14	6	12	ml/min
Coflow air flowrate	130-195	77-178	77-178	l/min
Peak droplet diameter	15-35	50-80	60-85	
Location of peak SMD	at or close to spray core	at or close to spray core	at or close to spray core	-
Peak droplet velocity	7-23	10-40	10-35	m/s
Effect of temperature on SMD variation	reduced the effect of ϕ at 490 K	reduced the effect of ϕ at 323 K	reduced the effect of ϕ at 323 K	-
SMD variation along transverse direction	generally decreased and then increased	decreased	decreased	-
Droplet axial velocity variation along transverse direction	decreased	decreased	increased	-

Table 4.3 Results of vaporization experiments without porous media

Coflow air temperature, K	Presence of porous medium?	Results
500 K and above	No	Kerosene droplets were vaporized completely with 3 cm from the exit of the injector
477 K	No	A minimum distance of 9 cm was needed for complete vaporization
450 K and below	No	More than 15 cm was needed for complete vaporization
400 K	<i>Yes*</i>	<i>With the use of porous media, only a minimum of 9 cm was needed for complete vaporization</i>

*Heat feedback rate supplied to the evaporation porous medium was 1% of the average heat released in the combustion zone

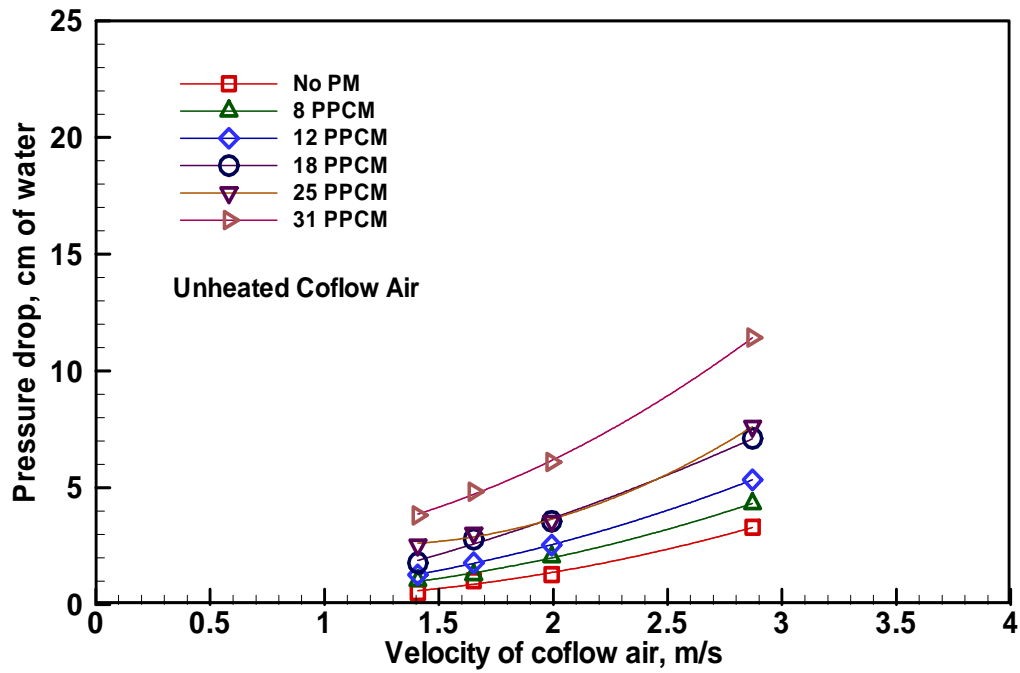


Fig. 4.1 Measured pressure drop across porous media of different pores per centimeter at various coflow air velocities (unheated)

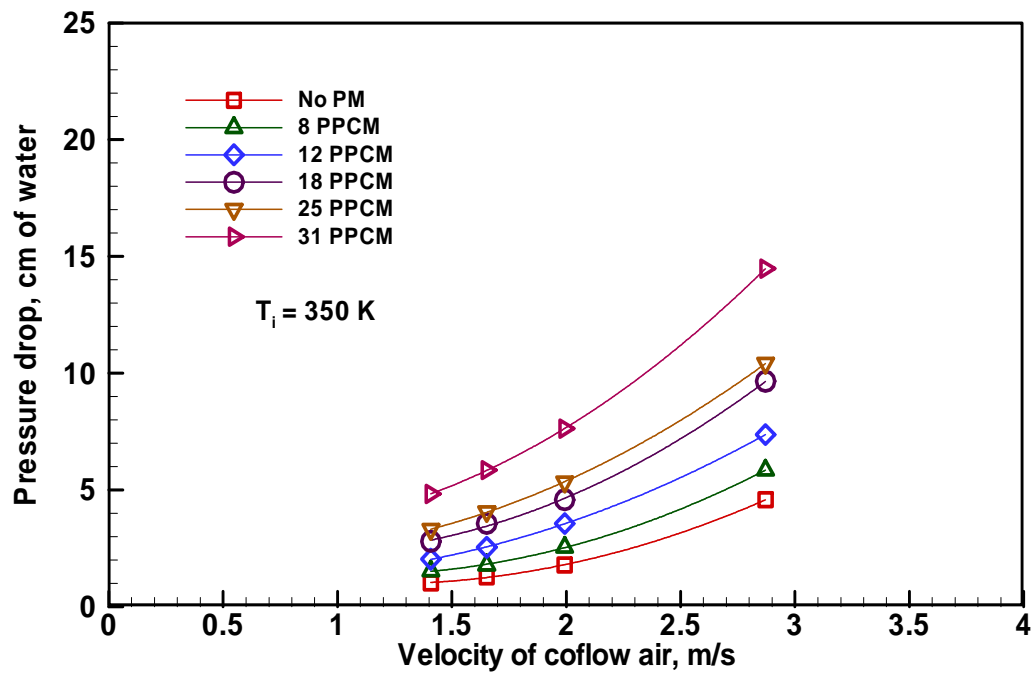


Fig. 4.2 Measured pressure drop across porous media of different pores per centimeter at various coflow air velocities (Coflow air temperature = 350 K)

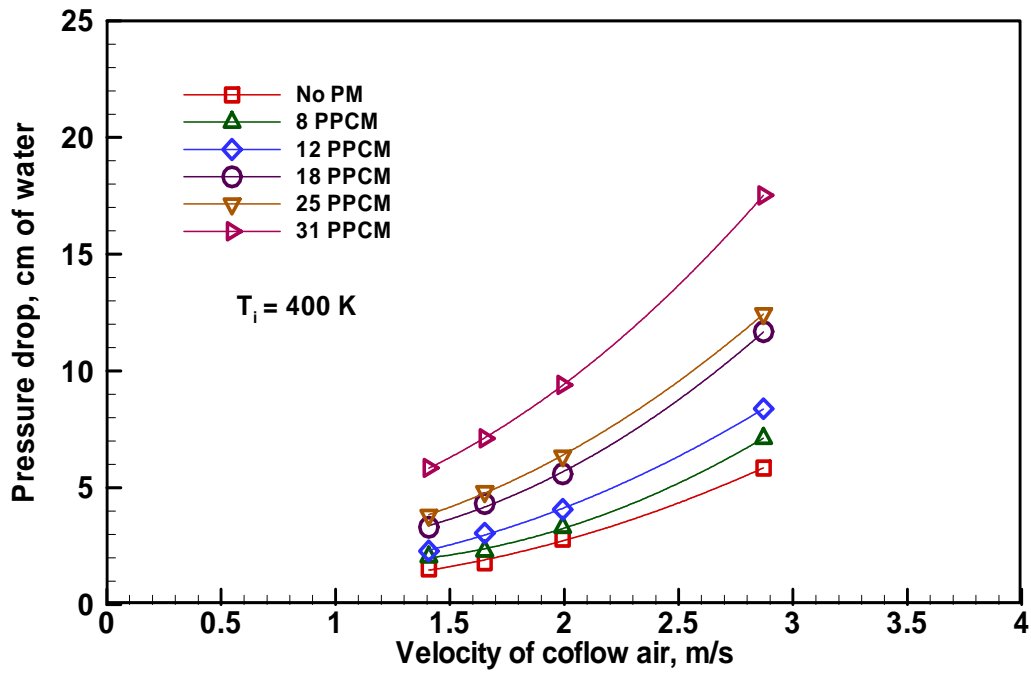


Fig. 4.3 Measured pressure drop across porous media of different pores per centimeter at various coflow air velocities (Coflow air temperature = 400 K)

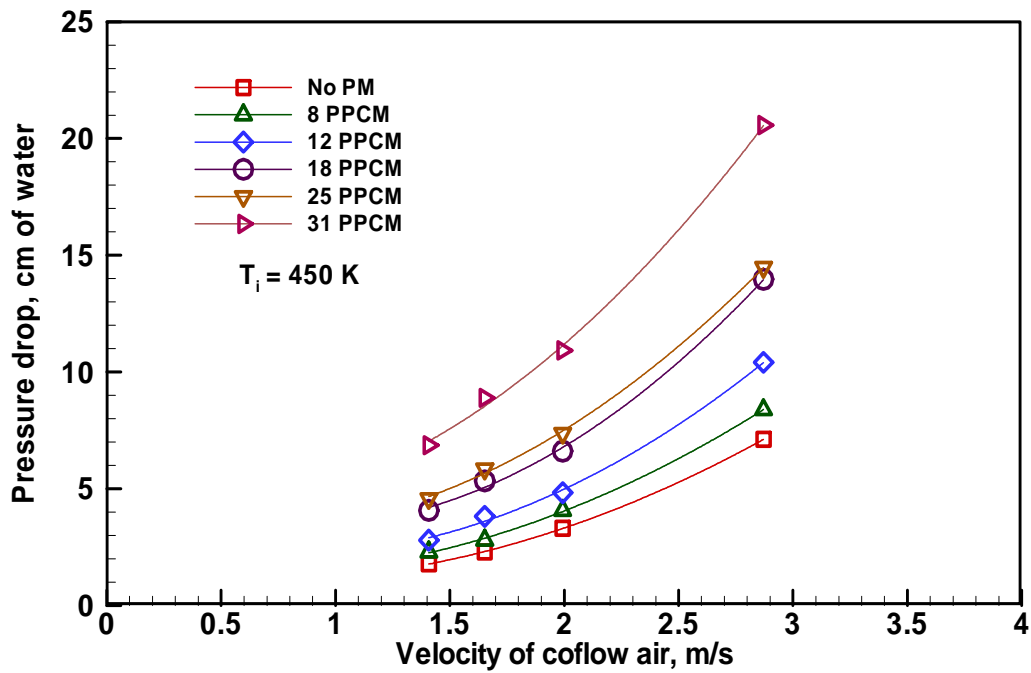


Fig. 4.4 Measured pressure drop across porous media of different pores per centimeter at various coflow air velocities (Coflow air temperature = 450 K)

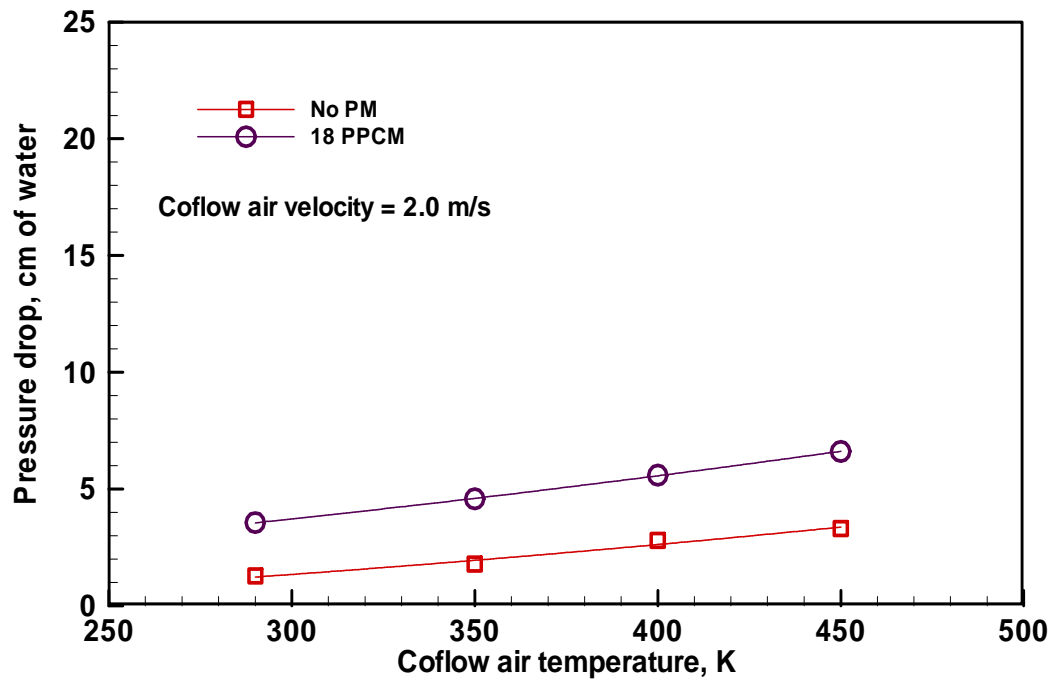


Fig. 4.5 Effect of coflow air temperature on the pressure drop across 18 PPCM porous media at a coflow air flow rate of 195 l/min

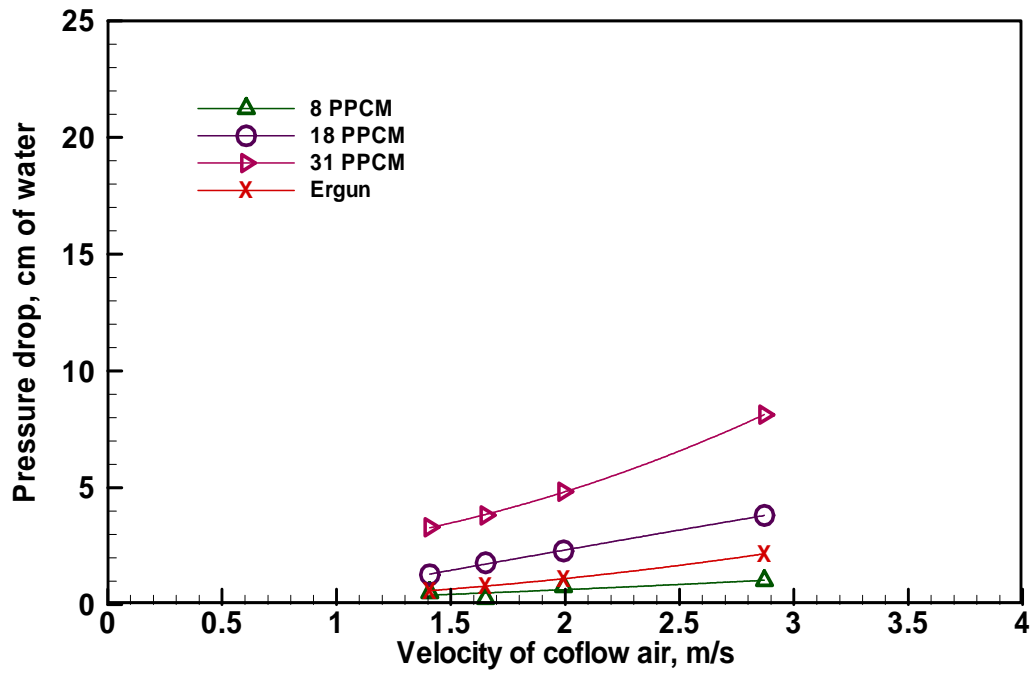


Fig. 4.6 Comparison of measured pressure drop across porous media with Ergun equation (unheated coflow air)

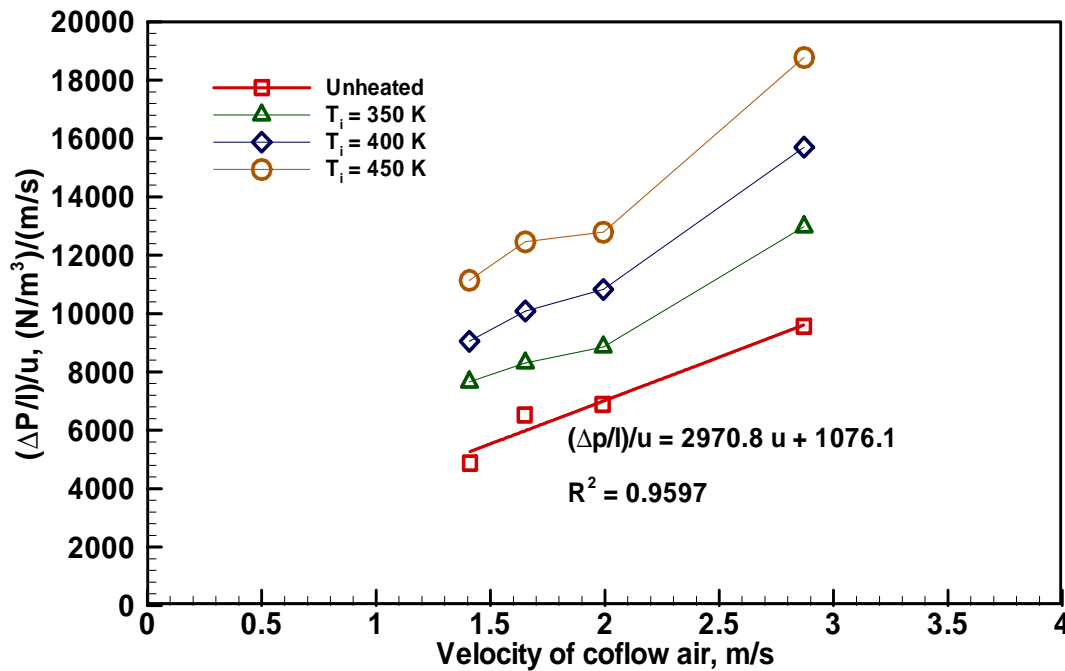
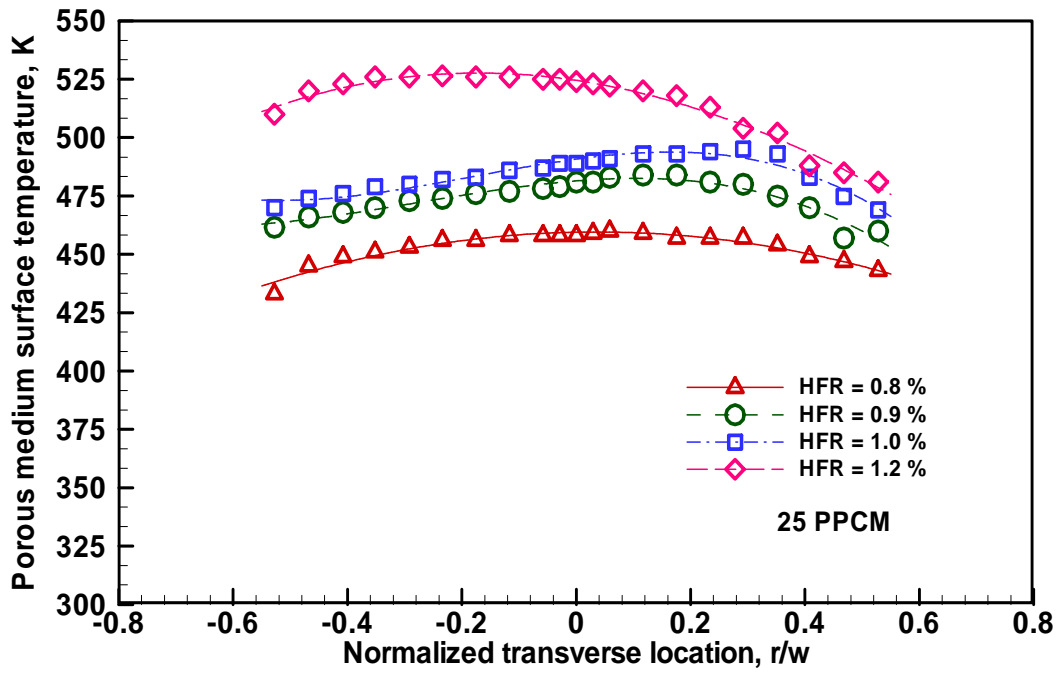
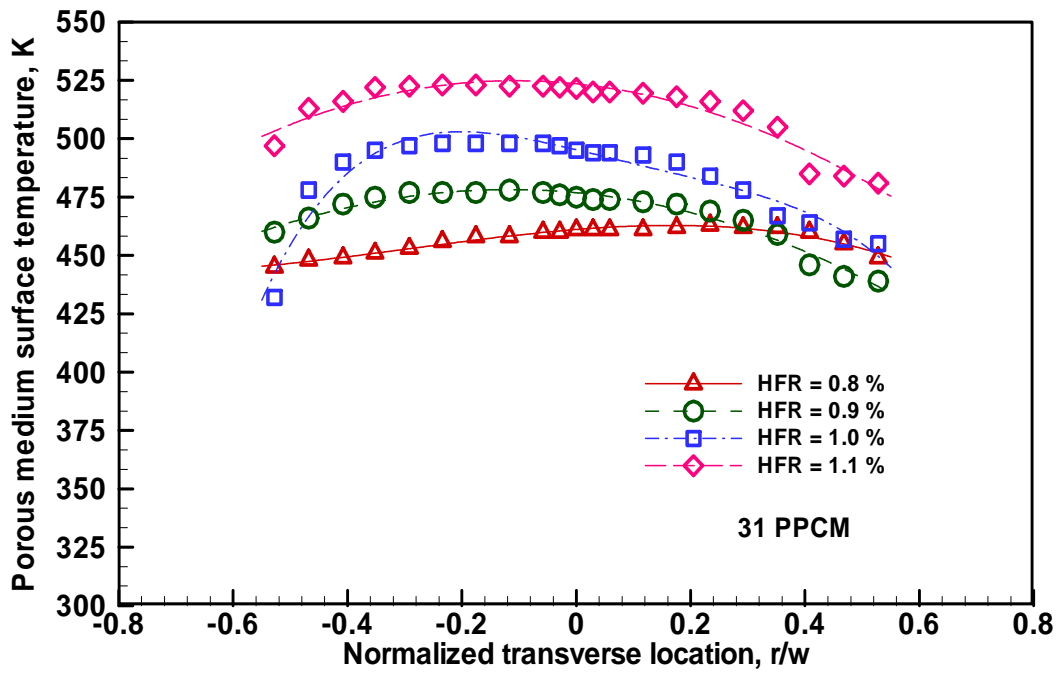


Fig. 4.7 Calculation of permeability of porous media from the measured pressure drop data (PPCM = 18)



(a) 25 PPCM



(b) 31 PPCM

Fig. 4.8 Measured surface temperature distribution in 25 and 31 PPCM porous media with different heat feedback

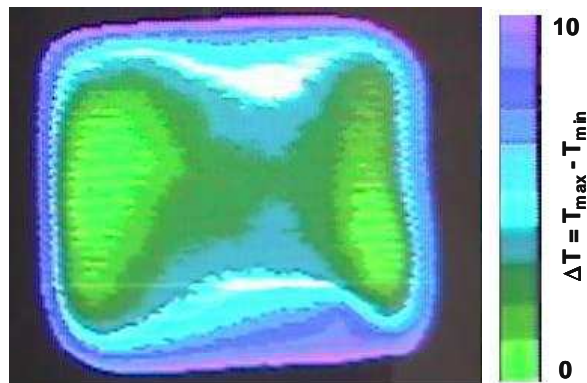


Fig. 4.9 Qualitative IR images of surface temperature of 25 PPCM porous media with a simulated heat feed back of 1% (No kerosene fuel was supplied; Air inlet temperature = 400 K; Volume flow rate = 195 l/min)



Fig. 4.10 Qualitative IR images of surface temperature of 31 PPCM porous media with a simulated heat feed back of 1 % (No kerosene fuel was supplied; Air inlet temperature = 400 K; Volume flow rate = 195 l/min)

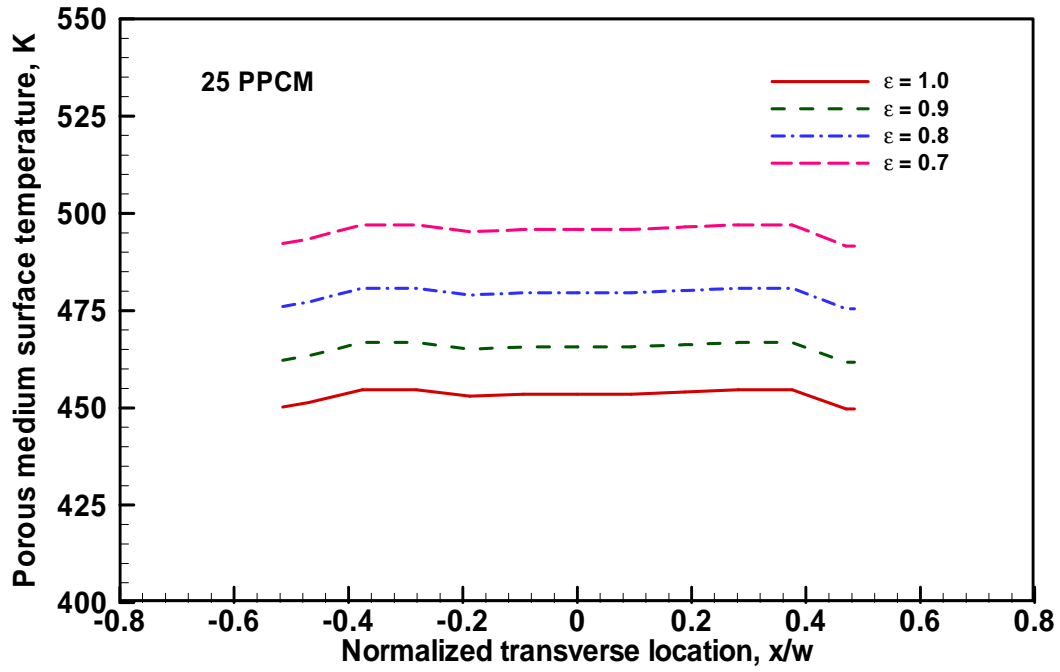


Fig. 4.11 Surface temperature distribution of 25 PPCM porous medium with assumed emissivities (w = half-width of the test section, 2.5 cm; Heat feedback = 1 %; No kerosene fuel was supplied; Air inlet temperature = 400 K; Volume flow rate = 195 l/min)

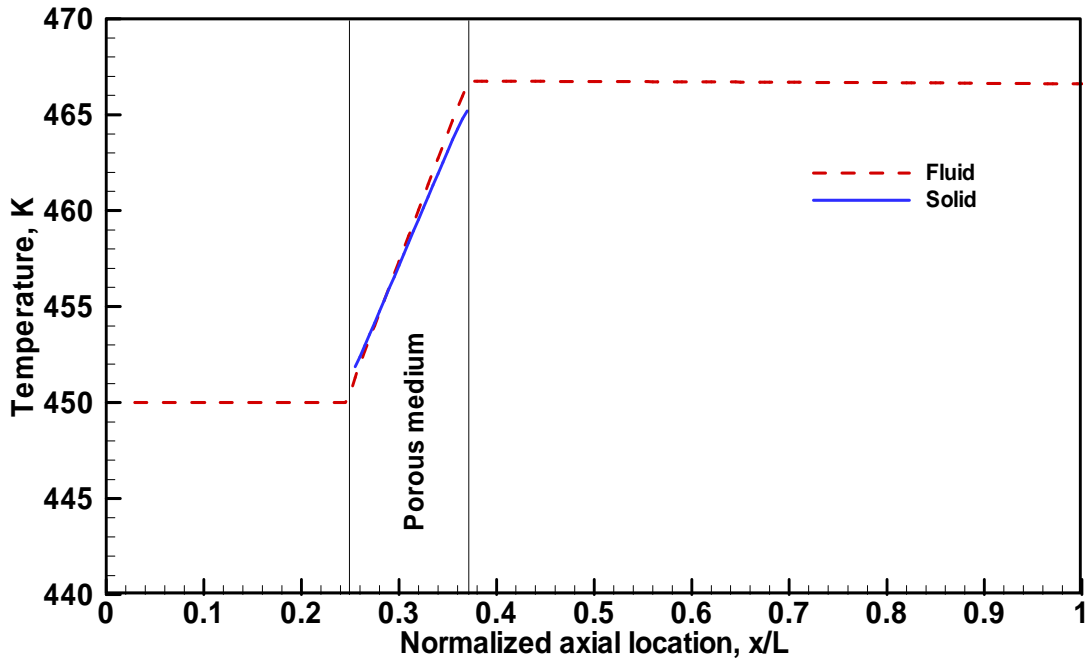


Fig. 4.12 Axial variation of porous medium and gas-phase temperature in the computational domain (Heat feedback rate = 1%; no fuel spray)

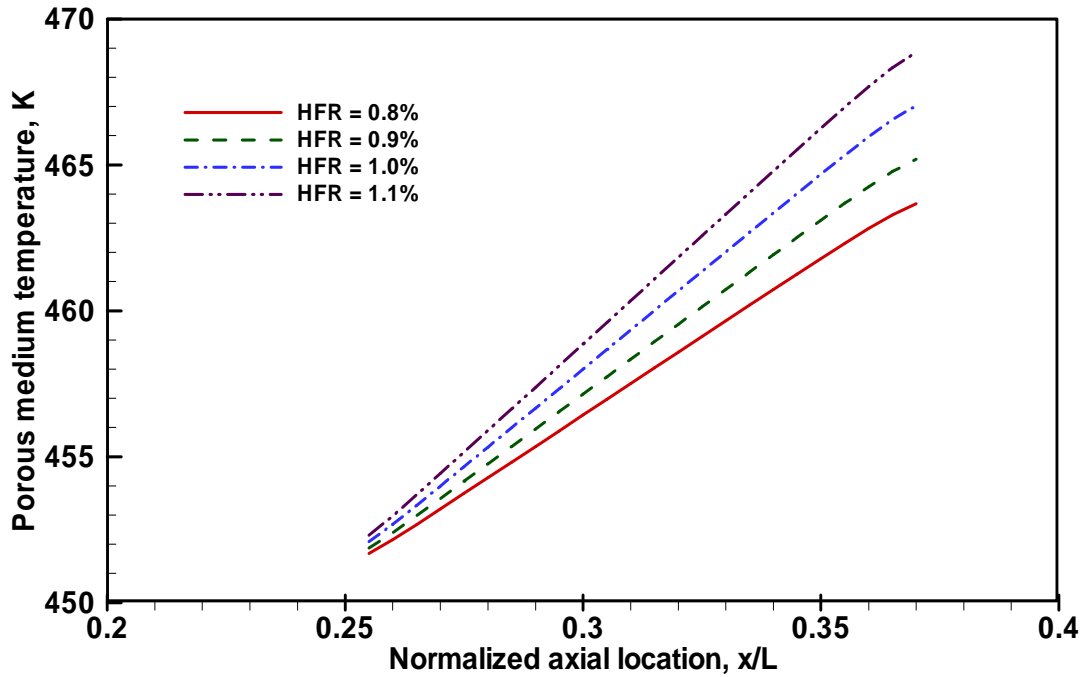


Fig. 4.13 Effect of heat feedback rate on the axial variation of porous medium centerline temperature ($T_i = 450$ K; No fuel spray was considered; Air flowrate = 190 l/min)

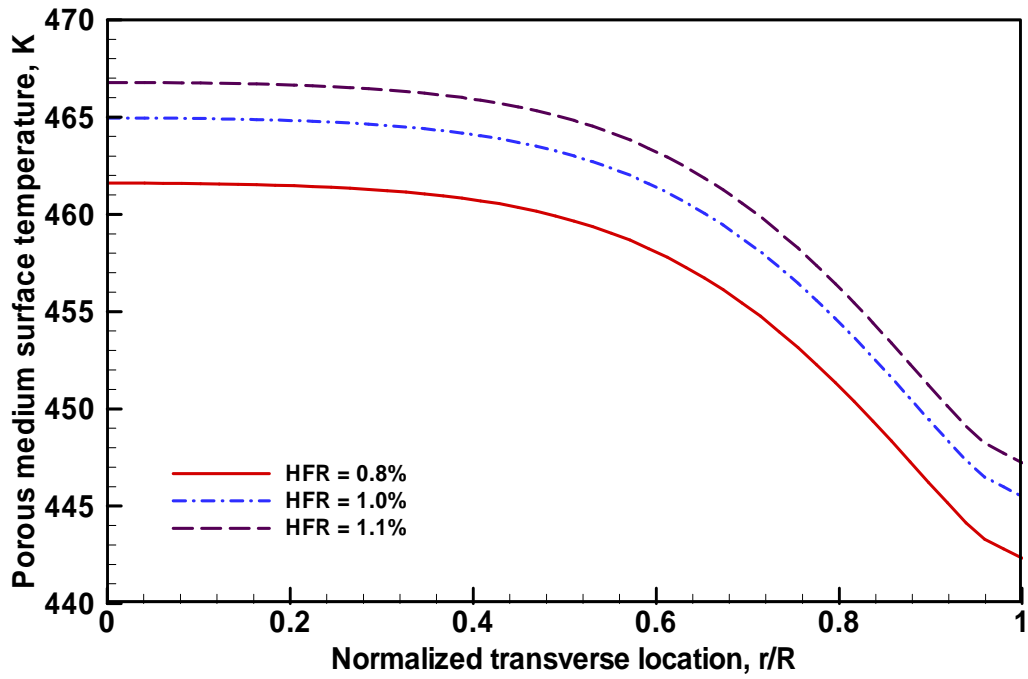


Fig. 4.14 Predicted porous medium surface temperature for different heat feedback rates (R = radius of the computational domain, 2.15 cm)

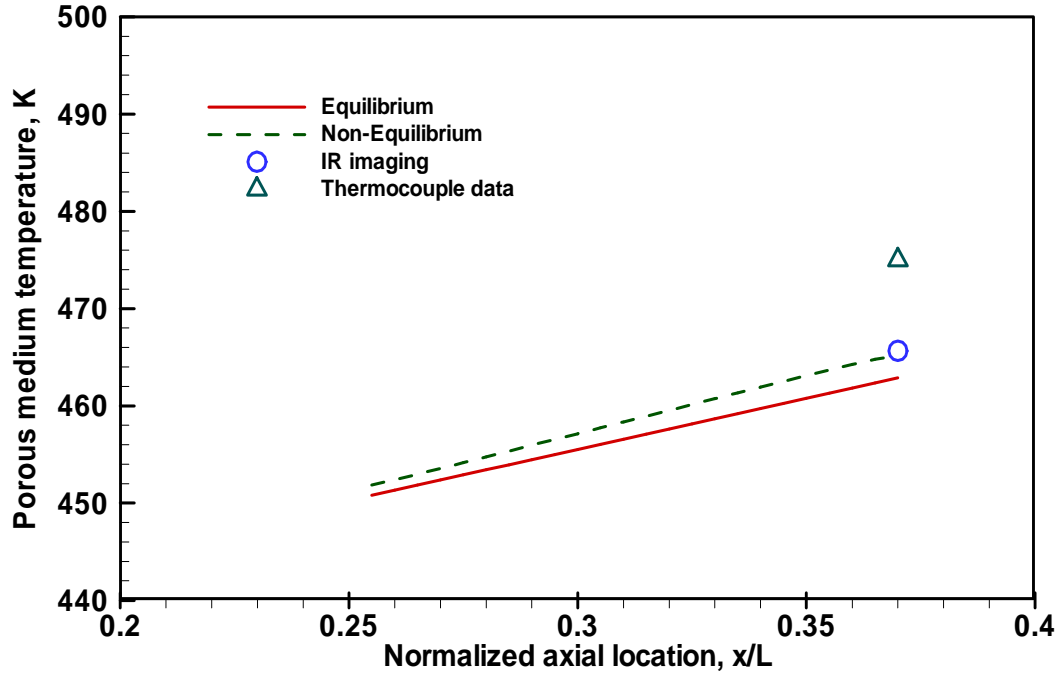


Fig. 4.15 Comparison of porous medium axial temperature predicted by local thermal equilibrium and non-equilibrium models (heat feedback rate = 1%; no fuel spray)

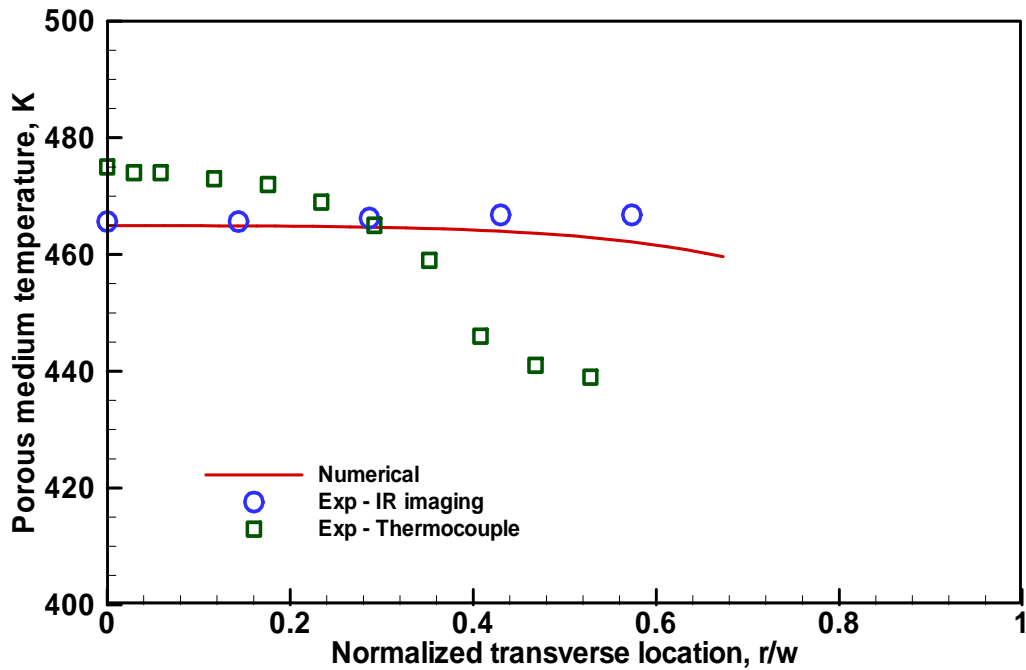
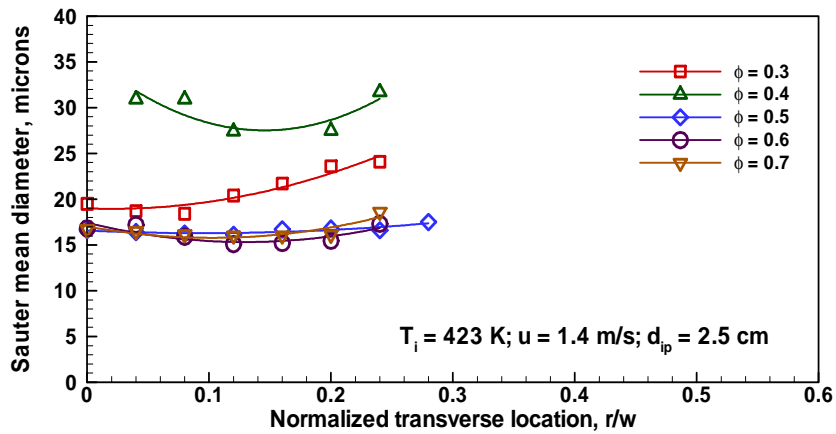
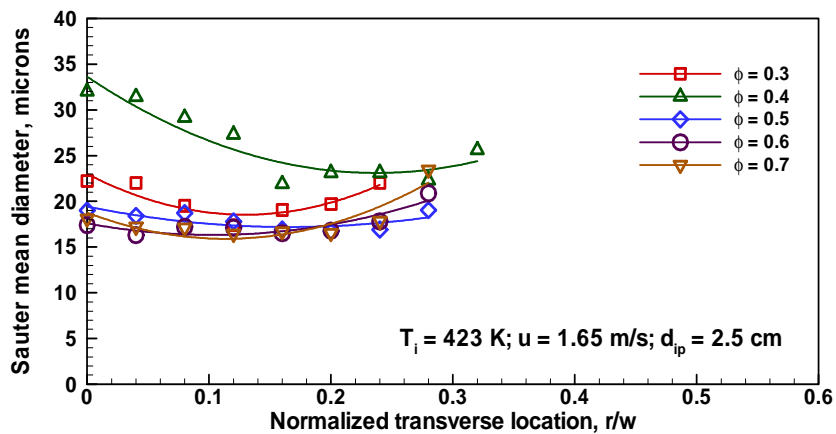


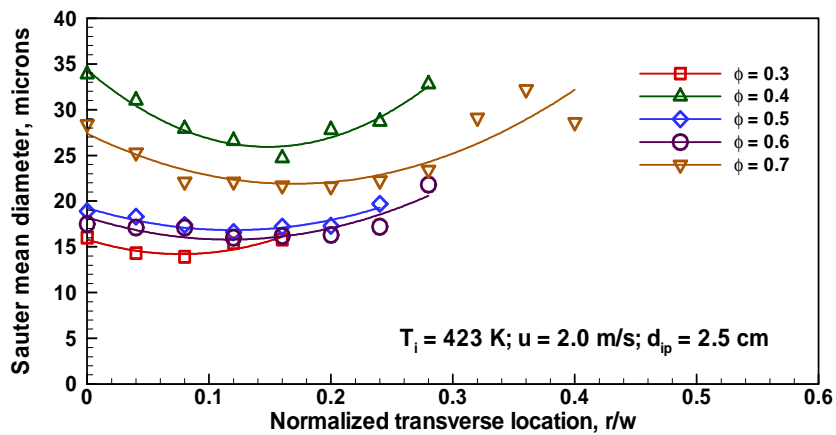
Fig. 4.16 Comparison of measured and predicted porous medium temperature at the exit surface for 1% combustion heat feedback rate



(a) Coflow air velocity = 1.4 m/s

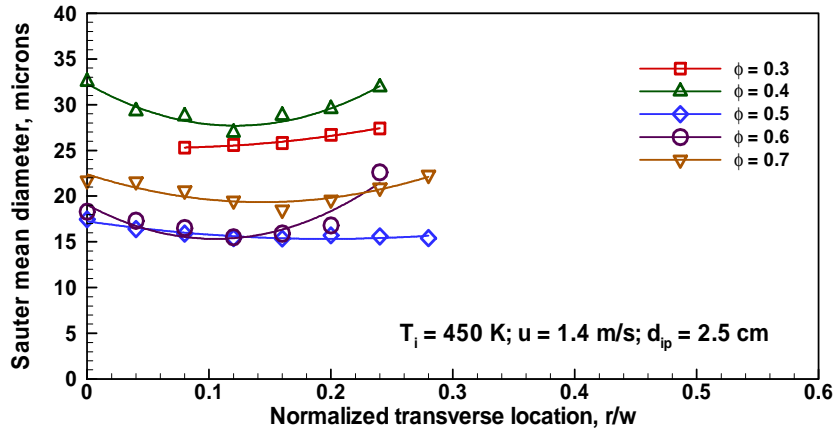


(b) Coflow air velocity = 1.65 m/s

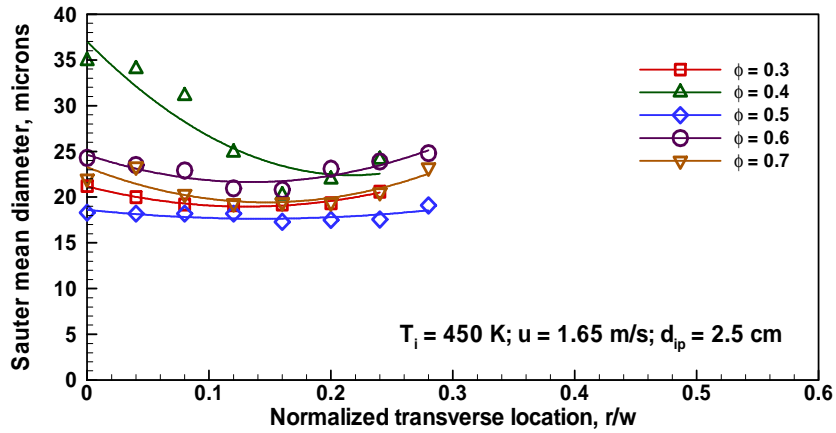


(c) Coflow air velocity = 2.0 m/s

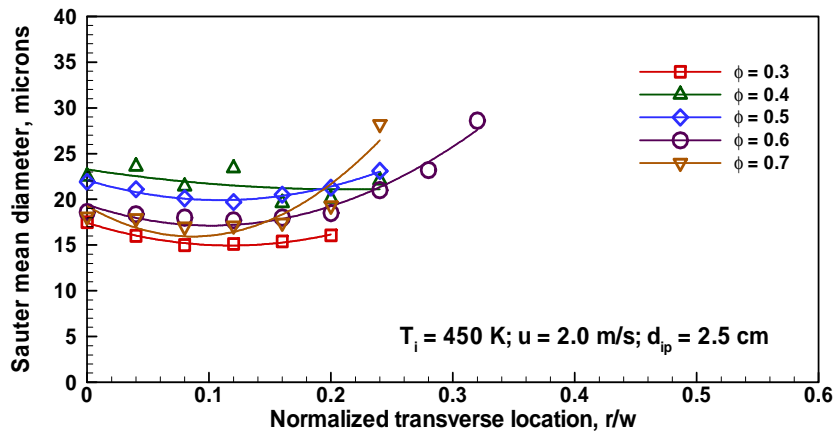
Fig. 4.17 Transverse Sauter mean diameter profiles of kerosene spray at 2.5 cm upstream of porous media (Coflow temperature – 423 K)



(a) Coflow air velocity = 1.4 m/s

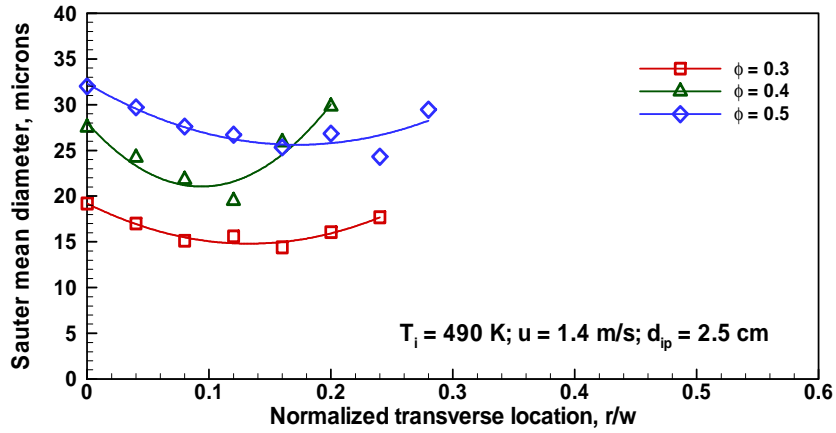


(b) Coflow air velocity = 1.65 m/s

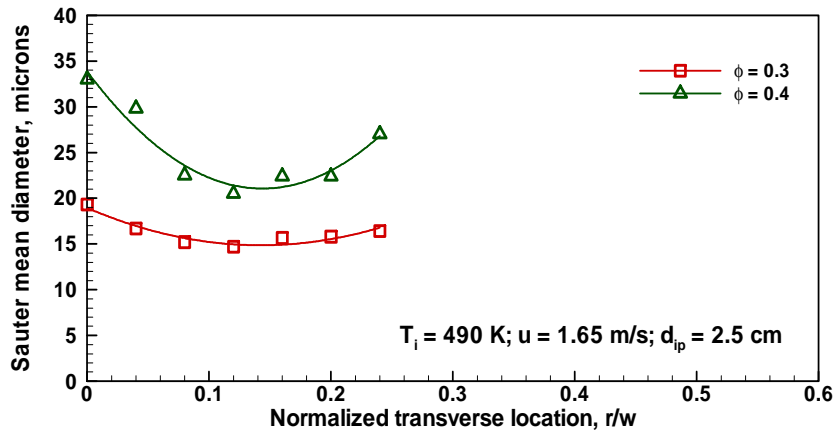


(c) Coflow air velocity = 2.0 m/s

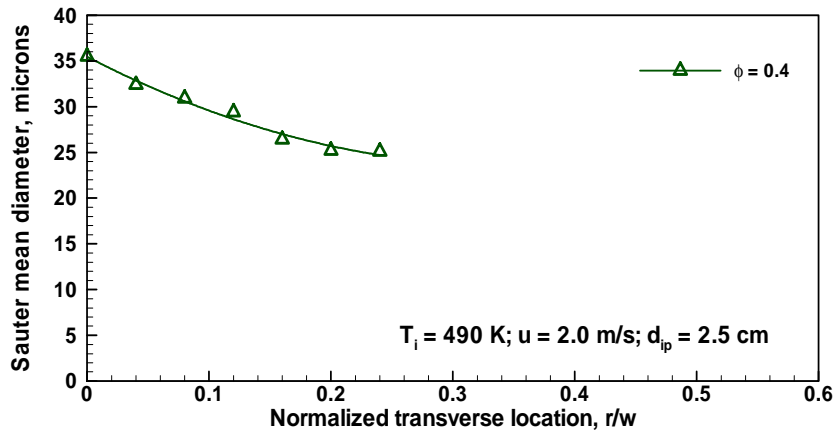
Fig. 4.18 Transverse Sauter mean diameter profiles of kerosene spray at 2.5 cm upstream of porous media (Coflow temperature – 450 K)



(a) Coflow air velocity = 1.4 m/s

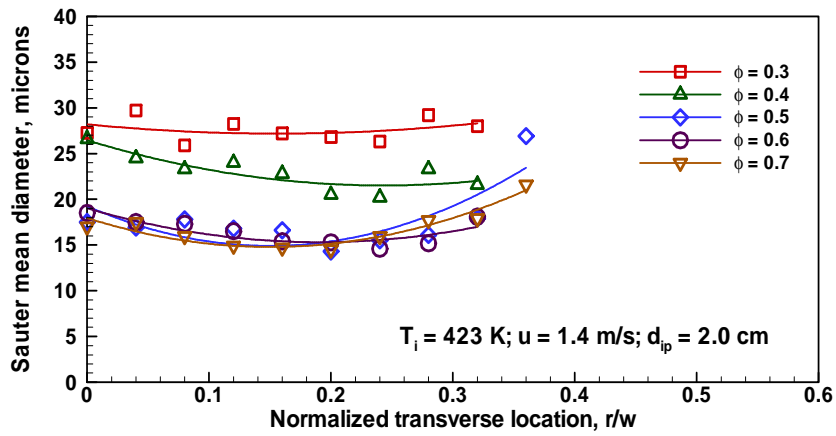


(b) Coflow air velocity = 1.65 m/s

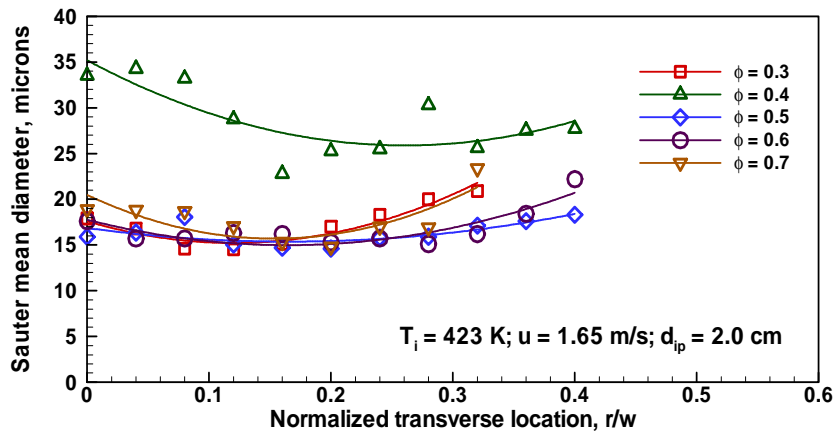


(c) Coflow air velocity = 2.0 m/s

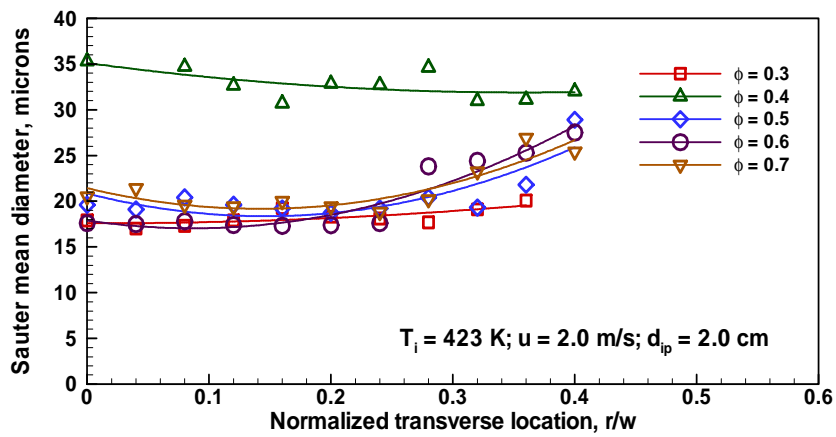
Fig. 4.19 Transverse Sauter mean diameter profiles of kerosene spray at 2.5 cm upstream of porous media (Coflow temperature – 490 K)



(a) Coflow air velocity = 1.4 m/s

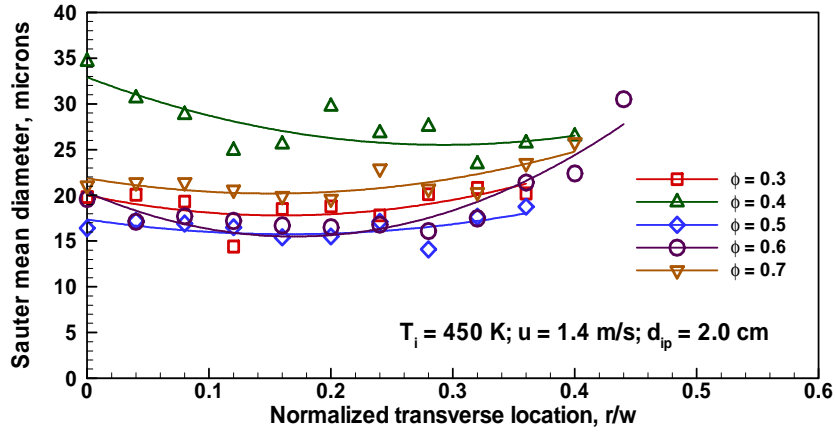


(b) Coflow air velocity = 1.65 m/s

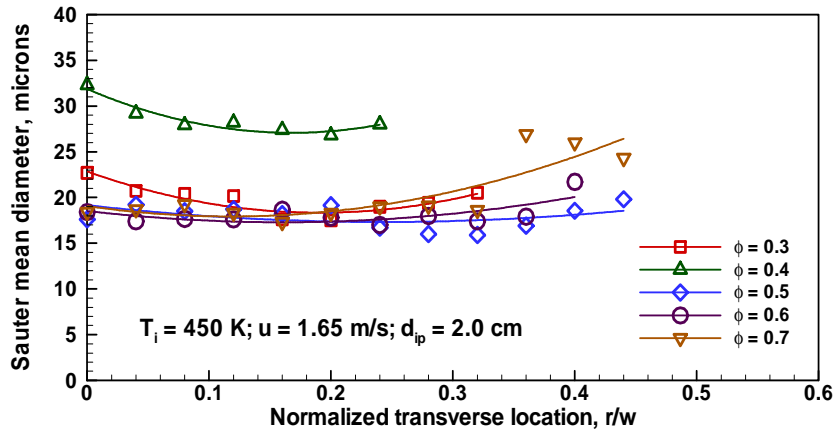


(c) Coflow air velocity = 2.0 m/s

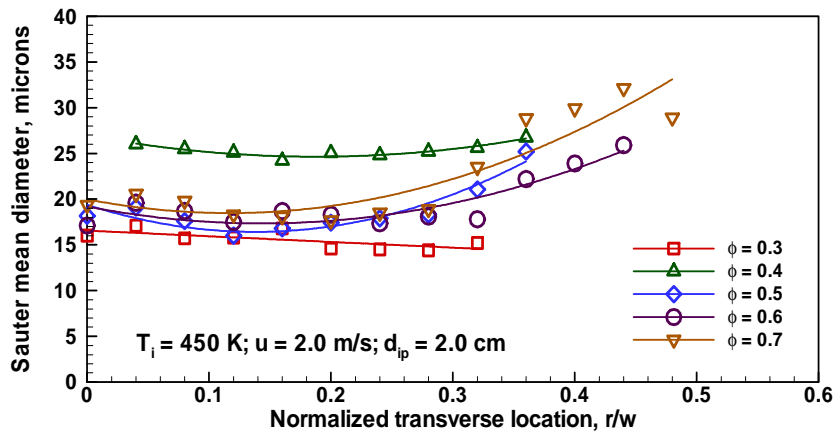
Fig. 4.20 Transverse Sauter mean diameter profiles of kerosene spray at 2.0 cm upstream of porous media (Coflow temperature – 423 K)



(a) Coflow air velocity = 1.4 m/s

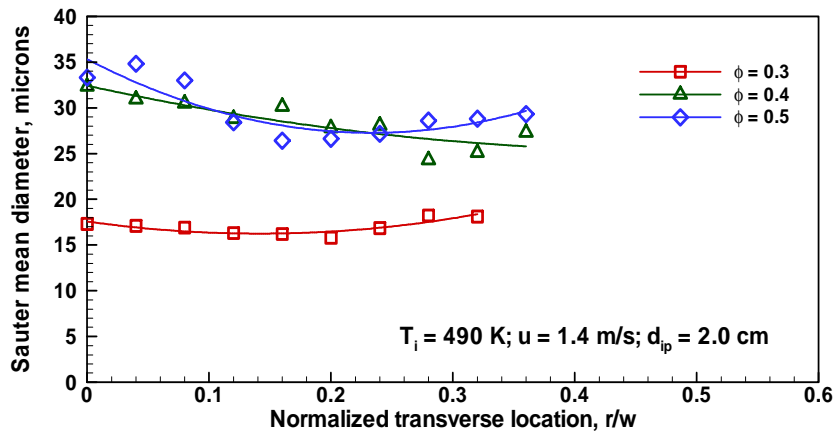


(a) Coflow air velocity = 1.65 m/s

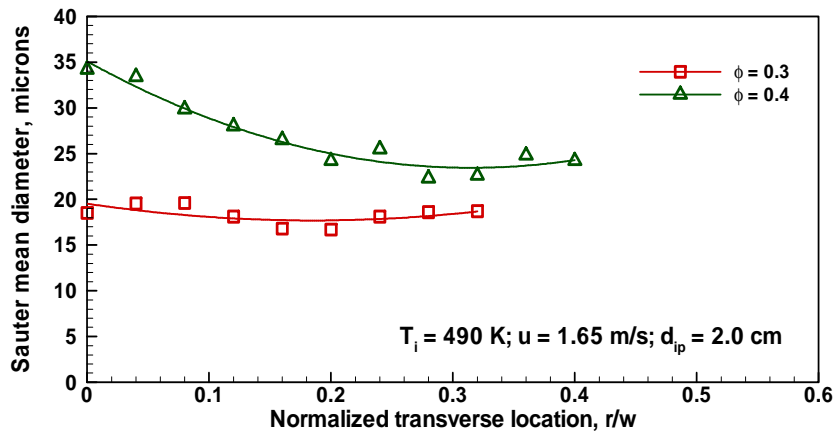


(c) Coflow air velocity = 2.0 m/s

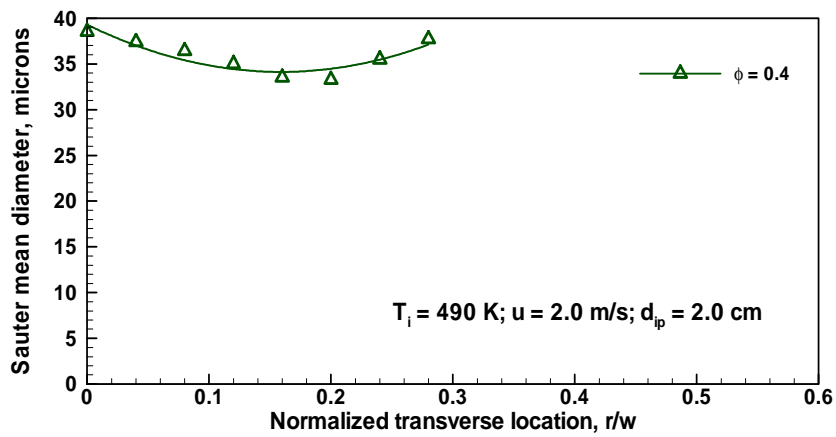
Fig. 4.21 Transverse Sauter mean diameter profiles of kerosene spray at 2.0 cm upstream of porous media (Coflow temperature – 450 K)



(a) Coflow air velocity = 1.4 m/s

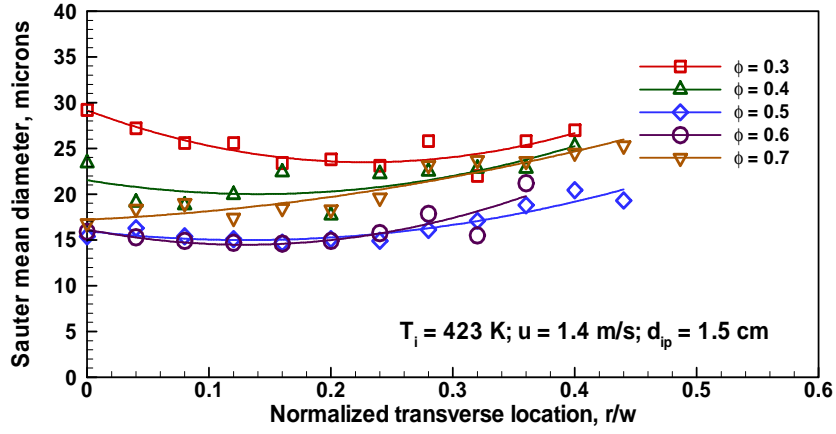


(b) Coflow air velocity = 1.65 m/s

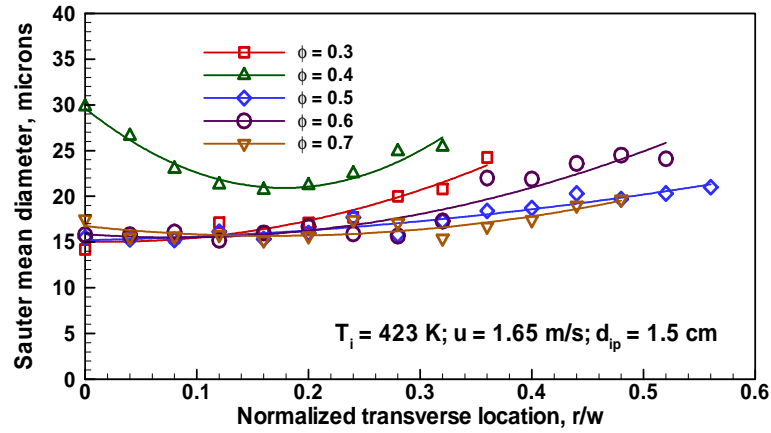


(c) Coflow air velocity = 2.0 m/s

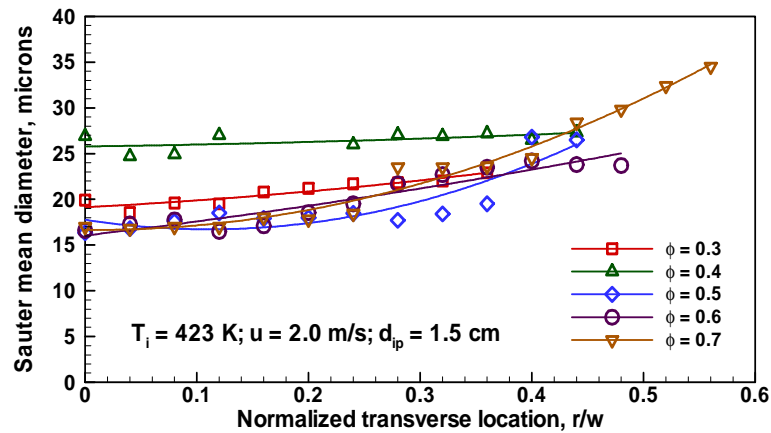
Fig. 4.22 Transverse Sauter mean diameter profiles of kerosene spray at 2.0 cm upstream of porous media (Coflow temperature – 490 K)



(a) Coflow air velocity = 1.4 m/s

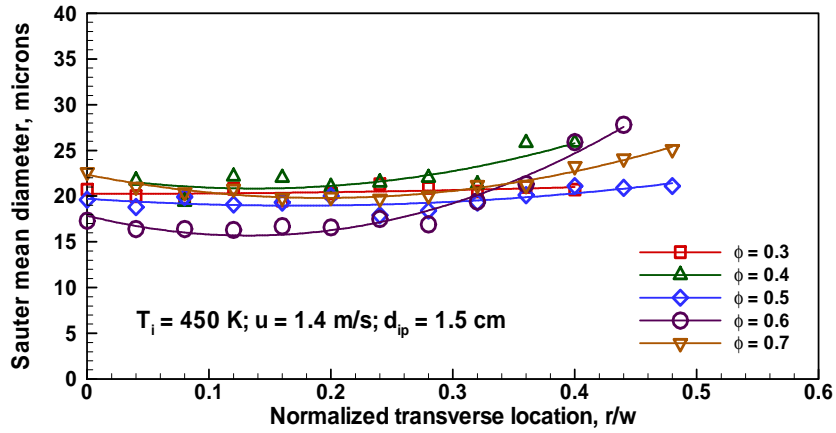


(b) Coflow air velocity = 1.65 m/s

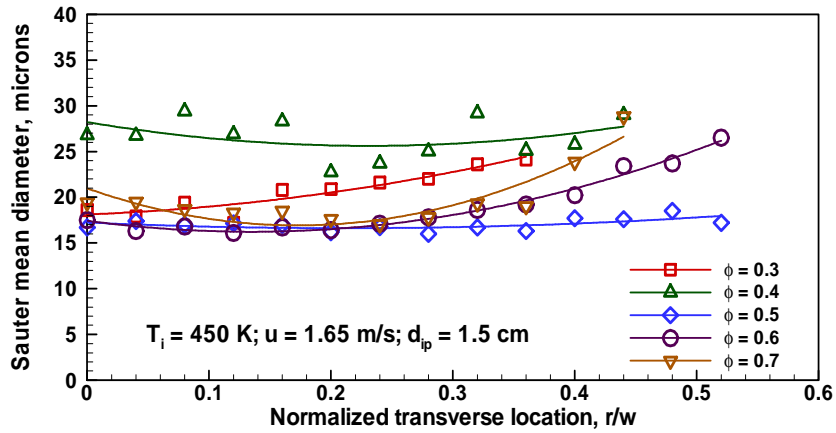


(c) Coflow air velocity = 2.0 m/s

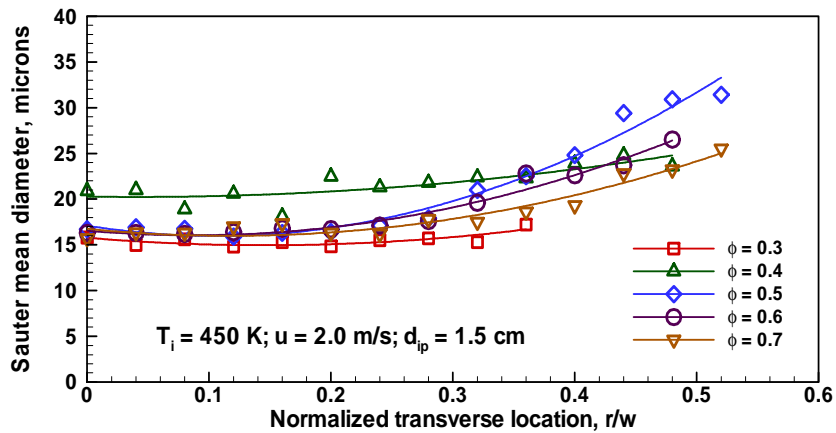
Fig. 4.23 Transverse Sauter mean diameter profiles of kerosene spray at 1.5 cm upstream of porous media (Coflow temperature – 423 K)



(a) Coflow air velocity = 1.4 m/s

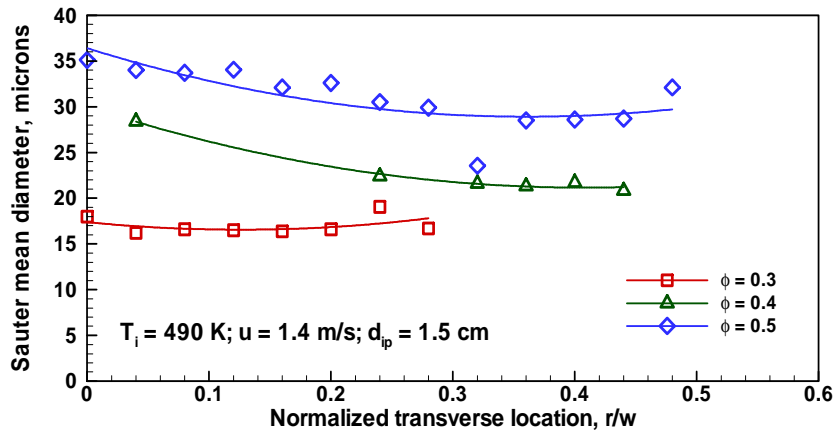


(a) Coflow air velocity = 1.65 m/s

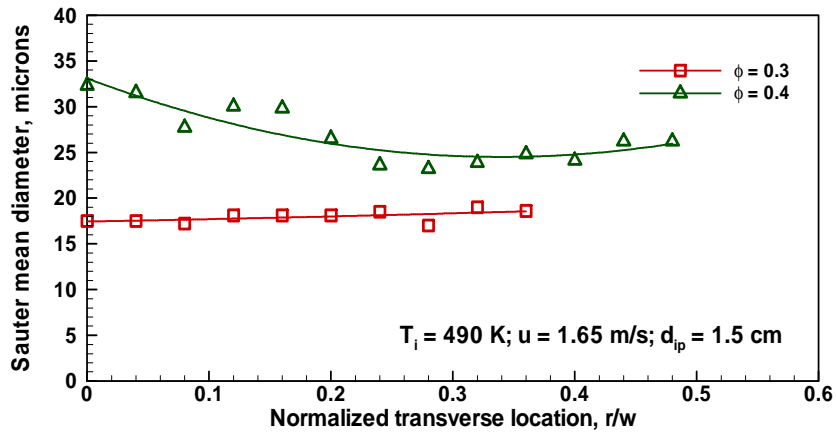


(c) Coflow air velocity = 2.0 m/s

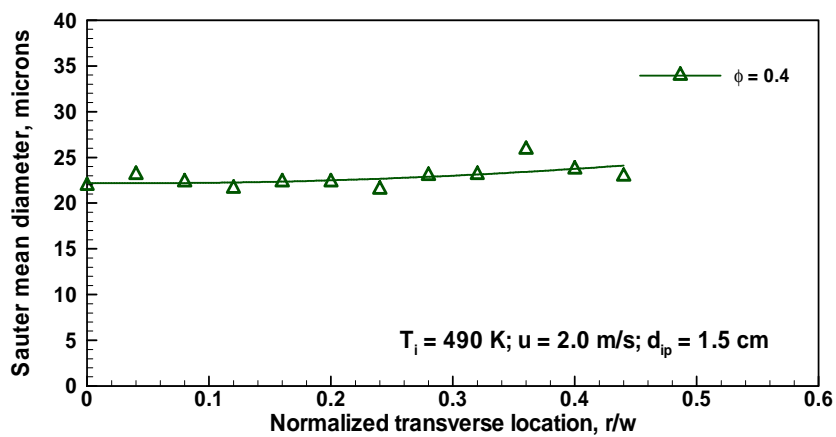
Fig. 4.24 Transverse Sauter mean diameter profiles of kerosene spray at 1.5 cm upstream of porous media (Coflow temperature – 450 K)



(a) Coflow air velocity = 1.4 m/s



(b) Coflow air velocity = 1.65 m/s



(c) Coflow air velocity = 2.0 m/s

Fig. 4.25 Transverse Sauter mean diameter profiles of kerosene spray at 1.5 cm upstream of porous media (Coflow temperature – 490 K)

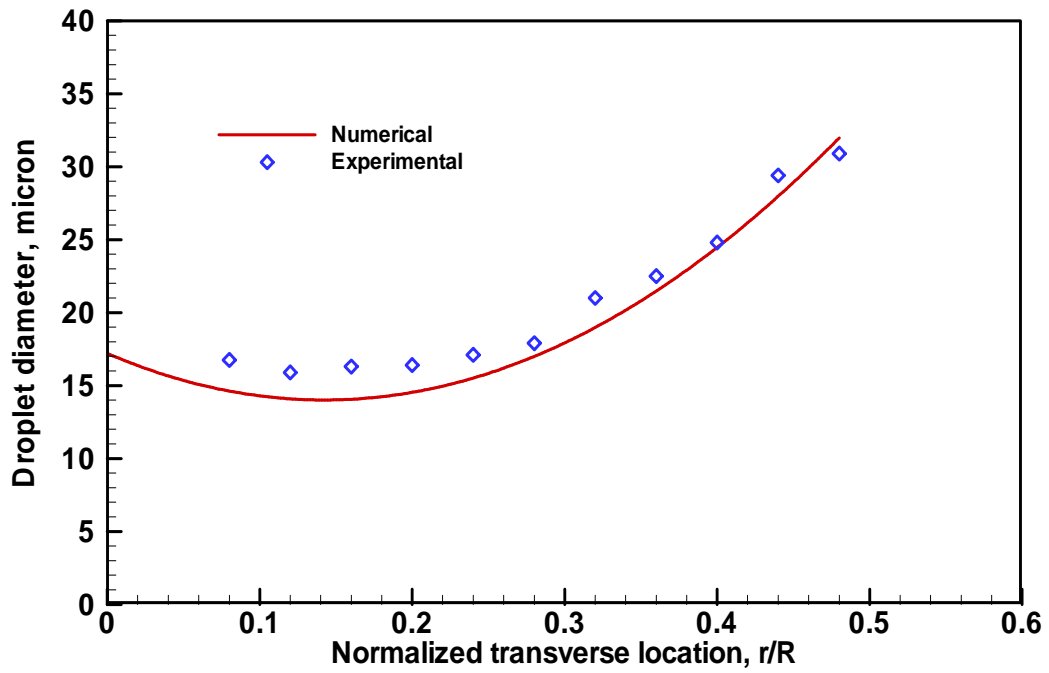
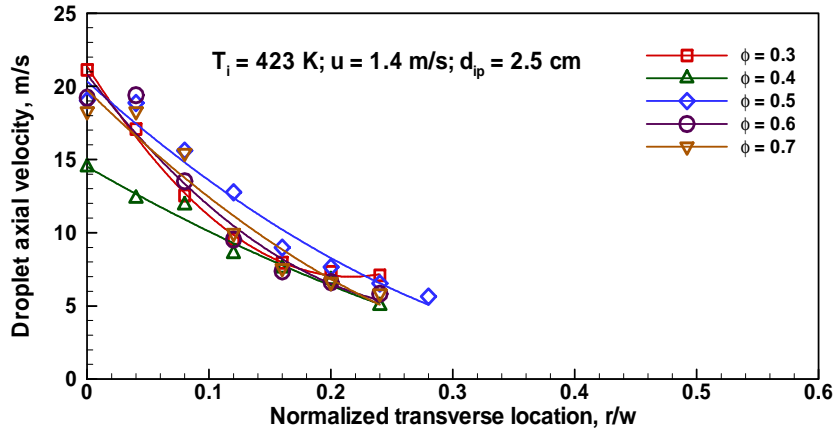
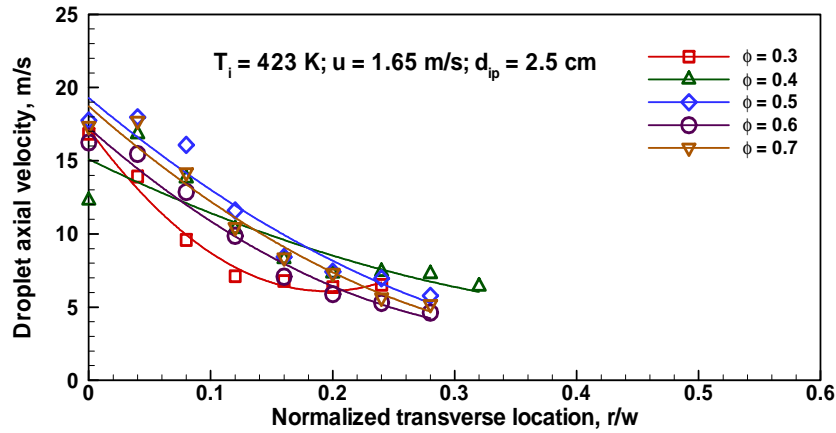


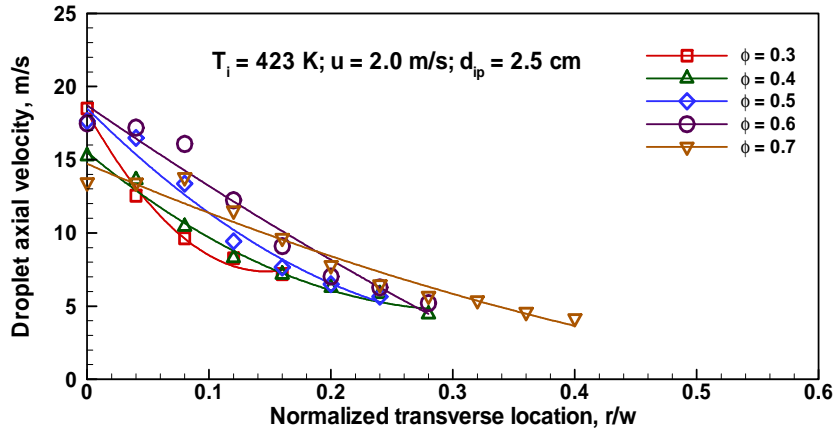
Fig. 4.26 Comparison of measured and predicted droplet diameter at 1.5 cm upstream of the leading edge of the porous medium (R = radius of the computational domain, 2.15 cm; $\phi = 0.5$; $T_i = 450$ K)



(a) Coflow air velocity = 1.4 m/s

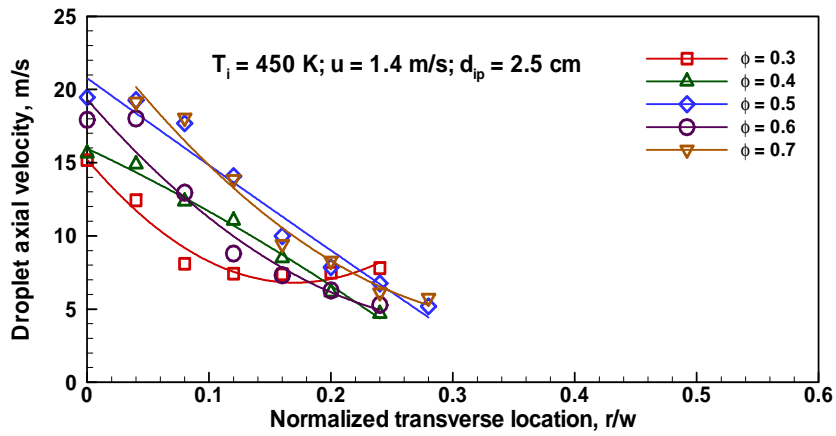


(b) Coflow air velocity = 1.65 m/s

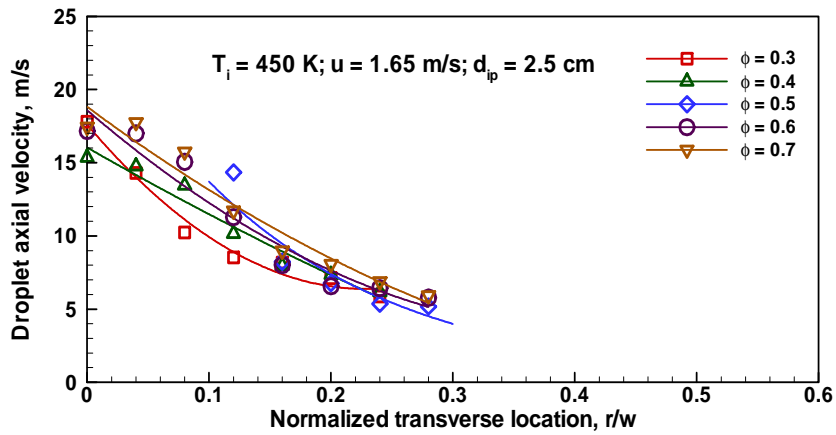


(c) Coflow air velocity = 2.0 m/s

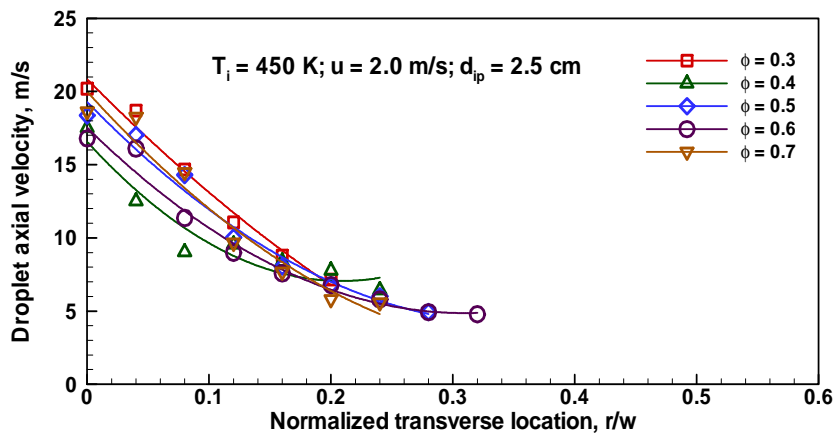
Fig. 4.27 Transverse droplet axial velocity profiles of kerosene spray at 2.5 cm upstream of porous media (Coflow temperature – 423 K)



(a) Coflow air velocity = 2.0 m/s

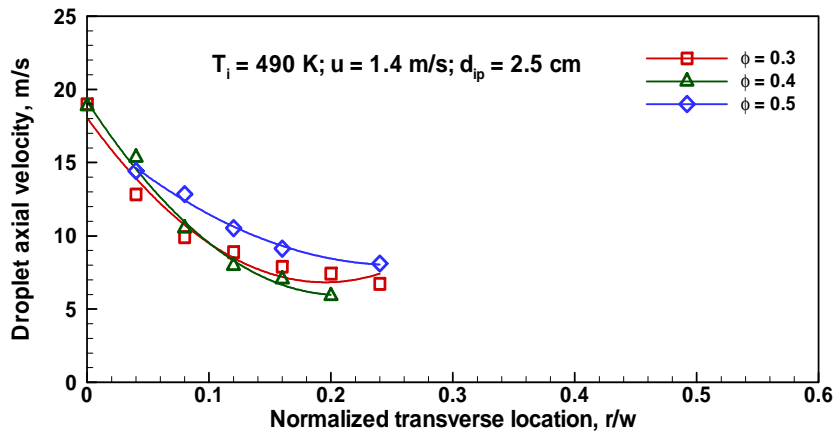


(b) Coflow air velocity = 1.65 m/s

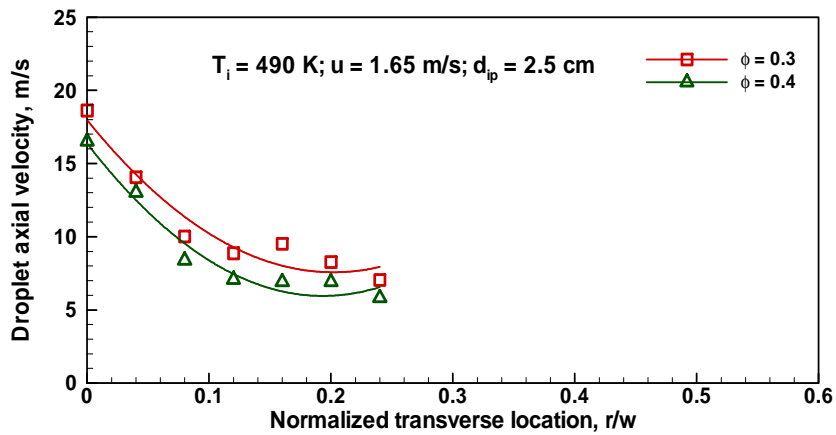


(c) Coflow air velocity = 2.0 m/s

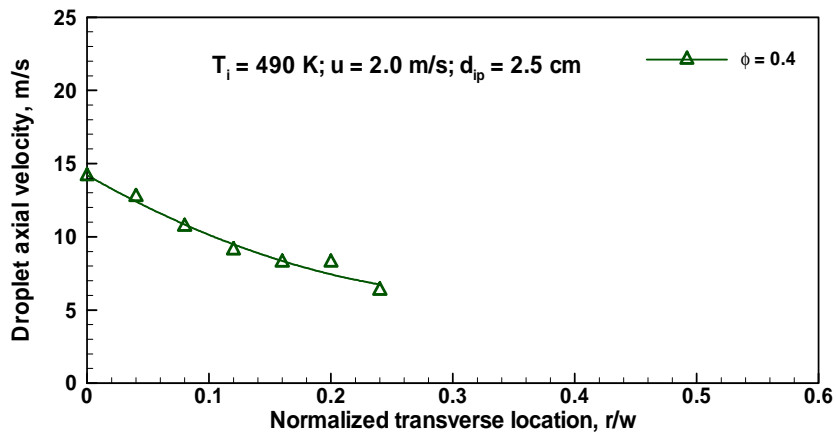
Fig. 4.28 Transverse droplet axial velocity profiles of kerosene spray at 2.5 cm upstream of porous media (Coflow temperature – 450 K)



(a) Coflow air velocity = 1.4 m/s

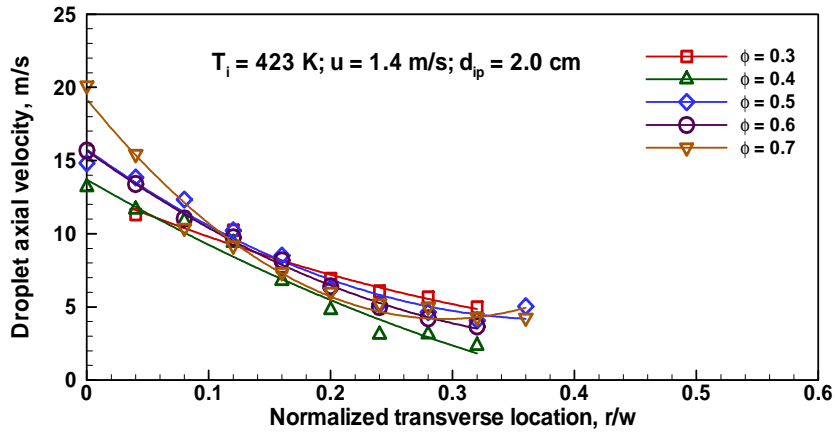


(b) Coflow air velocity = 1.65 m/s

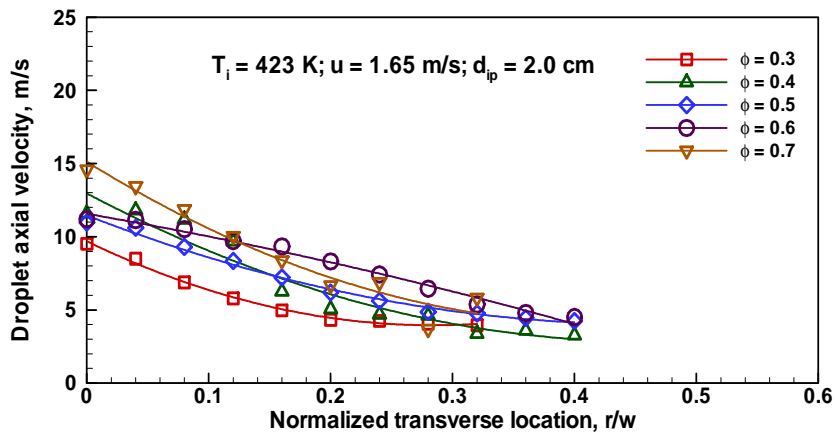


(c) Coflow air velocity = 2.0 m/s

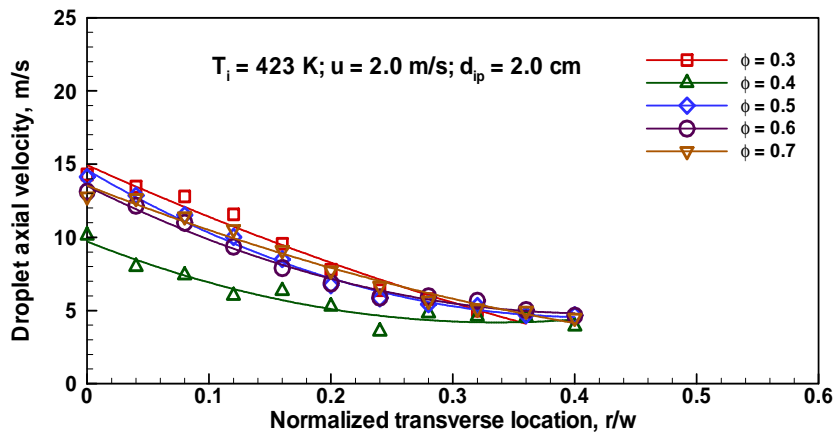
Fig. 4.29 Transverse droplet axial velocity profiles of kerosene spray at 2.5 cm upstream of porous media (Coflow temperature – 490 K)



(a) Coflow air velocity = 1.4 m/s

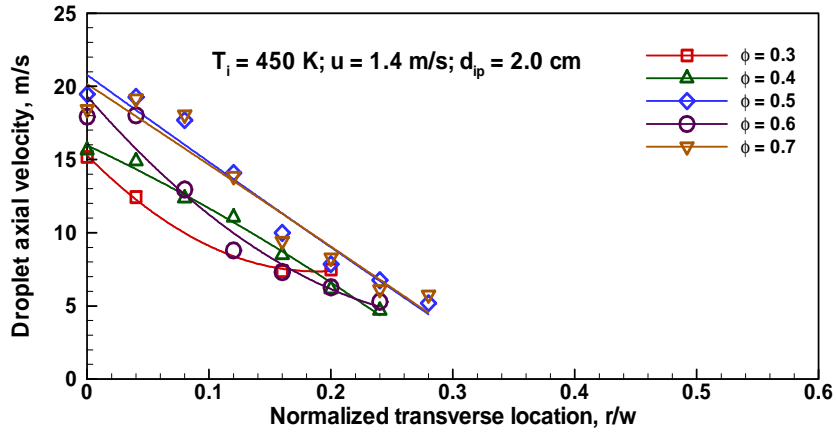


(b) Coflow air velocity = 1.65 m/s

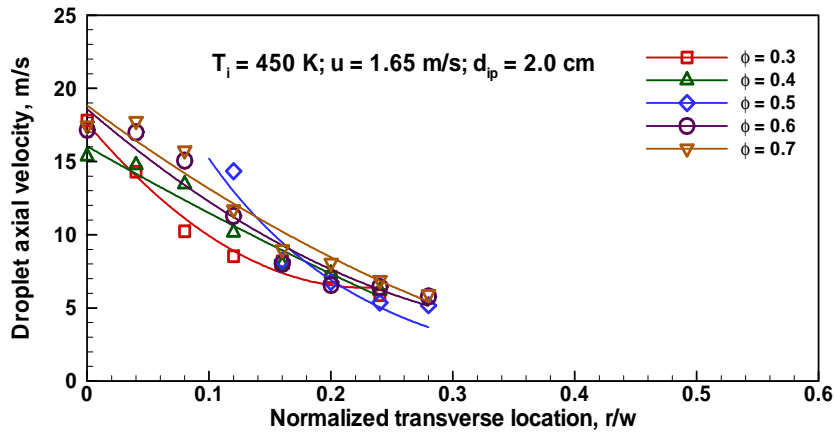


(c) Coflow air velocity = 2.0 m/s

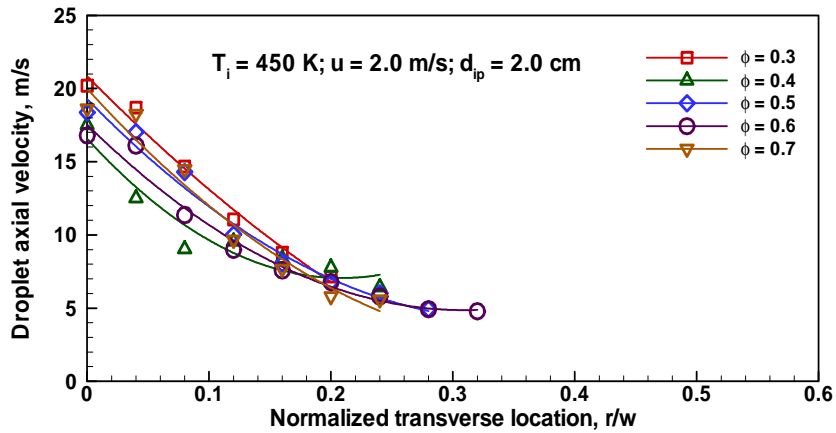
Fig. 4.30 Transverse droplet axial velocity profiles of kerosene spray at 2.0 cm upstream of porous media (Coflow temperature – 423 K)



(a) Coflow air velocity = 1.4 m/s

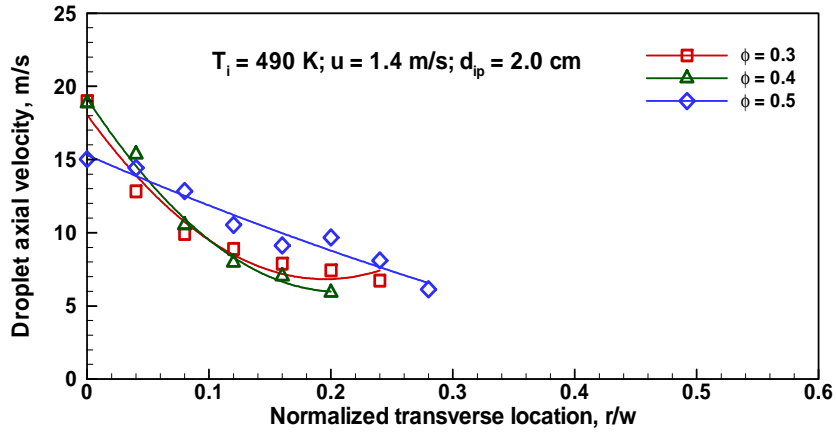


(b) Coflow air velocity = 1.65 m/s

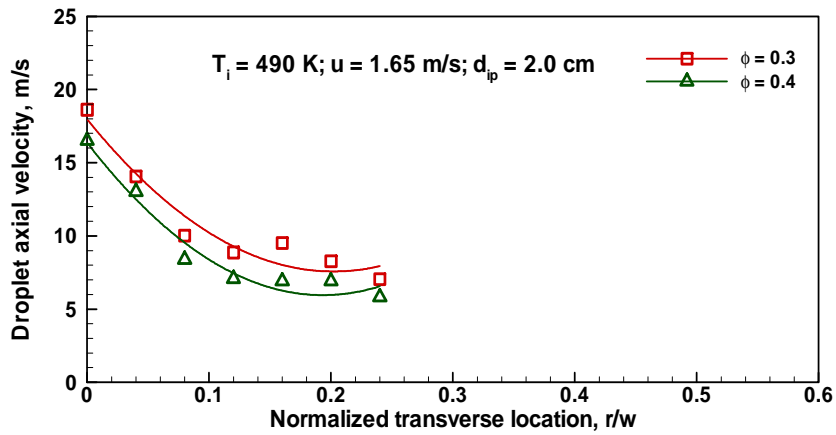


(c) Coflow air velocity = 2.0 m/s

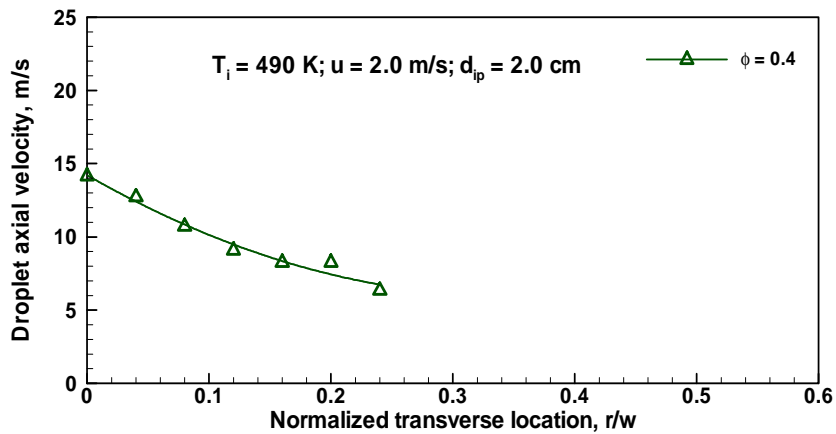
Fig. 4.31 Transverse droplet axial velocity profiles of kerosene spray at 2.0 cm upstream of porous media (Coflow temperature – 450 K)



(a) Coflow air velocity = 1.4 m/s

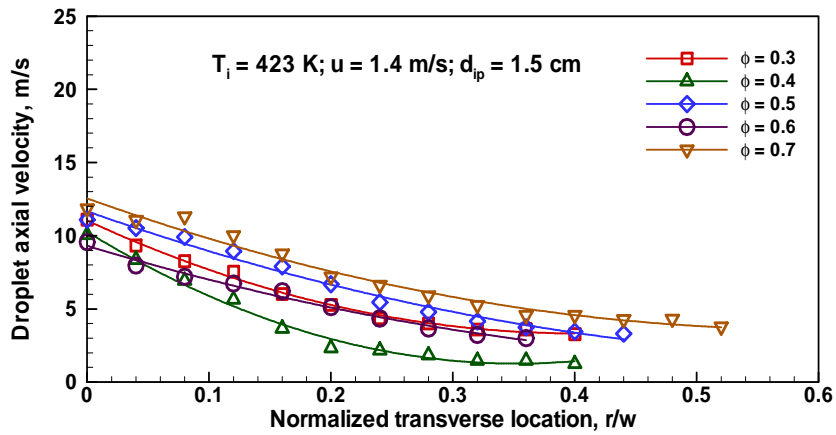


(c) Coflow air velocity = 1.65 m/s

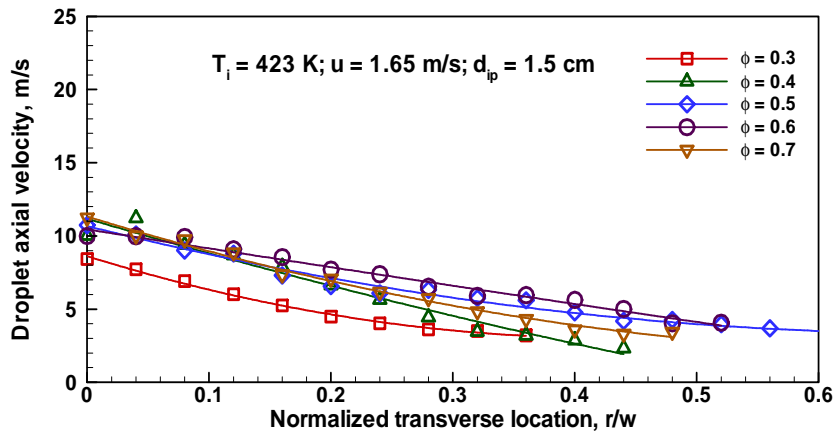


(c) Coflow air velocity = 2.0 m/s

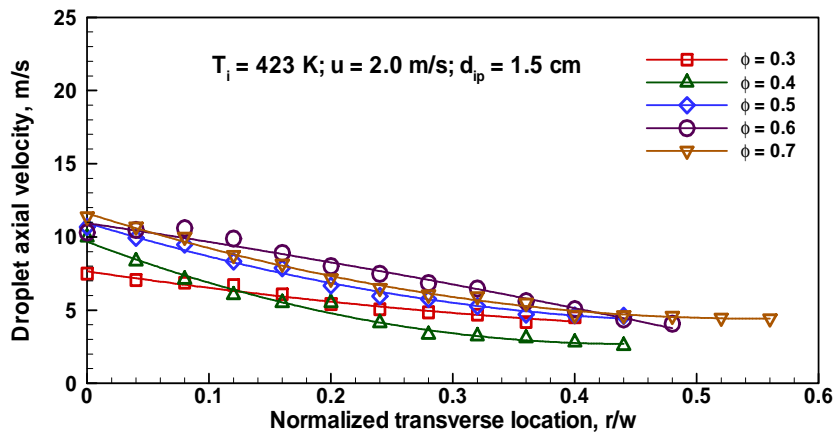
Fig. 4.32 Transverse droplet axial velocity profiles of kerosene spray at 1.5 cm upstream of porous media (Coflow temperature – 490 K)



(a) Coflow air velocity = 1.4 m/s

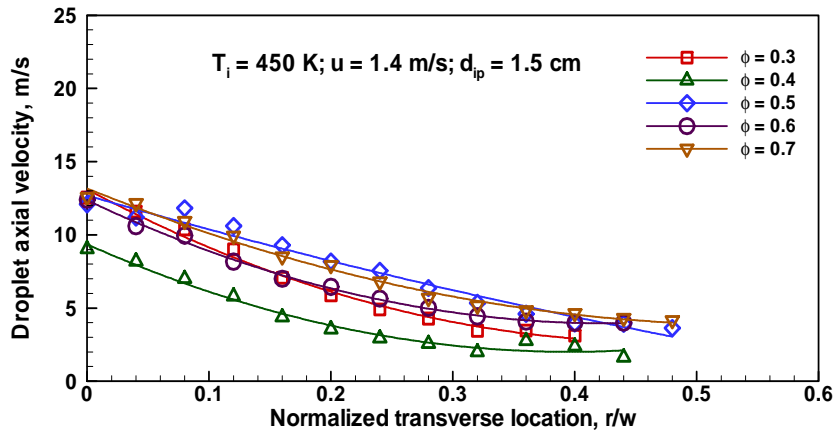


(b) Coflow air velocity = 1.65 m/s

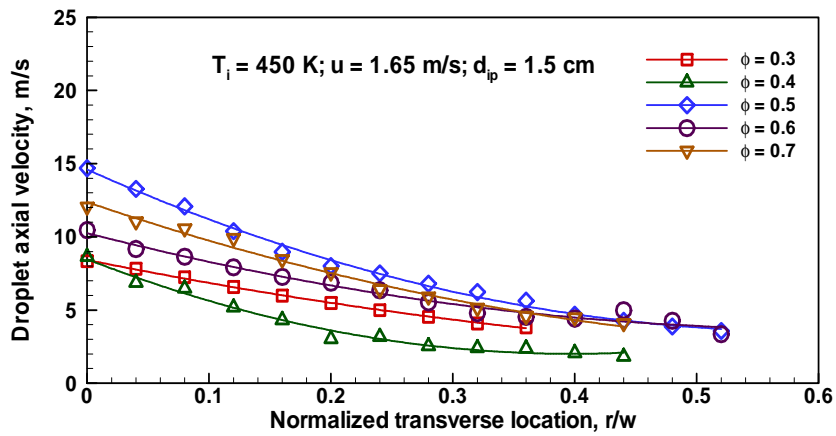


(c) Coflow air velocity = 2.0 m/s

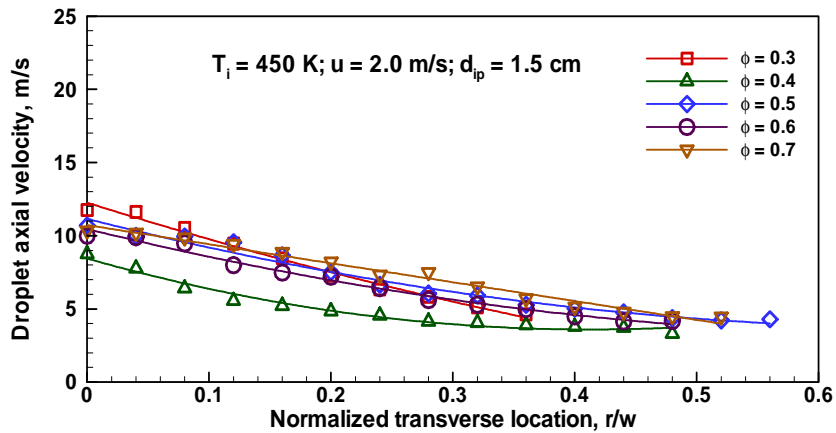
Fig. 4.33 Transverse droplet axial velocity profiles of kerosene spray at 1.5 cm upstream of porous media (Coflow temperature – 423 K)



(a) Coflow air velocity = 1.4 m/s

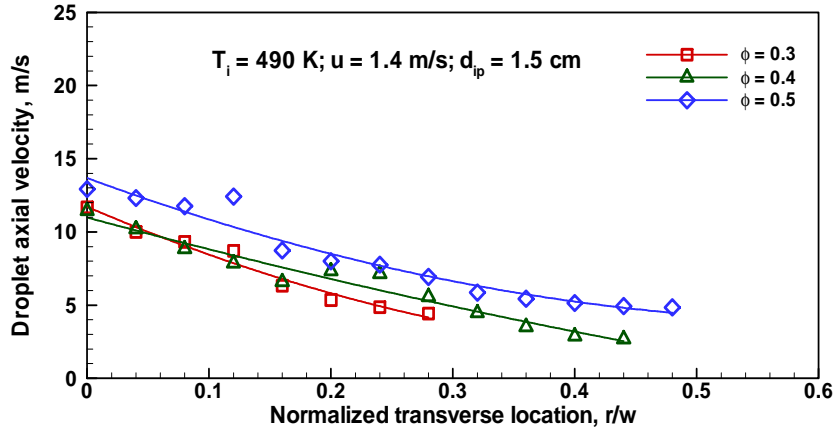


(b) Coflow air velocity = 1.65 m/s

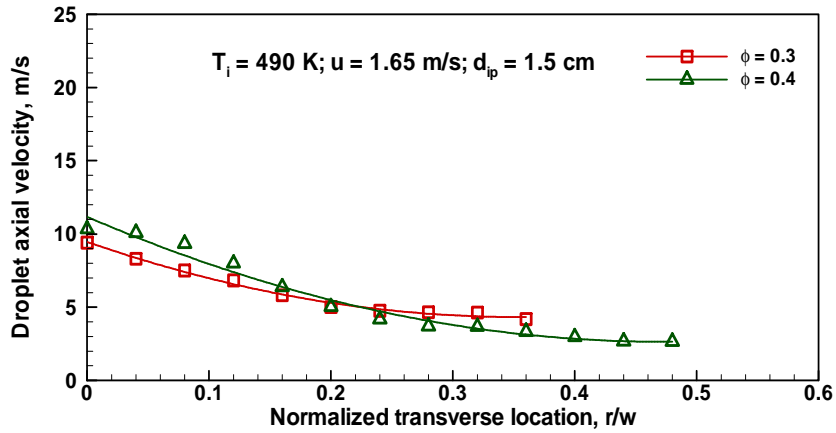


(c) Coflow air velocity = 2.0 m/s

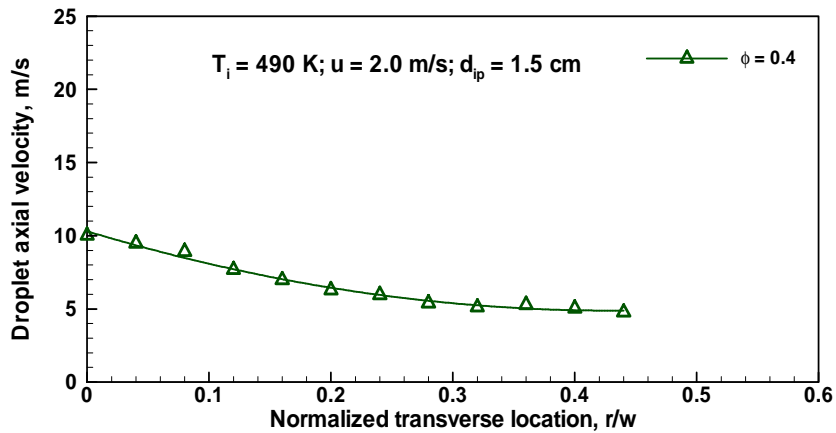
Fig. 4.34 Transverse droplet axial velocity profiles of kerosene spray at 1.5 cm upstream of porous media (Coflow temperature – 450 K)



(a) Coflow air velocity = 1.4 m/s

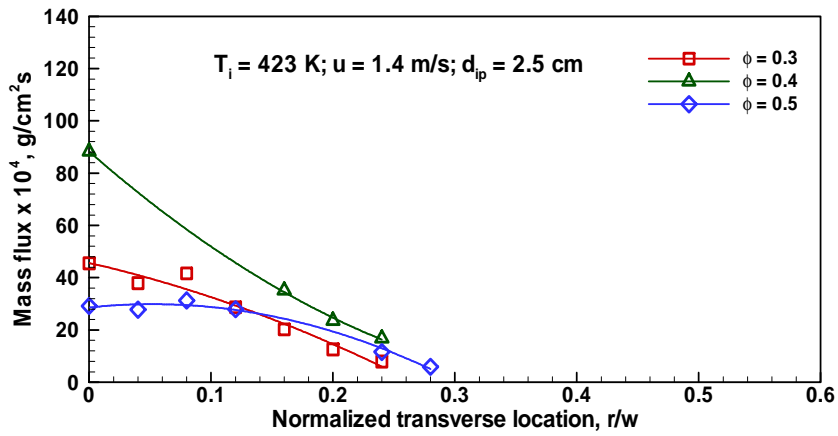


(b) Coflow air velocity = 1.65 m/s

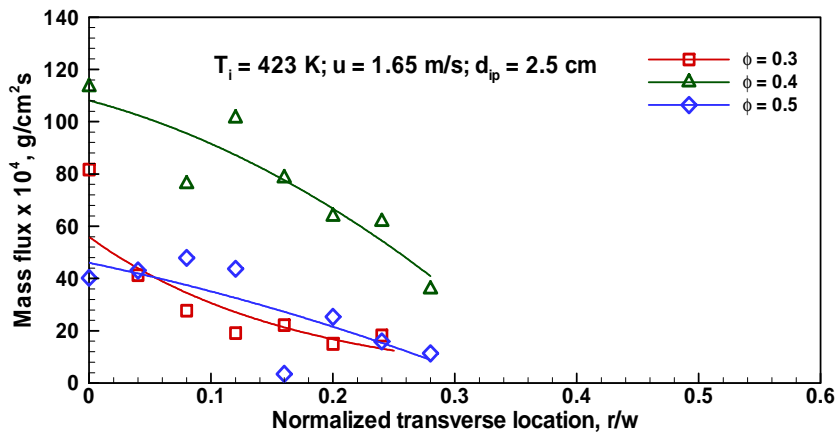


(c) Coflow air velocity = 2.0 m/s

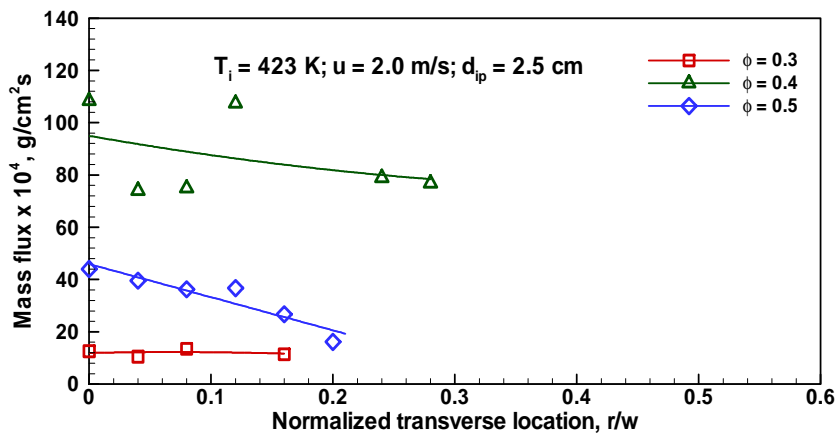
Fig. 4.35 Transverse droplet axial velocity profiles of kerosene spray at 1.5 cm upstream of porous media (Coflow temperature – 490 K)



(a) Coflow air velocity = 1.4 m/s

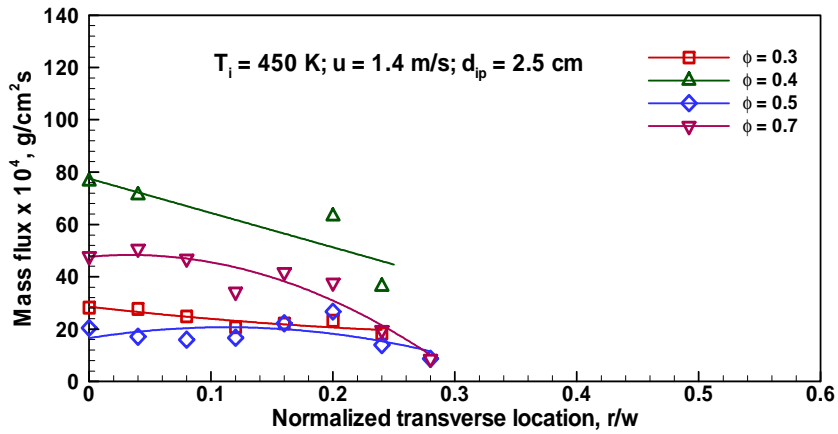


(b) Coflow air velocity = 1.65 m/s

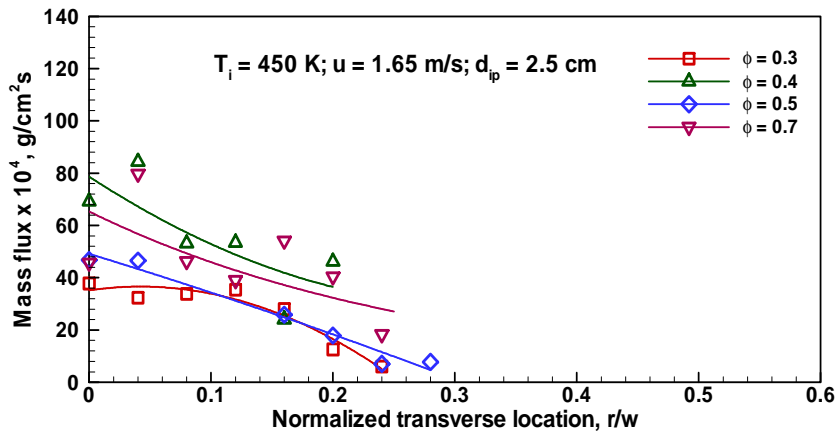


(c) Coflow air velocity = 2.0 m/s

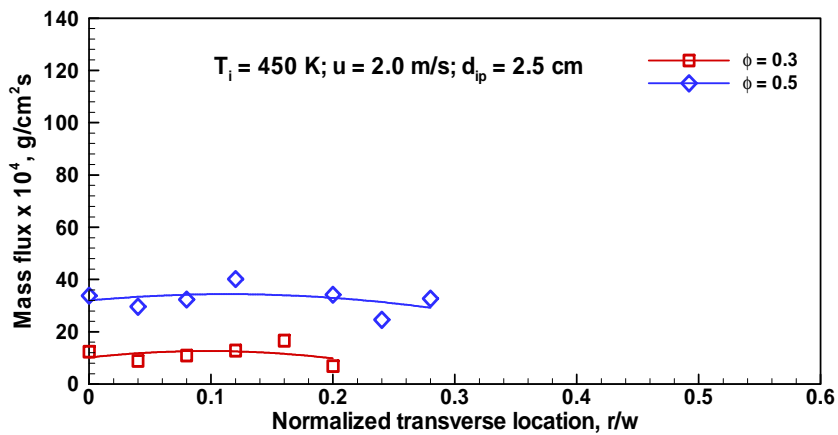
Fig. 4.36 Transverse liquid mass flux profiles of kerosene spray at 2.5 cm upstream of porous media (Coflow temperature – 423 K)



(a) Coflow air velocity = 1.4 m/s

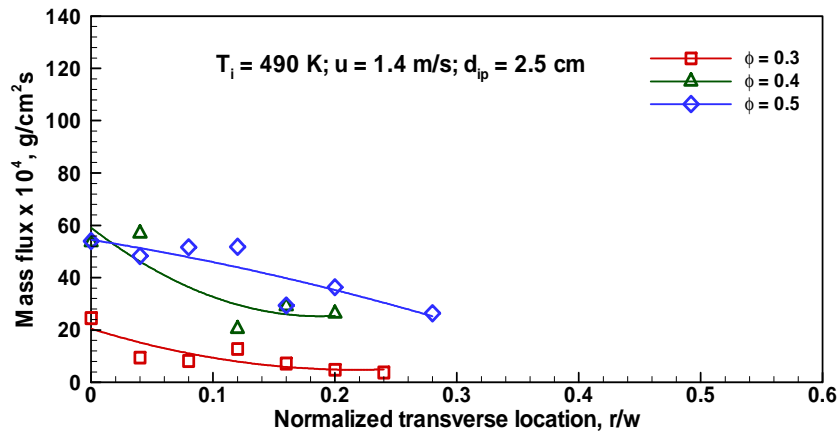


(b) Coflow air velocity = 1.65 m/s

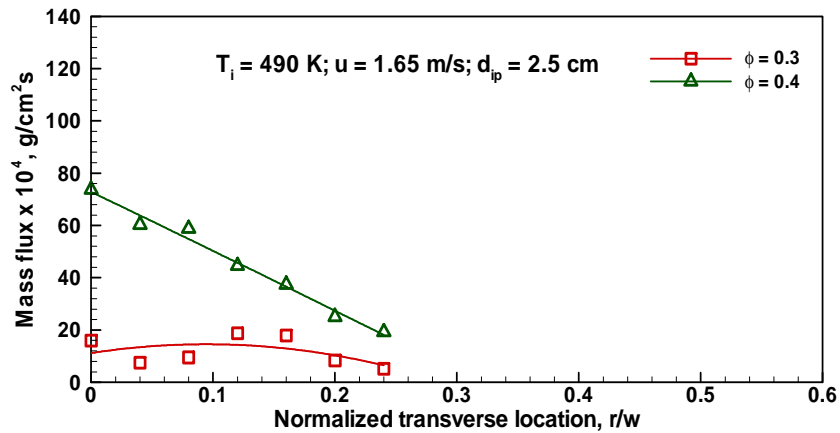


(c) Coflow air velocity = 2.0 m/s

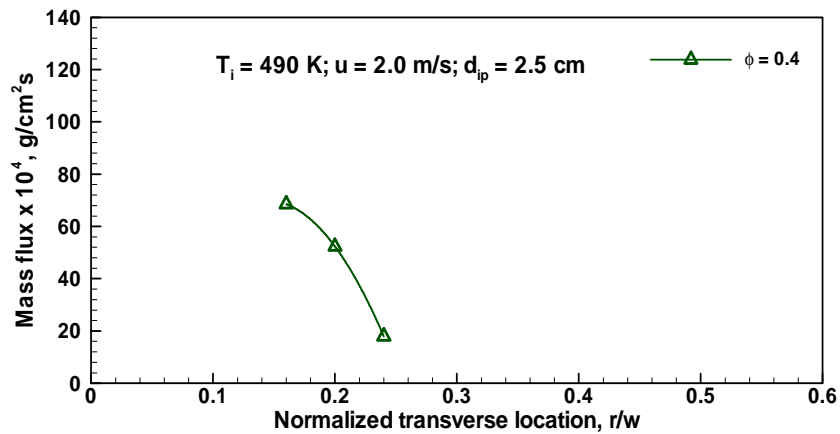
Fig. 4.37 Transverse liquid mass flux profiles of kerosene spray at 2.5 cm upstream of porous media (Coflow temperature – 450 K)



(a) Coflow air velocity = 1.4 m/s

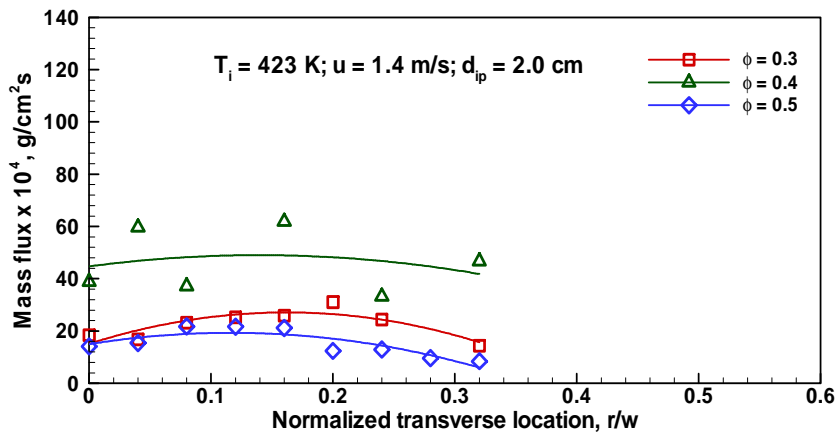


(b) Coflow air velocity = 1.65 m/s

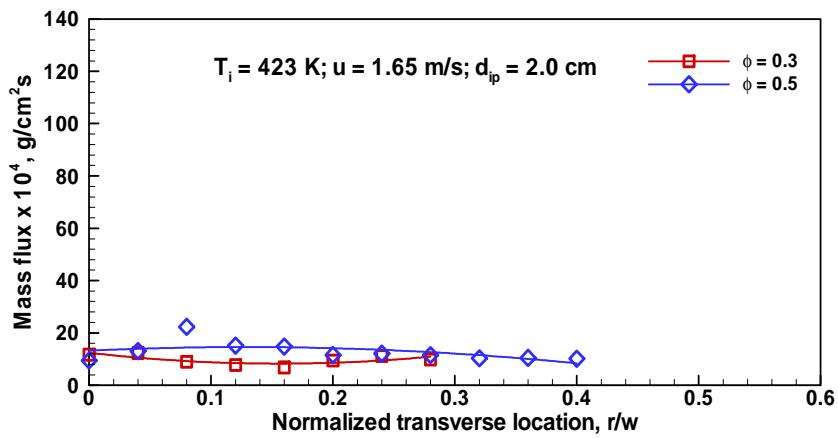


(c) Coflow air velocity = 2.0 m/s

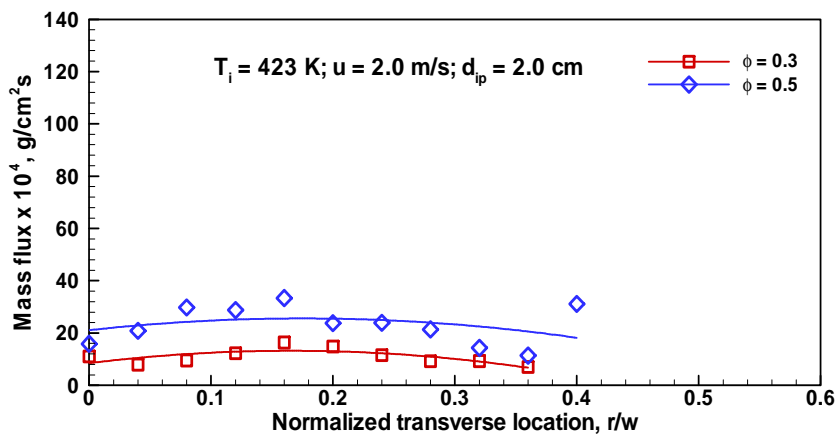
Fig. 4.38 Transverse liquid mass flux profiles of kerosene spray at 2.5 cm upstream of porous media (Coflow temperature – 490 K)



(a) Coflow air velocity = 1.4 m/s

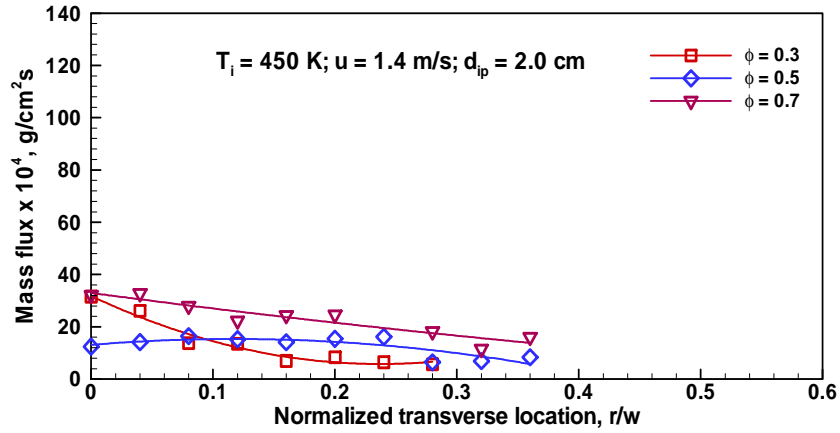


(b) Coflow air velocity = 1.65 m/s

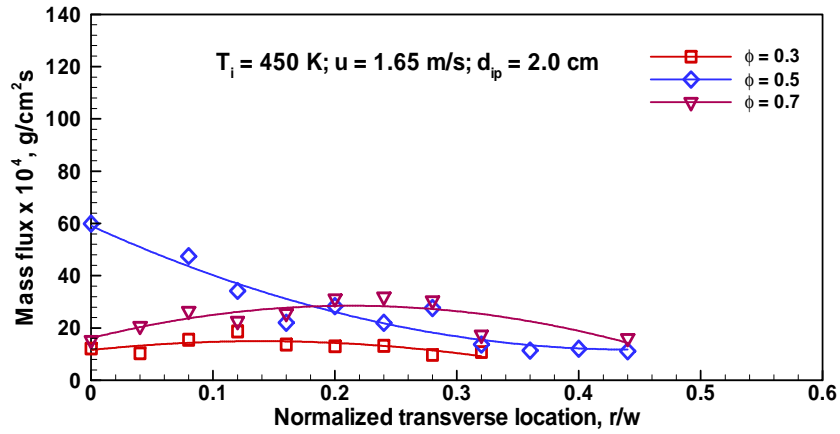


(c) Coflow air velocity = 2.0 m/s

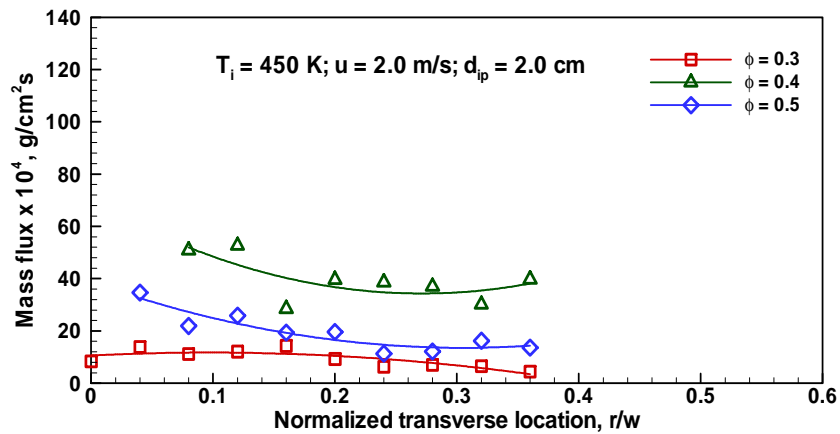
Fig. 4.39 Transverse liquid mass flux profiles of kerosene spray at 2.0 cm upstream of porous media (Coflow temperature – 423 K)



(a) Coflow air velocity = 1.4 m/s

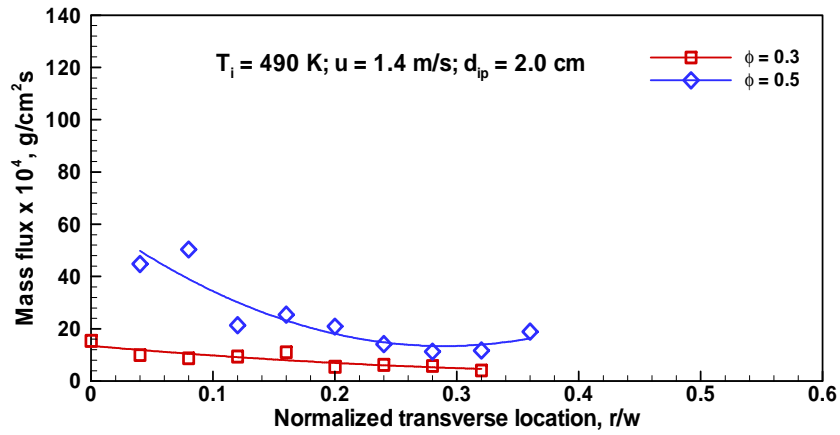


(b) Coflow air velocity = 1.65 m/s

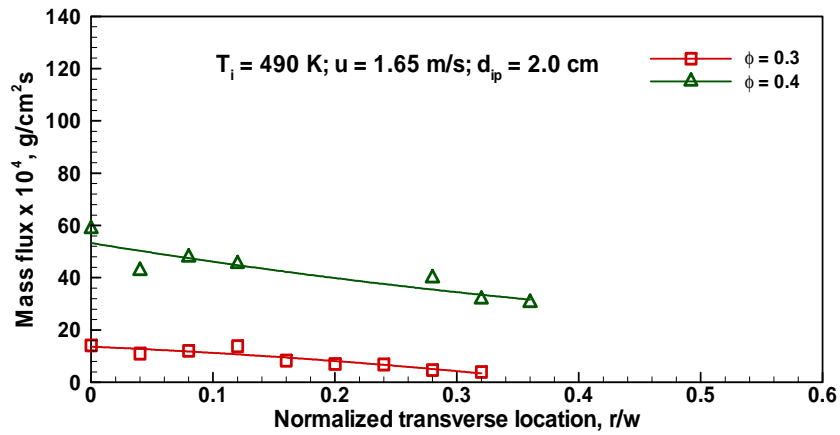


(c) Coflow air velocity = 2.0 m/s

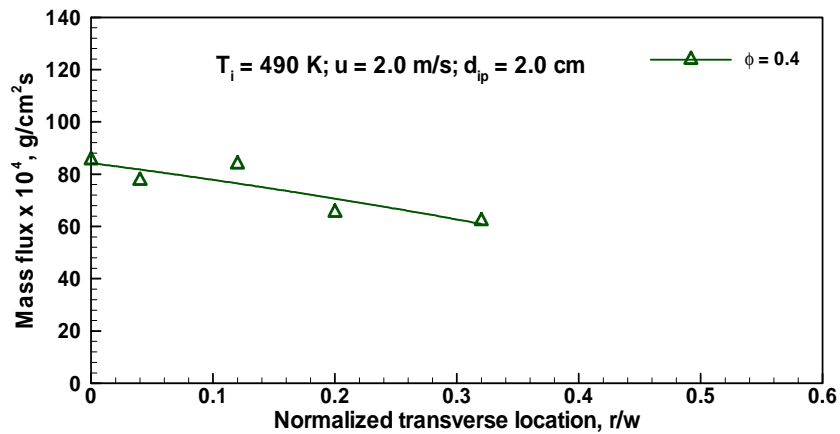
Fig. 4.40 Transverse liquid mass flux profiles of kerosene spray at 2.0 cm upstream of porous media (Coflow temperature – 450 K)



(a) Coflow air velocity = 1.4 m/s

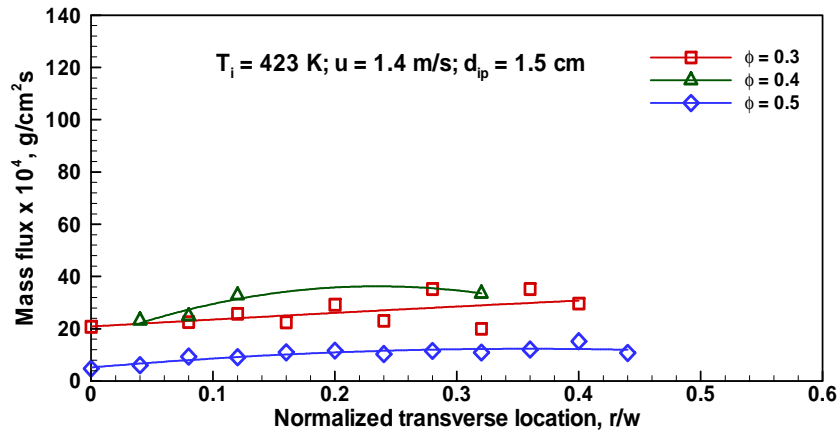


(b) Coflow air velocity = 1.65 m/s

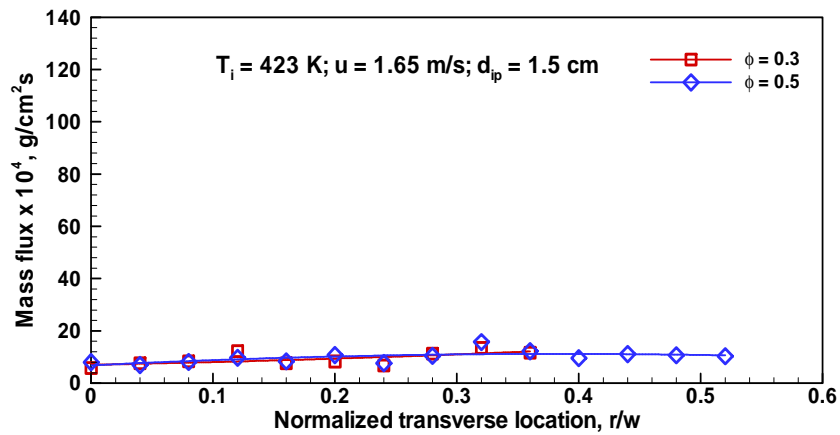


(c) Coflow air velocity = 2.0 m/s

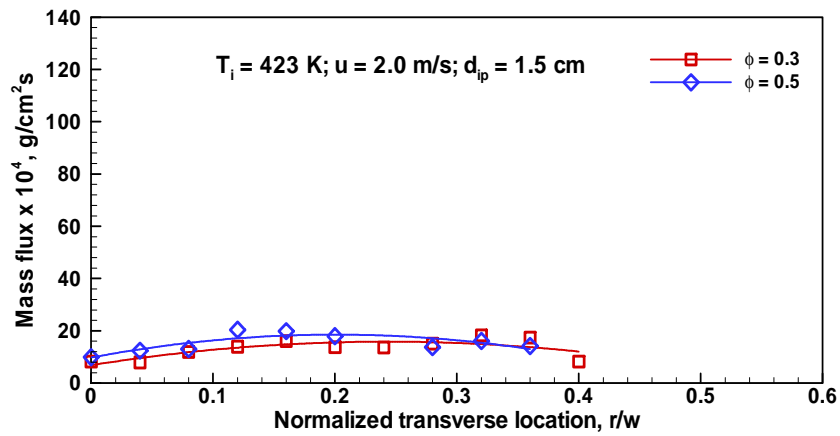
Fig. 4.41 Transverse liquid mass flux profiles of kerosene spray at 2.0 cm upstream of porous media (Coflow temperature – 490 K)



(a) Coflow air velocity = 1.4 m/s

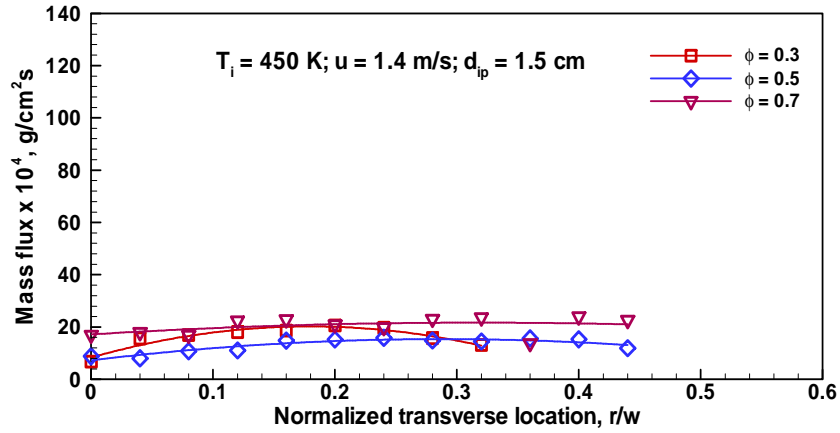


(b) Coflow air velocity = 1.65 m/s

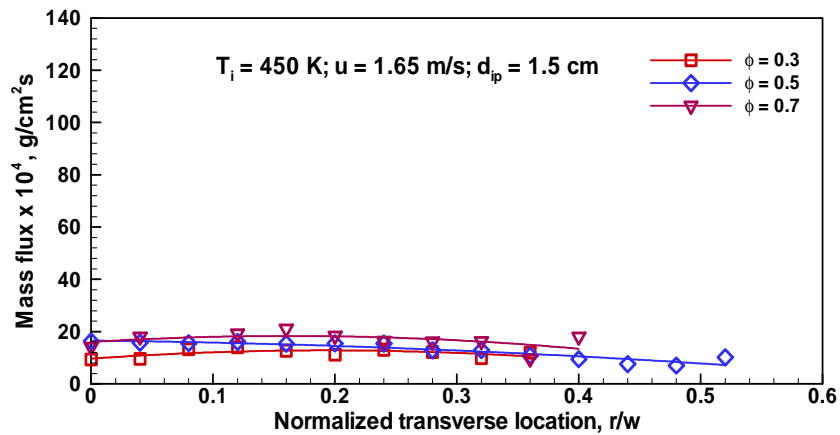


(c) Coflow air velocity = 2.0 m/s

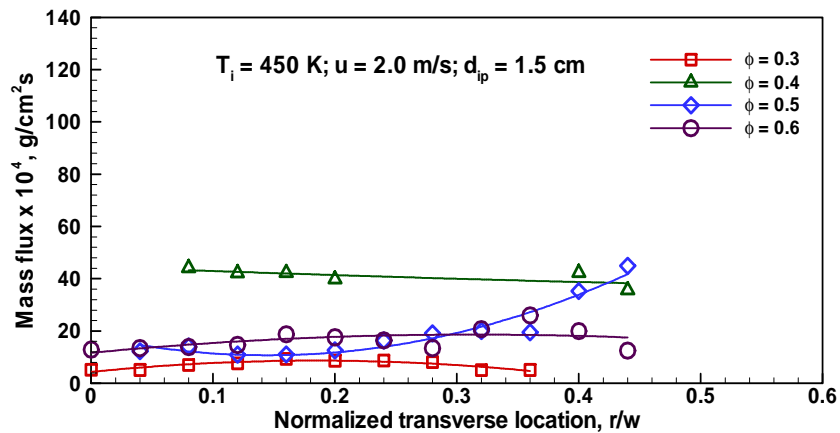
Fig. 4.42 Transverse liquid mass flux profiles of kerosene spray at 1.5 cm upstream of porous media (Coflow temperature – 423 K)



(a) Coflow air velocity = 1.4 m/s

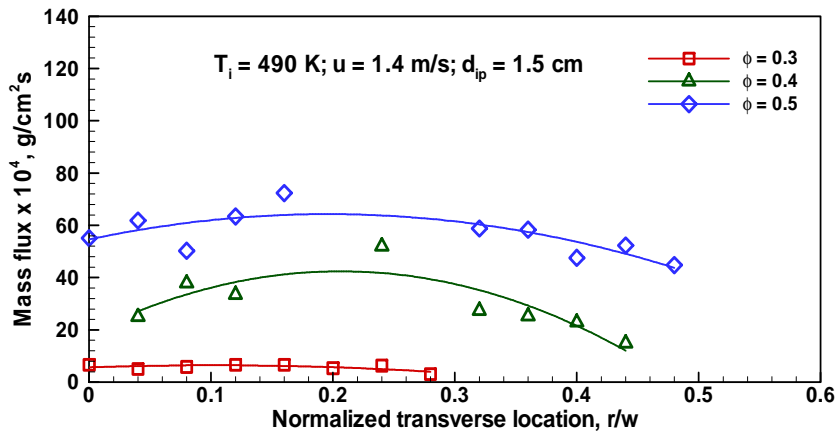


(b) Coflow air velocity = 1.65 m/s

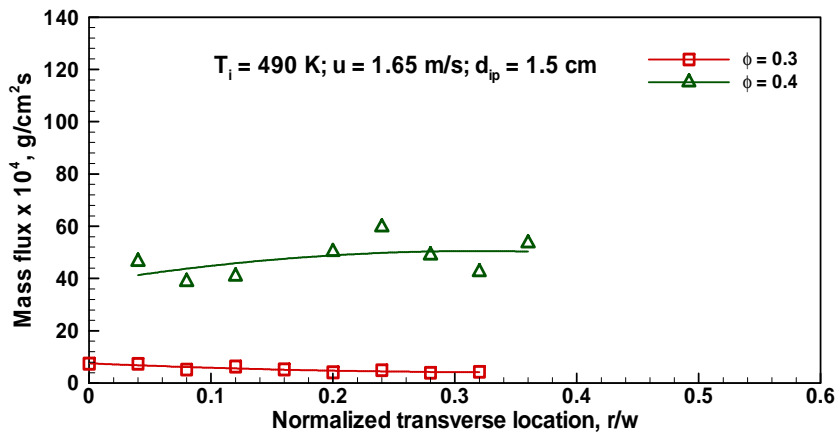


(c) Coflow air velocity = 2.0 m/s

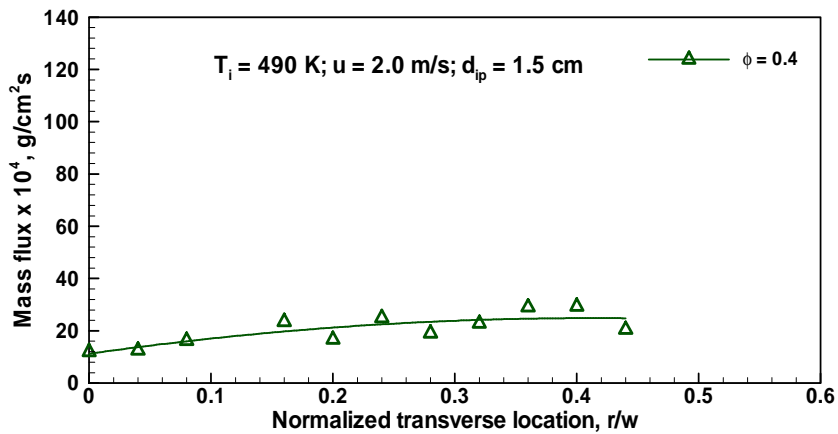
Fig. 4.43 Transverse liquid mass flux profiles of kerosene spray at 1.5 cm upstream of porous media (Coflow temperature – 450 K)



(a) Coflow air velocity = 1.4 m/s

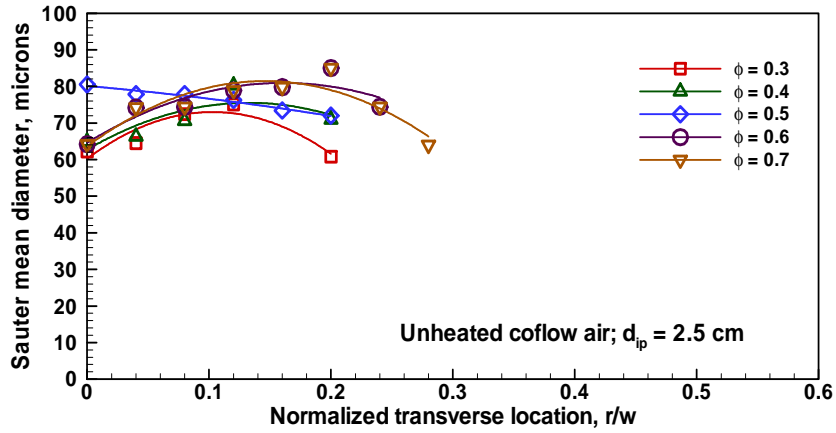


(b) Coflow air velocity = 1.65 m/s

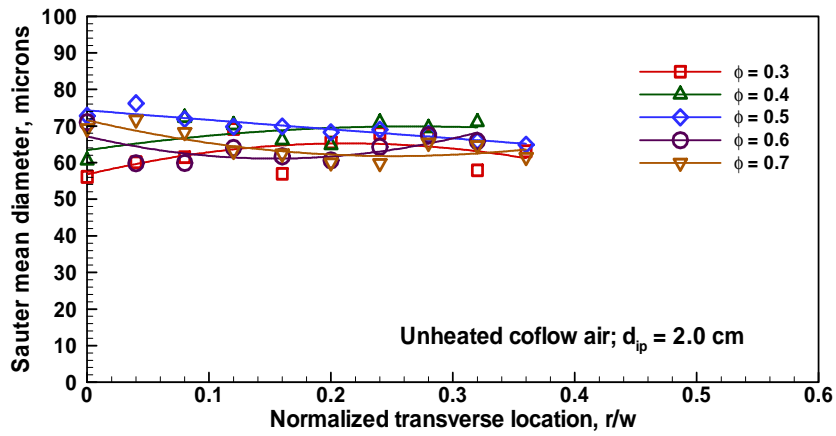


(c) Coflow air velocity = 2.0 m/s

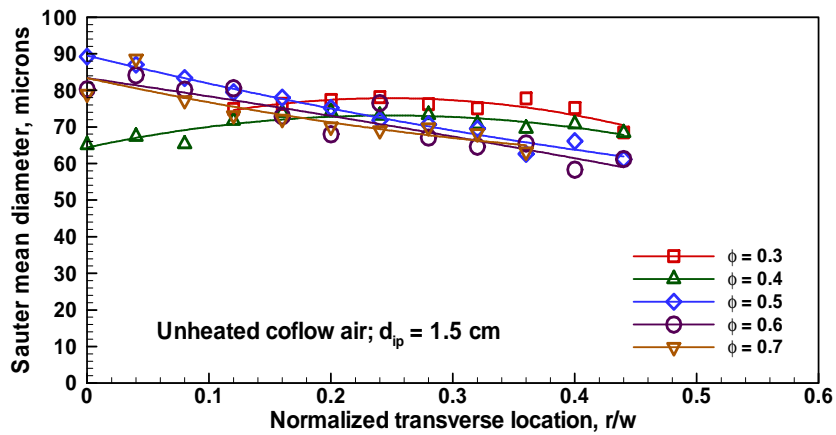
Fig. 4.44 Transverse liquid mass flux profiles of kerosene spray at 1.5 cm upstream of porous media (Coflow temperature – 490 K)



(a) 2.5 cm upstream of porous media

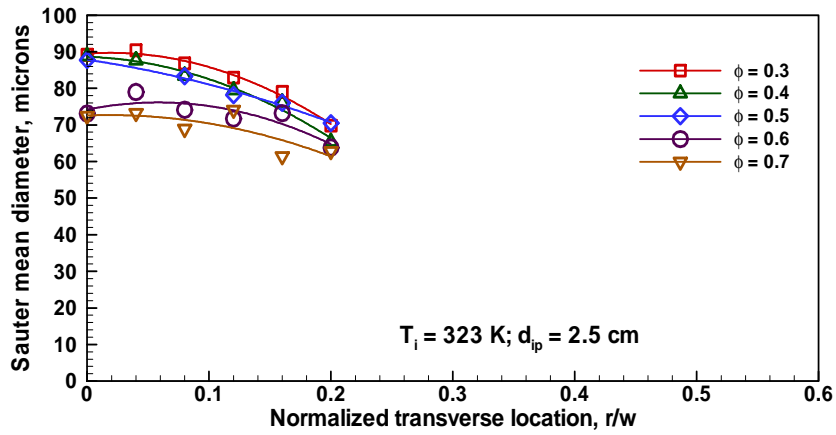


(b) 2.0 cm upstream of porous media

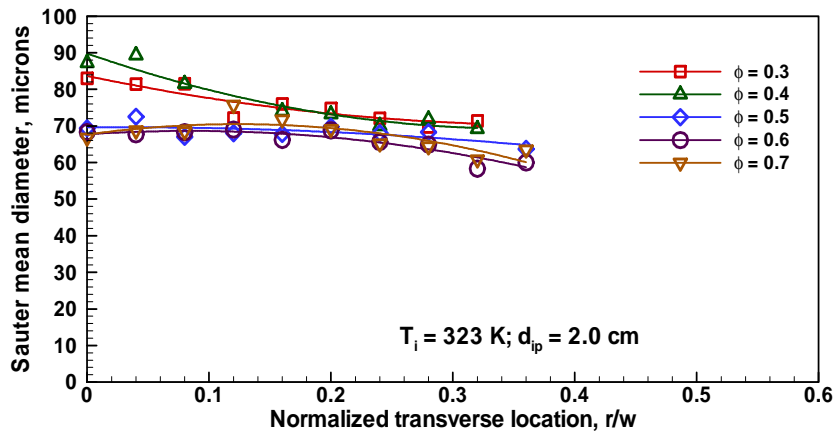


(c) 1.5 cm upstream of porous media

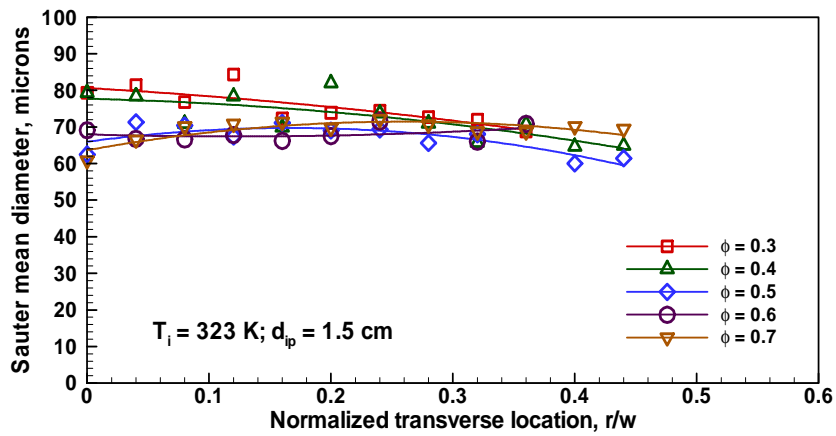
Fig. 4.45 Transverse Sauter mean diameter profiles of n-heptane spray at different axial locations upstream of porous media (Unheated coflow)



(a) 2.5 cm upstream of porous media

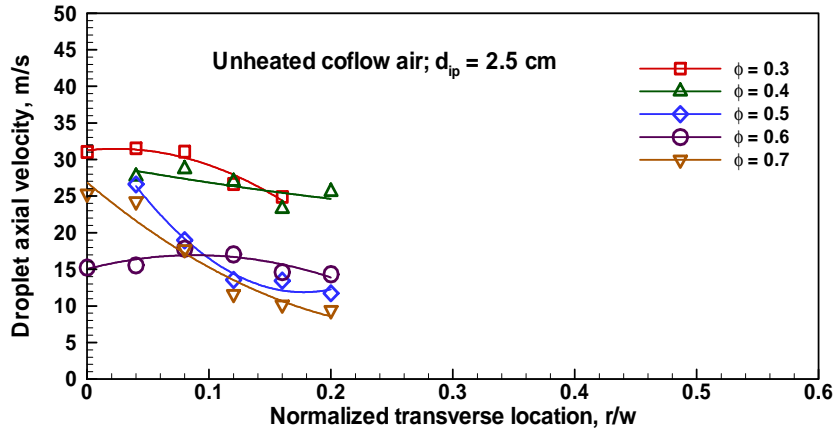


(b) 2.0 cm upstream of porous media

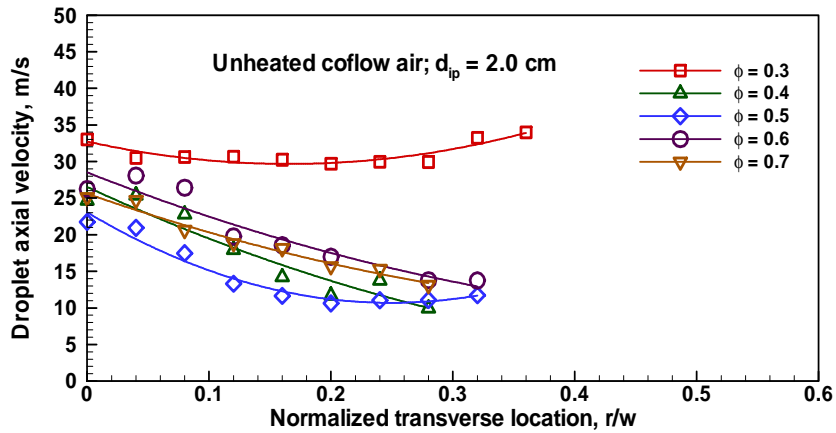


(c) 1.5 cm upstream of porous media

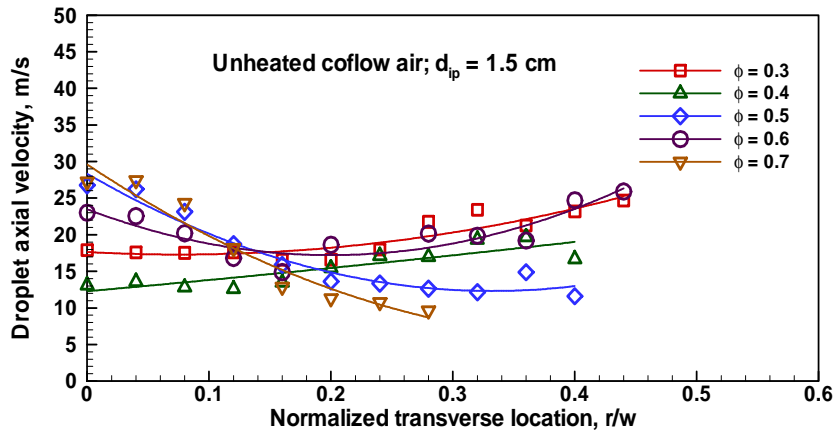
Fig. 4.46 Transverse Sauter mean diameter profiles of n-heptane spray at different axial locations upstream of porous media ($T_i = 323 \text{ K}$)



(a) 2.5 cm upstream of porous media

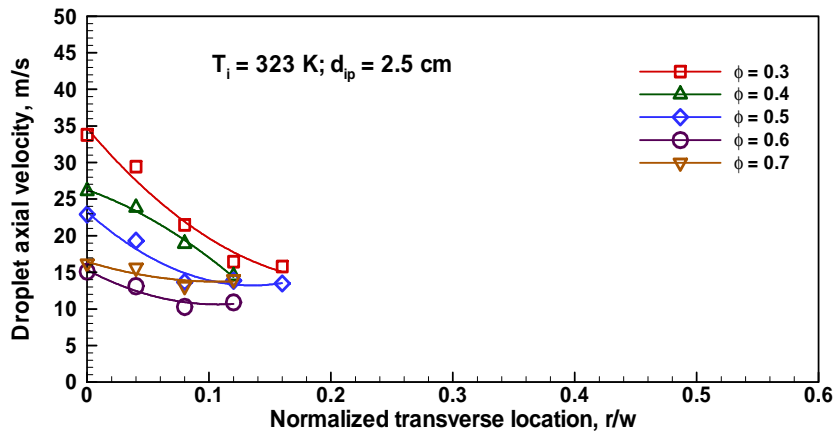


(b) 2.0 cm upstream of porous media

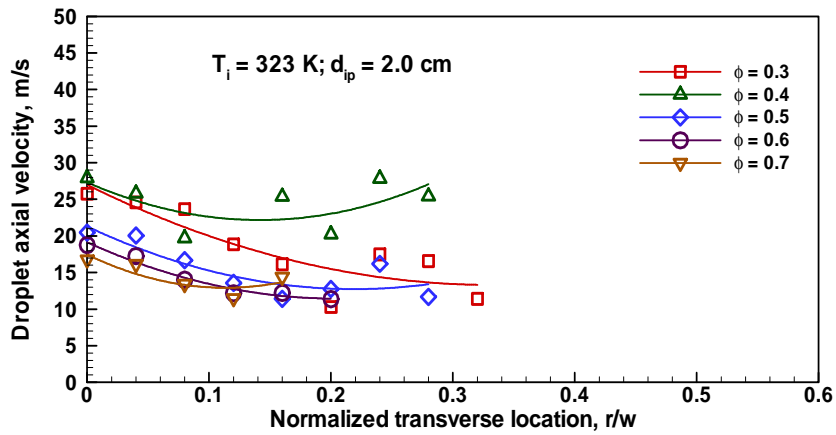


(c) 1.5 cm upstream of porous media

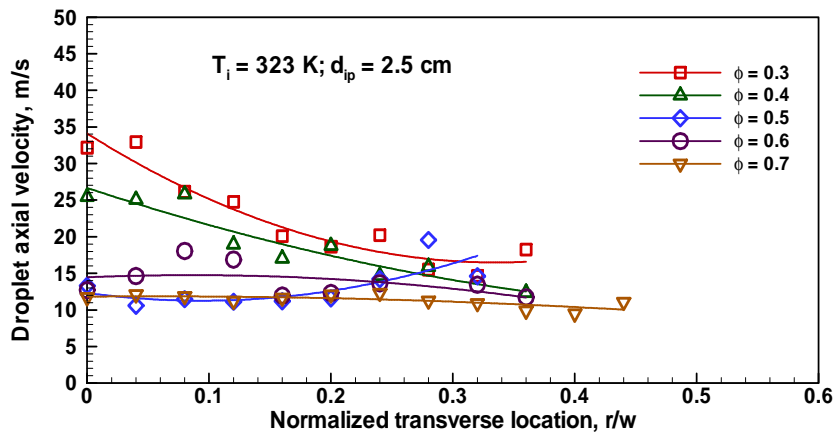
Fig. 4.47 Transverse droplet axial velocity profiles of n-heptane spray at different axial locations upstream of porous media (Unheated coflow)



(a) 2.5 cm upstream of porous media

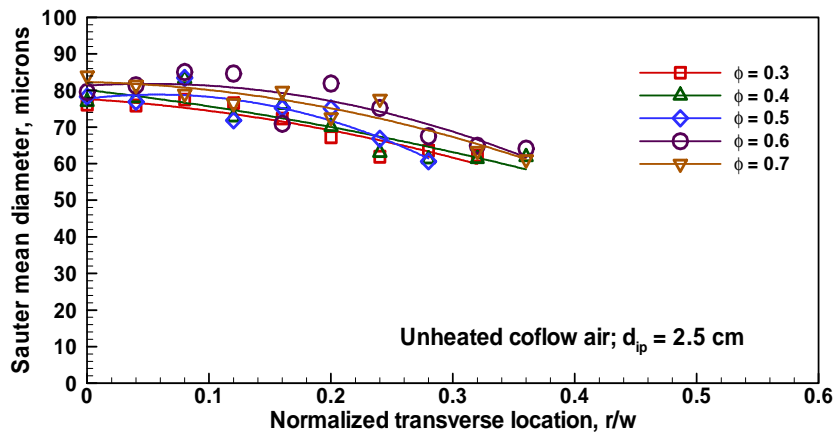


(b) 2.0 cm upstream of porous media

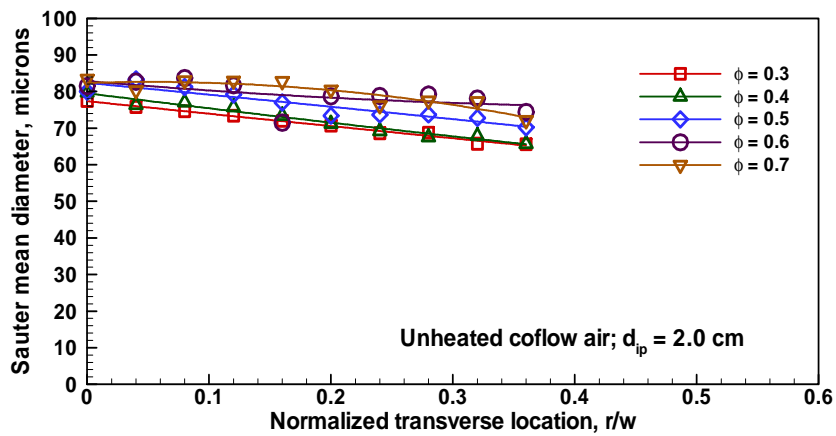


(c) 1.5 cm upstream of porous media

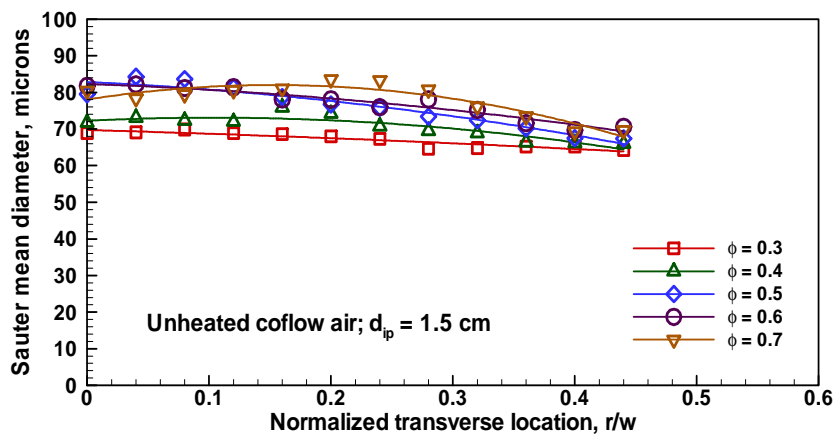
Fig. 4.48 Transverse droplet axial velocity profiles of n-heptane spray at different axial locations upstream of porous media ($T_i = 323 \text{ K}$)



(a) 2.5 cm upstream of porous media

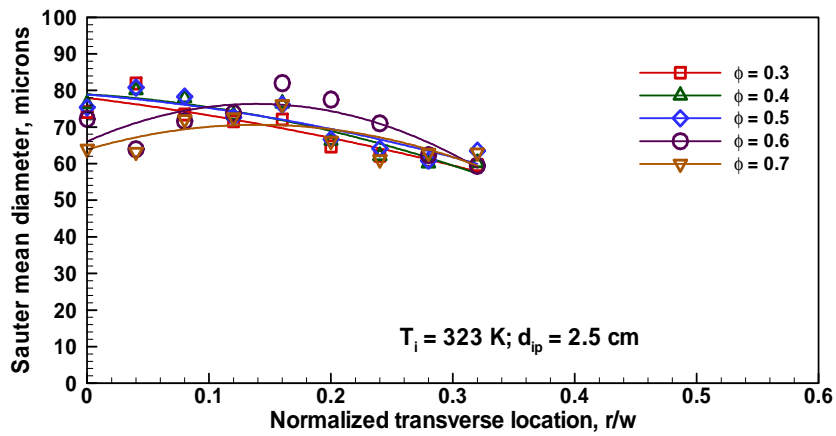


(b) 2.0 cm upstream of porous media

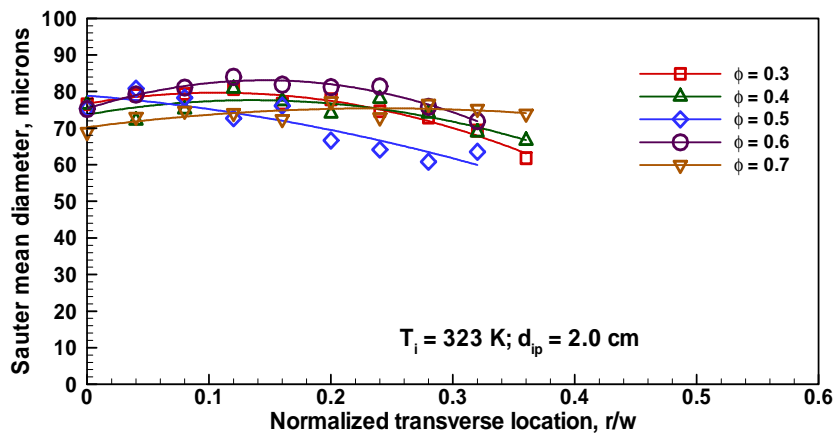


(c) 1.5 cm upstream of porous media

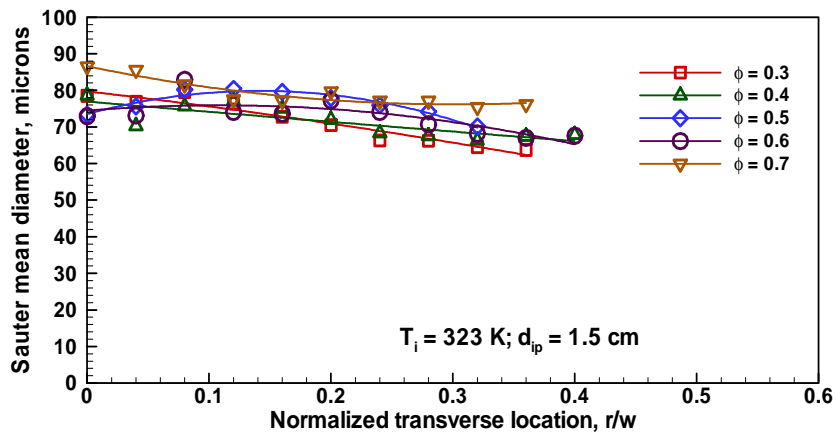
Fig. 4.49 Transverse Sauter mean diameter profiles of methanol spray at different axial locations upstream of porous media (Unheated coflow)



(a) 2.5 cm upstream of porous media

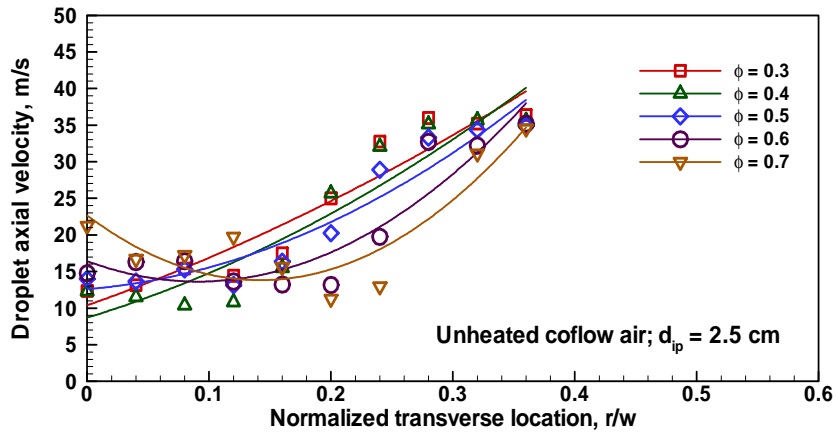


(b) 2.0 cm upstream of porous media

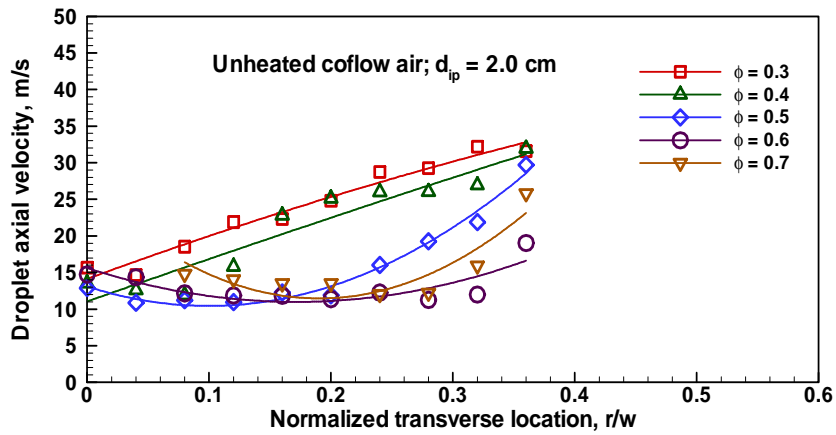


(c) 1.5 cm upstream of porous media

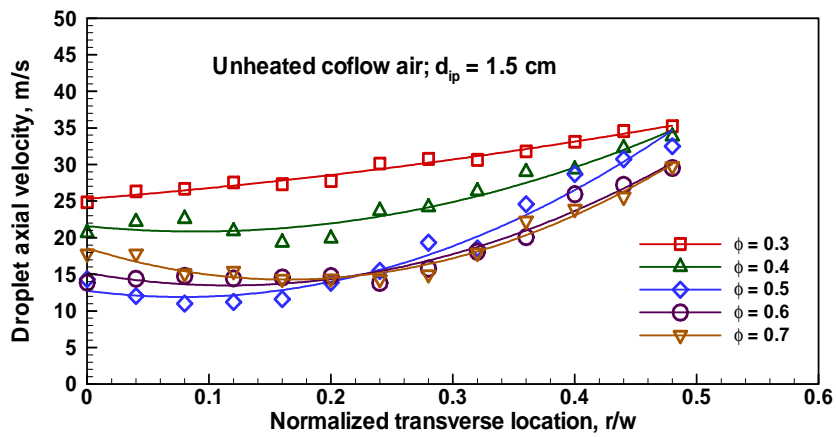
Fig. 4.50 Transverse Sauter mean diameter profiles of methanol spray at different axial locations upstream of porous media ($T_i = 323 \text{ K}$)



(a) 2.5 cm upstream of porous media

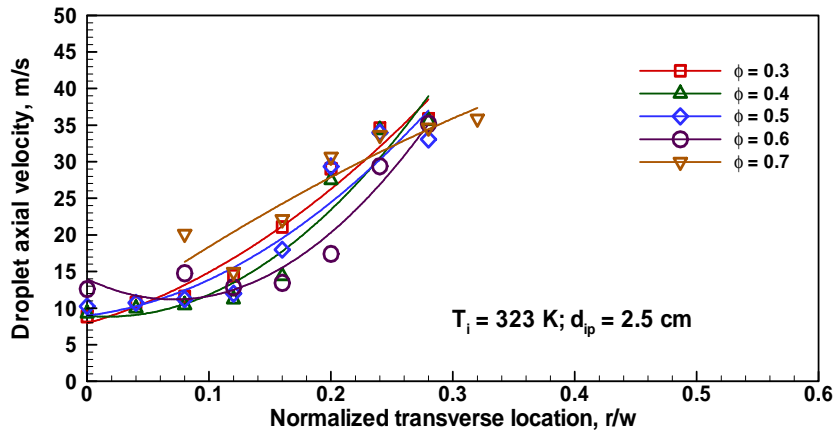


(b) 2.0 cm upstream of porous media

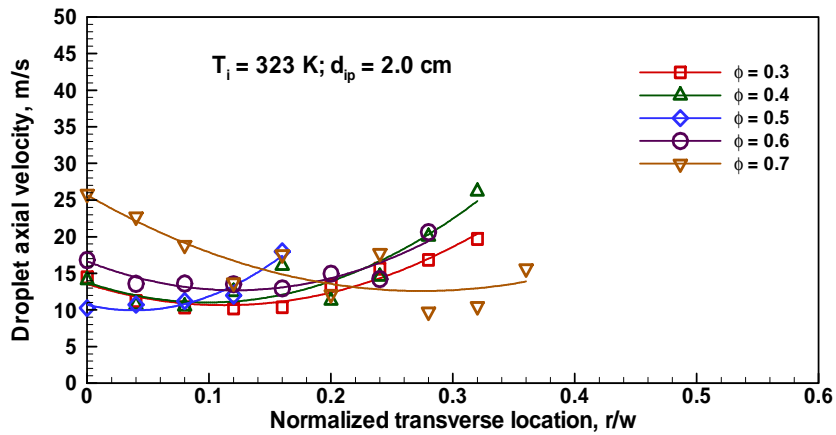


(c) 1.5 cm upstream of porous media

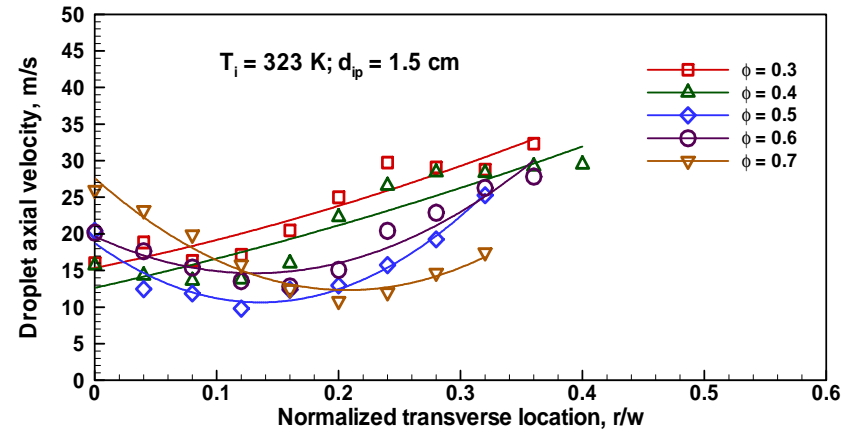
Fig. 4.51 Transverse droplet axial velocity profiles of methanol spray at different axial locations upstream of porous media (Unheated coflow)



(a) 2.5 cm upstream of porous media

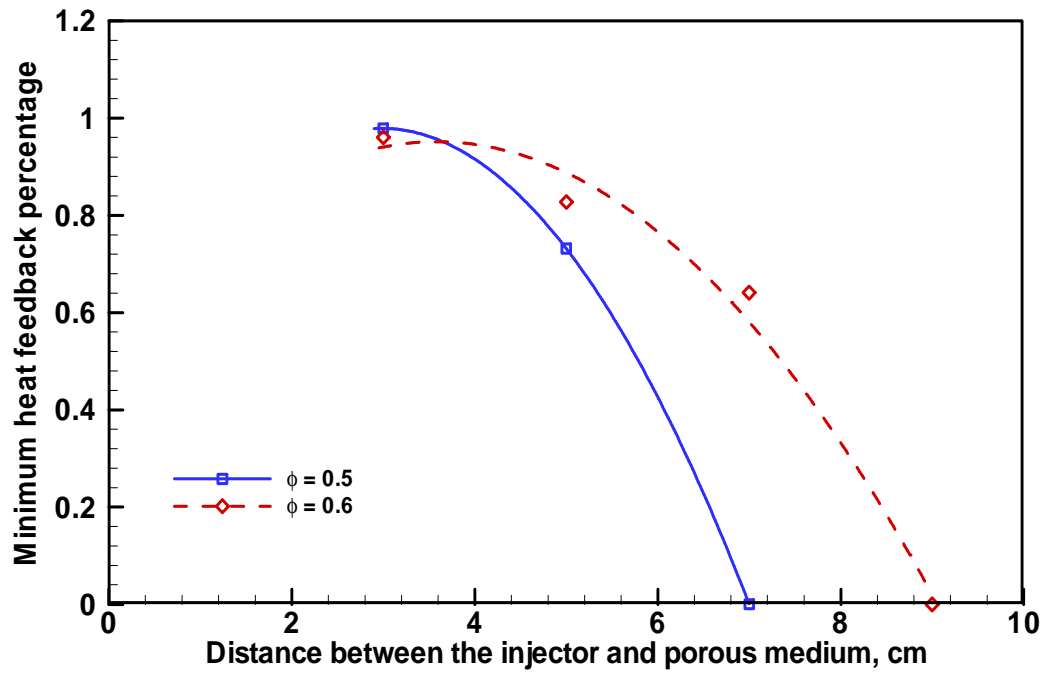


(b) 2.0 cm upstream of porous media

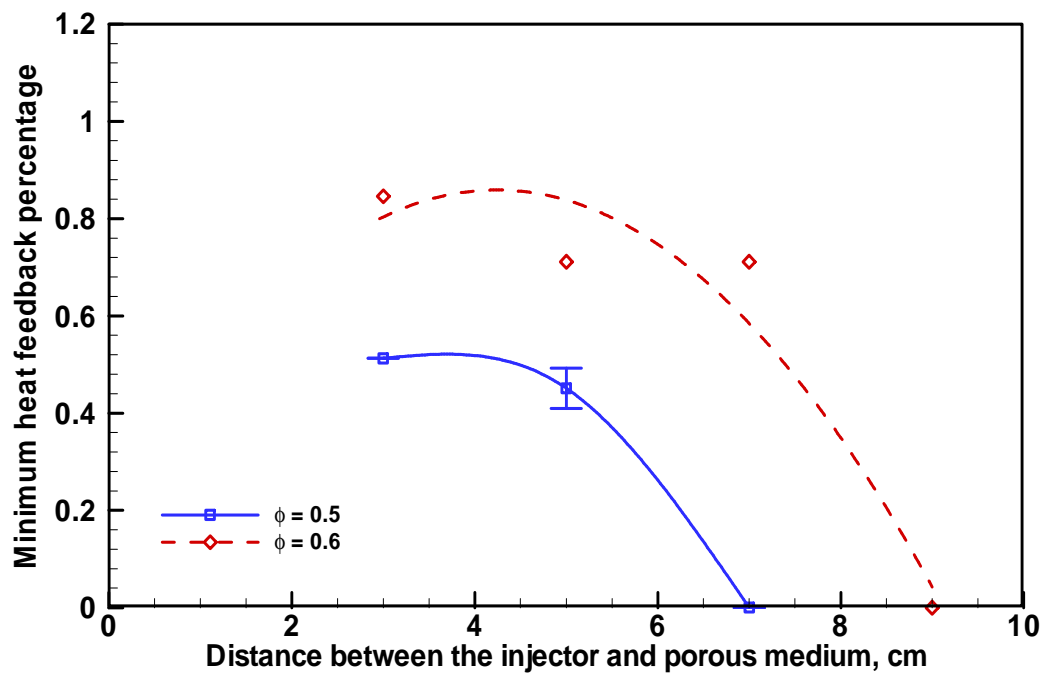


(c) 1.5 cm upstream of porous media

Fig. 4.52 Transverse droplet axial velocity profiles of methanol spray at different axial locations upstream of porous media ($T_i = 323\text{ K}$)

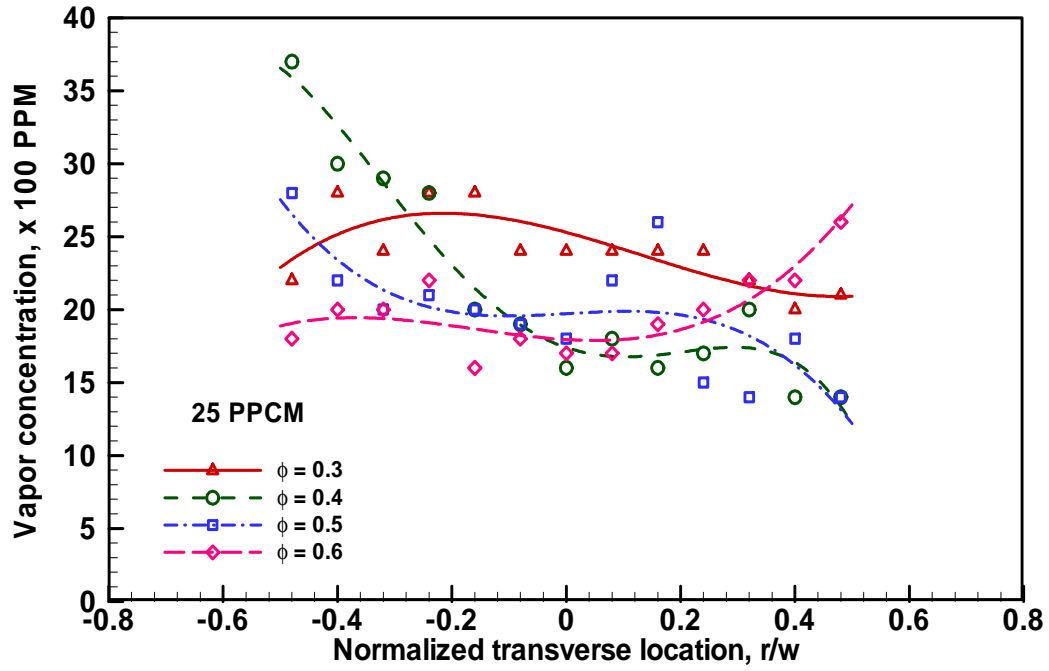


(a) 25 PPCM

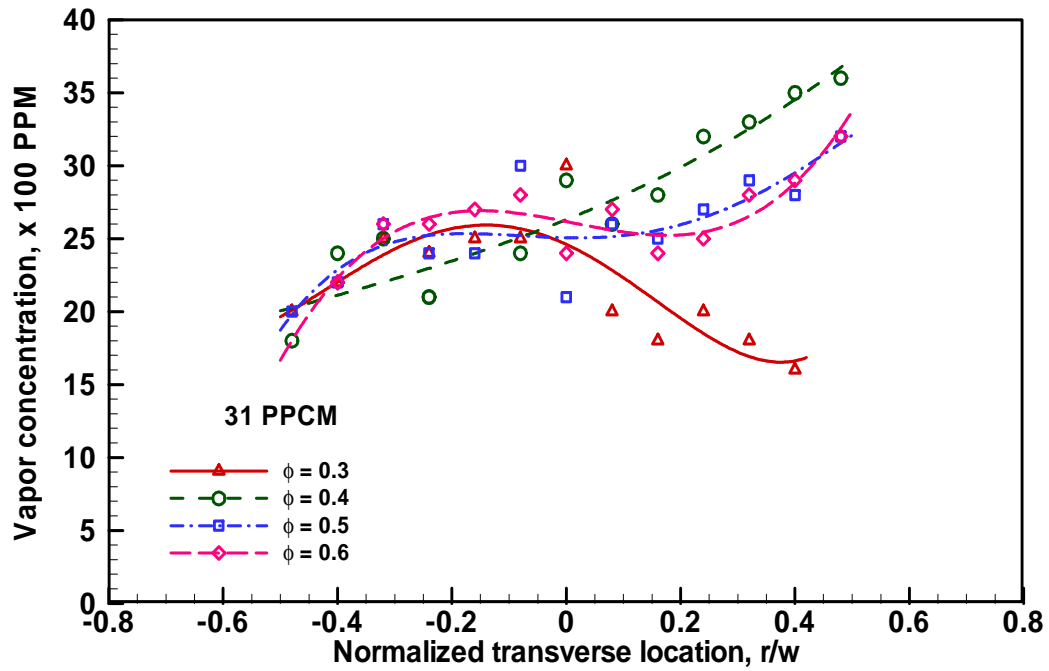


(b) 31 PPCM

Fig. 4.53 Variation of minimum heat feedback requirement with the distance between the injector and porous medium for 25 and 31 PPCM porous media (Coflow air flowrate = 195 l/min; Coflow air temperature = 450 K)



(a) 25 PPCM



(b) 31 PPCM

Fig. 4.54 Measured transverse kerosene vapor concentration profiles at 5 cm downstream of the porous medium for 25 and 31 PPCM porous media with different equivalence ratios (No combustion heat feedback; Coflow air flowrate = 195 l/min; Coflow air temperature = 450 K)

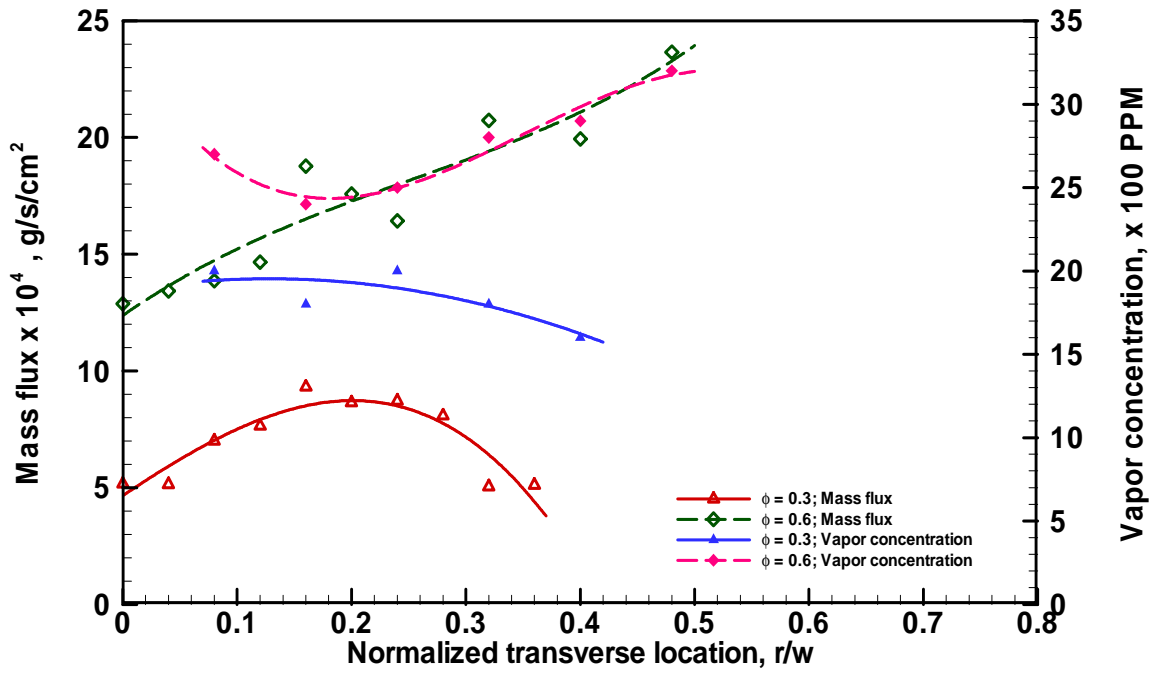


Fig. 4.55 Liquid mass flux distribution (MF) and vapor concentration profiles (VC) with 25 PPCM porous medium at 0.3 and 0.6 equivalence ratios (No combustion heat feedback; Coflow air flowrate = 195 l/min; Coflow air temperature = 450 K)

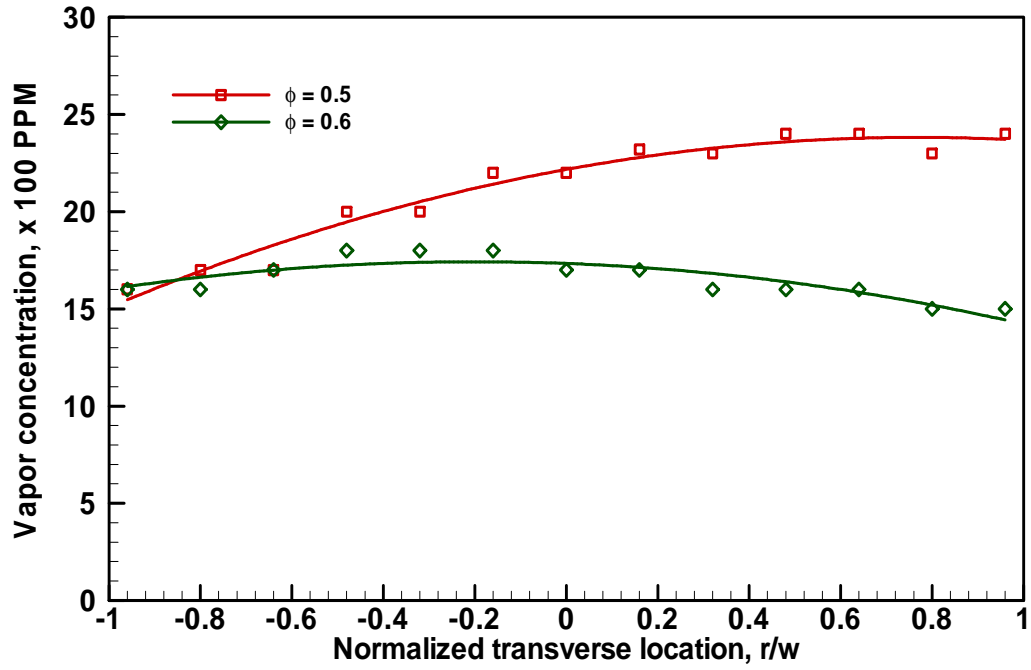


Fig. 4.56 Measured transverse n-heptane vapor concentration profiles at 5 cm downstream of the porous medium for 25 PPCM porous media with different equivalence ratios (No combustion heat feedback; Unheated coflow)

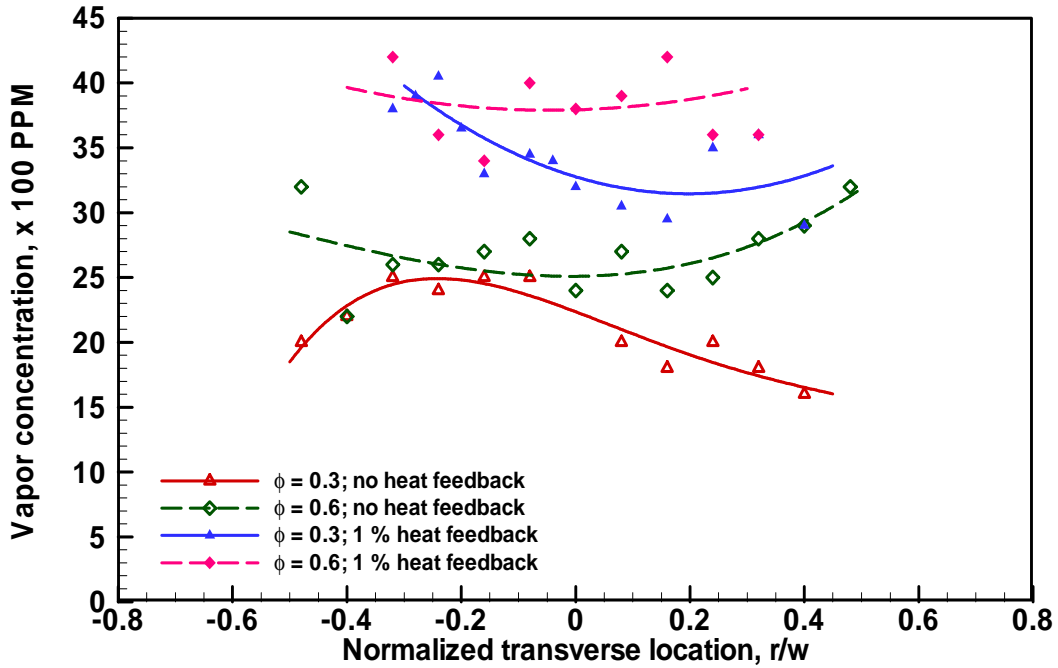


Fig. 4.57 Vapor concentration profiles with 31 PPCM porous medium at $\phi = 0.3$ and 0.6 with and without combustion heat feedback ($w =$ half width of the test section, 2.5 cm; Coflow air flowrate = 195 l/min; Coflow air temperature = 450 K)

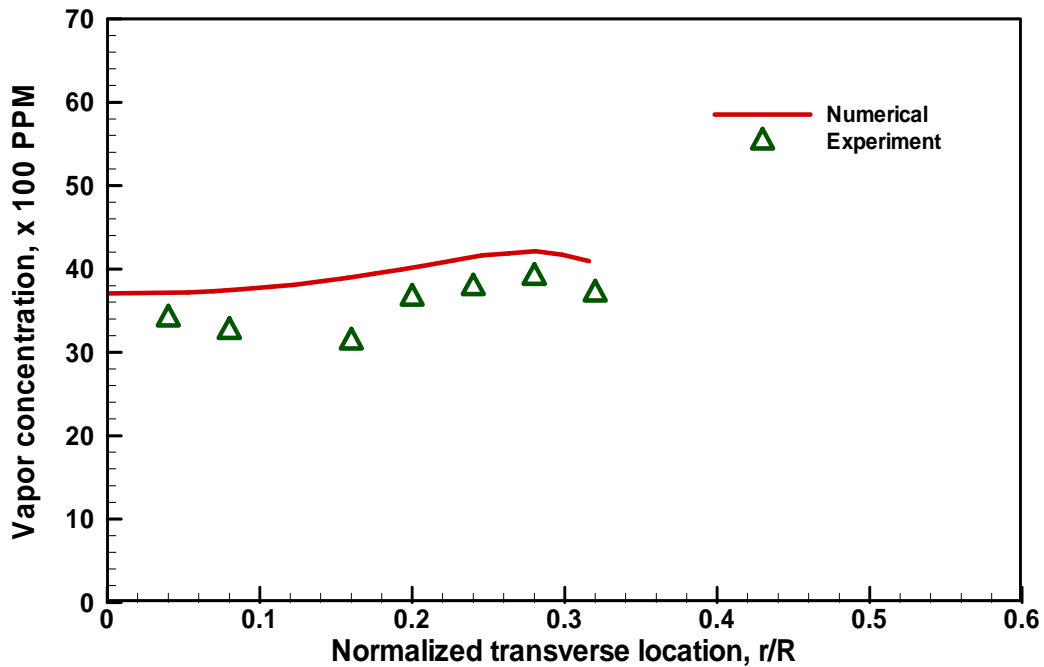


Fig. 4.58 Comparison of predicted and measured kerosene vapor concentration profile at 5 cm downstream of porous medium ($R =$ radius of the computational domain, 2.15 cm; $\phi = 0.3$; heat feedback rate = 1%)

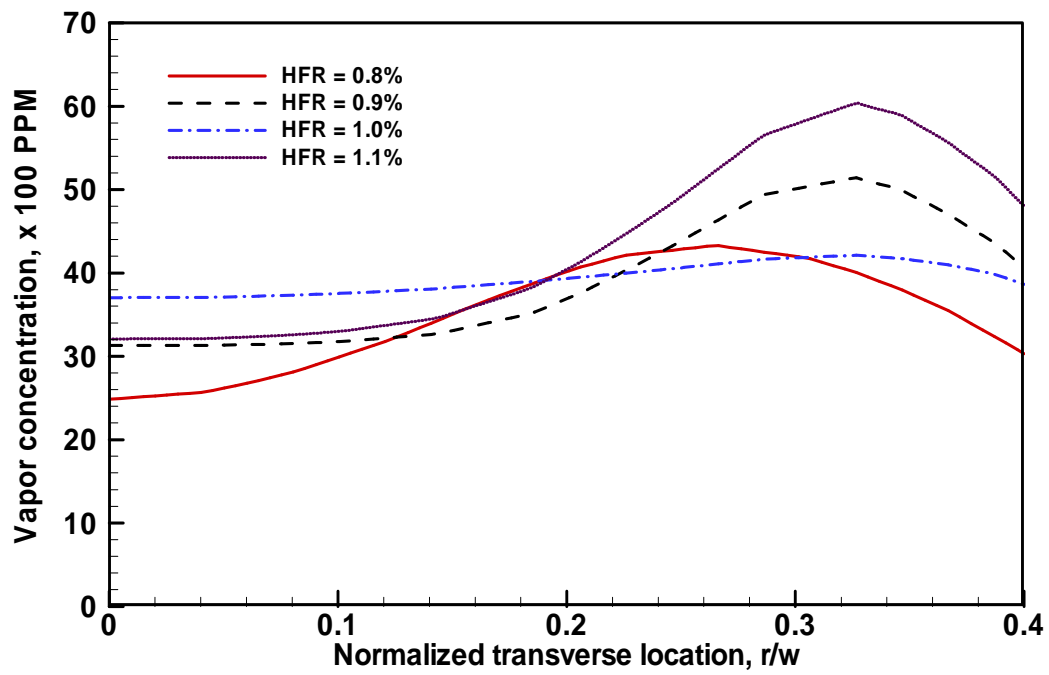


Fig. 4.59 Effect of combustion heat feedback rate on predicted transverse distribution of kerosene vapor concentration ($\phi = 0.3$; $T_i = 450$ K; $\varepsilon = 0.87$)

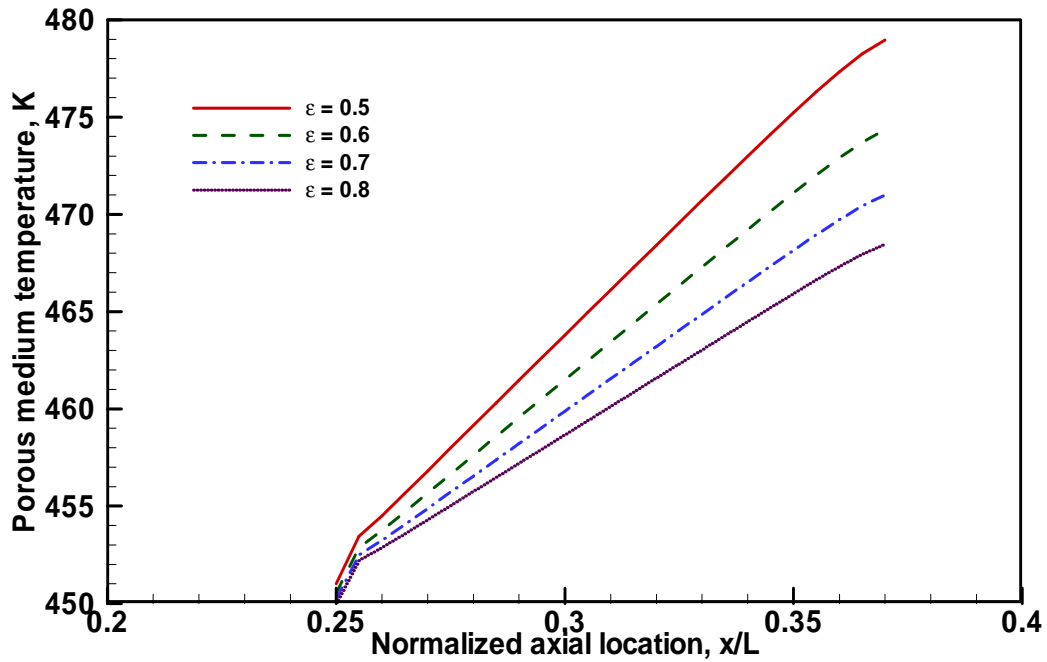


Figure 4.60 Effect of porosity on axial temperature profiles in porous media (No liquid fuel supplied; $T_i = 450$ K; Heat feedback rate = 1.0%)

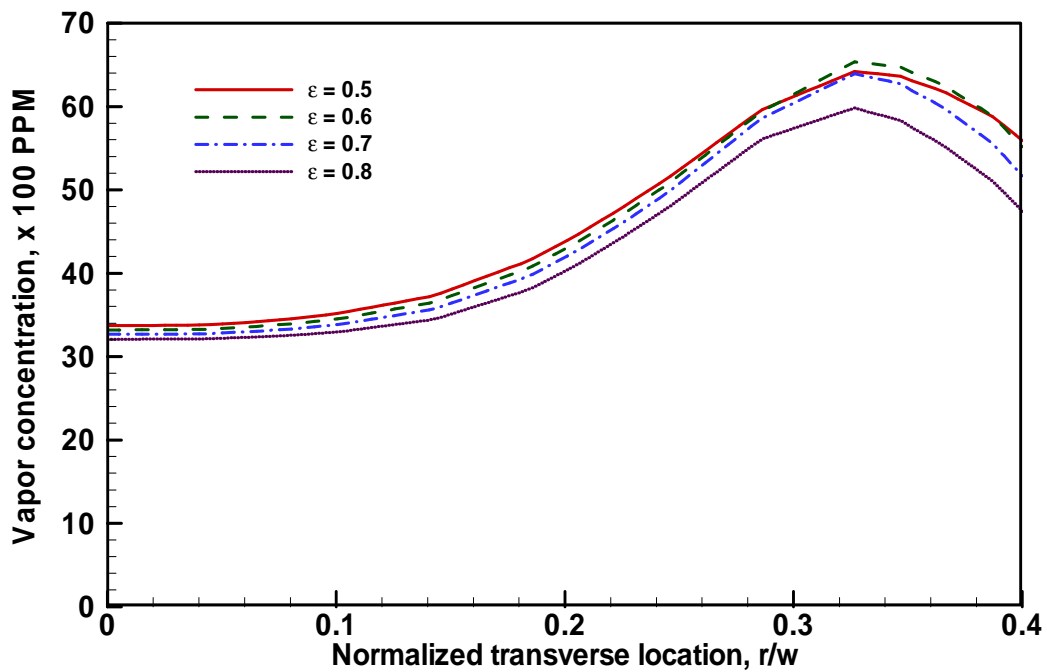


Figure 4.61 Effect of porosity on transverse kerosene vapor concentration profiles at 5 cm downstream of porous media ($\phi = 0.3$; $T_i = 450$ K; Heat feedback rate = 1.0%)

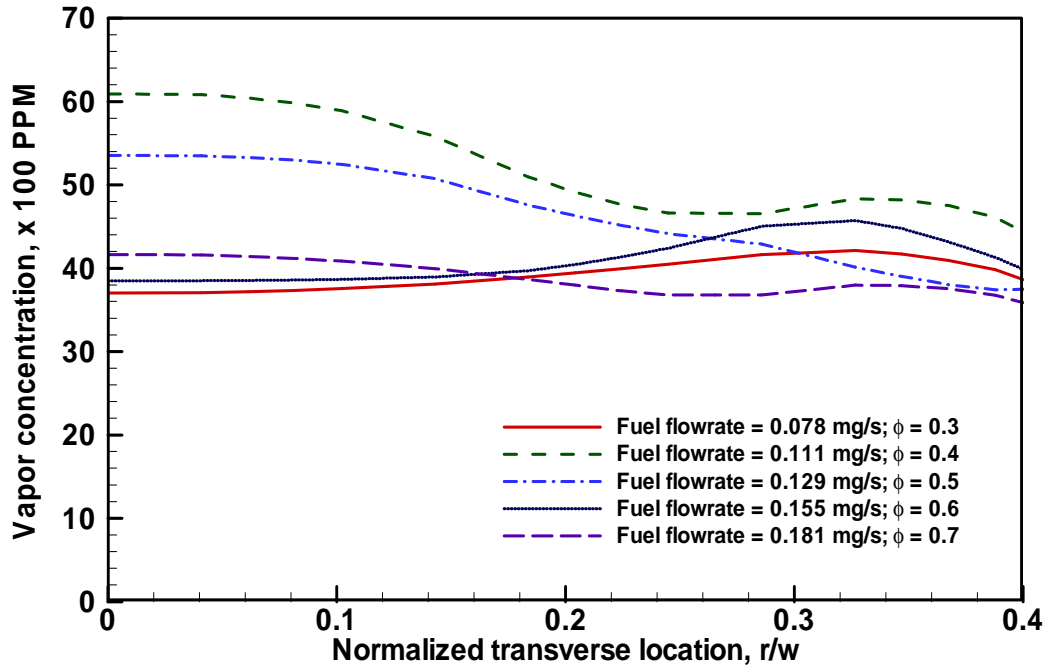


Figure 4.62 Effect of fuel flowrate on transverse kerosene vapor concentration profiles at 5 cm downstream of porous media ($T_i = 450 \text{ K}$; $\epsilon = 0.87$; Heat feedback rate = 1.0%)

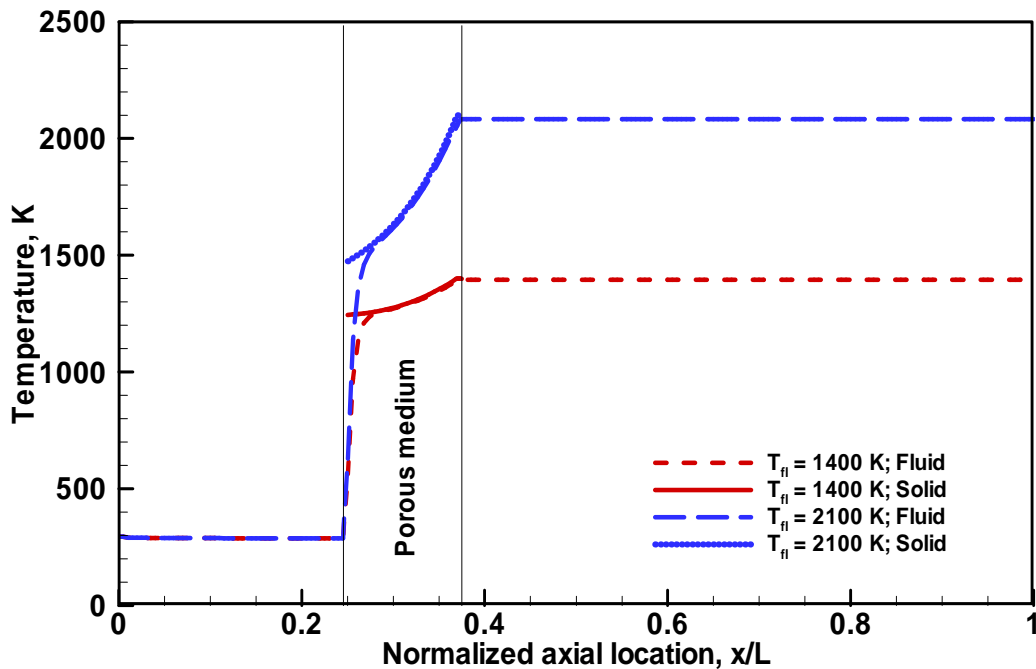


Figure 4.63 Effect of flame temperature on predicted axial porous medium and fluid temperature profiles for different assumed flame temperatures ($T_i = 450 \text{ K}$; $\epsilon = 0.87$)

Chapter 5

Combustion of Liquid Spray in Porous Media

5.1 Introduction

In the previous chapter, evaporation enhancement of liquid spray in porous media has been studied with a *simulated combustion heat feedback*. This chapter extends the study by replacing the simulated heat feedback source with the combustion of liquid spray in the porous media located downstream. This chapter presents the interactions between combustion and evaporation. Stable operating regimes, porous medium temperature near extinction, surface temperature uniformity, radiative heat release, and pollutant emission of spray flames in porous media are discussed.

5.2 Flame Appearance

As mentioned in Section 2.3.5, a high-temperature Vycor® glass test section was used during the combustion experiments. The aluminum porous medium housing was replaced with a stainless steel housing. A fine-structured 25 PPCM porous medium was used as evaporation and fuel vapor–air mixing medium (EPM). A coarse 8 PPCM porous medium was used as combustion porous medium (CPM) and placed immediately downstream of evaporation porous medium. Figure 5.1 shows the typical porous media setup employed in this study.

First, the coflow air preheater was turned on and the desired coflow air temperature was set. The flow rate of air was set to produce the desired velocity in the test section using a calibrated rotameter. The fuel tank was pressurized using compressed nitrogen. A pilot flame was ignited at the exit of downstream glass test section. The fuel flowrate was set at the desired value and the atomizing air was set to attain steady spray.

After a 1-2 minute start up period, the fuel spray emanated from the injector, and subsequently, vaporized and mixed with air in the EPM. The fuel vapor–air mixture was ignited by the pilot flame and a stable flame was established in the porous medium. Initially, a fuel flowrate corresponding to a fuel-rich condition was set. Once the flame was established, the desired condition was set. A stable flame is defined as one that is entirely contained within or on the surface of the porous medium for a given fuel and air flowrate and remained steady. The former is referred to as interior flames and the latter is referred to as surface flames.

5.2.1 Interior Flames

In the interior combustion mode, the flame was stabilized inside the combustion porous medium. The flame was completely contained within the porous medium. Figure 5.2 shows a typical view of the top surface of the combustion porous medium during the interior combustion mode. The porous medium glowed in a bright orange color. Occasionally, a long streak of yellow flame was observed downstream of the porous medium. With a reduction in fuel flowrate below a certain value

(corresponding to the stable lean limit of interior flames, discussed in Section 5.3), the flame appeared as a transient weak blue flame on the surface and immediately extinguished.

The porous medium was able to withstand combustion continuously for more than two hours. The combined operation of one porous medium exceeded more than 100 hours maintaining structural stability. No clogging of pores was observed. Further, interior flames operated quieter than surface flames.

5.2.2 *Surface Flames*

In the surface combustion mode, the flame was always stabilized on the downstream exit surface of the combustion porous medium. The flame covered the entire porous medium surface. Figure 5.3 shows a typical surface flame observed in this study. The flame exhibited a cellular structure or appeared as contiguous flat bright blue sheet. The flame zone was located about 1-3 mm above the porous medium surface.

As the fuel flowrate was decreased below a certain equivalence ratio, the flame first lifted from the surface on locations where the gas velocity was higher than the local flame speed. As the mixture was made leaner, the flat flame structure weakened and transformed into cellular structure. With a further decrease in the fuel flowrate, the flame was completely lifted from the surface and was immediately extinguished. A fully lifted flame could not be stabilized.

5.3 Lean Extinction Limits

5.3.1 Definition of Flame Extinction in Porous Media

As mentioned earlier, interior and surface combustion flames could be stabilized inside and on the exit surface of combustion porous media, respectively. The specific mode of combustion depends on the flowrates of coflow air and fuel and the location of injector. However, only one mode of combustion could be established for the specified set of conditions. A stable interior flame once established in porous medium, remained stable as an interior flame until it blew out, and similarly, the surface flame remained stable on the exit surface of the porous medium until it blew out.

After a stable interior or surface flame was established, the fuel flowrate was decreased while keeping the coflow air velocity constant. During the interior combustion mode, below a critical fuel flowrate (or equivalence ratio), the flame appeared as a transient weak blue flame on the surface and blew out immediately. In the surface combustion mode, below a critical fuel flowrate, the flame lifted from the exit surface of combustion porous medium and blew out immediately. The condition where the flame (interior or surface) is not present in the porous medium is referred to as flame extinction. This flame extinction was detected by visual observation and porous medium surface temperature measurements.

5.3.2 Measurement of Flame Extinction in Porous Media

During the interior or surface combustion mode, the fuel flowrate just prior to the extinction of flame was recorded. Using the coflow air flowrate, the equivalence ratio at extinction was calculated, as follows:

$$\phi_{\text{ext}} = \frac{(F/A)_{\text{ext}}}{(F/A)_{\text{stoichiometric}}} \quad (5.1)$$

This procedure was repeated for a range of coflow air flowrates and injector locations. An effective gas velocity through the porous medium was calculated by dividing the coflow air volume flowrate by the porous medium surface area projected perpendicular to the mean flow direction, as follows:

$$u_{\text{eff}} = \frac{\text{Total air flowrate}}{\text{PM surface area}} \quad (5.2)$$

Figure 5.4 presents the variation of extinction equivalence ratio with effective gas velocity for different injector locations. Each data point in the figure denotes the lowest equivalence ratio up to which the flames (interior or surface combustion) could be established in porous medium. Surface combustion data points are shown as filled symbols in Figure 5.4. This figure illustrates the operating regimes of interior and surface combustion flames in porous media. The results show that a decrease in the effective gas velocity decreased the extinction equivalence ratio for all injector

locations. The effective gas velocity determined the location of the flame in the porous media and a decrease in the effective gas velocity moved the flame further inside the porous medium. Uncertainty in the measurement of extinction equivalence ratio was less than $\pm 8\%$ of the mean value. This was calculated using Student's t-distribution at 95% confidence interval.

When combustion occurred inside the porous medium, the heat transfer upstream to evaporation porous medium (EPM) became more efficient due to the increased porous medium temperature. In this study, interior combustion flames were stabilized at as low an equivalence ratio as 0.2. On the other hand, at higher effective gas velocities, flames were stabilized only on the surface of the porous medium. Further, a critical effective gas velocity that distinguished interior and surface combustion modes was found. In the present configuration, increasing the effective gas velocity beyond 130 cm/s resulted in surface flames.

5.4 Damköhler number Analysis at Flame Extinction

Based on the experimental results discussed in previous section, a generalized understanding of flame extinction in porous media has been developed. The Damköhler number is used to capture flame extinction behavior.

When the fuel spray is injected into a coflow environment, the residence time of fuel droplets depends on the coflow air velocity, injector location, and thickness of the

evaporation porous medium. In this study, a characteristic residence time for the fuel spray upstream and inside evaporation porous medium (t_{res}) can be calculated as follows:

$$t_{res} = \frac{d_{ip} + a \cdot t_p}{u} \quad (5.3a)$$

where,

- d_{ip} - Distance between injector and porous medium
- a - Porous medium thickness correction factor
- t_p - Porous medium thickness
- u - Axial gas velocity

Note that one unit length of porous medium provides more residence time than one unit length of open space. Resistance offered by the porous medium could be calculated using Hydraulic Radius Model (Kaviany, 1995). This model assumes the presence of imaginary hydraulic tubes in the porous medium. These hydraulic tubes are responsible for the randomness in the porous medium structure, since they do not generally follow a straight path. The resistance offered by the porous medium depends on the length of hydraulic tubes (L_H) in the medium.

Tortuosity (τ) is defined as the ratio of the thickness of the porous medium and the length of longest hydraulic tube in the porous medium, as follows:

$$\tau = \frac{t_p}{L_H} \quad (5.3b)$$

Typical tortuosity values are presented in Kaviany (1995). In the present study, a tortuosity of 0.3, typically corresponding to packed beds, was chosen. For a porous medium of thickness 2.54 cm, the length of longest hydraulic tube was calculated to be 8.54 cm. The porous medium thickness correction factor, a in Equation 3.4a, was calculated to be 3.4. Note that for porous medium with high porosity ($\epsilon > 0.4$), the effect of tortuosity could also be neglected.

Figure 5.5 presents the effect of preheating residence time on the extinction equivalence ratio. The figure indicates that increasing the preheating residence time decreased the extinction equivalence ratio. A large preheating residence time denotes more time for spray evaporation and mixing, and hence, leads to interior combustion. If the residence time is small, evaporation and mixing are not complete, and a surface combustion mode is favored.

A characteristic chemical time (t_{chem}) for the combustion of kerosene spray can be calculated as follows:

$$t_{\text{chem}} = \frac{\delta}{S_L} \quad (5.4)$$

where

δ - Laminar flame thickness

S_L - Laminar flame speed of kerosene with air at stoichiometric conditions

In Equation 5.4, the laminar flame thickness and flame speed of kerosene with air at stoichiometric conditions were used (Annamalai and Puri, 2006). In the present study, the equivalence ratio employed ranged from 0.9 to 0.2. Hence, the flame thickness and speed were extrapolated to lean conditions and employed in the above expression.

Using the characteristic residence and chemical time scales, a Damköhler number (Da) can be calculated as follows:

$$Da = \frac{t_{res}}{t_{chem}} \quad (5.5)$$

Figure 5.6 presents the effect of Damköhler number on extinction equivalence ratio for different injector locations. The operation regimes of interior and surface combustion modes are also marked in the figure. The specific mode of combustion is determined by the completeness of vaporization and the quality of reactant mixture in combustion porous medium. Availability of a flammable mixture in CPM favors interior combustion. If a flammable mixture is not prepared until the exit surface of

EPM and CPM, surface combustion is most likely to occur. Since the air flowrate was held constant, the average gas velocity through the porous medium was also constant. A decrease in fuel flowrate reduced the flame speed. At some fuel flowrate, the local gas velocity exceeded the flame speed, and blew out the flame.

The figure shows that a nominal Damköhler number of 5.0 was required to initiate the interior combustion mode. As Da was increased, the extinction equivalence ratio decreased. At a given Da , interior flames could be stabilized over a range of equivalence ratios. For instance, at a Da of 6.0, interior flames were stabilized over an equivalence ratio range of 0.2 to 0.45. A large Damköhler number denotes higher preheating spray residence time; if the residence time is higher, as mentioned earlier, the fuel spray vaporizes more completely and mixes better with air. Also since this is in the fuel lean regime, more fuel vapors tend to move the mixture towards an equivalence ratio of unity, and thus increases the reaction rate. Hence, a stable interior combustion mode is established under these conditions.

Our results show that both surface and interior combustion modes could exist in porous media over a range of Damköhler numbers. The surface combustion mode is similar to the operation of flat flame burner but with a thicker porous disk functioning as evaporator, mixer, and flame holder. In the interior combustion mode, combustion takes place inside the porous medium, and hence, heat transferred to the solid portion is more efficient. This, in turn, improves upstream heat transfer to EPM and fuel spray.

5.5 Temperature Characteristics near Extinction

The porous medium interior temperature and surface temperature uniformity measurements were taken to understand the upstream heat feedback rate and detection of flame extinction. Interior temperature measurements were taken using a thermocouple at nine locations in CPM prior to extinction. The surface temperature uniformity measurements were taken using infrared camera (Section 2.4.2).

5.5.1 Porous Medium Interior Temperature

Figure 5.7 shows the locations of thermocouple measurements in combustion porous medium. Six K-type thermocouples were embedded on two opposite walls of the porous medium and three thermocouples were installed inside the porous medium along the centerline at uniform intervals. Figure 5.8 presents the measured centerline temperature profile in the evaporation and combustion porous media during interior combustion. The coflow air velocity was held constant at 126 cm/s. The figure indicates that the axial temperature in the evaporation porous medium increased only slightly. On the other hand, at the interface between the evaporation and combustion porous media, the temperature increased rapidly. This indicates that the combustion occurred at the interface between the evaporation and combustion porous media. After the flame zone, the axial temperature profiles exhibited a decreasing trend.

The axial distribution of the porous medium temperature during flame extinction is presented in Figure 5.9. Coflow air velocity was held constant at 126 cm/s and the distance between injector and evaporation porous medium was 6 cm. The figure

presents the axial distribution of porous medium temperature at different equivalence ratios prior to flame extinction. It shows that the peak temperature attained in the porous medium at each equivalence ratio decreased with decreasing equivalence ratio. In this case, stable interior combustion was observed until an equivalence ratio of 0.35.

Figures 5.10 to 5.12 present porous medium interior temperature at two locations: 18.4 cm from injector (I2, See Fig. 5.7) and 19 cm from injector (I3, See Fig. 5.7) prior to extinction for different injector locations and coflow air velocities. The figures show that the temperature decreased, as the equivalence ratio was reduced i.e., lean extinction was approached. At interior locations, the flames were stable at as low as a temperature of 1000 K. The temperature at I3 was higher than that at I2 at most equivalence ratios. This means that the flame zone was located near the interface between evaporation and combustion porous media.

Since surface temperature is easier to measure than the interior temperature, it is useful to relate flame extinction to surface temperature measurements. Temperature measurements at the centerline near the porous medium exit surface (I1, See Fig. 5.7) were also taken for this purpose. Figure 5.13 shows such results at different equivalence ratios prior to extinction for a Damköhler number of 5.0. The figure shows that the surface temperature decreased as the fuel flowrate was reduced i.e., the lean extinction was approached. All the flames were extinguished below a surface temperature of 900 K. Babb et al. (1999) experimentally measured an extinction

temperature of 1500 K for liquid heptane open diffusion flames (no porous medium was employed). In the present study, an extinction temperature of less than 900 K was recorded. This demonstrates that combustion in porous medium could be stabilized at much lower temperatures than that in open flames. Hence, the insertion of porous medium in the combustion zone of a spray flame widens the range of stable burner operation.

5.5.2 Adiabatic Flame Temperature

Adiabatic flame temperature calculation of pre-vaporized premixed kerosene-air combustion (with no porous medium) for equivalence ratios from 0.2 to 2.0 was performed using Olikara & Borman (1975) routine. Figure 5.14 presents the effect of equivalence ratio on adiabatic flame temperature. The adiabatic flame temperature showed a peak value of 2300 K at an equivalence ratio of 1.1 and decreased when the mixture was made fuel leaner or richer. At a very lean equivalence ratio of 0.2, the adiabatic flame temperature was 850 K. Also shown in the figure is the measured porous medium temperature at the flame zone near extinction conditions corresponding to a coflow air velocity of 126 cm/s. The distance between the porous medium and the injector was 6 cm.

Although the porous medium housing was insulated, there were some radiative losses occurred from the walls. Recall that the experimental data reported in Figure 5.14 correspond to the porous medium temperature. Since a thermocouple was used to make the measurements, the measured temperature was an average between the gas

phase and solid phase temperatures. The measured data was about 200 K lower than the adiabatic flame temperature at the equivalence ratio of 0.65. This difference could be attributed to the heat loss from chamber walls and the measurement nature of flame temperature in the porous media. Also, note that the adiabatic flame calculations were performed by assuming $C_{12}H_{23}$ for kerosene fuel. However, kerosene is a multi-component fuel and this simplification could also contribute to the differences between measurements and calculations.

5.5.3 Comparison with Literature

Khanna et al. (1994) measured the exit plane temperatures of methane-air combustion in porous medium. They reported a temperature of 1250 K for an equivalence of 0.6. In the present study with kerosene spray flames in porous medium, the surface temperature measured was 1241 K. A comparison of our results with that of Khanna et al. (1994) reveals that our data are in good agreement with literature.

Sathe et al. (1990) numerically studied the heat transfer and combustion of methane-air in porous radiant burners. Their results showed that stable flames could be established at the center of the upstream and downstream surfaces. Barra et al. (2003) numerically studied the effect of material properties on the stabilization of methane-air combustion in a two-section burner. They concluded that the flame was stabilized at the interface between the two sections. In the present study, it was observed that the flame was located near the interface between evaporation and combustion porous

media (Figs. 5.8 and 5.9). Hence, our results are in good agreement with previously published data.

5.5.4 Surface Temperature Uniformity

The porous medium surface temperature uniformity denotes spacious homogeneity of fuel air-mixture prior to flame zone. Figures 5.15 to 5.17 present porous medium surface temperature uniformity during interior combustion spray flames at four different equivalence ratios prior to extinction for a Damköhler number of 5.0. The figures show that the peak temperature decreased as the equivalence ratio was decreased, as also observed with thermocouple measurements. The results further show that the surface temperature was uniform within $\pm 50^\circ\text{C}$. Note that the figure shows only the difference between the maximum and minimum temperatures since the emissivity of the porous medium was not known accurately. Semi-quantitative results could, however, be obtained by combining the thermocouple and infrared images.

5.6 Flame Radiation

Radiation from the porous medium during combustion was measured by using a radiometer. The radiometer was located directly 35 cm above the exit surface of combustion porous medium. A quartz window (spectral transmission of 0.2 to 4.5 microns) was used to cover the sensing surface, and hence, only the radiant energy

output over a wavelength range of 0.2 to 4.5 microns from the porous medium surface was measured.

Figure 5.18 presents the radiation from the combustion porous medium at different injector locations during the interior combustion mode. While the coflow air flowrate was held constant at 90 l/min, the fuel flowrate was decreased. The figure shows that the flame radiation decreased as the extinction was approached. As the fuel flowrate was reduced, the heat input was decreased, and hence, the radiant heat energy from the flames was also decreased. Decreasing porous medium surface temperature profiles (Fig. 5.9) during flame extinction also support the decreasing trend of flame radiation. Although there were some non-systematic variations in the radiant energy output with the location of injector observed, these were within the experimental uncertainties (mean value $\pm 100 \text{ W/m}^2$).

5.7 Pollutant Emissions

Emission indices of carbon monoxide (CO) and nitric oxide (NO), and exhaust concentration levels of carbon dioxide (CO₂) and oxygen (O₂) of spray flames stabilized on the downstream exit surface of combustion porous medium were measured. A Pyrex® glass funnel was placed directly 1 cm above the exit plane of combustion test section to collect the combustion products. A quartz probe was inserted at the exit of the glass funnel, and the sample was drawn (see Section 2.4.6 for details).

5.7.1 Equilibrium Composition

The equilibrium composition of kerosene–air combustion products was calculated using Olikara and Borman (1975) routine. This code solves for the composition of 12 species in C-H-O-N combustion system using seven equilibrium reactions and four atom-conservation equations. Kerosene was assumed to be a single-component fuel of $C_{12}H_{23}$. Figure 5.19 presents the mole fractions of carbon monoxide (CO), nitric oxide (NO), oxygen (O_2), water vapor (H_2O), and carbon dioxide (CO_2) for equivalence ratios (ϕ) from 0.2 to 2.0. Note that there was no porous medium considered for this analysis. As the equivalence ratio was increased from 0.2, mole fraction of CO increased only slowly until $\phi = 1.0$. However, it increased significantly after $\phi = 1.0$, as more fuel was available than the required amount (fuel-rich combustion). The mole fraction of O_2 decreased as equivalence ratio was increased, and became negligible beyond $\phi = 1.0$, due to burning in fuel rich condition.

The mole fractions of CO_2 and H_2O increased as the equivalence ratio was increased, both attained peak values near $\phi = 1.0$ (due to theoretical complete combustion), and decreased thereafter. The mole fraction of NO also showed a trend similar to that of CO_2 and H_2O . The production of thermal NO primarily depends on flame temperature, and hence, peak values of NO were obtained near stoichiometric condition (high flame temperature regime).

5.7.2 Emission Indices of Carbon Monoxide (EI_{CO})

The exit concentration levels of CO and CO₂ were measured downstream of the combustion test section containing combustion porous medium. From the measured data, global emission index of CO was calculated using Equation 2.1 (Turns, 2000). Figure 5.20 presents global emission indices for four equivalence ratios prior to extinction, and two locations of injector. CO emission indices ranged from 13 to 100 g/kg of fuel. Equilibrium calculations showed a CO emission index of 4.77 g/kg of fuel at an equivalence ratio of 0.7. Note that the above equilibrium calculations assume pre-vaporized, pre-mixed combustion of kerosene vapors with air. Also, no porous medium was employed. As the equivalence ratio was decreased or flame extinction was approached, EI_{CO} showed a somewhat non-systematic variation. This variation was, however, within the experimental uncertainty of ± 12 g/kg of fuel. The injector located farther from the leading edge of evaporation porous medium produced lower EI_{CO} . Such emission index measurements are independent of any dilution by air, and widely used in evaluating the efficiency of combustion systems.

Another common way of representing pollutant emissions is by correcting it with a fixed amount of oxygen content, according to the following equation:

$$C_r = C_m \frac{r}{m} \quad (5.6)$$

where,

C_r - Measured concentration level in a dry gas sample containing 'm' amount of oxygen

C_m - Corrected concentration level in a dry gas sample containing a reference amount 'r' of oxygen, usually 3%

Figure 5.21 presents emission levels of CO in parts per million (ppm) corrected to 3% oxygen content in product gases for two locations of injector and four equivalence ratios prior to extinction. CO emission level varied from 40 to 160 ppm. The figure indicates that CO emission increased as extinction was approached. When the injector was located farther, due to larger droplet residence time, more complete combustion occurred resulting in lower CO. On the other hand, as the injector was moved closer to the evaporation porous medium, residence time at both upstream and in porous medium region decreased, and the degree of combustion decreased, and hence, increased the CO emission level.

In a methane-fueled porous medium burner, Khanna et al. (1994) measured the CO emissions as 5 - 120 ppm for equivalence ratios of 0.6 to 0.87. In the present study, depending upon the location of injector, CO emissions were obtained from 40 to 160 ppm, corrected to 3% oxygen. Note that the Khanna et al. (1994) used gaseous methane as fuel. However, a comparison of our results with Khanna et al. (1994) reveals that the results are in good agreement with literature.

5.7.3 Emission Indices of Nitric Oxide (EI_{NO})

Emission indices of NO were calculated using the measured global emission data downstream of the combustion test section and Equation 2.1 (Turns, 2000). Figure 5.22 presents EI_{NO} for four equivalence ratios prior to extinction and at two locations of injector. Results show that EI_{NO} were less than 2.5 g/kg of fuel. EI_{NO} did not vary significantly with the location of injector or the equivalence ratio. This demonstrates the benefits of porous medium in making NO emission somewhat insensitive to operating parameters. This is due to uniformity as well as low dependence of reaction zone temperature to operational parameters due to the large thermal mass of porous medium and its role in evenly distributing fuel. Measurement uncertainties calculated using Student's t-distribution at 95% confidence level are ± 0.46 g/kg of fuel. Figure 5.23 presents global emission of NO corrected to 3% oxygen content in combustion products for similar conditions as that of Figure 5.22. NO emission results were less than 6.5 ppm.

In combustion systems, following are the three major mechanisms that describe the formation nitric oxides:

- (i) Thermal or Zeldovich mechanism
- (ii) Fenimore or prompt mechanism
- (iii) N_2O intermediate mechanism

Thermal or Zeldovich mechanism describes NO formation in high temperature combustion system over a wide range of equivalence ratios. Fenimore or prompt

mechanism describes NO formation in fuel-rich combustion systems. The N_2O intermediate mechanism explains NO formation in fuel-lean, low-temperature combustion systems. In the present study, porous medium interior temperature (close to flame temperature) increased with equivalence ratio. According to the Zeldovich mechanism, an increase in flame temperature also increases the NO concentration level. The Zeldovich mechanism does not only depend on high temperature, but also on the amount of time spent in the high temperature region.

The peak temperature attained at the leading edge of combustion porous medium due to the burning of spray flames decreased downstream immediately (See Figure 5.9), due to conduction and radiation heat feedback upstream. This means that the residence time in the high temperature region was small, and hence, the formation of NO was reduced considerably in combustion in porous medium. Since lean combustion was established in this study, the N_2O intermediate mechanism could have also contributed to some level of NO formation.

Kaplan and Hall (1995) measured NO_x emissions from n-heptane fueled porous media radiant burner. Their results indicated that the NO_x concentration varied from 15 to 20 ppm, corrected for 3% oxygen. In the present study with kerosene combustion, NO concentration had a maximum value of 6.5 ppm, corrected to 3% oxygen. Although there is a difference in fuel, comparison of our results with Kaplan and Hall (1995) shows that the results are in excellent qualitative agreement. Similar

data were also obtained by Tseng and Howell (1998) for the combustion of n-heptane in porous media.

Puri and Gollahalli (1989) measured the transverse NO concentration profiles of kerosene spray flames without using a porous medium. Measurements were taken at different axial locations for a fuel flowrate of 0.35 g/s and a secondary air velocity of 0.4 m/s. At the centerline of the spray, the authors reported a NO concentration of 22 ppm (corrected to 3% oxygen). In the present study, the NO concentration (corrected to 3% oxygen) varied only from 2 to 7 ppm over an equivalence ratio range of 0.4 to 0.7. This demonstrates that the combustion in porous medium reduces the NO emission from spray flames considerably. This is due to the enthalpy augmentation of reactants via heat feedback and the shorter residence time in the flame zone.

5.7.4 Exit Concentration Levels of Carbon Dioxide (CO₂)

Measurements of concentration levels of CO₂ were made downstream of the combustion test section. CO₂ is the result of complete combustion, and hence, higher values of CO₂ concentration indicate the complete use of energy contained in the fuel. Figure 5.24 shows global concentration levels of CO₂ for two injector locations at four equivalence ratios prior to extinction. CO₂ concentration had a maximum value of 3.1%. With a decrease in equivalence ratio in fuel-lean region, CO₂ concentration also decreased. Concentration levels of CO₂ were higher when the injector was located farther from the leading edge of the evaporation porous medium. As mentioned earlier, locating injector farther away increases residence time, and hence,

promotes more complete combustion, resulting in increased values of CO₂ concentration.

5.7.5 Exit Concentration Levels of Oxygen (O₂)

The oxygen (O₂) concentration in combustion products was also measured. Figure 5.25 presents the global concentration levels of O₂ for two injector locations and at four equivalence ratios prior to extinction. The results showed that the O₂ concentration had a lowest value of 16.3%. The oxygen concentration increased as equivalence ratio was decreased. Here, the air flowrate was held constant, and fuel flowrate was reduced to attain flame extinction. Hence, as the extinction was approached, the O₂ concentration increased. With the injector located farther from the leading edge of the evaporation porous medium, the O₂ concentration levels measured were lower than that with injectors located closer to the porous medium.

5.8 Chapter Summary

This chapter presented an experimental study of spray flames stabilized both inside and on the downstream exit surface of the combustion porous medium. Lean extinction limits of interior and surface combustion flames in porous media were determined. A general Damköhler number approach was developed to understand flame extinction in porous media. Interior temperature and downstream exit surface temperature of the combustion porous medium was measured. Axial temperature distribution in evaporation porous medium due to combustion heat feedback was

reported. This chapter also presented radiative heat release from combustion porous medium downstream surface, and emission indices of CO and NO.

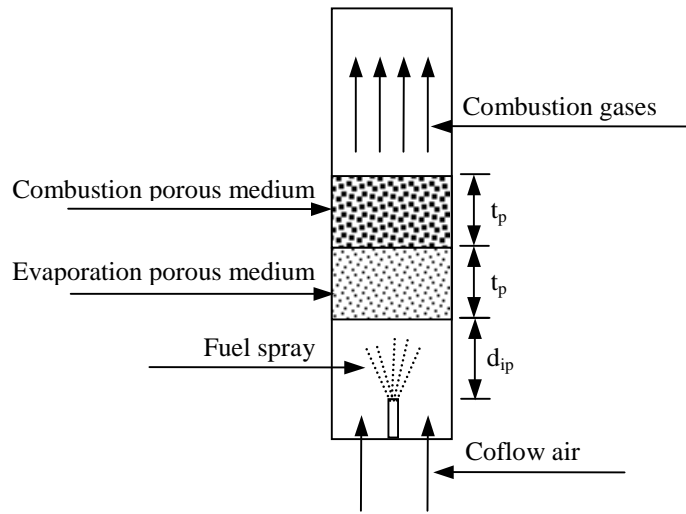


Figure 5.1 Experimental arrangement of evaporation and combustion porous media



Figure 5.2 Photograph of typical interior combustion flame in porous media



Figure 5.3 Photograph of a typical surface combustion flame in porous media

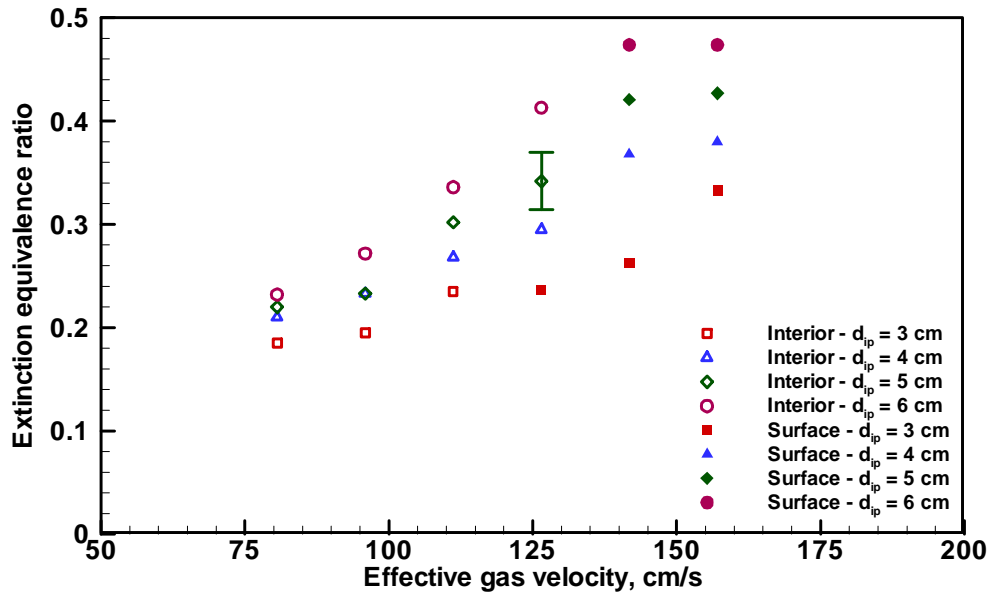


Figure 5.4 Effect of effective gas velocity on extinction equivalence ratio

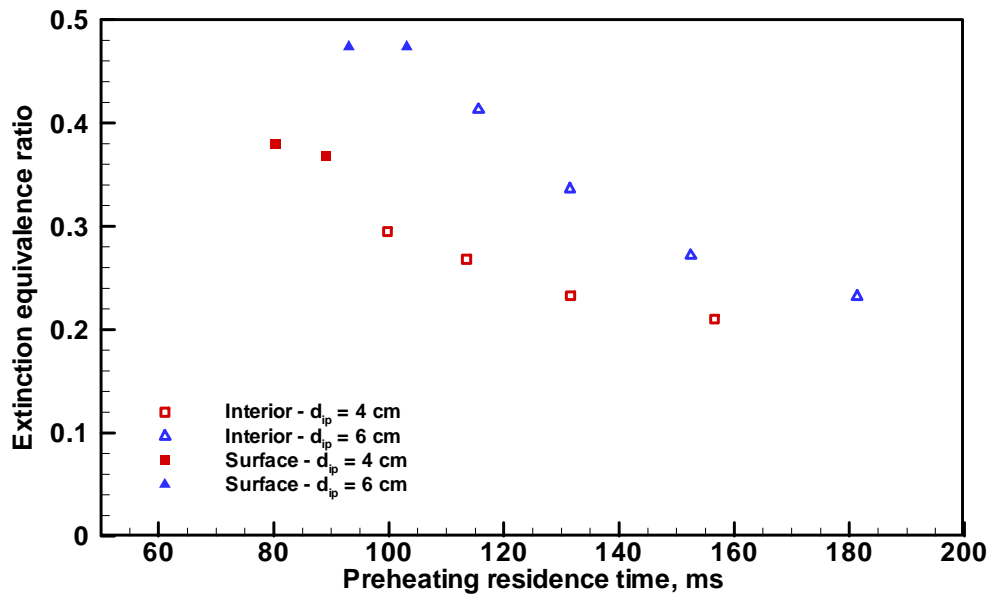


Figure 5.5 Effect of preheating residence time on extinction equivalence ratio

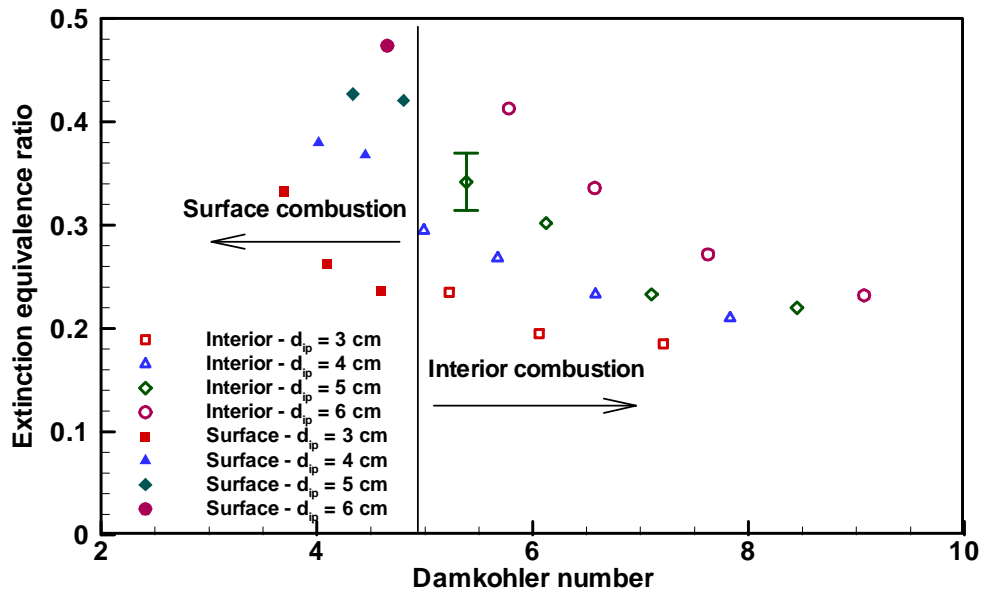


Figure 5.6 Effect of Damköhler number on extinction equivalence ratio

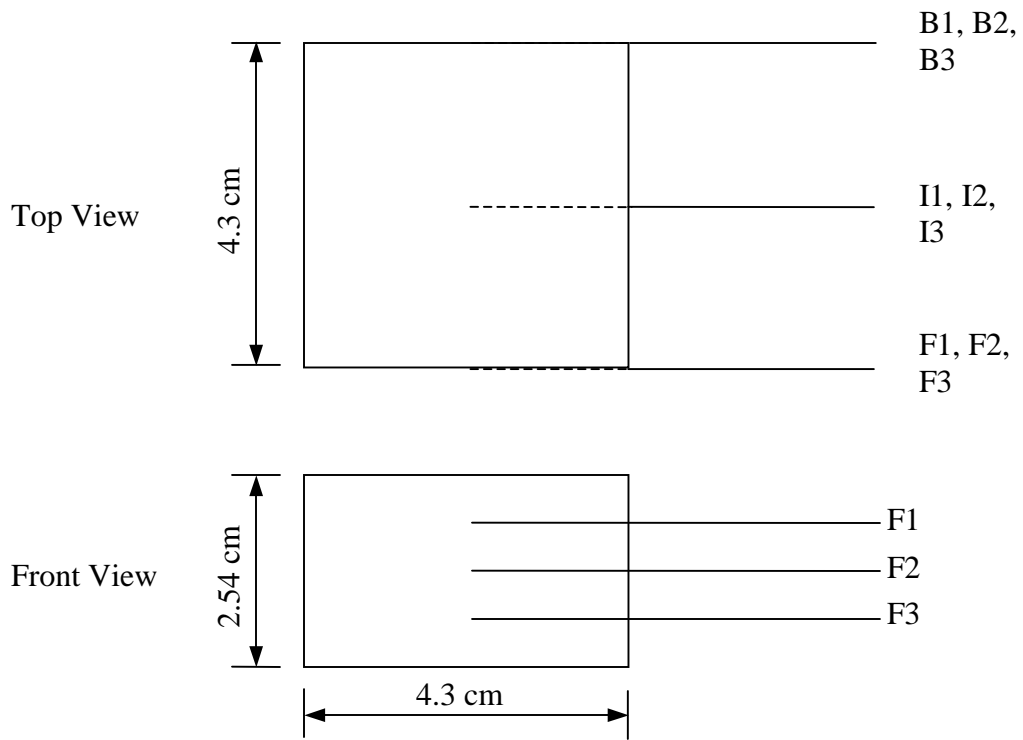


Figure 5.7 Locations of temperature measurement in combustion porous media

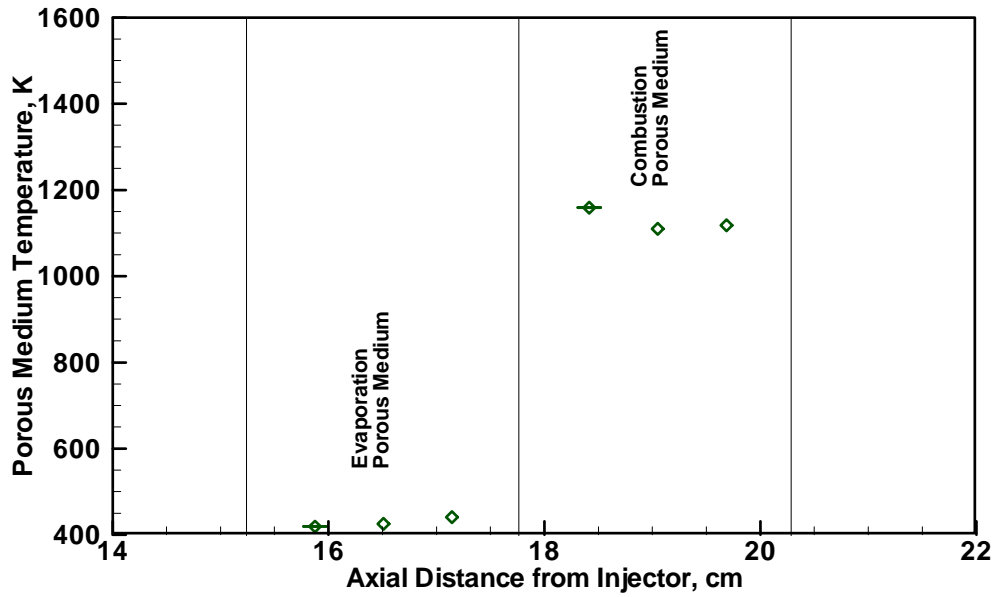


Figure 5.8 Axial variation of porous medium temperature in evaporation and combustion porous media ($d_{ip} = 6$ cm; Coflow air velocity = 126 cm/s; Equivalence ratio = 0.35; Damköhler number = 5.38)

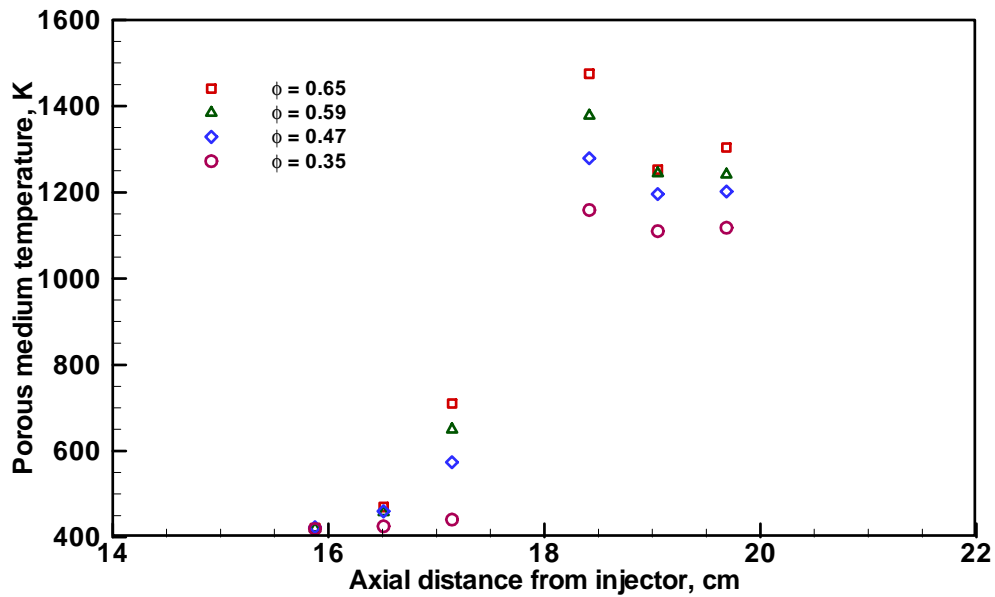


Figure 5.9 Effect of equivalence ratio on the axial variation of porous medium temperature in evaporation and combustion porous media during flame extinction ($d_{ip} = 6$ cm; Coflow air velocity = 126 cm/s)

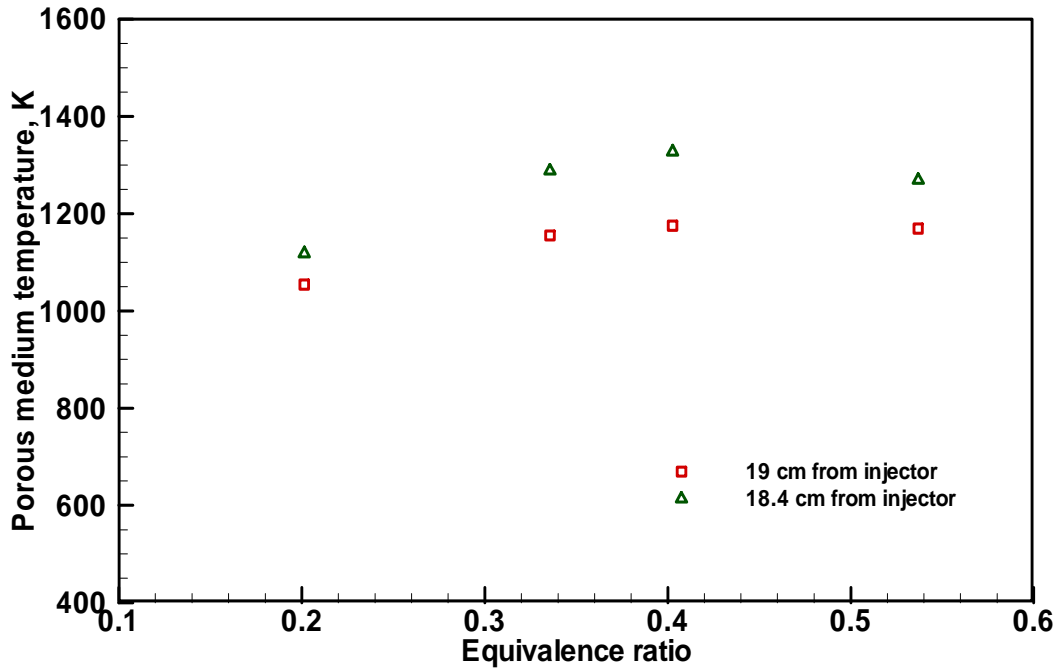


Figure 5.10 Temperature in combustion porous medium prior to flame extinction ($d_{ip} = 4$ cm; Coflow air velocity = 111 cm/s)

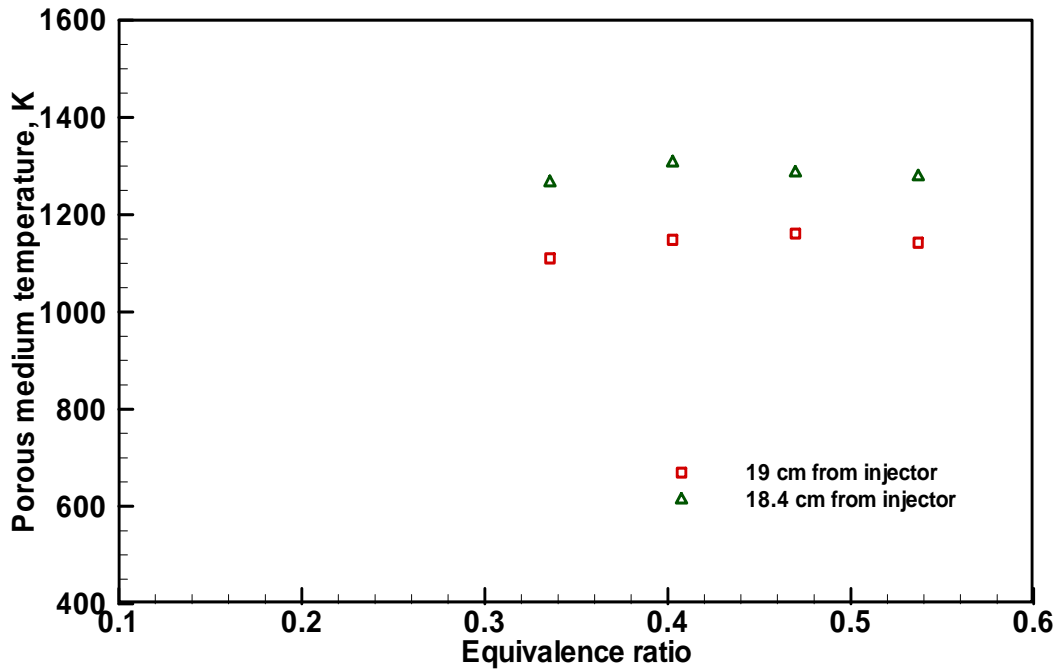


Figure 5.11 Temperature in combustion porous medium prior to flame extinction ($d_{ip} = 5$ cm; Coflow air velocity = 126 cm/s)

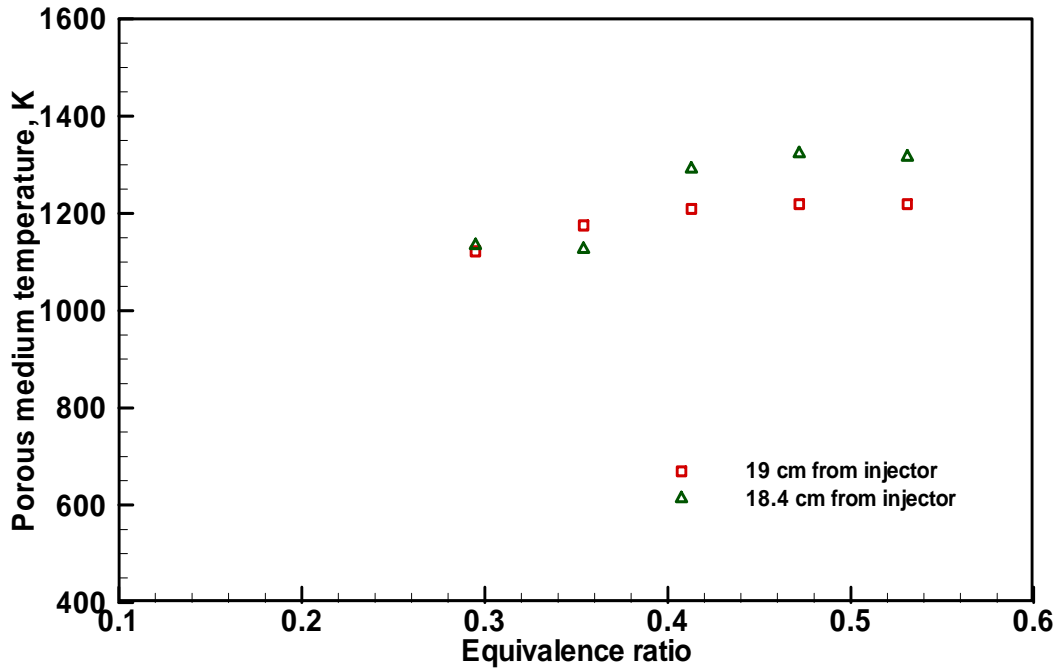


Figure 5.12 Temperature in combustion porous medium prior to flame extinction ($d_{ip} = 5$ cm; Coflow air velocity = 111 cm/s)

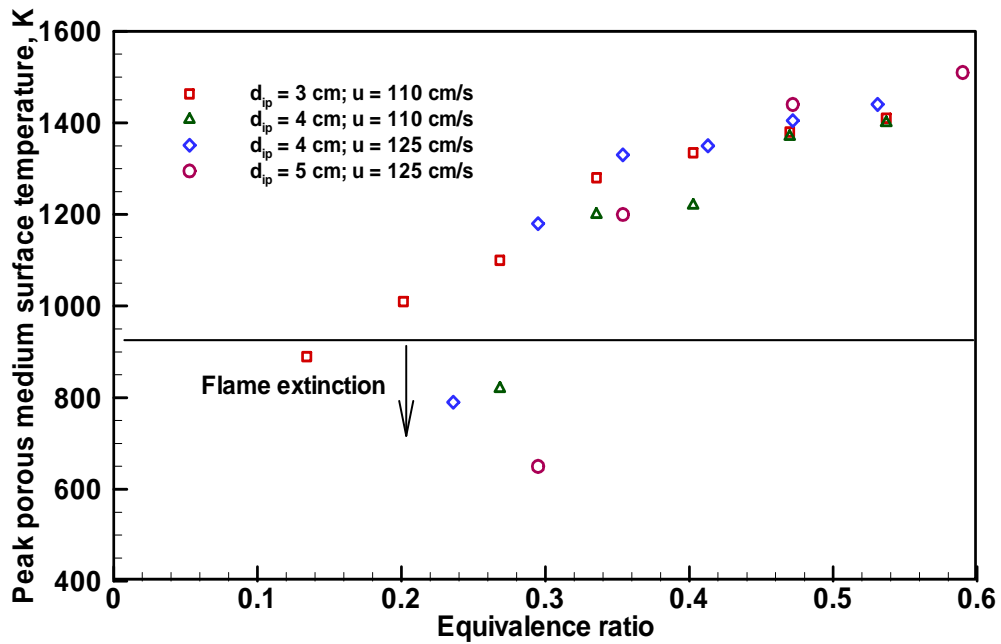


Figure 5.13 Decay of porous medium surface temperature of interior flames prior to extinction ($Da = 5.0$)

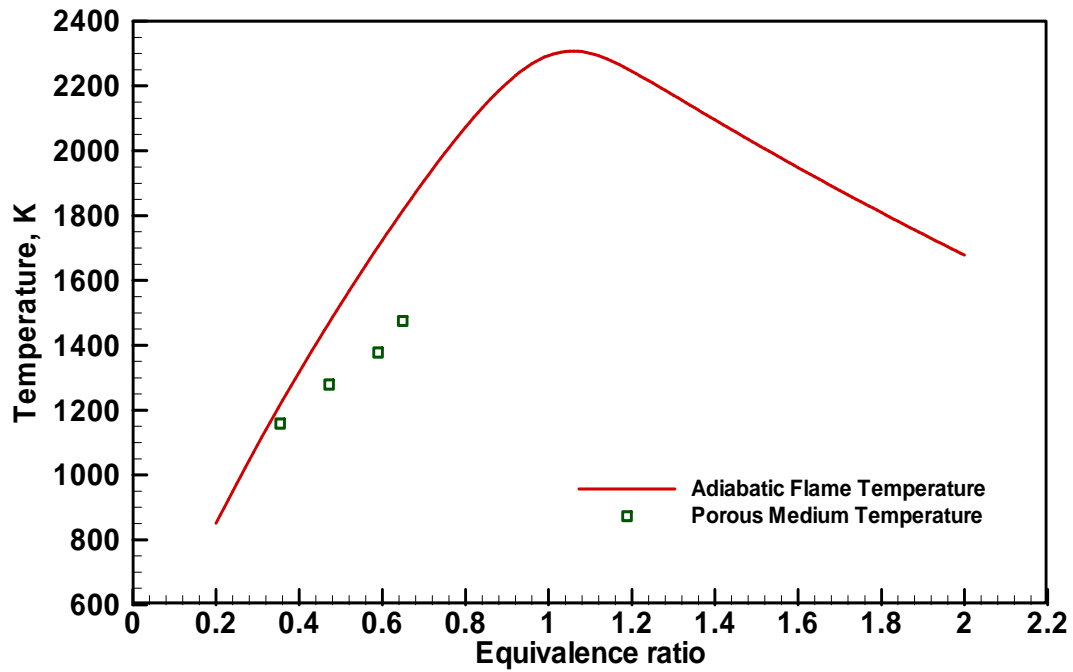


Figure 5.14 Effect of equivalence ratio on adiabatic flame temperature of pre-vaporized, premixed combustion kerosene-air with no porous medium. Also shown is the porous medium temperature corresponding to Coflow air velocity 126 cm/s, $d_{ip} = 6$ cm

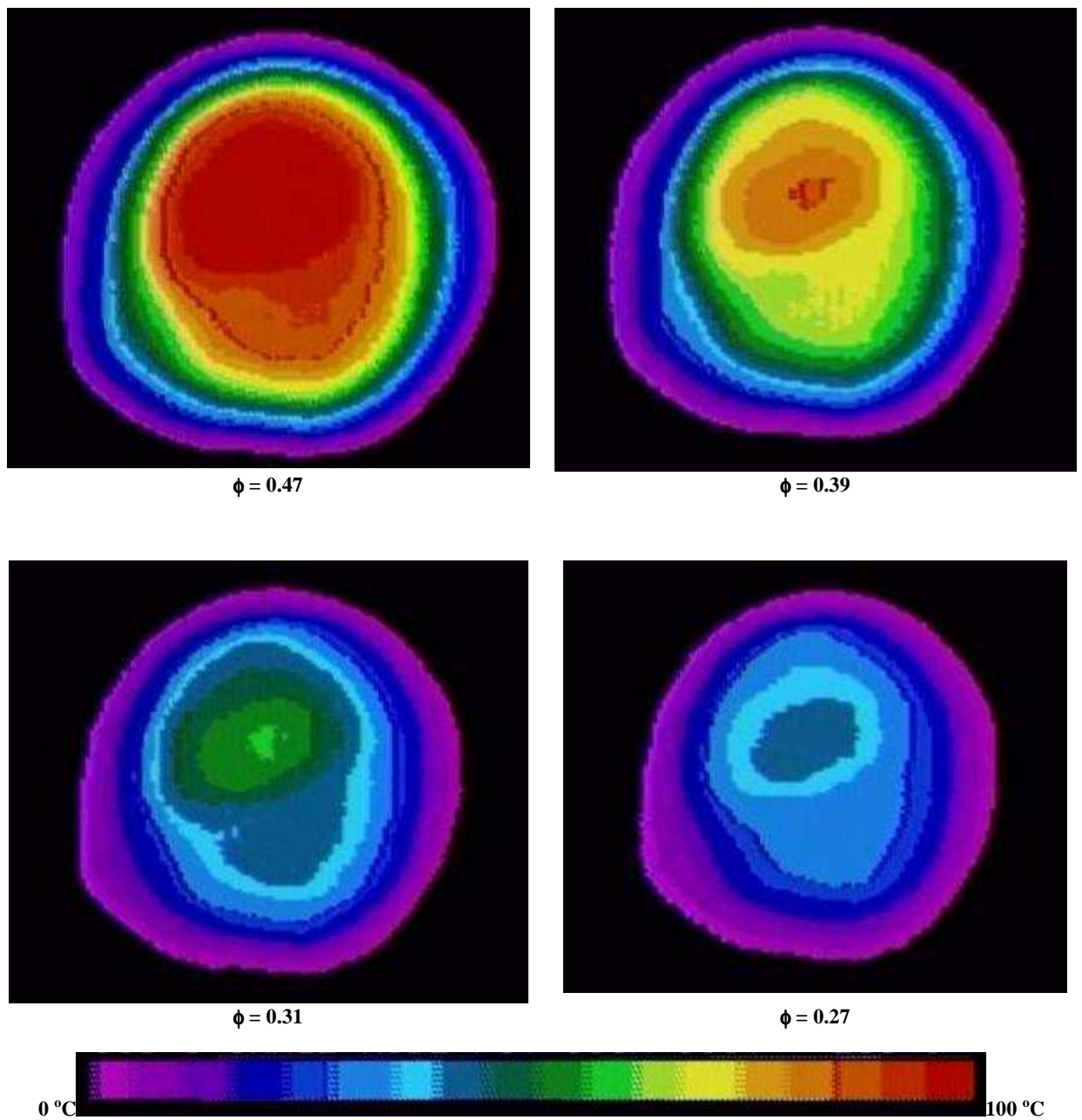


Figure 5.15 Contours of difference between maximum and minimum temperatures on the porous medium surface during interior combustion visualized by infrared imaging (Conditions: $d_{ip} = 4$ cm; Coflow air velocity = 96 cm/s)

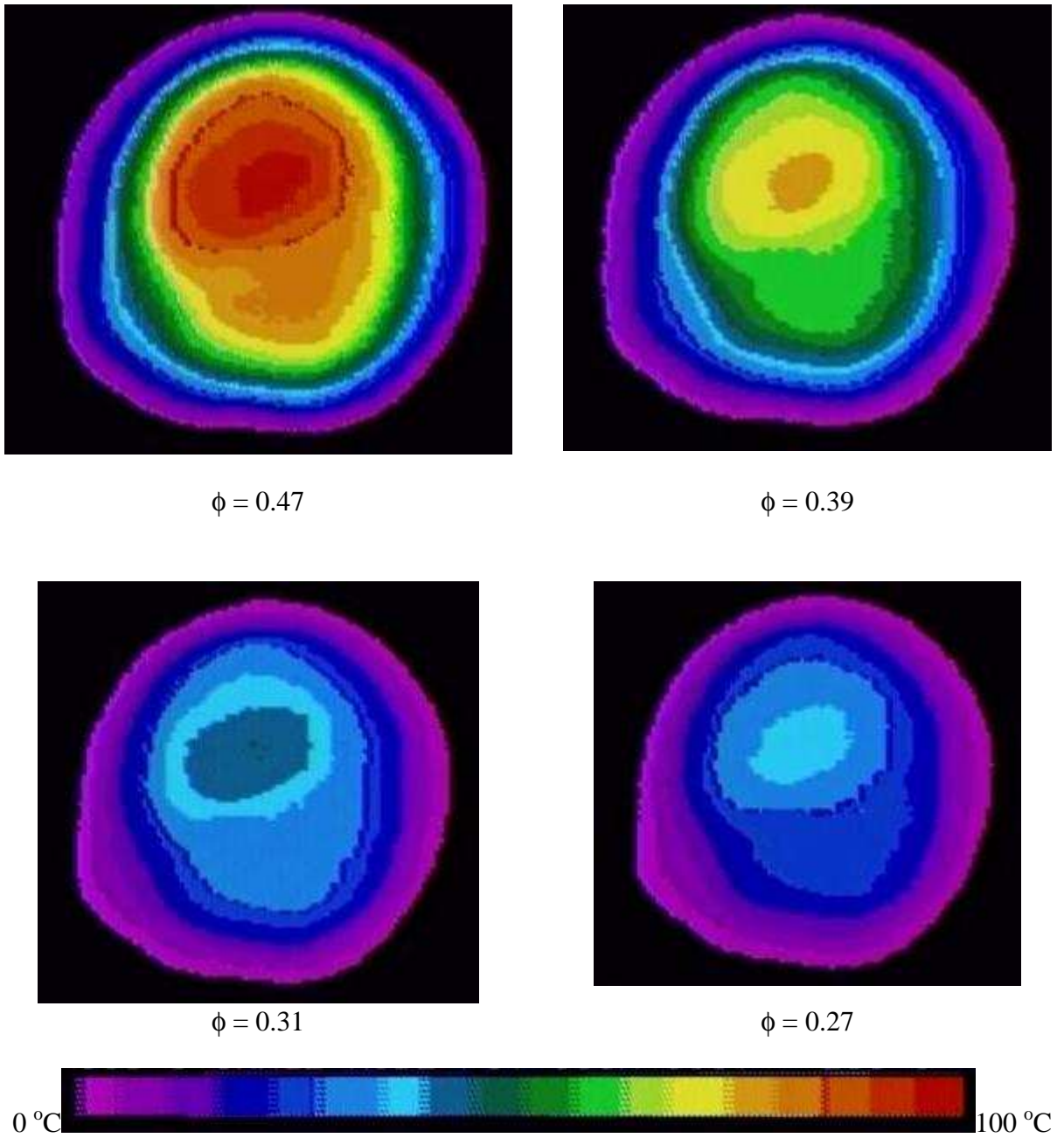


Figure 5.16 Contours of difference between maximum and minimum temperatures on the porous medium surface during interior combustion visualized by infrared imaging (Conditions: $d_{ip} = 5$ cm; Coflow air velocity = 96 cm/s)

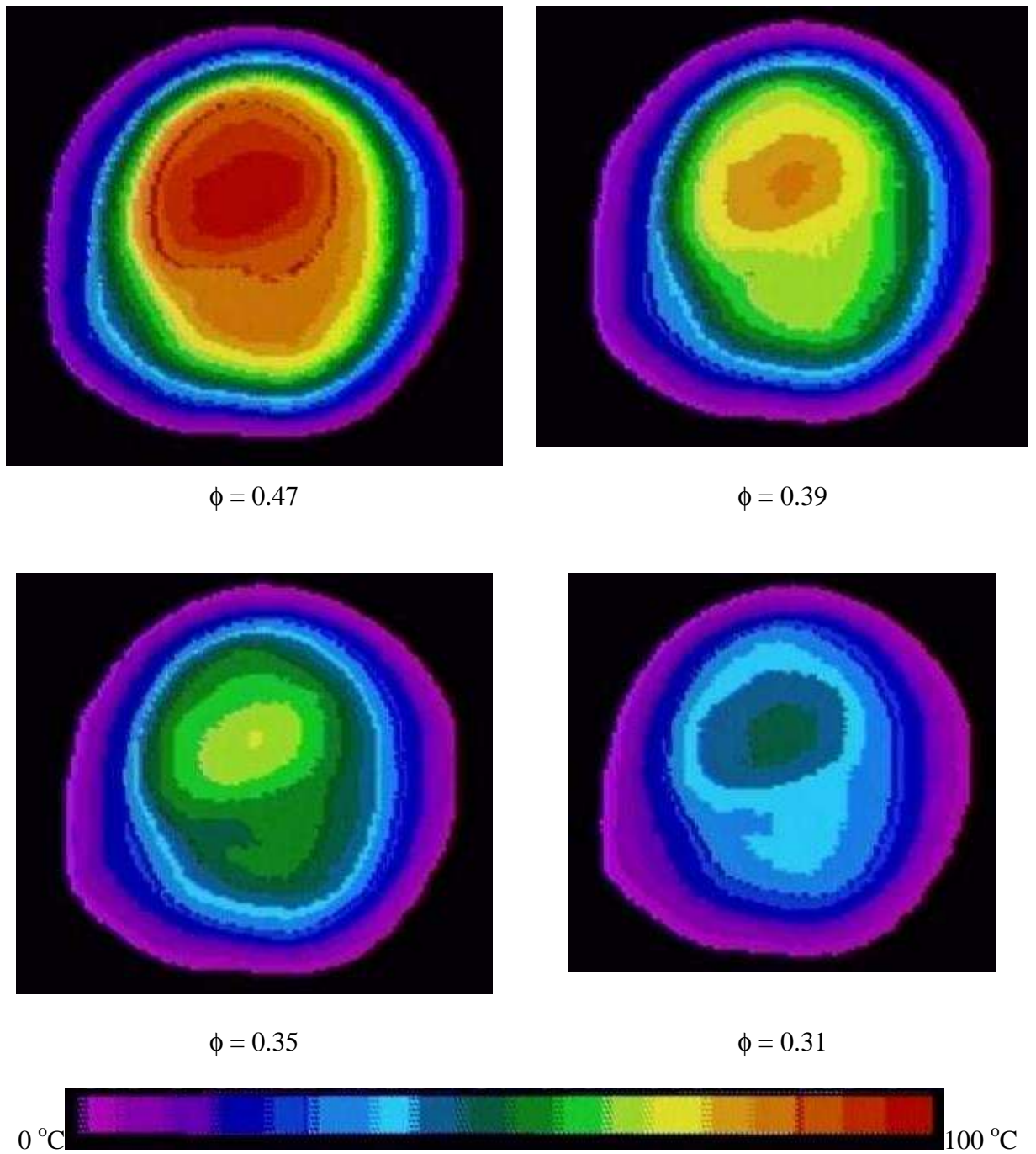


Figure 5.17 Contours of difference between maximum and minimum temperatures on the porous medium surface during interior combustion visualized by infrared imaging (Conditions: $d_{ip} = 6$ cm; Coflow air velocity = 96 cm/s)

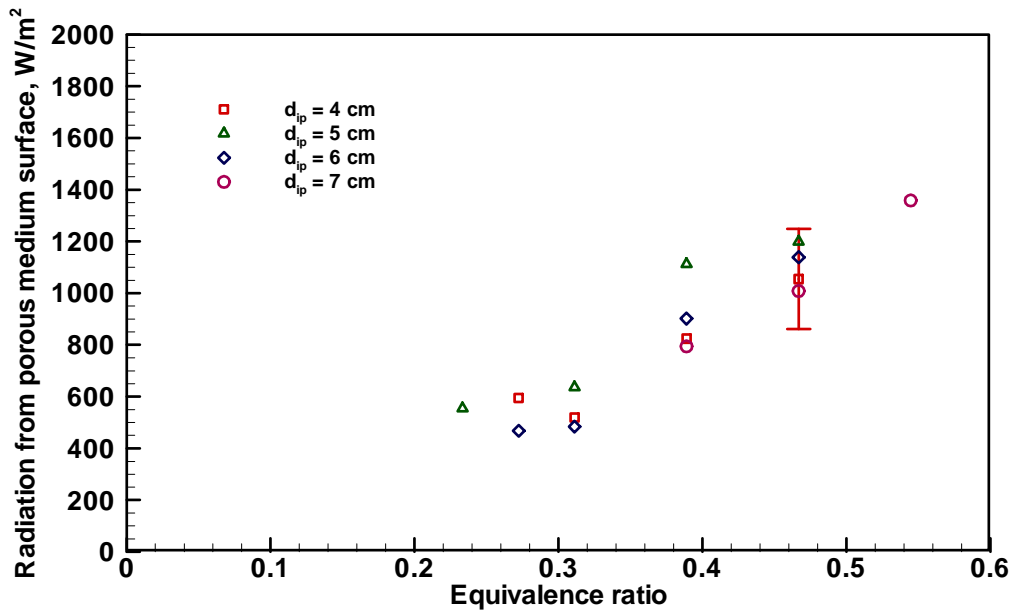


Figure 5.18 Radiation from porous medium surface during the extinction interior combustion (Coflow air velocity = 96 cm/s)

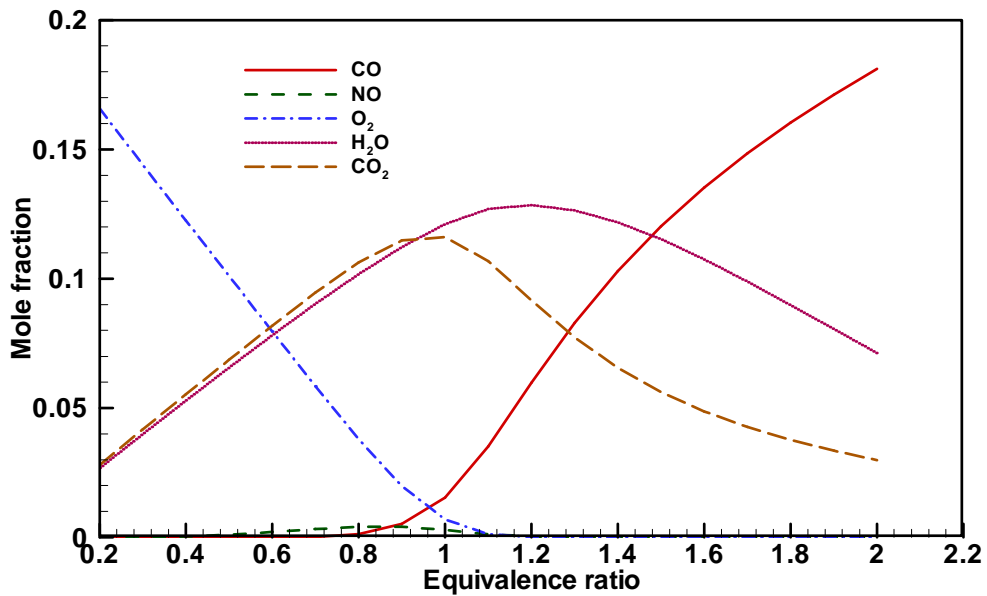


Figure 5.19 Equilibrium compositions of combustion products at different equivalence ratios for pre-vaporized premixed kerosene-air combustion (with no porous medium)

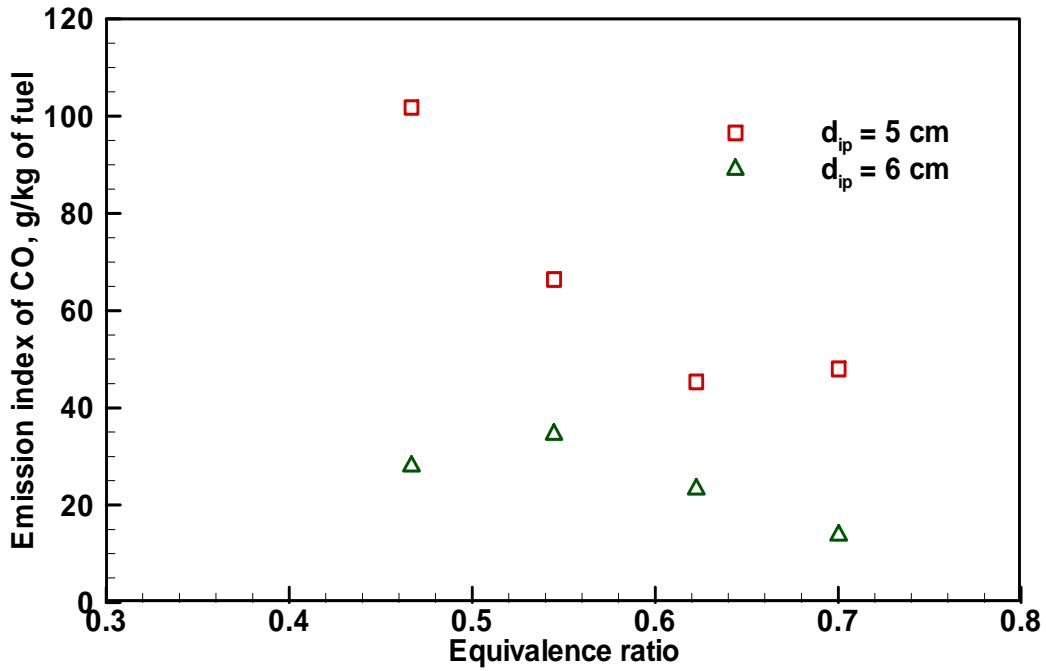


Figure 5.20 Measured emission indices of carbon monoxide (CO) at four equivalence ratios prior to extinction for two injector locations (Coflow air velocity = 96 cm/s)

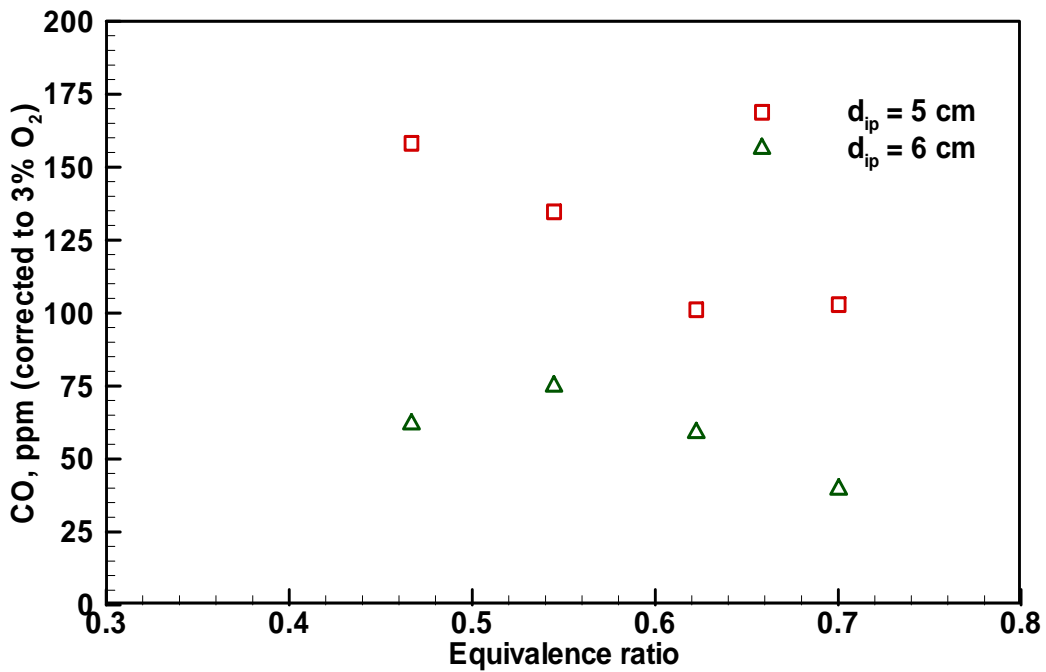


Figure 5.21 Measured emissions of CO (corrected to 3% oxygen) at four equivalence ratios prior to extinction for two injector locations (Coflow air velocity = 96 cm/s)

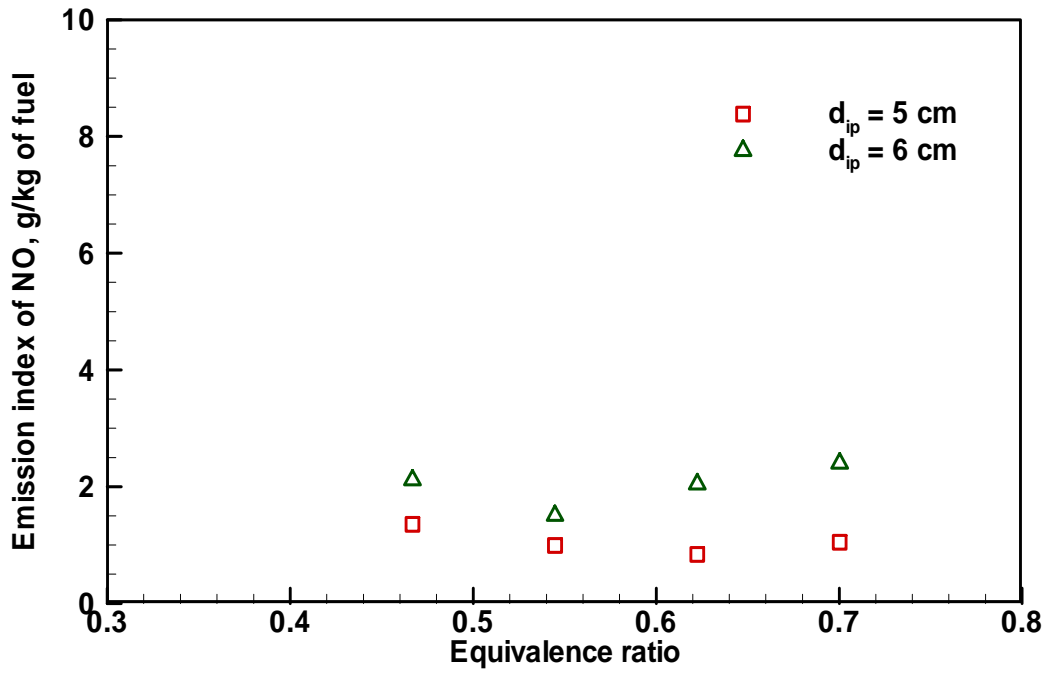


Figure 5.22 Measured emission indices of nitric oxide (NO) at four equivalence ratios prior to extinction for two injector locations (Coflow air velocity = 96 cm/s)

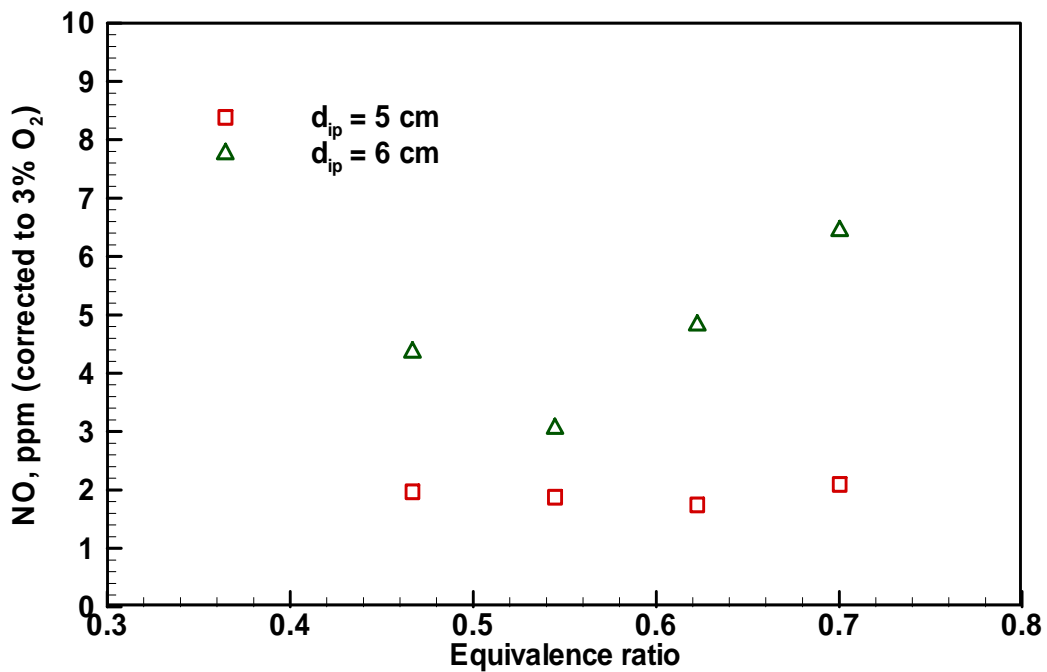


Figure 5.23 Measured emissions of NO (corrected to 3% oxygen) at four equivalence ratios prior to extinction for two injector locations (Coflow air velocity = 96 cm/s)

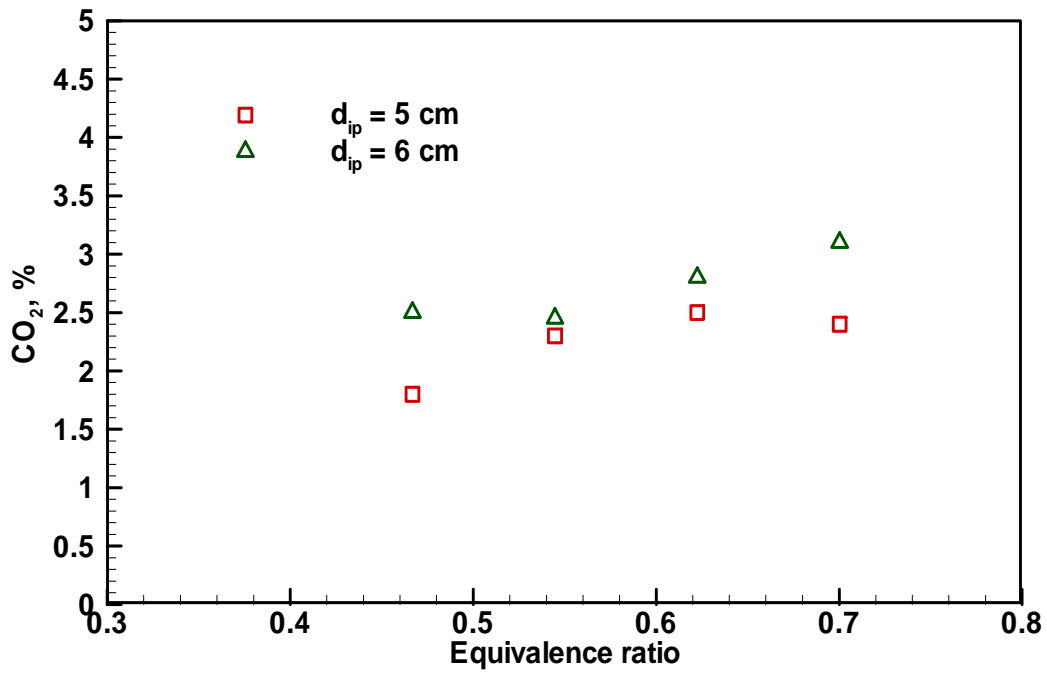


Figure 5.24 Measured exit concentration levels of carbon dioxide (CO₂) at four equivalence ratios prior to extinction for two injector locations
Coflow air velocity = 96 cm/s

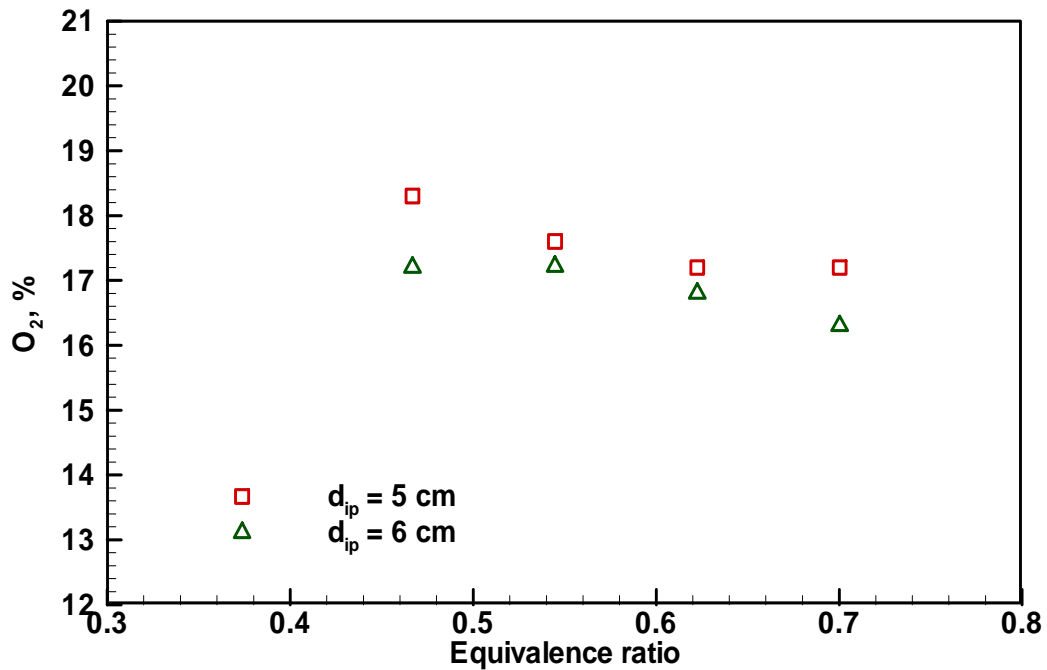


Figure 5.25 Measured exit concentration levels of oxygen O₂ at four equivalence ratios prior to extinction for two injector locations (Coflow air velocity = 96 cm/s)

Chapter 6

Overall Discussion, Conclusions and Recommendations

6.1 Overall Discussion

Burning of liquid fuels in the form of either individual droplets or spray critically depends on evaporation rate. The objective of this research was to understand evaporation enhancement and combustion of liquid fuel spray in porous media. First, combustion was decoupled, and heat feedback due to combustion in porous media was simulated by using a resistive heating mechanism. This allowed us to vary the heat feedback in a controlled manner. Next, combustion of fuel spray in porous media was studied and the interactions between evaporation and combustion were delineated. Appendix I presents a list of publications from this research. Following subsections present a summary of results and an overall discussion:

6.1.1 Porous Medium Characteristics

The presence of porous medium in a combustor causes additional pressure drop. This must be determined first before it can be used in combustion systems. Experimental measurements of pressure drop were taken at unheated coflow conditions (~ 294 K) and heated conditions (350, 400, and 450 K) with different porous media. Results showed that the pressure drop increased as the coflow air velocity was increased. The pressure drop also increased with linear pore density (number of pores per centimeter) and coflow air temperature. The measured pressure drop across the porous media was less than 1% of the operating pressure. For instance, in industrial burners,

additional pressure drop of less than 1% is reasonable (Lefebvre, 1999), considering the benefits offered by the porous medium in evaporation enhancement and combustion.

The temperature distribution in porous medium significantly affects the uniformity of the fuel-air mixture. The porous medium surface temperature was measured and also predicted. The results indicate that the temperature of porous medium was uniform within ± 5 and 25 K with IR imaging and thermocouple measurements, respectively at a feedback rate of 1% of the energy content of the liquid fuel evaporated. Further, the porous medium axial and surface temperature profiles, predicted using a two-energy equation model, revealed that the peak temperature increased with an increase in heat feedback rate. Model predictions agree well with experimental measurements.

6.1.2 Spray Characteristics

Liquid fuels are usually injected into combustion chambers using atomizers such as pressure-swirl and air-blast. In this study, an air-blast atomizer was used to inject the fuel. Characteristics such as droplet Sauter mean diameter, axial velocity, and liquid mass flux of fuel spray were measured upstream of evaporation porous medium. Smaller droplet diameters were recorded in the spray core. The droplet diameter increased radially outward, and also with an increase in equivalence ratio. In most cases, an increase in the coflow air temperature from 423 to 490 K caused significant evaporation of kerosene droplets, and hence, reduced Sauter mean diameter values.

The droplet axial velocity was higher at spray core and decreased radially. Peak values of the axial velocity decreased along the axis from the injector exit. Due to the swirl imparted to fuel spray, large particles were thrown away from the spray core, which moved at lower velocities. The mass flux at a given transverse location also increased with increase in equivalence ratio. The liquid mass flux profiles followed the trend of Sauter mean diameter profiles at corresponding equivalence ratios.

6.1.3 Evaporation Enhancement

Enhancement of the evaporation was quantified with simulated combustion heat feedback. The electric input supplied to the porous medium for resistive heating was represented as a fraction of heat released in the combustion zone. At low equivalence ratios such as 0.3 and 0.4, no heat feedback was required to achieve complete vaporization of the kerosene fuel; the preheated coflow air itself was sufficient to completely vaporize the fuel. However, at higher equivalence ratios, a heat feedback rate of about 1% of the average energy content (LHV) was needed to completely vaporize the fuel.

Experiments were conducted without the porous medium also to isolate the role of the porous medium in the evaporation enhancement. The vaporization experiments without porous medium showed that at a given coflow air temperature and fuel flowrate, a longer vaporization section was needed to achieve complete vaporization. In the present configuration, complete vaporization of the kerosene spray was achieved at 1% heat feedback rate with a vaporization section of only 4 cm long. On

the other hand, when no porous medium was employed, this would translate to the use of a coflow air temperature of at least 500 K or a vaporization section of more than 15 cm long. Thus, employing porous media enhances evaporation considerably, and allows operation at a lower coflow air temperature or with a shorter evaporation section.

The vapor concentration measurements downstream of evaporation porous medium were measured and predicted. This was conducted for two reasons: (i) to study the effect of heat feedback rate on vapor concentration, and (ii) to measure spatial uniformity of the vapor concentration. The peak vapor concentration with 1% combustion heat feedback showed 63% higher than that with no heat feedback. The vapor concentration in transverse locations of up to 50% on either side from the centerline of the test section was uniform within $\pm 20\%$ (maximum). This demonstrates that the porous medium not only enhances fuel evaporation rate but is also effective in producing a spatially uniform fuel vapor-air mixture downstream of evaporation porous medium.

Computational results also showed that the peak vapor concentration increased when the heat feedback rate was made stronger. For instance, the peak concentration obtained with a heat source of 1.1% was 40% times higher than that of the case with 0.8% heat feedback rate. This indicates that the thermal effects of the porous medium are dominant in the evaporation enhancement. A computational parametric study on

the effects of heat feedback rate, porous medium structure, fuel flowrate, and air inlet temperature was also conducted.

When there is no porous medium employed, the vapor concentration profiles should follow the liquid mass flux profiles assuming uniform spatial vaporization rate. The presence of the porous medium increases the residence time, and the inherent random porous matrix structure helps prepare the uniform vapor concentration downstream of porous medium. The combustion heat feedback to the porous medium increases the temperature of the evaporation porous medium, which in turn, improves the heat transfer to droplets, and enhances evaporation.

6.1.4 Combustion of Fuel Spray in Porous Media

Stable spray flames were established both inside and on the surface of the combustion porous medium. While the interior flame was completely contained within the combustion porous medium, the surface flame was stabilized on the downstream exit surface. For a given porous medium, the specific mode of combustion depended on the flowrates of coflow air and fuel and the location of injector. Only one mode of combustion (interior or surface) could be established for specified set of conditions. A decrease in effective gas velocity decreased extinction equivalence ratio for all injector locations. The completeness of evaporation and the quality of fuel-air mixture available at the combustion porous medium determined the flame stability. The availability of flammable mixture in combustion porous medium favored interior combustion. If a flammable mixture is not prepared until the exit surface of

evaporation and combustion porous media, surface combustion was most likely to occur.

A Damköhler number analysis was developed to provide a general understanding of flame extinction in porous media. The Damköhler number is the ratio between a characteristic residence time and chemical time. In this study, the characteristic preheating residence time of fuel spray was varied by changing: (i) distance between the porous medium and the injector, and (ii) the coflow air flowrate. Since the air flowrate was held constant at a given Damköhler number, the average gas velocity through the porous medium was also constant. A decrease in the fuel flowrate reduced the flame speed. At some critical fuel flowrate, the local gas velocity exceeded the flame speed, and blew out the flame. A nominal Damköhler number of 5.0 was required to initiate the interior combustion mode.

Axial temperature profiles in the evaporation porous medium showed only a slight increase. However, across the interface between evaporation and combustion porous media, the solid temperature increased rapidly. This indicates that the combustion occurred at the interface between evaporation and combustion porous media. Porous medium surface temperature uniformity experiments showed that the temperature distribution was uniform within ± 50 K. The flame radiation decreased as the flame extinction limit in porous media was approached. CO emission indices ranged from 13 to 100 g/kg of fuel. The measured NO emission indices were less than 2.5 g/kg of fuel. Also, NO emission indices were somewhat insensitive to operating parameters

such as equivalence ratio and the location of injector. The exit CO₂ concentration had a maximum value of 3.1% and exit O₂ concentration had a lowest value of 16.3%. Concentration levels of CO₂ and O₂ indicate the degree of combustion.

6.2 Conclusions

From the present study, following conclusions are drawn:

- The pressure drop across the porous medium increases as the gas velocity increases. It also increases with linear pore density.
- The surface temperatures of the evaporation and combustion porous medium in the present study are uniform within ± 25 and 50 K, respectively.
- The porous medium peak temperature increases with an increase in heat feedback rate.
- Lower droplet diameters exist in the spray core and the droplet diameter increases radially outward. The droplet velocities are higher at spray core and decreases radially and also along the axial direction.
- A heat feedback rate to the evaporation porous medium section of about 1% of average heat release in the combustion section is needed to completely vaporize the kerosene fuel.
- The measured peak vapor concentration at the exit of the evaporation porous medium with 1% combustion heat release feedback is 63% higher than that with no heat feedback.

- The predicted vapor concentration downstream of evaporation porous medium increases when the heat feedback rate is stronger.
- The porous medium allows operation at a lower coflow air temperature or with a shorter evaporation section.
- Stable spray flames can be established both inside and on the downstream exit surface of the combustion porous medium.
- The extinction equivalence ratio decreases with a decrease in effective gas velocity through porous medium.
- The stable operating regime i.e., lowest equivalence ratio the burner can operate with, increases with Damköhler number.
- A nominal Damköhler number of 5.0 was required to initiate interior combustion mode.
- The radiation from porous medium surface decreases as extinction is approached.
- NO emission indices are insensitive to operating parameters such as equivalence ratio and the location of injector.

6.3 Practical Impacts

The porous burner concepts developed in this study could be employed in gas turbine combustors, air-heating systems, industrial burners, porous chemical reactors, and hybrid burners for bio-fuels. In lean premixed combustor gas turbines, when the output power falls below 50% of the nominal value, unstable combustion is likely to

occur (Mößbauer et al., 1999). The use of porous medium in such situations reduces the fluctuations in turndown ratios, since the porous medium could provide a large thermal storage.

Porous medium technology can be in heat recirculating burners. Since the combustion heat is fed back upstream, the inlet reactants can be preheated, and the combustion performance can be improved. Porous medium also finds applications in radiant burners. In particular, where there is no direct contact of combustion products and heating medium is required, use of porous medium could effectively transfer the heat via radiation. The porous media burner technology can also be used in boilers, oil refinery process heaters, and steam generators (Kamal and Mahamad, 2006a).

Some materials, such as municipal waste and vegetable oil-derived fuels or coal-derived synthetic gases usually contain low calorific values. With porous medium, such fuels could be effectively burned because the inlet enthalpy could be augmented due to upstream heat transfer. Further, porous medium burners are used in hydrogen and synthetic gases production.

6.4 Recommendations for Further Study

This dissertation presented a comprehensive study of evaporation enhancement and combustion of liquid spray in porous media. Previous sections in this chapter

summarized the findings of this research. The study could further be extended in the following directions:

Experimental Work:

1. Droplet residence time in porous media is an important parameter in evaporation enhancement. The length of evaporation porous medium could be varied to study the effects of droplet residence time in evaporation enhancement.
2. In this study, an air-blast atomizer was employed to inject liquid fuel. However, other types of injectors such as pressure swirl and effervescent (or even no injector) could be used to generate different spray pattern upstream of evaporation porous medium.
3. The length of combustion porous media could be varied to promote fuel vapor-air mixing. Influence of different flame locations on heat feedback rate to evaporation porous medium could be investigated.
4. Different types of porous media and fuels could be used and the Damköhler number analysis could be developed into a more generic model for flame stability and extinction in porous media.
5. Due to the enhanced upstream heat transfer, fuels with low calorific value could be burned effectively using porous medium. However, a detailed investigation of this combustion phenomenon needs to be conducted.

Computational Work:

1. Droplets' flow pattern inside the porous medium could be included in the computational model. This would enable us to better understand droplet-porous medium momentum and heat transfer.
2. Computational models for the combustion of liquid spray in porous medium could also be developed and compared with experimental data.

REFERENCES

- Abd-Alla, G. H. (2002), "Using Exhaust Gas Recirculation in Internal Combustion Engines: A Review," *Energy Conversion and Management*, Vol. 43, No. 8, pp. 1027-1042.
- Aggarwal, S. K., Tong, A. Y., and Sirignano, W. A., (1984), "A Comparison of Vaporization Models in Spray Calculations," *AIAA Journal*, Vol. 22, No. 10, pp. 1448-1457.
- Alazmi, B., and Vafai, K. (2000), "Analysis of Variants Within the Porous Media Transport Models," *Journal of Heat Transfer, Transactions of the ASME*, Vol. 122, pp. 303-326.
- Annamalai, K., and Puri, I. K. (2007), Combustion Science and Engineering. CRC Press, New York, pp. 987-992.
- Babb, M., Gollahalli, S. R., and Sliepcevich, C. M., "Extinguishment of Liquid Heptane and Gaseous Propane Diffusion Flames," *Journal of Propulsion and Power*, Vol. 15, No. 2, 1999, pp. 260-265.
- El Banhawy, Y., and Whitelaw, J. H. (1980), "Calculation of the Flow Properties of a Confined Kerosene Spray Flame," *AIAA Journal*, Vol. 18, No. 12, pp. 1503-1510.
- Barra, A. J., Diepven, G., Ellzey, J. L., and Henneke, M. R. (2003), "Numerical Study of the Effects of Material Properties on Flame Stabilization in a Porous Burner," *Combustion and Flame*, Vol. 134, pp. 369-379.
- Barra, A. J., and Ellzey, J. L. (2004), "Heat Recirculation and Heat Transfer in Porous Burners," *Combustion and Flame*, Vol. 137, pp. 230-241.
- Bell, J., Day, M., Almgren, A., Lijewski, M., Rendleman, C., Cheng, R., and Shepherd, I. (2006), "Simulation of Lean Premixed Turbulent Combustion," *Journal of Physics: Conference Series*, Vol. 46, No. 1, pp. 1-15.
- Benaissa, A., Gauthier, J. E. D., Bardon, M. F., and LaViolette, M. (2002), "Modeling Evaporation of Multi-component Fuel Droplets Under Ambient Temperature Conditions," *Journal of the Institute of Energy*, Vol. 75, No. 502, pp. 19-26.
- Bird, R. B., Stewart, W. E., and Lightfoot, E. N. (2002), Transport Phenomena. 2nd Edition, John Wiley & Sons, New York.

Birouk, M., and Gökalp, I. (2006), "Current Status of Droplet Evaporation in Turbulent Flows," *Progress in Energy and Combustion Science*, Vol. 32, pp. 408-423.

Bouma, P. H., Eggels, R. L. G. M., de Goey, L. P. H., Nieuwenhuizen, J. K., and van der Drift, A. (1995), "A Numerical and Experimental Study of the NO-Emission of Ceramic Foam Surface Burners," *Combustion Science and Technology*, Vol. 108, pp. 193-203.

Bouma, P. H., and de Goey, L. P. H. (1999), "Premixed Combustion on Ceramic Foam Burners," *Combustion and Flame*, Vol. 119, pp. 133-143.

Brzustowski, T. A., Gollahalli, S. R., Gupta, M. P., Kaptein, M., and Sullivan, H. F. (1975), "Radiant Heating from Flares," *ASME Paper 75-HT-4, American Society of Mechanical Engineers*, New York.

Card, J. M., and Williams, F. A., (1992), "Asymptotic Analysis with Reduced Chemistry for the Burning of n-Heptane Droplets," *Combustion and Flame*, Vol. 91, pp. 187-199.

Civan, F., and Evans, R. D. (1996), "Determination of Non-Darcy Flow Parameters Using a Differential Formulation of the Forchheimer Equation," SPE 35621.

Civan, F., and Evans, R. D. (1998), "Determining the Parameters of the Forchheimer Equation From Pressure-Squared vs. Pseudopressure Formulations," Society of Petroleum Engineers.

Darcy, H. (1856), "Les Fontaines Publiques de la ville de Dijon," Dalmont, Paris.

Dual, F., Fichot, F., and Quintard, M. (2004), "A Local Thermal Non-equilibrium Model for Two-phase Flows with Phase-change in Porous Media," *Int. J. Heat Mass Transfer*, Vol. 47, pp. 613-639.

Ellzey, J. L., and Goel, R. (1995), "Emissions of CO and NO from a Two Stage Porous Media Burner," *Combustion Science and Technology*, Vol. 107, pp. 81-91.

Ergun, S. (1952), "Fluid Flow Through Packed Columns," *Chemical Engineering Progress*, Vol. 48, No. 2, pp. 89-94.

Faeth, G. M. (1983), "Evaporation and Combustion of Sprays," *Progress in Energy and Combustion Science*, Vol. 9, pp. 1-76.

Fand, R. M., Kim, B. Y. K., Lam, A. C. C., and Phan, R. T. (1987), "Resistance to the Flow of Fluids Through Simple and Complex Porous Media whose Matrices are

Composed of Randomly Packed Spheres,” *Journal of Fluids Engineering*, Vol. 109, pp. 268-274.

Forchheimer, P. (1901), “Wasserbewegung durch Boden,” *Z. Ver. Deutsch. Ing.*, Vol. 45, pp. 1782-1788.

Fu, X., Viskanta, R., Gore, J. P. (1997), “A Model for the Volumetric Radiation Characteristics of Cellular Ceramics,” *International Communications in Heat and Mass Transfer*, Vol. 24, No. 8, pp. 1069-1082.

Fu, X., Viskanta, R., Gore, J.P. (1998), “Prediction of Effective Thermal Conductivity of Cellular Ceramics,” *International Communications in Heat and Mass Transfer*, Vol. 25, No. 2, pp. 151-160.

Goldstein, R. J. (1996), Fluid Mechanics Measurements, 2nd Edition, Taylor & Francis, Washington D.C.

Gollahalli, S. R., Khanna, T., and Prabhu, N. (1992), “Diffusion Flames of Gas Jets Issued From Circular and Elliptic Nozzles,” *Combustion Science and Technology*, Vol. 86, pp. 267-288.

Gomez, A., and Russo, S. (2006), “Physical Characterization of Laminar Spray Flames in the Pressure Range 0.1-0.9 MPa,” *Combustion and Flame*, Vol. 145, No. 1-2, pp. 339-356.

Haack, D. P. (1993), “Mathematical Analysis of Radiatively Enhanced Liquid Droplet Vaporization and Liquid Fuel Combustion Within a Porous Inert Media,” M.S. Thesis, Univ. Texas, Austin, TX.

Hardesty, D. R., and Weinberg, F. J. (1974), “Burners Producing Large Excess Enthalpies,” *Combustion Science and Technology*, Vol. 8, pp. 201-214.

Henneke, M. R., and Ellzey, J. L. (1995), “Modeling of Filtration Combustion in a Packed Bed,” *Combustion and Flame*, Vol. 117, pp. 832-840.

Howell, J. R., Hall, M. J., and Ellzey, J. L. (1996), “Combustion of Hydrocarbon Fuels Within Porous Inert Media,” *Progress in Energy and Combustion Science*, Vol. 22 pp. 121-145.

Hsu, P.-F., Evans, W. D., and Howell, J. R. (1993), “Experimental and Numerical Study of Premixed Combustion within Nonhomogeneous Porous Ceramics,” *Combustion Science and Technology*, Vol. 90, No. 1-4, pp. 149-172.

Huang, Y., Wang, S., and Vigor, Y. (2006), “Systematic Analysis of Lean-Premixed Swirl-Stabilized Combustion,” *AIAA Journal*, Vol. 44, No. 4, pp. 724-740.

Jugjai, S., Wongpanit, N., Laoketkan, T., and Nokkaew, S. (2002), "The Combustion of Liquid Fuels Using a Porous Medium," *Experimental Thermal and Fluid Science*, Vol. 26, pp. 15-23.

Jugjai, S., and Polmart, N. (2003), "Enhancement of Evaporation and Combustion of Liquid Fuels through Porous Media," *Experimental Thermal and Fluid Science*, Vol. 27, pp. 901-909.

Kamal, M. M., and Mohamad, A. A. (2006a), "Combustion in Porous Media," *Proceedings of the Institution of Mechanical Engineers, Part A: Journal of Power and Energy*, Vol. 220, No. A5, pp. 487-508.

Kamal, M. M., and Mohamad, A. A. (2006b), "Effect of Swirl on Performance of Foam Porous Medium Burners," *Combustion Science and Technology*, Vol. 178, No. 4, pp. 729-761.

Kamiuto, K., and Yee, S. S. (2005), "Heat Transfer Correlations for Open-Cellular Porous Materials," *International Communications in Heat and Mass Transfer*, Vol. 32, No. 7, pp. 947-53.

Kaplan, M., and Hall, M. J. (1995), "The Combustion of Liquid Fuels Within a Porous Media Radiant Burner," *Experimental Thermal and Fluid Science*, Vol. 11, pp. 13-20.

Kaviany, M. (1995), Principles of Heat Transfer in Porous Media. Springer-Verlag New York, Inc.

Khanna, V., Goel, R., and Ellzey, J. L. (1994), "Measurements of Emissions and Radiation for Methane Combustion within a Porous Medium Burner," *Combustion Science and Technology*, Vol. 99, pp. 133-142.

Kotani, Y., and Takeno, T. (1982), "An Experimental Study on Stability and Combustion Characteristics of an Excess Enthalpy Flame", *Nineteenth Symposium (International) on Combustion*, pp. 1503-1509.

Kuo, K. K. (1986), Principles of Combustion. John Wiley & Sons, New York.

Kuwahara, F., Shiota, M., and Nakayama, A. (2001), "A Numerical Study of Interfacial Convective Heat Transfer Coefficient in Two-energy Equation Model for Convection in Porous Media," *International Journal of Heat and Mass Transfer*, Vol. 44, pp. 1153-1159.

Lammers, F. A., and de Goey, L. P. H. (2003), "A Numerical Study of Flash back of Laminar Premixed Flames in Ceramic-foam Surface Burners," *Combustion and Flame*, Vol. 133, pp. 47-61.

- Launder, B.E., and Spalding, D. B. (1974), "The Numerical Computation of Turbulent Flows," *Computer Methods in Applied Mechanics and Engineering*, Vol. 3, pp. 269-289.
- Law, C. K. (1982), "Recent Advances in Droplet Vaporization and Combustion," *Progress in Energy and Combustion Science*, Vol. 8, pp. 171-201.
- Lee, K-B., and Howell, J.R. (1991), "Theoretical and Experimental Heat and Mass Transfer in Highly Porous Media," *International Journal of Heat and Mass Transfer*, Vol. 34, No. 8, pp. 2123-2132.
- Lefebvre, A. H. (1999), Gas Turbine Combustion. Taylor & Francis, Philadelphia.
- Leonardi, S. A., Viskanta, R., and Gore, J. P. (2003), "Analytical and Experimental Study of Combustion and Heat Transfer in Submerged Flame Metal Fiber Burners/Heaters," *Journal of Heat Transfer, Transactions of the ASME*, Vol. 125, pp. 118-125.
- Liu, S., and Masliyah, J. H. "Single Fluid Flow in Porous Media," *Chemical Engineering Communications*, Vol. 148-150, pp. 653-732.
- Ma, A-Z., Muhler, M., Gruenert, W. (2000), "Selective Catalytic Reduction of NO by Ammonia over Raney-Ni Supported Cu-ZSM-5. I. Catalyst Activity and Stability," *Chemical Engineering and Technology*, Vol. 23, No. 3, pp. 273-278.
- Macdonald, I. F., El-Sayed, M. S., Mow, K., and Dullien, F. A. L. (1979), "Flow Through Porous Media – the Ergun Equation Revisited," *Industrial and Engineering Chemistry Fundamentals*, Vol. 18, No. 3, pp. 199-208.
- Martynenko, V. V., Echigo, R., and Yoshida, H. (1998), "Mathematical Model of Self-sustaining Combustion in Inert Porous Medium with Phase Change under Complex Heat Transfer," *International Journal of Heat and Mass Transfer*, Vol. 41, No. 1, pp. 117-126.
- Mathis Jr., W. M., and Ellzey, J. L. (2003), "Flame Stabilization, Operating Range, and Emissions for a Methane/Air Porous Burner," *Combustion Science and Technology*, Vol. 175, pp. 825-839.
- Mital, R., Gore, J. P., and Viskanta, R. (1997), "A Study of the Structure of Submerged Reaction Zone in Porous Ceramic Radiant Burners," *Combustion and Flame*, Vol. 111, pp. 175-184.
- Mital, R., Gore, J. P., and Viskanta, R. (1998), "A Radiation Efficiency Measurement Procedure for Gas-Fired Radiant Burners," *Experimental Heat Transfer*, Vol. 11, pp. 3-21.

- Mößbauer, S., Pickenäcker, O., Pickenäcker, K., and Trimis, D. (1999), "Application of the Porous Burner Technology in Energy- and Heat- Engineering," *Fifth International Conference on Technologies and Combustion for a Clean Environment (Clean Air V)*, Lisbon (Portugal), 12-15 July 1999, Volume 1, Lecture 20.2, pp. 519-523.
- Modest, M. F. (2003), Radiative Heat Transfer. 2nd Edition, Elsevier Science (USA), San Diego, CA.
- Morsi, S. A., and Alexander, A. J. (1972), "An Investigation of Particle Trajectories in Two-Phase Flow Systems," *Journal of Fluid Mechanics*, Vol. 55, No. 2, pp. 193-208.
- Nakayama, A. (1995), PC-Aided Numerical Heat Transfer and Convective Flow. CRC Press, Boca Raton, Florida, p. 183.
- Nakayama, A., Kuwahara, F., Sugiyama, M., and Xu, G. (2001), "A Two-energy Equation Model for Conduction and Convection in Porous Media," *International Journal of Heat and Mass Transfer*, Vol. 44, pp. 4375-4379.
- Olikara, C., and Borman, G. L. (1975), "A Computer Program for Calculating Properties of Equilibrium Combustion Products with Some Applications to I.C. Engines," SAE Paper 750468.
- Oliveira, A. A. M., Kaviany, M. (2001), "Nonequilibrium in the Transport of Heat and Reactants in Combustion in Porous Media," *Progress in Energy and Combustion Science*, Vol. 27, pp. 523-545.
- Park, C-W., and Kaviany, M. (2002), "Evaporation-Combustion Affected by In-cylinder, Reciprocating Porous Regenerator," *Journal of Heat Transfer, Transactions of the ASME*, Vol. 124, pp. 184-194.
- Patankar, S. V., and Spalding, D. B., (1972), "A Calculation Procedure for Heat, Mass and Momentum Transfer in Three-dimensional Parabolic Flows," *International Journal of Heat and Mass Transfer*, Vol. 15, pp. 1787-1806.
- Periasamy, C., Sankara Chinthamony, S. K., and Gollahalli, S. R. (2004), "Modeling Liquid Spray Evaporation in Heated Porous Media with a Local Thermal Non-equilibrium Model," IMECE2004-61300, 2004 ASME International Mechanical Engineering Congress, Anaheim, CA, November 13-19, 2004.
- Periasamy, C., and Gollahalli, S. R. (2006), "A Parametric Simulation of the Evaporation in Liquid-Fueled Porous Burners," ASME Power 2006, PWR2006-88016, Atlanta, GA, May 2-4, 2006.

Presser, C., Gupta, A. K., Avedisian, C. T., and Semerjian, H. G. (1990), "Fuel Property Effects on the Structure of Spray Flames," *23rd Symposium (International) on Combustion*, The Combustion Institute, pp. 1361-1367.

Presser, C., Gupta, A. K., Avedisian, C. T., and Semerjian, H. G. (1993), "Aerodynamic Characteristics of Swirling Spray Flames: Pressure-Jet Atomizer," *Combustion and Flame*, Vol. 92, pp. 25-44.

Puri, R., and Gollahalli, S. R. (1989), "Effects of Location and Direction of Diluent Injection on Radiation and Pollutant Emissions of a Burning Spray," *Transactions of the ASME, Journal of Energy Resources Technology*, Vol. 111, No. 1, pp. 16-21.

Ranz, W. E., and Marshall Jr., W. R. (1952a), "Evaporation from Drops Part I," *Chemical Engineering Progress*, Vol. 48, No. 3, pp. 141-146.

Ranz, W. E., and Marshall Jr., W. R. (1952b), "Evaporation from Drops Part II," *Chemical Engineering Progress*, Vol. 48, No. 4, pp. 173-180.

Rao, K. V. L., and Lefebvre, A. H. (1976), "Evaporation Characteristics of Kerosine Sprays Injected into a Flowing Air Stream," *Combustion and Flame*, Vol. 26, pp. 303-309.

Reitz, R. D., and Bracco, F. V., (1982), "Mechanism of Atomization of a Liquid Jet," *Physics of Fluids*, Vol. 25, No. 10, pp. 1730-1742.

Rumminger, M. D., Dibble, R. W., Heberle, N. H., and Crosley, D. R. (1996), "Gas Temperature Above a Porous Radiant Burner: Comparison of Measurements and Model Predictions", *26th Symposium (International) on Combustion*, pp.1755-1762.

Runge, T., Teske, M., and Polymeropoulos, C. E. (1998), "Low-temperature Vaporization of JP-4 and JP-8 Fuel Droplets," *Atomization and Sprays*, Vol. 8, pp. 25-44.

Sahraoui, M., and Kaviany, M. (1994), "Direct Simulation vs Volume-averaged Treatment of Adiabatic, Premixed Flame in a Porous Medium," *International Journal of Heat and Mass Transfer*, Vol. 37, No. 18, pp. 2817-2834.

Sathe, S. B., Peck, R. E., and Tong, T. W. (1990a), "Flame Stabilization and Multimode Heat Transfer in Inert Porous Media: A Numerical Study," *Combustion Science and Technology*, Vol. 70, pp. 93-109.

Sathe, S. B., Peck, R. E., and Tong, T. W. (1990b), "A Numerical Analysis of Heat Transfer and Combustion in Porous Radiant Burners," *International Journal of Heat and Mass Transfer*, Vol. 33, No. 6, pp. 1331-1338.

Sazhin, S. S. (2005), "Advanced Models of Fuel Droplet Heating and Evaporation," *Progress in Energy and Combustion Science*, Vol. 32, pp. 162-214.

Schmidt, D. P., Nouar, I., Senecal, P. K., Rutland, C. J., Martin, J. K., Reitz, R. D., and Hoffman, J. A. (1999), "Pressure-Swirl Atomization in the Near Field," SAE Paper 1999-01-0496, 1999.

Siegel, R., and Howell, J. R. (2002) Thermal Radiation Heat Transfer. 4th Edition, Taylor & Francis, New York.

Sirignano, W. A. (1983), "Fuel Droplet Vaporization and Spray Combustion Theory," *Progress in Energy and Combustion Science*, Vol. 9, pp. 291-322.

Smith, T. L., Periasamy, C., Baird, B. D., and Gollahalli, S. R. (2006), "Trajectory and Characteristics of Buoyancy and Momentum Dominated Horizontal Jet Flames from Circular and Elliptic Burners," *Transactions of the ASME, Journal of Energy Resources Technology*, Vol. 128, pp. 300-310.

Spalding, D. B. (1952), "The Combustion of Liquid Fuels," *Fourth Symposium (International) on Combustion*, pp. 847-864.

Takeno, T., and Sato, K. (1979), "An Excess Enthalpy Flame Theory", *Combustion Science and Technology*, Vol. 20, pp. 73-84.

Trimis, D., Durst, F., Pickenacker, O., and Pickenacker, K. (1997), "Porous Medium Combustor versus Combustion Systems with Free Flames," *2nd International Symposium on Heat Transfer Enhancement and Energy Conservation, ISHTEEC '97*, 16-19 June 1997, Guangzhou, China.

Tseng, C.-J., and Howell, J. R. (1996), "Combustion of Liquid Fuels in a Porous Radiant Burner," *Combustion Science and Technology*, Vol. 112, pp. 141-161.

Turns, S. R. (2000), An Introduction to Combustion: Concepts and Applications. 2nd Edition, McGraw-Hill International Editions, Singapore.

Vafai, K. (2005), Handbook of Porous Media. 2nd Edition, CRC Press, Taylor & Francis, Boca Raton, Florida.

Vafai, K., and Kim, S. J. (1989), "Forced Convection in a Channel Filled with a Porous Medium: An Exact Solution," *Journal of Heat Transfer, Transactions of the ASME*, Vol. 111, pp. 1103-1106.

Viskanta, R. (1995), "Interaction of Combustion and Heat Transfer in Porous Inert Media", in *Transport Phenomena in Combustion*, Ed. S. H. Chan, Taylor and Francis, pp. 64-87

Wakao, N., and Kaguei, S. (1982), Heat and Mass Transfer in Packed Beds. Gordon and Breach Science Publishers, New York.

Weinberg, F. J. (1971), "Combustion Temperatures: The Future?," *Nature*, Vol. 233, September 24, pp. 239-241.

Wheeler, A. J., and Ganji, A. R. (1996), Introduction to Engineering Experimentation. Prentice Hall, New Jersey.

Widmann, J. F., and Presser, C. (2002), "A Benchmark Experimental Database for Multiphase Combustion Model Input and Validation," *Combustion and Flame*, Vol. 129, No. 1-2, pp. 47-86.

Williams, A. (1973), "Combustion of Droplets of Liquid Fuels: A Review," *Combustion and Flame*, Vol. 21, pp. 1-31.

Younis, L. B., and Viskanta, R. (1993), "Experimental Determination of the Volumetric Heat Transfer Coefficient between Stream of Air and Ceramic Foam," *International Journal of Heat and Mass Transfer*, Vol. 36, No. 6, pp. 1425-1434.

Yule, A. J., Seng, C. Ah., Felton, P. G., Ungut, A., and Chigier, N. A. (1982), "A Study of Vaporizing Fuel Sprays by Laser Techniques," *Combustion and Flame*, Vol. 44, pp. 71-84.

Yule, A. J., Ereaud, P. R., and Ungut, A. (1983), "Droplet Sizes and Velocities in Vaporizing Sprays," *Combustion and Flame*, Vol. 54, pp. 15-22.

Zeng, Z., and Grigg, R. (2006), "A Criterion for Non-Darcy Flow in Porous Media," *Transport in Porous Media*, Vol. 63, 57-69.

Zhou, X. Y., and Pereira, J. C. F. (1997), "Numerical Study of Combustion and Pollutants Formation in Inert Nonhomogeneous Porous Media," *Combustion Science and Technology*, Vol. 130, pp. 335-364.

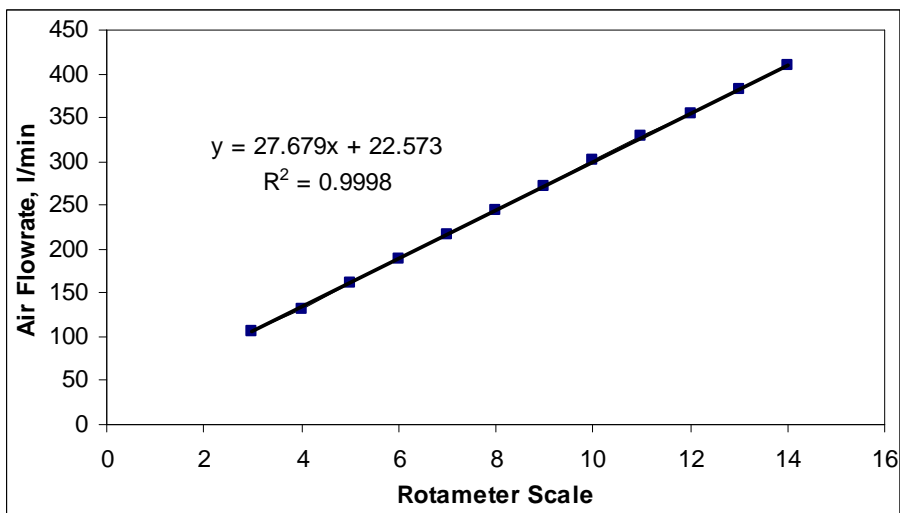
Appendix A

Calibrations Charts

A.1 Calibration of Rotameter for Coflow Air

Make: Ametek, S & K Co.
Model: 4-HCFB
Float: 42-J

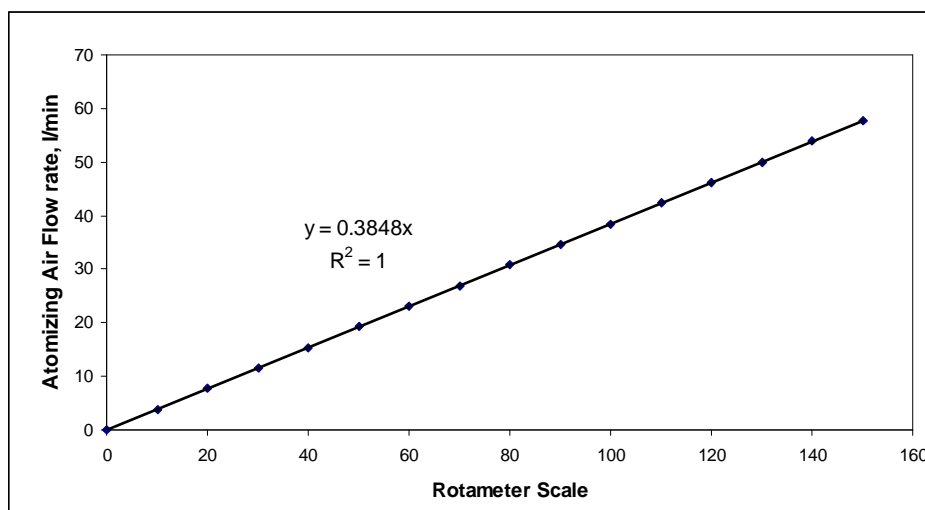
Rotameter Scale	Air Flowrate (l/min)
3	105.87
4	132.12
5	160.70
6	188.64
7	216.91
8	243.34
9	270.94
10	302.17
11	328.83
12	354.38
13	381.62
14	408.66



A.2 Calibration of Rotameter for Atomizing Air

Make: Cole Parmer
Model: N044-40C
Float: Stainless steel

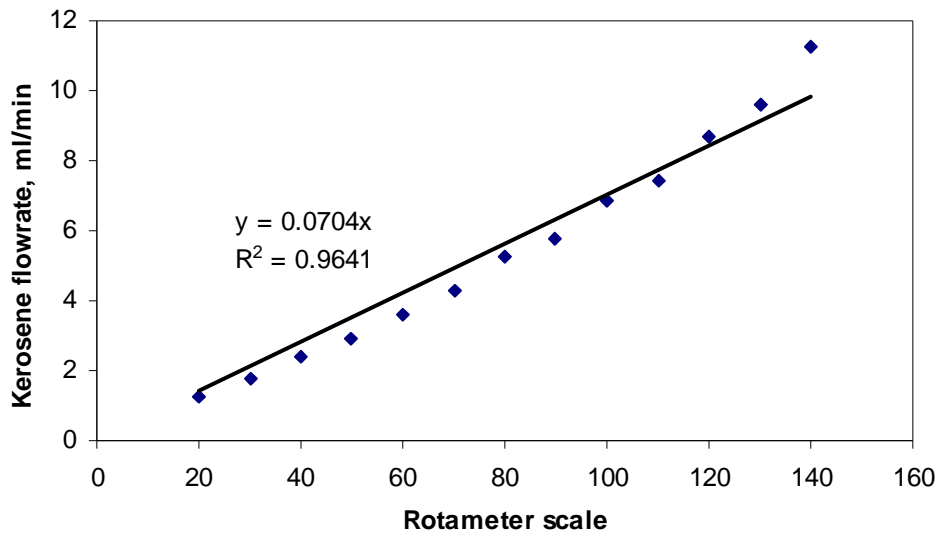
Rotameter Scale	Air Flowrate (l/min)
0	0.0
10	3.8
20	7.7
30	11.5
40	15.4
50	19.2
60	23.1
70	26.9
80	30.8
90	34.6
100	38.5
110	42.3
120	46.2
130	50.0
140	53.9
150	57.7



A.3 Calibration of Rotameter for Kerosene

Make: Omega
Model: FL-3802ST
Float: Stainless steel

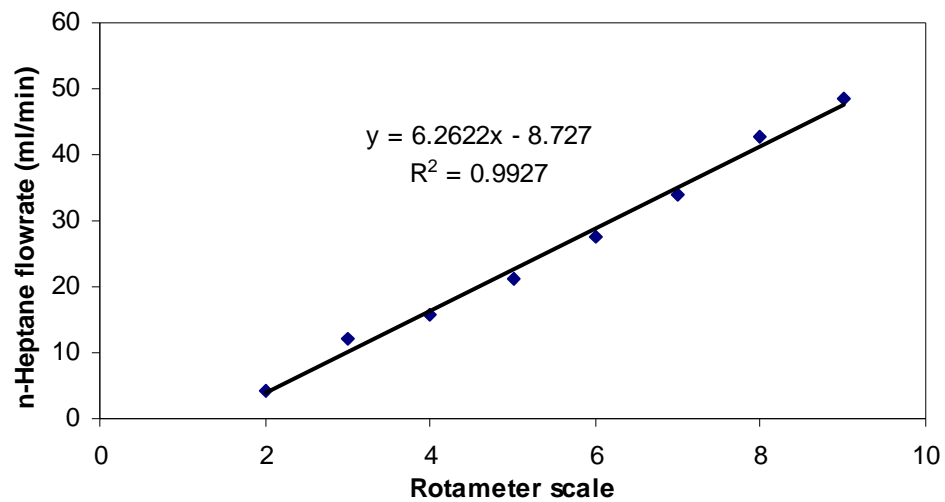
Rotameter scale	Flow rate (ml/min)
20	1.24
30	1.76
40	2.37
50	2.93
60	3.62
70	4.27
80	5.24
90	5.8
100	6.87
110	7.41
120	8.66
130	9.58
140	11.26



A.4 Calibration of Rotameter for n-Heptane

Make: Ametek, S & K Co.
Model: Lo-Flow SK-1/8"-15-G5
Float: Stainless steel

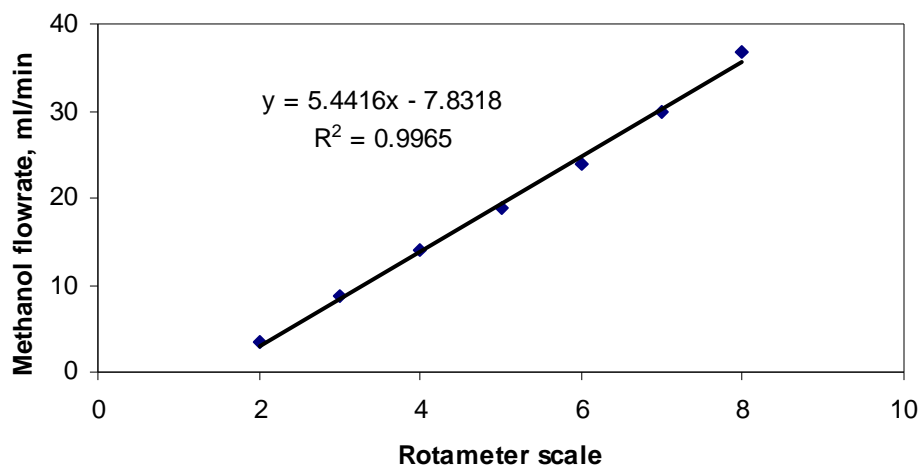
Rotameter scale	Flowrate (ml/min)
2	4.11
3	12
4	15.63
5	21.13
6	27.52
7	34.09
8	42.86
9	48.39



A.5 Calibration of Rotameter for Methanol

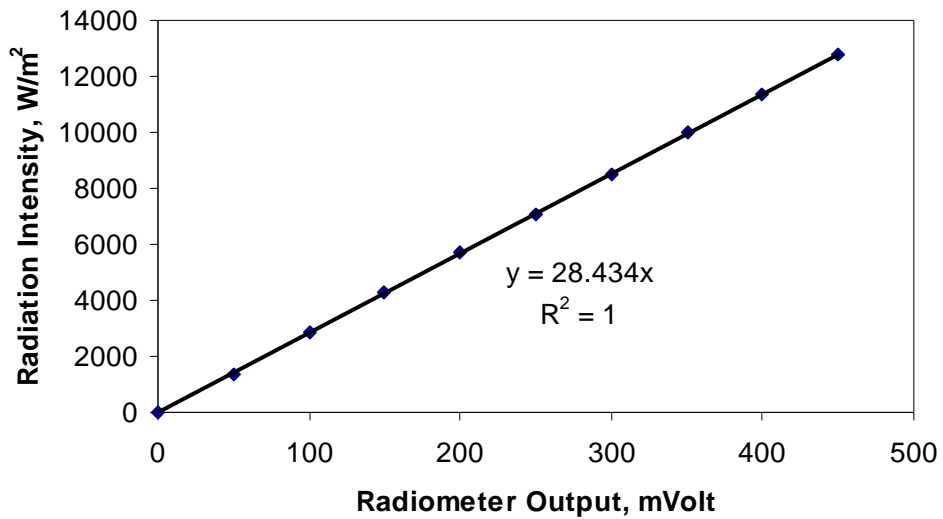
Make: Ametek, S & K Co.
Model: Lo-Flow SK-1/8"-15-G5
Float: Stainless steel

Rotameter scale	Flowrate (ml/min)
2	3.43
3	8.75
4	14.08
5	18.75
6	23.81
7	30.00
8	36.81



A.6 Calibration Chart for Radiometer Output

Radiometer output	Solar constant	Radiation intensity
mv		W/m ²
0	0	0
50	1.025	1386.825
100	2.1	2841.3
150	3.175	4295.775
200	4.2	5682.6
250	5.25	7103.25
300	6.3	8523.9
350	7.375	9978.375
400	8.4	11365.2
450	9.45	12785.85



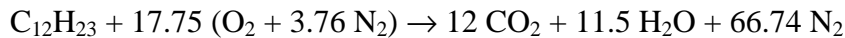
Appendix B

Sample Calculations

B.1 Stoichiometric Combustion Calculation

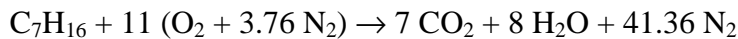
B.1.1 Kerosene

Kerosene is assumed to be a single-component fuel of $C_{12}H_{23}$. Stoichiometric combustion equation for kerosene-air combustion is written as follows:



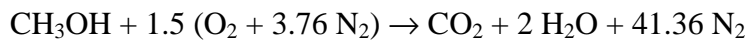
$$\frac{F}{A}\bigg|_{\text{mass}} = \frac{(12 \cdot 12 + 23 \cdot 1)}{17.75 \times (32 + 3.76 \cdot 28)} = 0.06853$$

B.1.2 n-Heptane



$$\frac{F}{A}\bigg|_{\text{mass}} = \frac{(7 \cdot 12 + 16 \cdot 1)}{11 \times (32 + 3.76 \cdot 28)} = 0.06622$$

B.1.3 Methanol



$$\frac{F}{A}_{\text{mass}} = \frac{(1 \cdot 12 + 4 \cdot 1 + 1 \cdot 16)}{1.5 \times (32 + 3.76 \cdot 28)} = 0.1554$$

B.2 Calculation of Kerosene Spray Mass Flux

Equivalence ratio = 0.4; Location of injector = 2.5 cm upstream of EPM

Density of kerosene = 0.78 g/cm³

Radial location = 1 mm from the spray core

Sauter mean diameter = 24.2 microns

Droplet axial velocity = 15.353 m/s; RMS velocity = 6.926 m/s

Probe area = 0.00162 cm²

Total droplet volume = 4.66 x 10⁻⁵ cm³

Runtime = 3.94 s

Volume flux = total volume / (probe area x run time)

$$= 4.66 \times 10^{-5} / (0.00162 \times 3.94)$$

$$= 7.3 \times 10^{-3} \text{ cm}^3/\text{cm}^2\text{s}$$

Mass flux = volume flux x liquid density

$$= 5.69 \times 10^{-3} \text{ g/cm}^2\text{s}$$

B.3 Calculation of Minimum Heat Feedback Rate for Complete Vaporization

Fuel = Kerosene

Location of injector = 6 cm upstream of EPM

Equivalence ratio = 0.5

Calculated combustion heat release = 5577.8 kW

Heat supplied to EPM for resistive heating to attain complete vaporization = 25.17 W

Combustion heat feedback rate required to achieve complete vaporization

= Heat supplied to resistive heating / combustion heat release

= $25.17 \times 100 / 5577.8$

= 0.45 %

B.4 Determination of Extinction Equivalence Ratio

Fuel = Kerosene

Coflow air: Rotameter scale – 4 units; Flowrate – 119.836 l/min;

Atomizing air: Rotameter scale – 10 units; Flowrate – 4 l/min

Total flowrate: 2063 cc/s; Porous medium surface area: 16.3 cm²

Coflow air velocity through porous medium: 126.5 cm/s

Kerosene fuel flowrate just prior to extinction: Rotameter scale - 60 units

Flowrate – 4.224 ml/min

Fuel/Air (actual): 0.0241

Extinction equivalence rate: 0.35

B.5 Calculation of Damköhler number

Distance between the leading edge of evaporation porous medium and injector (d_{ip}) =

5 cm; Effective gas velocity, $V_g = 126.5$ cm/s

Residence time, t_{res} :

$$t_{res} = \frac{d_{ip} + a \cdot t_p}{u}$$
$$t_{res} = \frac{5 + 3 \cdot 2.54}{126.5} = 99.8 \text{ ms}$$

Characteristic chemical time is calculated as:

$$t_{chem} = \frac{\delta}{S_L}$$
$$t_{chem} = \frac{0.2}{10} = 20 \text{ ms}$$

Damköhler number is then calculated as:

$$Da = \frac{t_{res}}{t_{chem}}$$
$$Da = \frac{99.8}{20} = 5$$

B.6 Calculation of Emission Index

Fuel = Kerosene

d_{ip} = 6 cm

Equivalence ratio = 0.545

CO: - 430 ppm; Mole fraction, X_{CO} - 0.00043

CO₂ - 2.45 %; Mole fraction, X_{CO_2} - 0.0245

NO - 17.5 ppm; Mole fraction, X_{NO} - 1.75×10^{-5}

O₂ - 17.2 %; Mole fraction, X_{O_2} - 0.172

Number of carbon atoms per mole of fuel, x - 12

Molecular weight of CO - 12

Molecular weight of fuel - 168

$$\text{Emission index of CO, } EI_i = \frac{X_i}{X_{CO} + X_{CO_2}} \cdot \frac{x MW_i}{MW_{fuel}}$$

$$\text{Emission index of CO, } EI_{CO} = \frac{0.00043}{0.00043 + 0.0245} \cdot \frac{12 \times 28}{168}$$

$$= 0.034496 \text{ kg/kg of fuel or } 34.5 \text{ g/kg of fuel}$$

B.7 Calculation of Pressure drop using Ergun Equation

Pore diameter = 450 μm

Porosity = 0.87

Viscosity = 1.85×10^{-5} Ns/m²

Density = 1.1614 kg/m³

Gas velocity = 2 m/s

Ergun constants: $K_1 = 150$; $K_2 = 1.75$

Ergun equation is given below:

$$\frac{\Delta p}{l} = \frac{K_1(1-\epsilon)^2 \mu}{d_p^2 \epsilon^3} U + \frac{K_2 \rho (1-\epsilon)}{d_p \epsilon^3} U^2$$

$$\frac{\Delta p}{l} = \frac{150(1-0.87)^2 1.85 \cdot 10^{-5}}{(450 \cdot 10^{-6})^2 \cdot 0.87^3} 2 + \frac{1.75 \cdot 1.1614 \cdot (1-0.87)}{450 \cdot 10^{-6} \cdot 0.87^2} U^2$$

$$= 4.24 \times 10^3 \text{ N/m}^2/\text{m}$$

$$= 1.1 \text{ cm of water (across a porous medium of 2.54 cm thickness)}$$

Appendix C

Uncertainty Calculations

C.1 Uncertainty Analysis

Uncertainties in experimental measurements were estimated using statistical theory (Wheeler and Ganji, 1998). Uncertainty consists of two parts: random or precision error (P) and fixed or biased error (B). The steps involved in the calculation of uncertainties are described below:

1. Determine the standard deviation of the sample containing 'n' data points:

$$S_x = \sqrt{\frac{\sum (x_i - \bar{x})^2}{n-1}} \quad (\text{C.1})$$

2. Determine the standard deviation of the mean, as follows:

$$S_{\bar{x}} = \frac{S_x}{\sqrt{n}} \quad (\text{C.2})$$

3. The precision error (P) is given by:

$$P = t_{\alpha/2} \cdot S_{\bar{x}} \quad (\text{C.3})$$

The value of $t_{\alpha/2}$ is obtained from Student's t-distribution table for the given number sample. The value of $\alpha/2$ is 0.025 at 95% confidence level.

4. Determine the bias error in the measurement (B)

5. Determine the overall uncertainty of the measurement, as follows:

$$w = \sqrt{P^2 + B^2} \quad (C.4)$$

Measurement data are reported as $x \pm w$ at 95% confidence.

Uncertainty in a variable R is computed by making measurements of m different variables: z_1, z_2, \dots, z_m , as follows:

$$w_R = \sqrt{\left(\frac{\partial R}{\partial z_1} w_{z_1}\right)^2 + \left(\frac{\partial R}{\partial z_2} w_{z_2}\right)^2 + \dots + \left(\frac{\partial R}{\partial z_m} w_{z_m}\right)^2} \quad (C.5)$$

C.2 Uncertainty in Sauter Mean Diameter of n-Heptane Spray

Fuel = n-Heptane; Heated coflow condition

Equivalence ratio = 0.3

Fuel = 6 ml/min

Measurement location:

Axial location = 2.5 cm upstream of evaporation porous medium entry surface

Radial = 1 mm from the spray core

Data:

Trials	SMD, microns
Trial 1	82
Trial 2	82.8
Trial 3	81.5
Trial 4	82.4
Trial 5	78.5

Average = 81.44 microns

Standard deviation = 1.71 microns

Standard deviation of mean = 0.8563

Uncertainty = 81.44 ± 2.377

C.3 Uncertainty in Extinction Equivalence Ratio

Distance between injector and upstream surface of evaporation porous medium = 6
cm

Data:

Sample	Extinction Equivalence rate
Trial 1	0.354
Trial 2	0.295
Trial 3	0.354
Trial 4	0.354
Trial 5	0.354
Trial 6	0.354

Average = 0.344167

Standard deviation = 0.024087

Standard deviation of mean = 0.010772

Uncertainty = 0.344 ± 0.028

C.4 Uncertainty in Pollutant Emission

Fuel = Kerosene

$d_{ip} = 6$ cm

Equivalence ratio = 0.545

Number of carbon atoms per mole of fuel, x - 12

Molecular weight of CO - 12

Molecular weight of fuel - 168

Trial	ϕ	CO	CO ₂	NO	O ₂
		PPM	%	PPM	%
1		590	2.4	22	17.3
2		440	2.4	23	17.3
3		280	2.5	18	17.1
4		366	2.5	16	17.1
5		332	2.5	14	17.2
6		572	2.4	12	17.3
Average		430	2.45	17.5	17.22
Standard deviation		128.1	0.06	4.37	0.1
Standard deviation of mean		57.3	0.02	1.95	0.04
Uncertainty		430 ± 147.3	2.45 ± 0.06	17.5 ± 5.02	17.22 ± 0.11

Appendix D

Nomenclature

English Symbols

a	Absorption coefficient
c_p	Heat capacity (J/kg-K)
c_s	Heat capacity of the porous medium (J/kg-K)
d	Diameter (m)
d_{ip}	Distance between the location of the injector and leading surface of the evaporation porous medium and (m)
d_o	Most probable droplet diameter (m)
g_x	Gravitational force acting along the x direction (N)
h	Convective heat transfer coefficient (W/m^2-K)
h_{fg}	Latent heat (J/kg)
h_v	Volumetric convective heat transfer coefficient (W/m^3-K)
k	Thermal conductivity (W/m-K)
k_c	Mass transfer coefficient (m/s)
l	Length of porous medium (m)
m	Mass (kg)
\dot{m}	Mass flowrate (kg/s)
n	Refractive index
p	Static pressure (N/m^2)

r	Radial or transverse coordinate (m)
\vec{r}	Position vector
s	Path length
\vec{s}	Direction vector
\vec{s}'	Scattering direction vector
t	Time (s)
t_{chem}	Characteristic chemical time (s)
t_p	Thickness of porous medium (m)
t_{res}	Spray residence time in evaporation section (s)
\bar{u}	Axial component of velocity (m/s)
\bar{v}	Radial component of velocity (m/s)
w	Half-width of the evaporation test section (m)
x	Axial coordinate (m)
A	Surface area (m ²)
C_2	Inertial Coefficient (1/m)
C_D	Drag Coefficient
$C_{i,\alpha}$	Vapor concentration in bulk gas (kgmol/m ³)
$D_{i,m}$	Diffusion coefficient of vapor (m ² /s)
Da	Damköhler number
F_D	Drag force (N)
HS	Volumetric heat source supplied to the porous medium (W)
I	Radiation intensity
K_1	Ergun constant 1

K_2	Ergun constant 2
L	Length of computational domain (m)
$M_{w,i}$	Molecular weight of i^{th} species (kg/kgmol)
N	Total number of species considered
Nu	Nusselt number
Nu_v	Volumetric Nusselt number
Oh	Ohnesorge number
Pr	Prandtl number
Q_{in}	Volumetric heat input rate to simulate combustion heat feedback (W/m^3)
R	Radius of the computational domain (m)
Re	Reynolds number
S	Swirl number
Sc	Schmidt number
S_{fd}	Source term in the gas-phase momentum conservation equation due to the presence of porous medium
S_{fp}	Source term in the gas-phase momentum conservation equation due to droplet momentum exchange
S_i	Source term of the i^{th} species in the species conservation equation due to droplet vaporization
S_L	Laminar flame speed
S_m	Source term in the continuity equation due to droplet vaporization
T	Temperature (K)
T_i	Inlet temperature of the coflow air (K)

U, u Gas velocity (m/s)
 We Weber number
 Y_i Mass fraction of i^{th} species

Greek Symbols

α	Permeability ($1/m^2$)
β	Coefficient of thermal expansion
δ	Laminar flame thickness
Δt	Time step in the liquid phase calculations
ρ	Fluid density (kg/m^3)
ρ_s	Density of the solid (kg/m^3)
ε	Porosity
μ	Viscosity (Ns/m^2)
ϕ	Overall equivalence ratio
σ	Stefan-Boltzmann constant ($5.672 \times 10^{-8} W/m^2-K^4$)
σ_s	Scattering coefficient
Φ	Phase function
Ω'	Solid angle

Subscripts

d	Droplet
eff	Effective
f	Fluid
g	Gas-phase
p	Pore
s	Solid
t	Turbulent
∞	Bulk gas (i.e., coflow air)

Superscripts

-	Mean quantity
'	Fluctuation quantity

List of Abbreviations

CO	Carbon monoxide
CO ₂	Carbon dioxide
CPM	Combustion porous medium
EPM	Evaporation porous medium
HFR	Heat feedback rate
NDIR	Non-dispersive infrared
NO	Nitric oxide
NO _x	Nitric oxide (NO + NO ₂)
O ₂	Oxygen
OH	Hydroxyl radical
LIF	Laser induced fluorescence
PDPA	Phase Doppler particle analyzer
PPCM	Pores per centimeter
PPI	Pores per inch
RSM	Reynolds stress model
SMD	Sauter mean diameter

Appendix E

Presented at 42nd AIAA Aerospace Sciences Meeting, Reno, NV, January 2004

NUMERICAL MODELING OF EVAPORATION PROCESS IN POROUS MEDIA FOR GAS TURBINE APPLICATIONS

Chendhil Periasamy¹, Sathish K. Sankara Chinthamony¹, and S. R. Gollahalli²
Combustion and Flame Dynamics Laboratory
School of Aerospace and Mechanical Engineering
The University of Oklahoma, Norman, OK-73019

ABSTRACT

A simplified numerical model for analyzing the evaporation processes in porous media for gas turbine applications has been developed. Evaporation of a pointwise-injected kerosene spray in a carbon-carbon porous medium is considered. The computational model consists of a two-dimensional domain of dimensions 20.32x4.04 cm. A control-volume based discretization method is adopted to solve the governing equations. The porous medium offers resistance to the flow of air-fuel mixture and is modeled as a momentum sink. Non-Darcy flow in porous medium is considered and the viscous and inertial contributions are evaluated using a modified Ergun equation. The transient and conduction flux terms in the energy equation are modified to account for the heat transfer in porous medium. Energy feedback from combustion porous media is also simulated using a source term. The effects of porous medium temperature, fuel flow rate, air inlet temperature and porous medium geometry on the evaporation of spray have been analyzed. For the size under consideration, a porous medium heat source of 642 W is required to achieve 97 % complete evaporation for an air inlet temperature of 473 K. The concentration of fuel vapor is found to be higher in the core region due to the nature of point injection. Simulations using different flow rate conditions show that a stronger heat source, in turn higher energy feed back, is required to attain complete vaporization. Approximately a 62 % stronger heat source is required when the

Keywords: Porous media, Liquid fuel, Evaporation, Numerical modeling

¹Graduate Research Assistant, Student Member AIAA

²Associate Fellow AIAA, Lesch Centennial Chair

fuel flow rate is increased from 0.24 to 0.48 mg/s. The increase in air inlet temperature is found to accelerate the evaporation process. At higher air inlet temperatures (573 K), the fuel is vaporized as soon as it gets injected. Evaporation characteristics are not found to vary much with porous medium geometry, as the porous medium is modeled as a momentum sink. Thermal effects of porous media are found to be more dominant in this study.

INTRODUCTION

Spray combustion is a common method of energy production using liquid fuels and it is an important mode of combustion in gas turbines. Current research on the gas turbines has been directed to the development of the engines with higher combustion efficiency and lower emission level. Combustion in porous media (PM) is a potential technique for reducing NO_x and CO emissions and improving the power density. It also possesses several other advantages such as extension of lean flammable limits, stable operation over a wide range of loads, and uniform mixing of fuel/air mixture. In the present study, a simplified computational model for analyzing the evaporation processes in porous media for gas turbine applications has been described.

Weinberg¹ showed that the recirculation of heat energy from reaction zone to the unburned mixture offers a number of benefits such as extension of lean flammability limits, increase in reaction rate, burning of low-grade fuels etc. The burners designed based on this concept can operate under locally higher enthalpy conditions than that of adiabatic ones. Such types of combustion systems are termed as 'excess enthalpy flames'. Experimental investigations of Kotani and Takeno² proved that the insertion of a

porous solid in the reaction zone makes the heat energy recirculate into the unburned mixture. Subsequently, a variety of research and industrial porous burners have been developed and tested. The current knowledge on the fluid mechanics and heat transfer aspects of porous medium³⁻⁶ helps us to measure the pressure drop, heat transfer coefficient, and radiative properties of the porous medium. Quantification of such parameters in porous media has led the combustion engineers to develop compact and efficient porous burners. In the past two decades, considerable amount of experimental and numerical work has been carried out on the combustion of gaseous fuels in porous media. Recently, Lammers and de Goey⁷ have conducted a numerical study on the flash back of the premixed flames, stabilized on the surface of a ceramic burner. They have reported the stability diagrams and flash-back regimes. Howell *et al.*⁸ and Viskanta⁹ have presented a critical review of this subject.

Combustion using liquid fuels has not been attempted until recently, owing to the belief that the liquid fuel could plug the medium. But, the experimental study conducted by Kaplan and Hall¹⁰ has not shown any evidence for this phenomenon. They tested various designs of heptane-fueled radiant burners to analyze the stable operating ranges and measured the emissions. Stable combustion was achieved over the equivalence ratio range of 0.57-0.67. The study reports that stability is primarily affected by the droplet size and the distance between the porous medium and nozzle. Combustion was complete and the emissions were found to be as low as 3-7 ppm and 15-20 ppm for CO and NOx respectively. Later, Jugjai *et al.*¹¹ supplied kerosene fuel dropwise, using a syringe, in an effort to understand the evaporation mechanism inside the porous burner. The combustion characteristics were also obtained by measuring the temperature profile. The flame stabilization was achieved by inducting a stream of swirling air. Complete vaporization was reported. The effects of equivalence ratio, optical thickness of the porous medium and thermal input on combustion characteristics were also determined. Haack¹² studied the evaporation and combustion of droplets in porous media numerically. Effects of radiative heat transfer have been described with respect to single-droplet conditions and flame speeds have been determined. However,

the implementation of porous medium combustion for gas turbine combustor applications is still in its infancy.

In gas turbine combustion systems, the pre-combustion events are very crucial and understanding them helps simplifying the complexities involved in the combustion processes. Such physical processes can be broadly divided into two regimes, namely, evaporation and mixing. Porous medium can be used to enhance evaporation and mixing, apart from improving combustion characteristics. In porous media combustion experiments, generally two porous media are placed in the chamber, one (combustion porous media, CPM) in the reaction zone, and the other (evaporation porous media, EPM) in the upstream of the reaction zone. A typical setup is shown in Fig. 1. CPM is heated during combustion and establishes a heat feedback to EPM by radiation. The heated EPM medium enhances the evaporation of liquid spray injected onto it. Small-scale turbulence, which is inherent to the porous media, improves the mixing. Since EPM is heated, it also preheats the vapor-air mixture and hence prepares uniform flammable mixture for combustion.

THEORY

This section describes the governing equations and solution procedure employed for the evaporation process in porous media. Equations for porous media and droplet phase are added to the gas phase equations and the resultant equations are solved.

Permeability Model

Pressure drop across the porous medium and the permeability of the porous media are related by flow rate, properties of the fluid, and the geometry of the medium³. Development of an analytical equation for pressure drop is a daunting task because of the complex structure of the medium. However, semi-empirical relationships do exist in the literature^{3,5}. At low flow rates, the pressure drop is proportional to the viscous forces and the flow obeys Darcy's law. But under high flow rate conditions, the inertial forces also contribute to the pressure drop and warrant the use of Forchheimer equation. Often, the pressure drop data at different flow rates are obtained and least-square

fits are made to fit the data in the following format:

$$\frac{(\Delta p/L)}{u} = A + Bu \quad (1)$$

where A and B are correlation coefficients.

In this work, the modified Ergun Equation⁴ shown below, is used to model the permeability of the medium:

$$\frac{\Delta p}{L} = \frac{K_1(1-\varepsilon)^2 \mu}{d_p^2 \varepsilon^3} u + \frac{K_2 \rho (1-\varepsilon)}{d_p \varepsilon^3} u^2 \quad (2)$$

where K_1 and K_2 are Ergun constants.

Model Assumptions

In order to simplify the modeling process, the following assumptions are made:

- (1) Local thermal equilibrium between the porous medium and the liquid spray is assumed. This eliminates the need for solving two energy equations.
- (2) No radiative heat transfer from the porous medium is considered.
- (3) Porous medium is modeled as a momentum sink. The effects of pore velocity are included in the source/sink term and the governing equations are written in terms of gas phase velocity.
- (4) Effects of porous medium on turbulence generation or dissipation are neglected.
- (5) Effects like film formation in the porous medium and fuel pyrolysis are neglected.

Governing Equations

Since liquid fuel is injected into a solid medium in the presence of co-flow air, a set of multi-phase governing equations is necessary to completely represent the problem. Based on the assumptions stated, the governing equations can be written as follows:

Continuity Equation

$$\frac{\partial(\rho\varepsilon)}{\partial t} + \nabla \cdot (\rho \vec{v}) = S_{md} \quad (3)$$

where S_{md} is the mass source term due to droplet vaporization.

Momentum Equation

$$\frac{\partial}{\partial t} (\rho\varepsilon \vec{v}) + \nabla \cdot (\rho \vec{v} \vec{v}) = -\nabla p + \nabla \cdot (\vec{\tau}) + S_{fp} + S_{fd} \quad (4)$$

where S_{fp} and S_{fd} are the source terms caused by porous media and droplet vaporization respectively.

The porous media source term depends on its permeability of the medium to the fuel-air mixture and is given the following form:

$$S_{fp} = -\left(\frac{\mu}{\alpha} u + C_2 \frac{1}{2} \rho u^2 \right) \quad (5)$$

In Equation 5, the first term represents the pressure drop due to viscous force and the second one accounts for the inertial force. The unknown quantities permeability and the inertial coefficient are calculated from the modified Ergun equation (by comparing Equations 2 and 5).

Energy Equation

Heat transfer in porous media region is modeled by introducing a thermal inertia of solid region on the medium (in the transient term) and by an effective thermal conductivity in the conductive flux. The resultant energy equation is given below:

$$\begin{aligned} & \frac{\partial}{\partial t} (\varepsilon \rho_f E_f + (1-\varepsilon) \rho_s E_s) + \nabla \cdot (\vec{v} (\rho_f E_f + p)) \\ & = \nabla \cdot \left[k_{eff} \nabla T - \left(\sum_i h_i J_i \right) \right] + S_{hp} \end{aligned} \quad (6)$$

Effective thermal conductivity, k_{eff} is calculated as a volumetric average between solid and gas phases, as shown in Eq. 7.

$$k_{eff} = \varepsilon k_f + (1-\varepsilon) k_s + k_t \quad (7)$$

where k_t is the turbulent thermal conductivity, which is calculated for non-porous regions as $\frac{c_p \mu_t}{Pr_t}$. In porous region, it is assumed to be 0 and in non-porous regions, it is set to 1. S_{hp} is the interphase exchange source term due to droplet vaporization.

Species Conservation

Species conservation for evaporated liquid can be given as:

$$\frac{\partial}{\partial t}(\rho \epsilon Y_i) + \nabla \cdot (\rho \vec{v} Y_i) = -\nabla \cdot \vec{J}_i + S_i \quad (8)$$

where S_i is the contributions from dispersed phase. The present study deals with evaporation and mixing, and hence no reaction is considered, only heat and mass transfer are considered. The diffusion flux of i^{th} species \vec{J}_i is calculated as, for turbulent flows:

$$\vec{J}_i = -\left(\rho D_{i,m} + \frac{\mu_t}{Sc_t} \right) \nabla Y_i \quad (9)$$

Droplet Heating and Vaporization

When the droplet temperature is lower than its critical vaporization temperature (a numerical property to trigger the vaporization process), heat is transferred to the droplet from the hot surroundings and the droplet is heated transiently. No mass is transferred from the droplet. If the droplet reaches the critical vaporization temperature, mass transfer occurs and the droplet size starts to decrease. This process continues to occur until it reaches its boiling point or the volatile fraction is completely consumed.

The heat transfer to the droplet during these processes is given as:

Heating:

$$m_d c_{p,d} \frac{dT_d}{dt} = h A_d (T_\infty - T_d) \quad (10)$$

Vaporization:

$$m_d c_{p,d} \frac{dT_d}{dt} = h A_d (T_\infty - T_d) + \frac{dm_d}{dt} h_{fg} \quad (11)$$

Heat transfer coefficient is evaluated from Ranz and Marshall type correlations^{13,14}.

Mass transfer:

The molar flux of droplet vapor into the continuous phase (N_i) is evaluated as follows:

$$N_i = k_c (C_{i,s} - C_{i,\infty}) \quad (12)$$

Mass transfer coefficient, k_c , is evaluated from Nusselt number correlation^{13,14}, which is given below.

$$Nu = 2.0 + 0.6 Re_d^{1/2} Sc^{1/3} = \frac{k_c d_d}{D_{i,m}} \quad (13)$$

The concentration of vapor at the droplet surface ($C_{i,s}$) is calculated by assuming the partial pressure of vapor at the interface between droplet and continuous phase is equal to the saturated vapor pressure. The reduction in mass is then computed according to the following equation:

$$m_d(t + \Delta t) = m_d(t) - N_i A_d M_{w,i} \Delta t \quad (14)$$

Droplet Boiling

When the droplet reaches its boiling point, a convective boiling rate equation¹⁵ shown below, is applied.

$$\frac{d(d_d)}{dt} = \frac{4k_\infty}{\rho_p c_{p,\infty} d_p} \left[1 + 0.23 \sqrt{Re_d} \right] \ln \left[1 + \frac{c_{p,\infty} (T_\infty - T_p)}{h_{fg}} \right] \quad (15)$$

The boiling condition requires that the continuous phase temperature be greater than the droplet temperature. Also, the droplet temperature remains fixed during boiling.

Boundary Conditions

Air stream: Stoichiometric fuel-air mass ratio is 0.06798. An equivalence ratio of 0.68 and an air

inlet velocity of 4.32 m/s were employed. The inlet air was preheated to 473 K.

Droplet stream: Kerosene droplets (treated as a single-component liquid of $C_{12}H_{23}$) were injected at 20 m/s with a mass flow rate of 0.24 mg/s. The droplet diameter was taken to be uniform (no variation in droplet diameter is considered) and equal to 50 μm . Duration of injection was 1 s. All the droplet properties were monitored at 10 ms interval.

Grid Generation

A 2D rectangular geometry (shown in Fig. 2) of size 0.0404 x 0.2032 m is considered for the study. Cartesian type, rectangular, uniform grid with 10 points per centimeter is generated using a commercial grid generation code *Gambit*. Shown in Fig. 3 is the computational grid employed in this study.

Solution Procedure

Governing differential equations are integrated about each control volume. This process yields a set of algebraic equations that conserve a quantity on a control-volume basis. The resultant algebraic equations are then solved numerically. Pressure and velocity coupling is achieved using SIMPLE algorithm¹⁶. Momentum, energy, turbulence and species transport equations are discretized using the First-order upwind scheme. Temporal differencing is achieved by second-order implicit method.

Coupling Between Continuous and Discrete Phases

When a particle stream passes through the control volume, heat, mass, and momentum exchange take place between the droplet stream and continuous phase. The exchange terms are calculated by coupling the discrete phase and continuous phase calculations. These appear as source or sink terms in the continuous phase governing equations.

The above-mentioned calculations for continuous and discrete phases are performed using a commercial solver *Fluent 6.0*.

RESULTS AND DISCUSSION

In this section, the results obtained using the simplified numerical model are discussed.

Properties of the Porous Medium

The porous medium properties are obtained from the manufacturer's (ULTRAMET) catalog¹². The important physical properties are listed in Table 1.

Table 1 Important physical properties of the porous medium

Property	Value
Porosity (approx.)	0.87
Pore size, micrometers	190
Pores Per Centimeter	31.5
Thermal conductivity at 200° C (W/m K)	1
Cp, J/kg-K	1422.6
Bulk Density, kg/m ³	320

Grid Sensitivity Analysis

Different grid sizes of 16x80, 32x160, 40x200, 48x240, 64x320, and 80x400 were tested and the vapor concentration profiles were obtained at an axial distance of 0.19 m. The result is given in Fig. 4. Solutions obtained using the grid sizes above 40x200 were found to be insensitive to the grid sizes employed. A grid size of 40x200 was therefore used in this study.

Droplet Transient Heating

The raise in droplet temperature along the centerline due to transient heating is shown in Fig. 5. The porous medium temperature and air inlet temperature were 596 K and 473 K respectively. It can be seen from Fig. 5 that the droplets are heated to 470 K before they enter the porous media. This heating is provided by the preheated co-flow air. However, this alone is not sufficient for complete vaporization. Additional energy input was supplied by porous medium and the droplets were brought to their boiling point.

Effect of Porous Medium Temperature

In actual combustion experiments, the energy feedback from combustion porous media heats the evaporation porous media. Since the present study deals with evaporation and does not model combustion, different temperatures for porous medium are achieved by introducing an energy source term in the porous medium. Fig. 6 shows the temperature attained by the medium as a function of heat source. In all the simulations, air inlet temperature was held constant at 473 K. The porous medium heat source was varied from 40 to 642 W and accordingly the temperature achieved by the porous medium was between 480 K and 596 K. In all the cases, vapor concentration profiles were obtained at $x=0.19$ m. Fig. 7 shows the vapor concentration profiles as a function of normalized transverse distance. It can be seen that the vaporization increases with increase in porous medium temperature. This is due to the thermal effects of the medium. For a complete vaporization case (i.e. 97 % of the injected fuel is vaporized and the rest are still within the domain in liquid phase), the vapor concentration profiles taken at $x=0.08$, 0.13, 0.15, and 0.19 m are shown in Fig. 8. This shows that only about less than 5 % vaporization takes place before the porous medium. The vaporization increases considerably towards the exit of the porous medium (40 %) and attains complete vaporization before it leaves the domain. It is also worth to note that the vapor is concentrated at the core due to the nature of point injection. However, it can be seen from Figs. 7 and 8 that the vapors start to diffuse radially.

The effect of heat source strength on percent mass evaporation is shown in Fig. 9. When a heat source of 41 W is supplied to the porous medium, the maximum temperature reached is 481 K. In this situation, the droplet particles are heated up to 475 K. It is observed that only 7.6 % of the supplied fuel evaporates completely. A further raise in heat source increases the completeness of evaporation. When the supplied heat source is at 642 W, 97 % of the injected particles are evaporated.

Effect of Fuel Flowrate

The flow rates of co-flow air and kerosene were varied in order to attain different operating

conditions. Various such conditions simulated in this study are listed in Table 2. For an overall equivalence ratio of 0.68, the complete evaporation was achieved when a porous heat source of 642 W was supplied. Fig. 10 shows the effect of heat source on percentage mass of evaporation for different fuel flow rates. As the fuel flow rate increases, it is found that a stronger heat source is required to completely vaporize the fuel. A heat source of 932 W was required to maintain the complete evaporation when the fuel flow rate was 0.48 mg/s. Under complete evaporation conditions, the radial profiles of vapor concentration at $x=0.19$ m for different flow rates are shown in Fig. 11. When the equivalence ratio was increased from 0.68 to 1.2, the peak vapor concentration was also increased by 62 %. In practical combustors employing porous medium, when the fuel flow rate increases, the power output will also increase. This could result in higher energy feedback from combustion porous media, which compensates the need for higher heat source.

Table 2 Test conditions for flow rate analysis

Air flow rate, kg/s	Fuel flow rate, mg/s	Equivalence Ratio
0.005198	0.24	0.6766
0.005854	0.36	0.9
0.005854	0.48	1.2

Effect of Inlet Air Temperature

In this case, the heat source strength supplied to the porous medium was held constant and hence the temperature of the medium was fixed at 595 K. Air inlet temperature was varied from 373 K to 573 K and kerosene vapor concentration profiles were obtained. The effect of air inlet temperature on the percentage evaporation is presented in Fig. 12 and the radial vapor concentration profiles at $x=0.19$ m for different inlet temperatures are given in Fig. 13. At 373 K, the droplets are found to be evaporating more in the porous medium than in the upstream section. However, at higher air inlet temperatures, almost all the liquid is evaporated even before entering the porous medium, since the air temperature itself is sufficient to vaporize the fuel.

Effect of Porous Medium Geometry

In this study, porosity and pore diameter are considered to represent the porous medium geometry. Two different simulations were performed. First, the porosity was varied from 0.4 to 0.87 keeping the pore diameter constant at 190 μm . Next, the pore diameter was varied from 190 to 450 μm while keeping the porosity constant at 0.87. In both the cases, the temperature of the medium was held constant at 595 K. The variations in vapor concentration and percentage mass evaporation were found to be not affected by the porous medium geometry. This could be due to the fact that this study treats the porous medium as a momentum sink and mainly the thermal effects are modeled here. Various values of porosity and pore size transform themselves into different values for resistance coefficients for the source/sink term. Inclusion of fluid dynamics aspects in the model would make this issue much clearer.

CONCLUSIONS

A simplified computational model has been developed in this study to analyze the evaporation process in a porous medium. Radial profiles of kerosene vapor concentration were obtained at different axial locations. The effects of porous medium temperature, fuel flow rate, inlet air temperature and the porous medium geometry on vaporization were analyzed. Thermal effects of porous medium was found to be more dominant in the evaporation process. However, in order to predict more realistic results, further research in this field is directed in the following areas: (1) accounting for the radiation from the porous medium, which leads to local thermal non-equilibrium (2) incorporation of more realistic porous models which includes turbulence generation inside the porous media.

NOMENCLATURE

$c_{p,d}$	Droplet heat capacity (J/kg-K)
d	Diameter (m)
h	Convective heat transfer coefficient (W/m ² -K)
h_{fg}	Latent heat (J/kg)
k	Thermal conductivity (W/m-K)

kc	Mass transfer coefficient (m/s)
m	Mass (kg)
p	Static pressure (N/m ²)
u	Axial velocity (m/s)
A	Surface area (m ²)
C_2	Inertial Coefficient (1/m)
$C_{i,\alpha}$	Vapor concentration in bulk gas (kgmol/m ³)
$D_{i,m}$	Diffusion coefficient of vapor (m ² /s)
E	Total energy ($h - \frac{p}{\rho} + \frac{v^2}{2}$)
L	Length of porous medium (m)
$M_{w,i}$	Molecular weight of i^{th} species (kg/kgmol)
Re	Reynolds number
Sc	Schmidt number
S_{hp}	Porous heat source (W/m ³)
T	Temperature (K)
T_i	Air inlet temperature (K)
T_p	Porous medium temperature (K)
T_∞	Local temperature of the gas phase (K)
Y_i	Mass fraction of i^{th} species

Greek symbols

α	Permeability (1/m ²)
ρ	Density (kg/m ³)
ε	Porosity
μ	Viscosity (Ns/m ²)
τ	Stress tensor ($\mu[(\nabla\vec{v} + \nabla\vec{v}^T) - \frac{2}{3}\nabla\cdot\vec{v}\mathbf{I}]$)

Subscripts

d	Droplet
eff	Effective
f	Fluid
p	Pore
s	Solid
t	Turbulent
∞	Bulk gas

REFERENCES

- ¹Weinberg, F.J. (1971), "Combustion Temperatures: The Future?," *Nature*, Vol. 233, September 24, pp. 239-241.
- ²Kotani, Y., and Takeno, T. (1982), "An Experimental Study on Stability and Combustion Characteristics of an Excess Enthalpy Flame,"

Nineteenth Symposium (International) on Combustion, pp. 1503-1509.

³Ergun, S. (1952), "Fluid Flow Through Packed Columns," *Chemical Engineering Progress*, Vol. 48, No. 2, pp. 89-94.

⁴Macdonald, I.F., El-Sayed, M.S., Mow, K., and Dullien, F.A.L. (1979), "Flow Through Porous Media – the Ergun Equation Revisited," *Industrial and Engineering Chemistry Fundamentals*, Vol. 18, No. 3, pp. 199-208.

⁵Kaviany, M. (1995), *Principles of Heat Transfer in Porous Media*. Springer-Verlag New York, Inc.

⁶Lee, K-B., and Howell, J.R. (1991), "Theoretical and Experimental Heat and Mass Transfer in Highly Porous Media," *Int. J. Heat Mass Transfer*, Vol. 34, No. 8, pp. 2123-2132.

⁷Lammers, F.A., and de Goey, L.P.H. (2003), "A Numerical Study of Flash back of Laminar Premixed Flames in Ceramic-foam Surface Burners," *Combustion and Flame*, Vol. 133, pp. 47-61.

⁸Howell, J.R., Hall, M.J., and Ellzey, J.L. (1996), "Combustion of Hydrocarbon Fuels Within Porous Inert Media," *Progress in Energy and Combustion Science*, Vol. 22 pp. 121-145.

⁹Viskanta, R. (1995), "Interaction of Combustion and Heat Transfer in Porous Inert Media," in *Transport Phenomena in Combustion*, Ed. S.H. Chan, Taylor and Francis, pp. 64-87

¹⁰Kaplan, M., and Hall, M.J. (1995), "The Combustion of Liquid Fuels Within a Porous Media Radiant Burner," *Experimental Thermal and Fluid Science*, Vol. 11, pp. 13-20.

¹¹Jugjai, S., Wongpanit, N., Laoketkan, T., and Nokkaew, S. (2002), "The Combustion of Liquid Fuels Using a Porous Medium," *Experimental Thermal and Fluid Science*, Vol. 26, pp. 15-23.

¹²Haack, D.P., *Mathematical Analysis of Radiatively Enhanced Liquid Droplet Vaporization and Liquid Fuel Combustion Within a Porous Inert Media*, MS Thesis, Dept. Mech. Eng., Univ. Texas, Austin, TX, May 1993.

¹³Ranz, W. E. and Marshall, Jr, W. R., (1952), "Evaporation from Drops, Part I," *Chem. Eng. Prog.*, Vol. 48(3), pp. 141-146.

¹⁴Ranz, W. E. and Marshall, Jr, W. R., (1952), "Evaporation from Drops, Part II," *Chem. Eng. Prog.*, Vol. 48(4), pp. 173-180.

¹⁵Kuo, K.K.Y., (1986), *Principles of Combustion*. John Wiley and Sons, New York.

¹⁶Patankar, S.V., (1980), *Numerical Heat Transfer and Fluid Flow*. Hemisphere Publishing Corporation.

¹⁷Ultrafoam website: <http://www.ultramet.com/>

ACKNOWLEDGEMENT

This work was supported by the US Army Research Laboratory and the US Army Research Office (Contract Number: DAAD 190210082). The authors thank Mr. Benjamin D. Baird and Dr. Sien-Fong Goh for their useful suggestions.

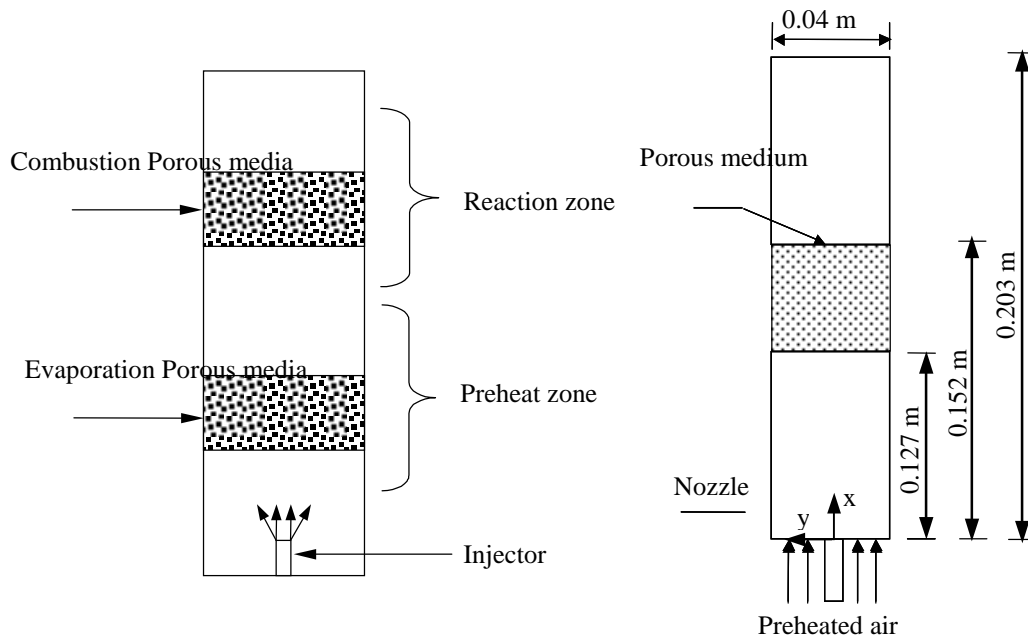


Fig. 1 Typical Porous Media Setup in Gas turbine Combustors

Fig. 2 Physical Geometry Considered for the Present Study

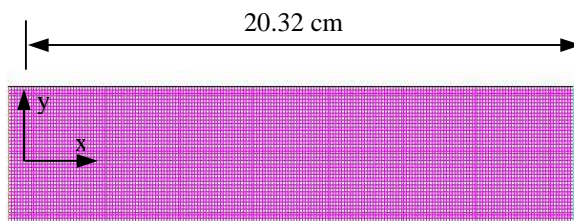


Fig. 3 Grid Employed in the Study

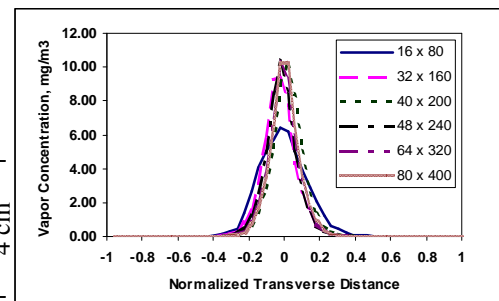


Fig. 4 Effect of Grid Size on Vapor Concentration at $x = 0.19$ m

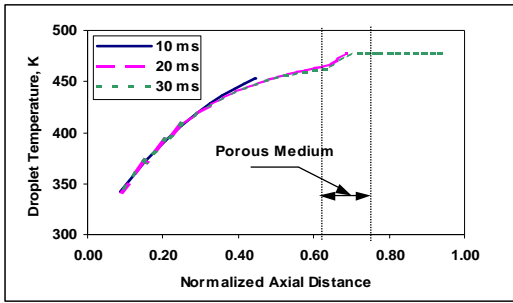


Fig. 5 Variation of Droplet Temperature along the Centerline of the Domain ($T_p=596\text{K}$ and $T_i=473\text{K}$)

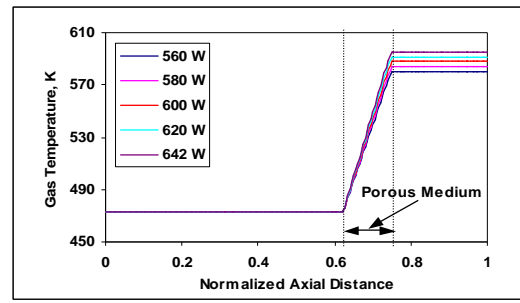


Fig. 6 Effect of Porous Medium Heat Source on the Gas Temperature along the Centerline of the Domain

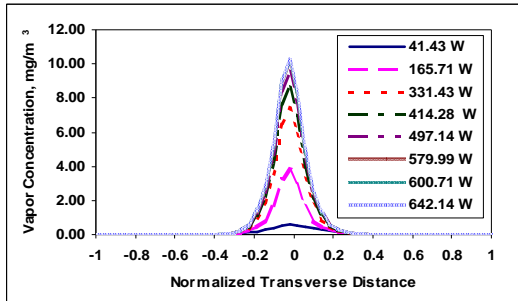


Fig. 7 Effect of Porous Medium Heat Source on Evaporation at $x = 0.19 \text{ m}$

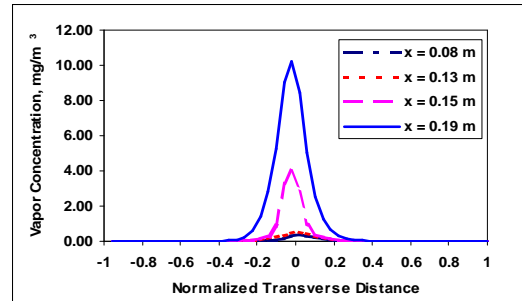


Fig. 8 Vapor Concentration Profiles at Different Axial Locations for a Porous Medium Heat Source of 642 W

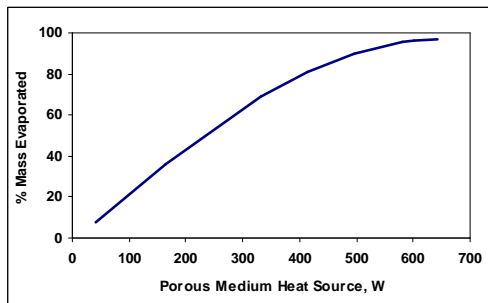


Fig. 9 Effect of Porous Medium Heat Source on the Completeness of Evaporation

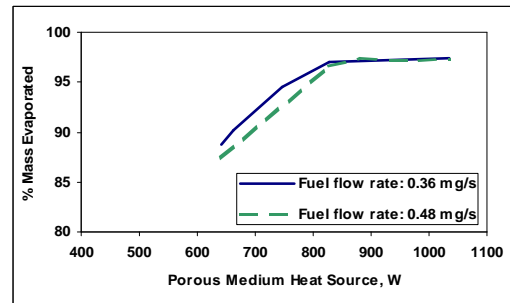


Fig. 10 Effect of Porous Medium Heat Source on Vaporization for Different Fuel Flow rates

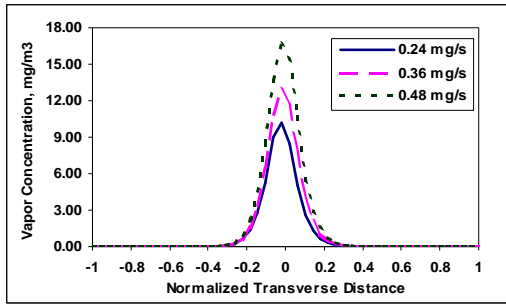


Fig. 11 Effect of Fuel Flow rate on Vapor Concentration (Axial Location, $x = 0.19$ m)

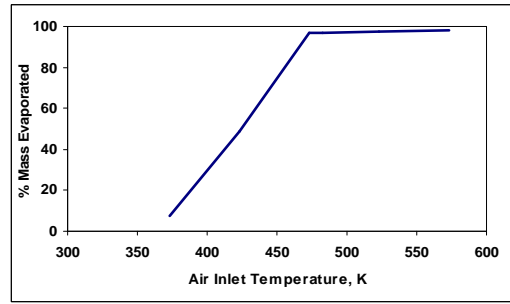


Fig. 12 Effect of Air Inlet Temperature on the Completeness of Evaporation

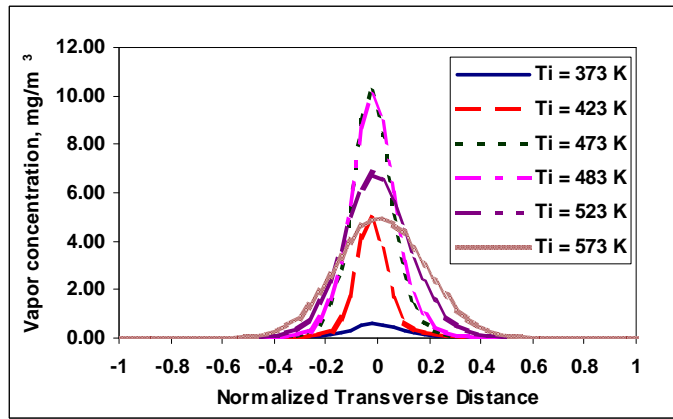


Fig. 13 Vapor Concentration Profiles at $x = 0.19$ m for Different Air Inlet Temperatures

Appendix F

Proceedings of ASME Power'04
March 30 – April 1, 2004, Baltimore, Maryland

PWR2004-52016

A COMPUTATIONAL STUDY OF THE EVAPORATION CHARACTERISTICS OF AN AIR-BLAST ATOMIZED, KEROSENE SPRAY IN POROUS MEDIA

Chendhil Periasamy*, **Sathish K. Sankara Chinthamony***, and **S. R. Gollahalli#**

Combustion and Flame Dynamics Laboratory
School of Aerospace and Mechanical Engineering
The University of Oklahoma, Norman, OK – 73019
E-mail: gollahalli@ou.edu

ABSTRACT

The evaporation characteristics of an air-blast atomized kerosene spray in porous media in a 2D-axisymmetric coflow environment were studied numerically. A swirling primary air stream with varying intensity was used to aid the atomization process. The effects of non-Darcy flow in porous medium were modeled using a modified form of Ergun equation. Local thermal equilibrium between the fluid mixture and porous medium was assumed. Conductive and transient heat flux terms in the energy equation were modified to include the effective thermal conductivity and thermal inertia of the solid region respectively. The effective thermal conductivity was defined as the volumetric average between solid and fluid media. First, the temperature characteristics of the porous medium, arising from different source terms, were obtained. Complete vaporization of kerosene was achieved when the maximum temperature of the porous medium was at 590 K. The effects of porous medium temperature, primary air swirl number, fuel flow rate, and secondary (coflow) air inlet temperature on vaporization were analyzed. For all cases, kerosene vapor concentration profiles at

five different axial locations in the domain (0.08, 0.12, 0.13, 0.14, and 0.19 m from the nozzle) were obtained. An increase in secondary air inlet temperature from 373 K to 473 K increased the completeness of evaporation from 94% to 97%. When the swirl number was increased from 0.14 to 0.34, the peak vapor concentration was reduced by 31% and more vapor spread radially. The porous medium temperature was found to be a crucial factor in obtaining the complete vaporization of the spray.

Key words: Porous media, evaporation, spray, and modeling.

INTRODUCTION

Porous media combustion, one of many modern combustion techniques, was developed mainly to reduce the emission level and increase power output of a combustor. If a porous solid is inserted in the flame zone, the product gas enthalpy can be transferred upstream in turn, preheating the fresh air-fuel mixture. This concept is described by Weinberg [1,2] and Takeno and his coworkers [3,4] and has been researched extensively in the recent past. Various studies reveal that combustion in porous media offers several benefits over open flames, such as reduced pollution level, compact burner

* Graduate Research Assistant

Fellow ASME, Lesch Centennial Chair

size, extended lean flammability limit, and increased reaction rate. Review articles by Howell et al. [5] and Viskanta [6] and a book by Kaviany [7] are worth to mention. However, most of the studies considered gaseous combustion [8-9]. Liquid fuel combustion constitutes a major portion in the power industry and thus the application of porous combustion to liquid fuels would lead to the potential development of more efficient engines.

Experimental studies on liquid fuel combustion in porous media were performed by Kaplan and Hall [10] for heptane-fueled radiant burners. Flame stability was found to be mainly affected by the droplet size and the distance between the porous medium and nozzle. Stable combustion was achieved over an equivalence ratio range of 0.57-0.67 and the emissions were found to be as low as 3-7 ppm and 15-20 ppm for CO and NO_x respectively. However, no detailed evaporation characteristics were reported. Jugjai et al. [11] conducted an experimental study using kerosene in a porous burner. The effects of equivalence ratio, optical thickness of the porous medium and thermal input on combustion characteristics were reported. Haack [12] numerically studied the evaporation and combustion of a single droplet in porous media. The effects of radiative heat transfer from porous media on the evaporation and combustion characteristics were analyzed.

In a previous paper [13], the authors have described a computational model for the evaporation of a point-wise injected kerosene spray in porous media. In this paper, the computational model has been extended to air-blast atomized spray evaporation in porous media. The specific objectives are to study the effect of primary air (atomizing) swirl on the evaporation process and to obtain the vapor concentration profiles for different porous medium temperatures, secondary air inlet temperatures, and fuel flow rates.

MODEL FORMULATION

A 2D-axisymmetric computational model is employed in this study and it is similar to the one presented in Ref. 13. Model assumptions, equations for permeability, and governing equations can be found in Ref. 13 and

will not be repeated for brevity. The porous media is represented as a source term (S_F) in the gas-phase momentum equation. The source term is given by,

$$S_F = -\left(\frac{\mu}{\alpha} v_i + C_2 \frac{1}{2} \rho |v_i| v_i\right) \quad (1)$$

where μ is the fluid viscosity, ρ is the fluid density, v_i is the velocity component, α is the permeability, and C_2 is the inertial coefficient.

The permeability and inertial coefficient in Eq. 1 are determined through a modified Ergun equation [13]. The inertial coefficient accounts for non-Darcy flow in the porous medium. Effective thermal conductivity of the porous medium is computed as a volumetric average between the gas and solid medium. In the porous region, the conductive heat flux is modified to include the effective thermal conductivity and the transient term is modified to include the thermal inertia of the solid. The convective heat transfer coefficient between the solid and fluid is assumed to be infinite (i.e., the assumption of local thermal equilibrium).

Atomizer Model

The air-blast atomizer model employed in this study is based on the Linearized Instability Sheet Atomization (LISA) model of Schmidt et al. [14]. This model neglects the nozzle internal details but relies on the external spray characteristics. In this model, a primary swirling air stream is supplied through the nozzle along with the liquid. The physical processes that convert the liquid into fully developed droplets can be thought of occurring in three stages: film formation, sheet breakup and atomization. Film formation is due to the centrifugal action of the swirling air. The liquid sheet breakup and formation of ligaments are due to the growth of long waves. Further breakup of ligaments results in droplets, which is called the atomization. Complete description about the LISA model can be found in Ref. 14. The most probable diameter (d_o) is related to ligament diameter (d_l) as follows:

$$d_o = d_l (1 + 3Oh)^{1/6} \quad (2)$$

In Eq. 2, the Ohnesorge number (Oh) is defined as $\sqrt{We/Re}$, where We and Re are the liquid Weber and Reynolds numbers respectively. The expression for swirl number (SN) of the primary air is given as follows [15]:

$$SN = \frac{G/2}{1-(G/2)} \quad (3)$$

where G is the ratio between swirl velocity and axial velocity.

Boundary Conditions

Primary air stream: Air at 300 K was supplied through the atomizer at various swirl strengths. In all the cases, the axial velocity component was held constant at 20 m/s and the swirl velocity component was varied to achieve different swirl numbers.

Secondary air stream: This was supplied as a coflow stream and was preheated to different temperatures (373 K-473 K). Depending on the overall equivalence ratio of the mixture, the inlet air mass flow rate was fixed. For instance, a mass flow rate of 5.85 mg/s was used for an overall equivalence ratio of 0.6, and inlet temperature of 473 K. The stoichiometric fuel-air mass ratio is 0.068.

Droplet stream: Kerosene was assumed to be a single-component liquid of $C_{12}H_{23}$. A 4 mm-diameter injector was used with the spray half angle of 15° . The fuel flow rate was 0.24 mg/s. The maximum relative velocity between the atomizing air and liquid sheet was 80 m/s and the sheet breakup and ligament constants were 10 and 0.5 respectively.

Grid Generation

The physical geometry of the problem under study and the typical grid used are shown in Figs. 1 and 2 respectively. The domain size is 20 x 2 cm. A grid size of 40x200 was selected. A commercial grid generation code *Gambit*, was used for this purpose. The atomizer was located at $x=0$ and the distance between the atomizer and porous media was 0.127 m.

Solution Methodology

A finite-volume based solution procedure [16] has been adopted in this work. The convective terms in the momentum, energy, turbulence and species transport equations were discretized using the Power-Law scheme and the pressure-velocity coupling was achieved using the SIMPLE algorithm. The heat and mass transfer from evaporating droplets were included via source and sink terms in the appropriate governing equations. All the calculations were performed using a commercial solver *Fluent 6.0*.

Since this model employs swirling flow, steady state calculations were performed first by introducing small swirl strength. Then the desired swirl number was achieved in steps, ensuring convergence at all the steps. Then the atomizer was turned on and unsteady calculations were performed.

Grid Sensitivity Analysis

Simulations were performed for different grid sizes of 16x80, 32x160, 40x200, 48x240, and 64x320 and kerosene vapor concentration profiles were obtained at an axial location of 0.19 m. The result is presented in Fig. 3. In all the cases, the qualitative trend was similar and the predicted peak concentration varied from 0.05% to 13.44%. Except the 16x80 grid size, the solutions showed a clear grid independency (<8% variation in peak concentration). So, striking a balance between the total run time and accuracy, a grid size of 40x200 was chosen for further analysis.

RESULTS AND DISCUSSION

The computational model described in the previous section has been applied to the evaporation of kerosene sprays. Detailed studies on the effects of porous medium temperature on the vapor concentration profiles have been performed. The effects of primary air swirl number, secondary air temperature, and fuel flowrate were also analyzed. This section discusses the results obtained.

Model Validation

In order to quantitatively evaluate the model and further rely on its predictions, a benchmark case was first simulated. The experimental data collected by Runge et al. [17] for a pure n-heptane single droplet with an initial diameter of 480 μm , evaporating in air at 24°C (ambient speed: 1 m/s) was used for this purpose. The temporal variation of droplet diameter was obtained and presented in Fig. 4 along with the experimental data and numerical predictions of Runge et al. [17]. Droplet diameter (D) was normalized by initial diameter (D_0) and time (t) was normalized by the ratio of square of initial droplet radius (R_0) and ambient kinematic viscosity (ν). In Fig. 4, the symbols denote the experimental data [17], solid line denotes the numerical results [17] and the dashed line represents the present model. Although the present model slightly underpredicts the experimental results, the diameter predictions agree quite well with the numerical work. This trend also represents the standard D^2 -Law. The validation of diameter predictions in turn validates the vapor concentration, owing to the fact that the droplet mass is conserved.

Droplet Heating and Size Distribution

After the droplets are released from the injector, they undergo three processes, namely heating, evaporation, and boiling. Evaporation is initiated as soon as the droplets reach a preset vaporization temperature (341 K) and continues until the boiling point (477 K). The droplet temperature distribution 30 ms after the injection is presented in Fig. 5. No temperature variation within the droplet is considered in this work. The temperature of the droplets attains a value of 433 K after 10 ms and finally reaches 477 K after 20 ms. It should be noted that the droplets remain at 477 K while undergoing boiling. This occurs in the porous media and gives rise to significant generation of vapor. Fig. 6 shows the droplet diameter distribution of particles in the domain 30 ms after the injection. Note that in both fig. 5 and 6, symbols are used to represent droplets and the respective field variable is used in the contours. Fig. 6 suggests that the larger droplet particles are thrown away from the core as the spray propagates. This is due to the presence of swirling air, which provides both axial and tangential momentum to the droplets.

Effect of Porous Medium Temperature and Discussion on Vapor Concentration Profiles

First, different porous medium heat input rates were supplied and the temperature characteristics were obtained. Fig. 7 shows the axial temperature variation as a function of heat input rate. Recall that in this study local thermal equilibrium is assumed and hence the temperature attained by the gas is equal to that of solid phase. It can be seen from Fig. 7 that the peak temperature reaches ~ 580 K when a heat source of 780 W is supplied. Once the temperature characteristics were obtained, the heat source was varied from 325 W to 732 W and vapor concentration profiles were obtained. Figs. 8(a)-8(d) show the radial vapor concentration profiles taken at five different axial locations ($x=0.08\text{m}$, 0.12m , 0.13m , 0.14m , 0.19m) for four different heat sources. Though the evaporation starts to occur in the upstream of the porous zone, significant evaporation takes place only in the porous region and thereafter. When the heat source was increased from 325 W to 732 W, the increase in peak vapor concentration was 20-30% between the upstream and downstream of the porous zone (i.e., between $x=0.08$ m and 0.19 m). Also, in the downstream of the porous zone, the vapors tend to diffuse radially. Such distribution of vapor concentration in the domain is due to the combined effects of air-blast atomization and internal swirl air. In addition, the porous medium, by itself can distribute the mixture uniformly. But, the present computational model does not employ the pore-level details and account for the droplet-solid interaction and thus these effects are not explicitly seen.

Figure 9 shows the radial vapor concentration profiles for different heat sources at an axial location of $x=0.19$ m. The vapor distribution trend remains same for all the cases. However, due to the stronger heat source, the peak concentration increases by 7.6%. Fig. 10 shows the temporal evolution of vapor concentration profiles for a heat source of 732 W and at $x=0.19$ m. The droplets need some time to travel through the domain and establish a vapor concentration pattern. This happens until about 30 ms after injection. During this period, the vapor concentration is negligible. Then it starts to build up. However, there is no uniform pattern followed. This could be due to the

random distribution of droplets and each droplet attains steady evaporation at different time. Of all the droplets injected, some droplets evaporate completely before leaving the domain and the rest partially evaporate and escape the domain with some unevaporated liquid. The summation of these two masses gives an indication of completeness of evaporation. The percentage completion of vaporization is presented in Fig. 11 as a function of porous heat source. From the figure it can be seen that the percentage completion increases, as the porous heat source increases.

Effect of Swirl Number

Swirl number of the primary air was varied from 0.14 to 0.34 while holding the porous medium heat source and secondary air inlet temperature constant. The radial concentration profiles at $x=0.19$ m were obtained and plotted in Fig. 12. As the swirl number increases, the peak value tends to lower and the flattening of the curve starts to occur. It is worth to mention that when the swirl number was increased, the axial velocity component was held constant and the swirl velocity was increased. As the swirl number increases, the droplets tend to spread more radially and results in the lowering of peak vapor concentration. The observation from Fig. 6 shows that the smaller particles are present in the core region. This means that the droplets at the core could have undergone evaporation. This is in good qualitative accordance with vapor concentration profiles (e.g., Fig. 8), where the peak concentration occurs in the core region and it decreases radially towards the end.

Effect of Secondary Air Inlet Temperature

For a fixed porous medium heat source and primary air swirl number, the secondary air inlet temperature was varied from 373 K to 473 K and vapor concentration profiles were obtained. The results are plotted in Fig. 13. The figure shows an increase in vaporization when the inlet temperature increases even though the porous medium heat source is constant. This is due to the fact that the secondary air also contributes to the evaporation. However, the secondary air by itself is not sufficient and may not always be preheated and thus necessitating the use of heated porous media.

Effect of Fuel Flowrate

Two fuel flowrates of 0.358 mg/s and 0.478 mg/s corresponding to overall equivalence ratios of 0.9 and 1.2 respectively were used. The secondary air inlet temperature was 473 K and primary air swirl number was 0.2. The radial vapor concentration profiles are shown in Fig. 14. The vapor distribution pattern remained same for both the cases and however, higher vapor concentrations were obtained for higher flow rates. Approximately 32% higher value was obtained for peak concentration for a fuel flow rate of 0.478 mg/s. This conforms the fact that the equivalence ratio was also increased by 33.33% when going from 0.9 to 1.2.

CONCLUSIONS

In this paper, a computational model capable of predicting the spray evaporation characteristics in porous media has been described. The effects of porous medium temperature, primary air swirl, secondary air inlet temperature, and fuel flow rate were analyzed. When the heat source temperature was increased, the increase in peak vapor concentration was 20-30% from porous upstream to downstream and 7.6% at $x=0.19$ m. The primary air swirling spreads the droplets and thus the vapor more radially. The porous medium temperature and hence the thermal effects were found to be crucial factors in obtaining the complete vaporization of the spray.

REFERENCES

1. Weinberg, F. J., 1971, "Combustion Temperatures: The Future?," *Nature*, Vol. 233, September 24, pp. 239-241.
2. Hardesty, D. R., and Weinberg, F. J., 1974, "Burners Producing Large Excess Enthalpies," *Combustion Science and Technology*, Vol. 8, pp. 201-214.
3. Kotani, Y., and Takeno, T., 1982, "An Experimental Study on Stability and Combustion Characteristics of an Excess Enthalpy Flame," *Nineteenth Symposium (International) on Combustion*, pp.1503-1509.

4. Takeno, T., and Sato, K., 1979, "An Excess Enthalpy Flame Theory," *Combustion Science and Technology*, Vol. 20, pp. 73-84.

5. Howell, J. R., Hall, M. J., and Ellzey, J. L., 1996, "Combustion of Hydrocarbon Fuels Within Porous Inert Media," *Progress in Energy and Combustion Science*, Vol. 22 pp. 121-145.

6. Viskanta, R., 1995, "Interaction of Combustion and Heat Transfer in Porous Inert Media," in *Transport Phenomena in Combustion*, Ed. S.H. Chan, Taylor and Francis, pp. 64-87.

7. Kaviany, M., 1995, *Principles of Heat Transfer in Porous Media*, Springer-Verlag, New York, Inc.

8. Mathis Jr, W. M., and Ellzey, J. L., 2003, "Flame Stabilization, Operating Range, and Emissions for a Methane/Air Porous Burner," *Combustion science and Technology*, Vol. 175, pp. 825-839.

9. Leonardi, S. A., Viskanta, R., and Gore, J. P., 2003, "Analytical and Experimental Study of Combustion and Heat Transfer in Submerged Flame Metal Fiber Burners/Heaters," *Journal of Heat Transfer*, Transactions of the ASME, Vol. 125, pp. 118-125.

10. Kaplan, M., and Hall, M. J., 1995, "The Combustion of Liquid Fuels Within a Porous Media Radiant Burner," *Experimental Thermal and Fluid Science*, Vol. 11, pp. 13-20.

11. Jugjai, S., Wongpanit, N., Laoketkan, T., and Nokkaew, S., 2002, "The Combustion of Liquid Fuels Using a Porous Medium," *Experimental Thermal and Fluid Science*, Vol. 26, pp. 15-23.

12. Haack, D. P., 1993, "Mathematical Analysis of Radiatively Enhanced Liquid Droplet

Vaporization and Liquid Fuel Combustion Within a Porous Inert Media," MS Thesis, Dept. Mech. Eng., Univ. Texas, Austin, TX.

13. Periasamy, C., Sankara Chinthamony, S. K., and Gollahalli, S. R., 2004, "Numerical Modeling of Evaporation Processes in Porous Media for Gas Turbine Applications," AIAA-2004-139, 42nd AIAA Aerospace Sciences Meeting and Exhibit, Reno, NV.

14. Schmidt, D. P., Nouar, I., Senecal, P. K., Rutland, C. J., Martin, J. K., Reitz, R. D., and Hoffman, J. A., 1999, "Pressure-Swirl Atomization in the Near Field," SAE Paper 1999-01-0496, 1999.

15. Gupta, A. K., Lilley, D. G., and Syred, N., 1984, *Swirl Flows*, Tunbridge Wells, Kent & Cambridge, Mass. Abacus Press, Massachusetts.

16. Patankar, S. V., 1980, *Numerical Heat Transfer and Fluid Flow*. Hemisphere Publishing Corporation.

17. Runge, T., Teske, M., and Polymeropoulos, C. E., 1998, "Low-temperature Vaporization of JP-4 and JP-8 Fuel Droplets," *Atomization and Sprays*, Vol. 8, pp. 25-44.

ACKNOWLEDGEMENT

This work was supported by the US Army Research Laboratory and the US Army Research Office (Contract Number: DAAD 190210082). The authors thank Mr. Benjamin D. Baird for his many useful suggestions during this work.

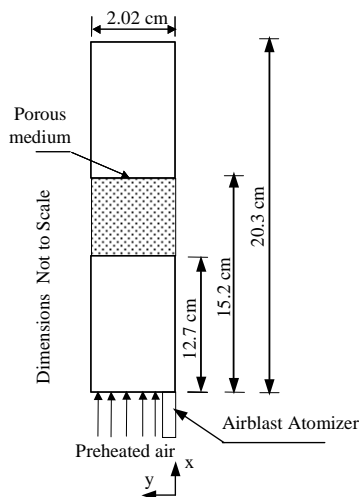


Fig. 1 Physical Geometry Considered for the Present Study.

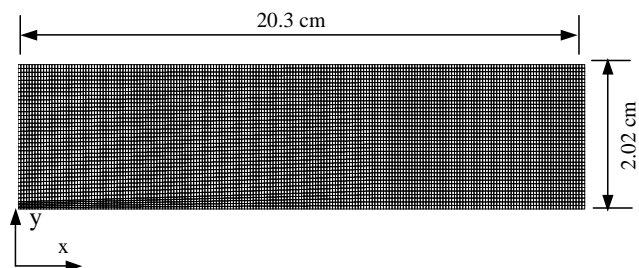


Fig. 2 Typical Grid Used in the Study.

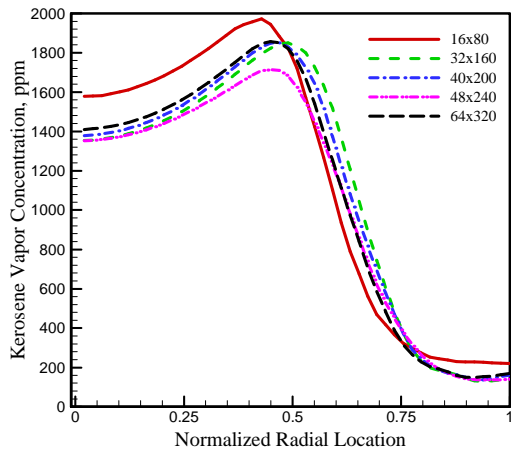


Fig. 3 Effect of Grid Size on Radial Vapor Concentration ($x=0.19$ m).

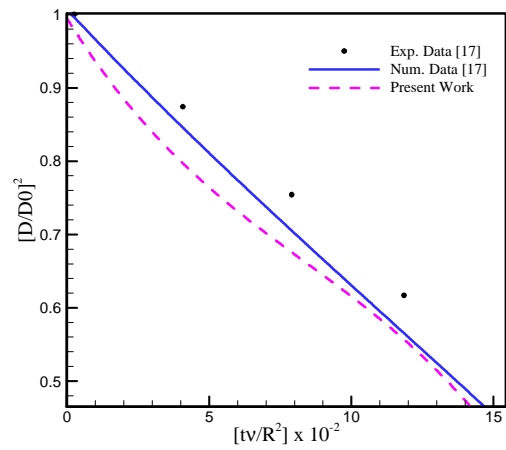


Fig. 4 Validation of Temporal Variation of Diameter for a Single Pure n-Heptane Droplet with Ref. 17.

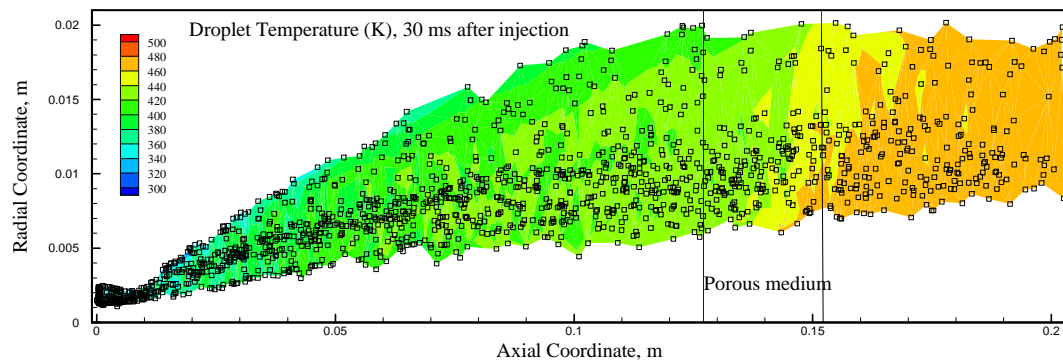


Fig. 5 Temperature Distribution of Droplets (30 ms after injection).

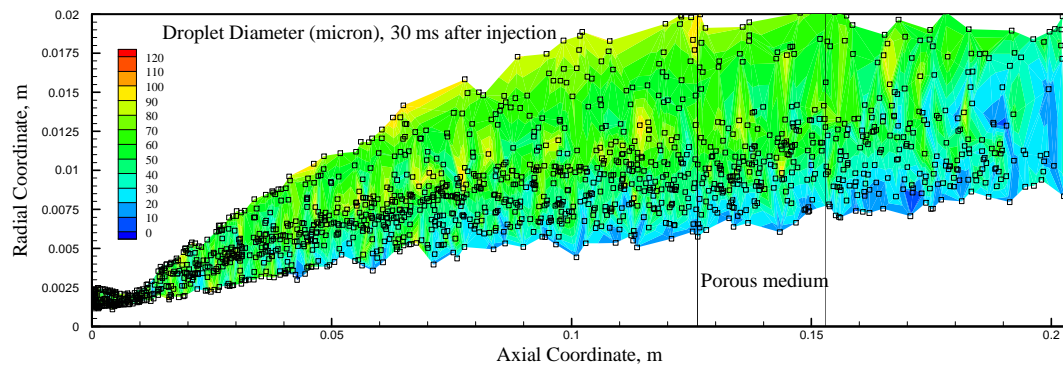


Fig. 6 Distribution of Droplet Sizes from the Air-blast Atomizer (30 ms after injection).

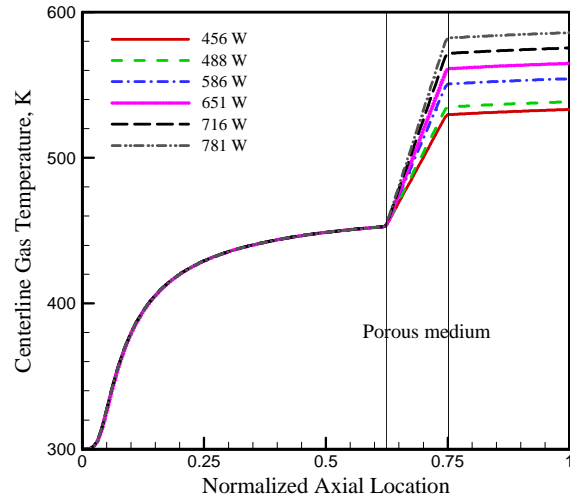


Fig. 7 Relationship between Porous Heat Source and Centerline Gas Temperature (SN=0.2).

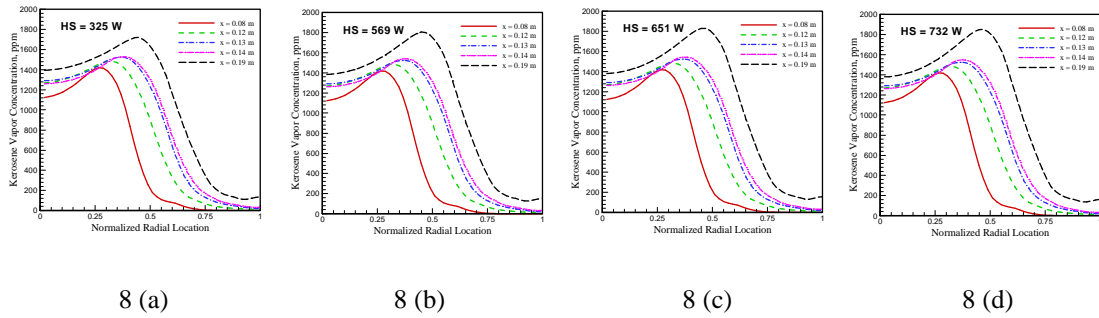


Fig. 8 Effect of Porous Medium Temperature on Vapor Concentration.

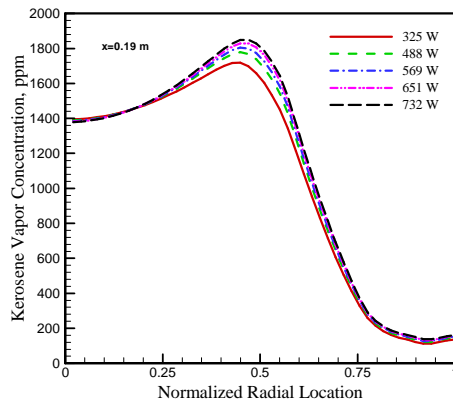


Fig. 9 Effect of porous medium temperature on vapor concentration $x = 0.19 \text{ m}$.

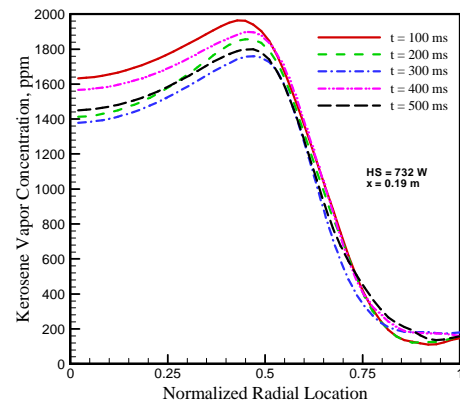


Fig. 10 Temporal Evolution of Vapor Concentration (HS=732 W, $x=0.19 \text{ m}$).

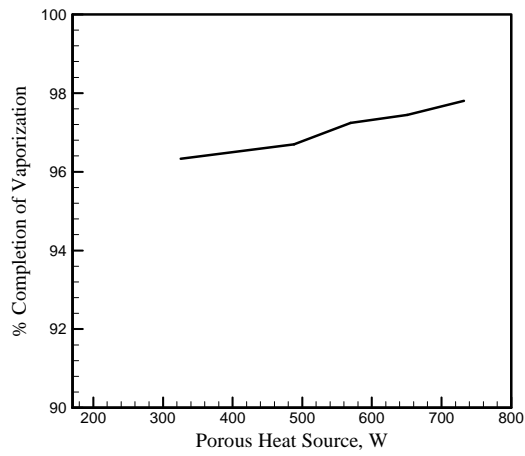


Fig. 11 Effect of Porous Heat Source on the Extent of Completeness of Evaporation.

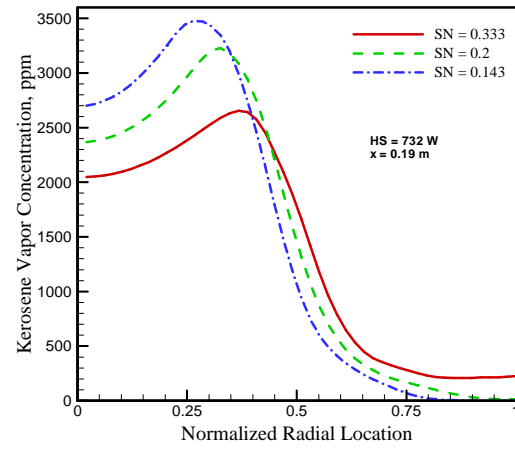


Fig. 12 Effect of Atomizing Air Swirl Number on Vapor Concentration (HS=732 W, x=0.19 m).

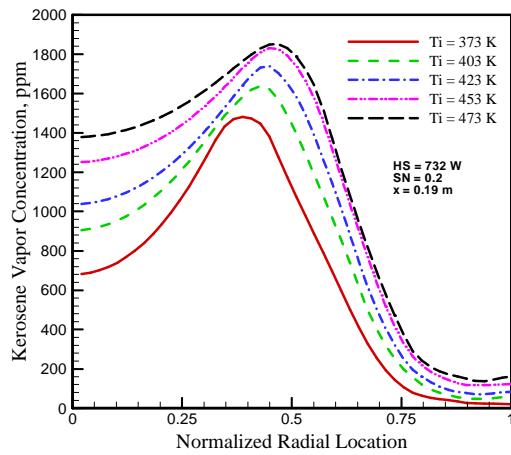


Fig. 13 Effect of Air inlet Temperature on Vaporization (HS=732 W, SN=0.2, x=0.19 m).

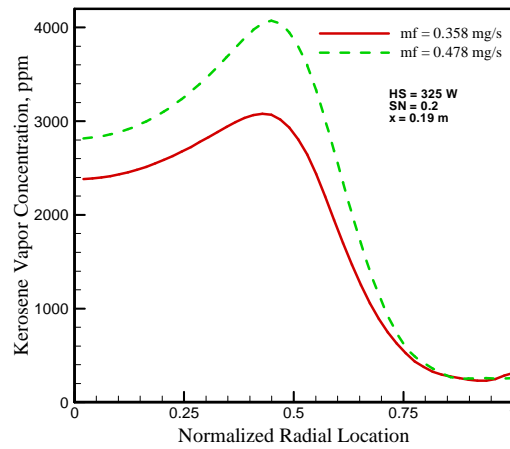


Fig. 14 Effect of Fuel Flowrate on Vapor Concentration (HS=732 W, SN=0.2, x=0.19 m).

Appendix G

Proc. of 2004 ASME International Mechanical Engineering Congress and RD&D Expo
November 13-19, 2004, Anaheim, California

IMECE2004-61300

MODELING LIQUID SPRAY EVAPORATION IN HEATED POROUS MEDIA WITH A LOCAL THERMAL NON-EQUILIBRIUM MODEL

Chendhil Periasamy*, Sathish K. Sankara Chinthamony*, and S. R. Gollahalli#

Combustion and Flame Dynamics Laboratory
School of Aerospace and Mechanical Engineering
The University of Oklahoma, Norman, OK – 73019
E-mail: gollahal@ou.edu

ABSTRACT

The situations such as rapid evaporation, and significant heat generation/convective heat transfer, typically encountered in liquid-fueled porous media combustors, warrant the use of local thermal non-equilibrium models. Knowledge of fuel vaporization and mixing is important to understand the combustion characteristics. In this paper, a two-energy equation model is presented to account for the non-equilibrium between the solid and liquid phases. In this approach, two energy equations for solid and gas phases were solved. Kerosene fuel, issued from an air-blast atomizer, was injected on to a heated porous medium. Governing equations were applied on a 2-D axisymmetric, computational domain of 20.3 cm x 2.5 cm. Computer simulations were conducted using a commercial code Fluent 6.0. Heat transfer from combustion porous medium was simulated by setting a volumetric heat source in the porous region. Accordingly, the peak temperatures in porous

Key words: Porous media, evaporation, local thermal non-equilibrium, and two-energy equation model.

* Graduate Research Assistant

Fellow ASME, Lesch Centennial Chair

media varied from 473 K to 590 K. Axial temperature profiles within the porous media were obtained with equilibrium and non-equilibrium models. Results indicated that the equilibrium models slightly underpredicted the peak temperature. Using non-equilibrium models, radial profiles of kerosene vapor concentration were obtained at different axial locations and the results showed that the thermal effects of the porous medium dominated in the evaporation process. Numerical results were also compared with available data and the agreement was found to be good.

NOMENCLATURE

c	Heat capacity (J/kg-K)
d_p	Pore diameter (m)
h_v	Volumetric convective heat transfer coefficient (W/m ³ -K)
k	Thermal conductivity of fluid (W/m-K)
p	Static pressure (N/m ²)
v	Velocity vector (m/s)
E	Total energy ($h - \frac{p}{\rho} + \frac{v^2}{2}$)
HS	Porous medium heat source (W)
J_i	Diffusion flux of i^{th} species (kg/m ² s)
Nu	Nusselt number

Pr	Prandtl number
Re _p	Pore Reynolds number
T	Temperature (K)
T _i	Coflow air inlet temperature (K)

Greek symbols

ρ	Density (kg/m ³)
ε	Porosity
ϕ	Overall equivalence ratio

Subscripts

g	Gas
s	Solid
v	Volumetric

INTRODUCTION

Combustion in porous media is a relatively new technique, which could potentially reduce the emissions of nitric oxide (NO_x) and carbon monoxide (CO), while improving the combustion efficiency. It offers several advantages such as extension of lean flammable limits, stable burner operation over a wide range of loads, and delivery of homogeneous fuel/air mixture. Fuels with low-calorific values can also be burned effectively. Attracted by these benefits, considerable amount of research [1-9] has been done in the past decade to understand the combustion characteristics of gaseous fuels in porous media. Howell et al. [3] and Viskanta [4] presented comprehensive reviews on this research area. The authors reviewed the correlations for estimating the heat transfer properties of porous media. CO and NO_x emissions and radiant thermal efficiency were presented as functions of flame speed [3]. Aspects of computational modeling were also highlighted.

Bouma and de Goeij [5] reported an experimental and numerical study on premixed combustion on ceramic foam burners. Solid and gas temperatures, and CO and NO emissions were predicted and compared with experiments. CO and NO concentrations were found to increase with an increase in thermal load. Henneke and Ellzey [6] modeled the filtration combustion of methane in packed beds with detailed chemical kinetics. Transient simulations were performed and solid and gas temperatures

and mass fractions of methane (CH₄), carbon monoxide (CO), and carbon dioxide (CO₂) were presented along the axial direction of the burner. Simulation results showed that the wave propagation was affected by gas-phase dispersion at equivalence ratios above 0.6. Leonardi et al. [7] performed theoretical and experimental investigations on combustion in submerged flame metal fiber burners/heaters. Results showed that the exit gas temperature and radiation efficiency of the burner increased, when the firing rate and equivalence ratio (0.9-1.1) were increased. 2-D direct numerical simulations and volume-averaged simulations were carried out by Sahraoui and Kaviany [8] for methane/air porous burners. They showed that the conduction through the porous medium was significant and influenced the flame structure and flame speed. The flame speed increased as the ratio of thermal conductivities of solid to gas increased and it decreased as the porosity was decreased. Rumminger et al. [9] predicted the gas temperatures above a porous burner and compared them with experimental values. Temperature measurements were obtained using an uncoated type-K thermocouple, OH-LIF, and laser absorption techniques. Results indicated that all of methane was consumed within the porous medium at a firing rate of 315 kW/m² and at an equivalence ratio of 0.9.

Alazmi and Vafai [10] presented a comprehensive analysis of various models used for studying the transport processes through porous media. Models with constant porosity, variable porosity, thermal dispersion, local thermal non-equilibrium were analyzed. Results showed that the differences between constant porosity and variable porosity models were negligible. Differences among the local thermal non-equilibrium models were significant only in the entry region. However, the models employing the dispersion effects showed different results depending on the inertia parameter. Local thermal non-equilibrium models for heat transfer have been investigated by several researchers [11-13]. Nakayama and his coworkers [11-12] developed correlations for the interfacial convective heat transfer coefficient for two-energy equation models using volume-averaged form of energy equation for solid and gas phases. For one-dimensional problems, the equations were simplified to a fourth order ordinary differential equation. Fluid

and solid temperature distributions in the porous medium were predicted. A complete description of heat and mass transfer phenomena in porous media can be found in Refs. 14 and 15.

Combustion of liquid fuels in porous media, however, has not received considerable attention. Only a few studies [16-20] have been performed to understand the combustion characteristics. Jugjai and Polmart [16] described a novel, down-flow, atomizer-free porous burner. Axial temperature profile in the porous burner and emitter was measured. Effects of heat input, equivalence ratio, porous bed height, and the distance between porous burner and emitter on combustion characteristics were analyzed. Stable combustion was achieved at as low as an equivalence ratio of 0.2. NOx emissions were lower than 160 ppm and CO emissions were found to be dependent on the operating conditions and porous bed emitted length. Kaplan and Hall [17] conducted an experimental study using liquid fuels in porous media. Four different designs of heptane-fueled radiant burners were tested to analyze the stable operating ranges and measure the emission characteristics. An air-blast atomizer was used to atomize the fuel. Stable combustion was achieved over the equivalence ratio range of 0.57-0.67. The study reported that burner stability was primarily affected by the droplet size and the distance between the porous medium and nozzle. The study did not show any evidence for plugging of the porous medium by liquid fuels. Emission measurements indicated that combustion was complete and the emissions were found to be as low as 3-7 ppm and 15-20 ppm for CO and NOx respectively.

Martynenko et al. [18] mathematically analyzed the one-dimensional, self-sustaining combustion in inert porous media with all modes of heat transfer. Droplet collisions with porous medium were modeled using a collision probability, which depended on particle Stokes number. Predicted axial profiles of solid, gas, and liquid temperatures, and mass fractions of liquid and vapor were presented. Tseng and Howell [19] investigated liquid fuel combustion in porous media numerically and experimentally. Multi-step chemical kinetics for n-heptane was included in the numerical code. The initial droplet size did not affect the burning rate, since all the droplets were completely vaporized

before the flame front. Flame stabilization was achieved at as low as an equivalence ratio of 0.3. They reported CO and NOx emissions of less than 10 ppm and 15-20 ppm respectively. Marbach and Agrawal [20] conducted experiments on the combustion of kerosene in inert porous media. Their results showed NOx and CO emissions of less than 30 ppm and 10 ppm respectively. They also varied the length of the mixing chamber and concluded that the interior combustion mode was effective in prevaporizing the fuel. Although the above-mentioned works describe the combustion characteristics of liquid fuels in porous media, detailed studies on the enhancement of evaporation due to the combustion heat feedback are not reported.

In the past, we have reported computational studies on the evaporation of point-wise injected [21] and air-blast atomized [22] kerosene spray in porous media using equilibrium models. We have also presented an experimental study [23] on this. The purpose of the present paper is to extend our computational model to include the local thermal non-equilibrium between the gas and solid phases. The specific objectives are to analyze the effects of local thermal non-equilibrium on evaporation characteristics.

MODEL FORMULATION

The present problem involves three phases namely, the gas (air), liquid spray (kerosene), and solid (porous medium). While the governing equations for gas and solid phases were written in Eulerian frame, the liquid phase equations were presented in Lagrangian frame of reference. Governing equations for momentum, and species conservation were similar to the ones presented in Ref. 21. Pressure drop in porous medium due to viscous and inertial effects were included via a Forchheimer equation and the permeability and inertia parameter were calculated using the Ergun equation. The porous medium was modeled as sink in the momentum conservation equations and the details are presented in Ref. 21. Governing equations for liquid phase are also presented in Ref. 21.

Local thermal non-equilibrium between the gas and solid phases was modeled by solving

two separate energy equations and coupling them through a volumetric heat transfer coefficient. The energy equations for fluid and solid phases are given below:

Energy Equation for Gas Phase:

$$\frac{\partial}{\partial t} (\rho E_g) + \nabla \cdot [\bar{v}(\rho E_g + p)] = \nabla \cdot [k \nabla T_g - (\sum_i h_i J_i)] + h_v (T_s - T_g) \quad (1)$$

Energy Equation for Solid Phase:

$$\frac{\partial T_s}{\partial t} = \nabla \cdot \left(\frac{k_s}{(1-\epsilon)\rho_s c_s} \nabla T_s \right) + \{Q_{in} - h_v (T_s - T_g)\} / (1-\epsilon) \rho_s \quad (2)$$

where Q_{in} is the volumetric heat input (W/m^3) to the porous media to simulate radiative heat feedback from the flame zone. Note that in the above equations, the term $h_v(T_s - T_g)$ appears as sink in solid phase equation and source in gas phase equation and the interfacial volumetric convective heat transfer coefficient (h_v) is used to couple the two equations. The h_v was calculated from the Nusselt number correlations as follows (Wakao and Kagueli [15]):

$$Nu = 2 + 1.1 Re_p^{0.6} Pr^{0.3} \quad (3)$$

where the Reynolds number is defined based on the pore diameter (490 μm). The properties of coflow were used in the calculation of Reynolds and Prandtl numbers. Once the Nusselt number was known, it was then converted into a volumetric Nusselt number as follows:

$$Nu_v = A_{sf} d_p Nu \quad (4)$$

where A_{sf} is the specific surface area (π/d_p). The volumetric heat transfer coefficient (units: W/m^3-K) was then calculated as shown below (Henneke and Ellzey [6]):

$$h_v = \frac{Nu_v k}{d_p^2} \quad (5)$$

Boundary Conditions

Air stream: Coflow air was preheated to different temperatures (373 K - 473 K). Coflow air mass flow rate was 3.8 mg/s for an overall equivalence ratio of 0.42 and an inlet temperature of 450 K. A swirling primary air stream at 300 K was also employed to promote atomization. The stoichiometric fuel-air mass ratio was 0.068. Nominal operating conditions are given in Table 1.

Droplet stream: Kerosene was assumed to be a single-component liquid of $C_{12}H_{23}$. A 4 mm-diameter injector was used with the spray half angle of 15° . The maximum relative velocity between the atomizing air and liquid sheet was 80 m/s and the sheet breakup and ligament constants used in the atomizer model were 5 and 0.2 respectively.

Table 1 Nominal operating conditions.

Sl. No.	Parameter	Value	Units
1.	Coflow air inlet temperature	450	K
2.	Mass flow rate of coflow air	3.8	mg/s
3.	Overall equivalence ratio	0.42	-
4.	Porous medium heat input	200	W
5.	Porosity of the medium	0.87	-

Grid Generation and Solution Procedure

The physical geometry considered for the analysis was of 2D axisymmetric type and is presented in Fig. 1. A domain size of 20.3 cm x 2.5 cm in the x and r direction respectively, was considered. Cartesian type, uniform grid of quadrilateral mesh elements with 10 points per centimeter was generated (after performing a grid sensitivity analysis) using a commercial grid generation code GAMBIT.

The governing equations were discretized using a finite-volume based approach. Unknown pressure field in the momentum equations was determined by solving the continuity equation iteratively, using a

pressure-correction algorithm. Convective terms in the governing equations were discretized by Power law scheme. The entire process follows the standard SIMPLE algorithm [24]. Interactions of porous media with gas-phase were programmed through a set of user-defined functions. Solutions were obtained using a commercial code FLUENT 6.0.

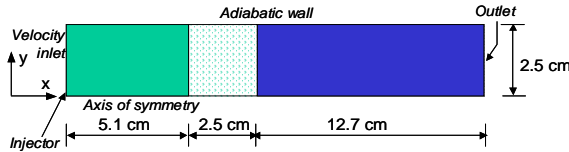


Fig. 1 Physical domain considered for the present analysis.

MODEL VALIDATION

In order to validate the model's predictions and have further confidence on the results, two benchmark cases have been simulated and compared with the results available in the literature. First, the evaporation of single droplet (liquid n-heptane) in quiescent environment (without porous media) was considered. Variation of droplet diameter as a function of time (i.e., the droplet life time) was captured and compared with those experimental and numerical data obtained by Runge et al. [25]. The results are presented in Fig. 2. After a small transient period, the results show a good agreement between the present model's predictions and the measured and computed data of Runge et al. [25]. The difference during the initial period could be due to a slight mismatch between the experimental conditions and the present computational model. Such a variation of the square of droplet diameter with respect to time is referred to as D^2 Law in the droplet evaporation literature. The model validation study, thus, shows that the predictions of droplet parameters are reliable and consistent.

Next, the predictions of porous medium model were compared with the results obtained by Vafai and Kim [26]. They derived an exact solution for forced convection in a channel filled with porous medium for an applied wall heat flux. For a given Darcy number of 0.01, a porosity of 87 %, the permeability was

calculated and supplied as input to the present model. A heat flux of 1 W/m^2 was applied and the transverse temperature profiles were obtained at different axial locations. The ratio between heat transfer coefficient and thermal conductivity of the medium (h/k) used in this study was 10.27 1/m. When normalized, the transverse temperature profiles collapse into a single curve and the results are shown in Fig. 3. The figure shows an excellent agreement with the analytical results of Vafai and Kim [26].

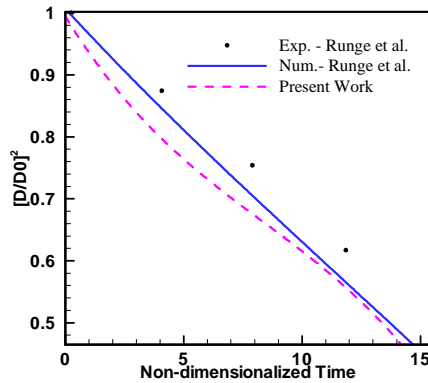


Fig. 2 Comparison of predicted droplet life time with the experimental and numerical study of Runge et al. [25].

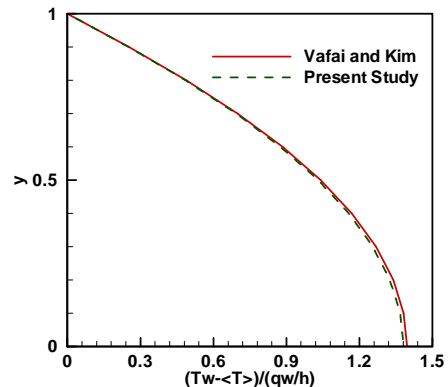


Fig. 3 Validation of transverse temperature profiles of the present model with the analytical solutions of Vafai and Kim [26].

RESULTS AND DISCUSSION

Droplet Size and Temperature Distribution

Understanding the size and temperature distribution of droplets and the temperature

distribution pattern in the porous media (due to heating) enables us to predict the vapor concentration profiles downstream of the porous media. The results of droplet size and temperature distribution upstream of porous media are presented first, followed by the temperature distribution in porous media.

Droplet size and temperature distribution in the domain at 200 ms after injection for a heat input of 200 W and a fuel flow rate of 0.11 mg/s are presented in Figs. 4 and 5 respectively. The small circles in the figures represent the position of droplets; while the colored, contour variables denote either Sauter mean diameter (Fig. 4) or temperature (Fig. 5). From Fig. 4, one can see that larger droplets are thrown out of the core region and smaller droplets are retained in the core region. This scattering is due to the swirling action imparted to the atomizing air. The results predicted by the model are in qualitative agreement with the experimental observations of Sankara et al. [22]. In typical industrial air-blast atomizers, rotating vanes provided in the nozzle impart a swirling motion to the atomizing air stream, which, in turn, creates a swirling spray of droplets (Reitz and Bracco [27]). Depending on the swirl strength, the droplet diameter and its spatial location vary.

From the droplet temperature distribution (Fig. 5), it can be seen that the temperature of the droplets continued to increase from the inlet boundary. The temperature was below 450 K until the droplets reach 5 cm from the inlet. As the droplets moved further in the domain, the temperature was increased to 477 K (boiling point) and it remained constant at 477 K

during vaporization. The temperature attained by the droplets depends on the surrounding air temperature, which, in turn, depends on the porous medium temperature and the effectiveness of the heat transfer between the porous medium and coflow air. The phenomenon of heat transfer between the porous medium and coflow air is explained in detail in the subsequent sections. Figure 5 also suggests that the radial variation of droplet temperature is negligible, due to the uniform radial temperature distribution of coflow air. Note that the present study assumes that the entire droplet is at a uniform temperature i.e., the temperature variation within the droplet is not considered.

Effects of Local Thermal Non-Equilibrium

When combustion takes place in a porous medium, the heat energy is recirculated upstream and the liquid spray is preheated. Since the present study is focused on the evaporation aspects, the combustion heat feedback is simulated by a volumetric heat source in the porous region. The heat source represents a fraction of heat feedback from the combustion zone. Temperature attained by the porous medium, thus, depends on the strength of the source term and the convective heat transfer to the coflow air. Simulations were performed with different strengths of heat sources (50–400 W) by holding the air inlet temperature constant at 450 K. The relationship between porous medium temperature and heat source strength was determined and the effects of local thermal non-equilibrium on the evaporation characteristics were analyzed from the results.

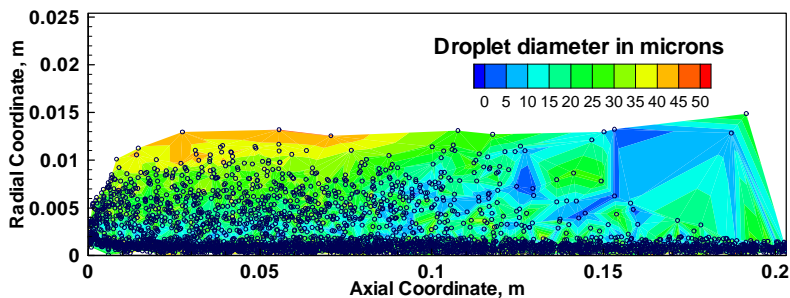


Fig. 4 Droplet size distribution at 200 ms after injection (HS = 200 W, $T_i = 450$ K).

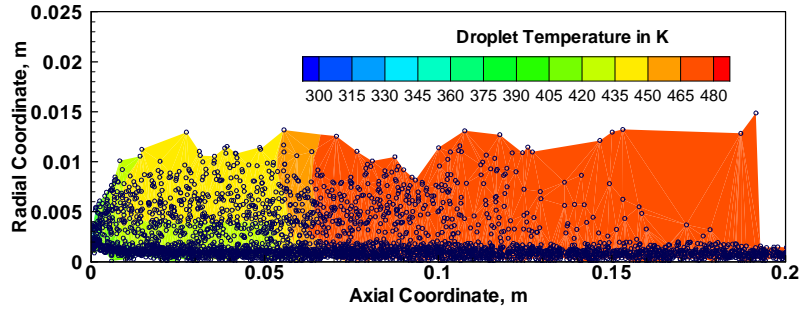


Fig. 5 Droplet temperature distribution at 200 ms after injection (HS = 200 W, $T_i = 450$ K).

The steady state, centerline, axial variation of porous medium temperature is presented in Fig. 6 for different heat inputs at a fixed T_i of 450 K. The porous medium temperature increased axially and attained a peak value closer to the exit of the porous medium. The peak temperatures corresponding to the lowest (50 W) and highest (400 W) heat input cases considered were 465 K and 570 K respectively. This increase in temperature is one of the crucial factors for evaporation enhancement. Other important factors are the porous medium structure and droplet size distribution. Using the two-energy equation model, the axial variations of porous medium and gas-phase temperatures for a heat input of 200 W were predicted and the results are presented in Fig. 7. As the coflow air flows through the porous medium, its temperature increases due to the convective heat transfer from the porous medium. This situation leads to a decrease in the temperature difference between the porous medium and coflow air, which lowers the porous medium temperature, since the heat source strength is held constant.

A study assuming local thermal equilibrium between the porous medium and coflow air was conducted to assess the equilibrium and non-equilibrium models. Fig. 8 shows the results of the two cases. Comparison of both the results yields that equilibrium models underpredicted the peak temperature by 10 K at the lowest heat input and 20 K at the highest input. In order to accurately predict the temperature distribution under rapid vaporization conditions (as in the present case), one should use local thermal non-equilibrium models (Dual et al. [13]). For local thermal non-equilibrium models, however, the proper selection of

interfacial heat transfer coefficient is essential as it affects the effectiveness of the heat transfer (Alazmi and Vafai [10]).

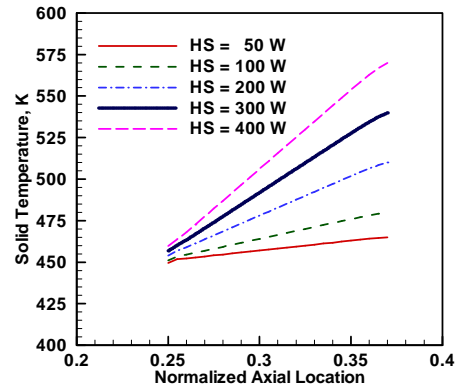


Fig. 6 Relationship between the porous medium heat source strength and temperature distribution ($T_i = 450$ K, $\epsilon = 0.87$).

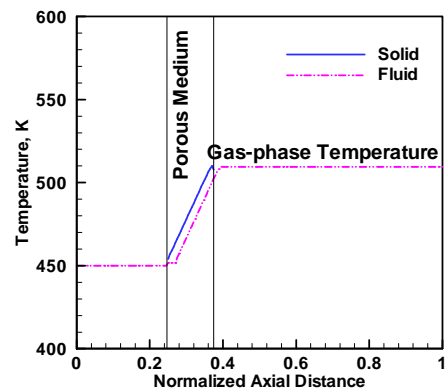


Fig. 7 Axial variation of porous medium and gas-phase temperature ($T_i = 450$ K).

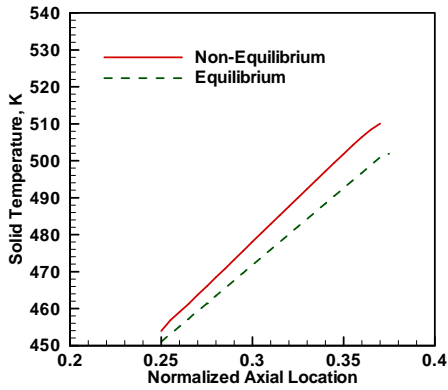


Fig. 8 Comparison of equilibrium model predictions with non-equilibrium models (HS = 200 W, $T_i = 450$ K).

Vapor Concentration Profiles

Radial vapor concentration profiles obtained using non-equilibrium models at different axial locations taken (at $t = 1000$ ms) are presented in Fig. 9 for the conditions given in Table 1. Peak vapor concentration upstream of and inside the porous medium is smaller; it increases in the downstream of the porous medium. For the case studied, the peak vapor concentration at $x = 10$ cm was about 68 % higher than that of 1.3 cm upstream of porous media. Figure 9 also indicates that the fuel vapor is concentrated at the core region and decreases radially. According to Fig. 4, the number density of the droplets is higher at the core region and decreases radially. Vapor concentration downstream of the porous medium, hence, follows the droplet size distribution upstream of the porous medium.

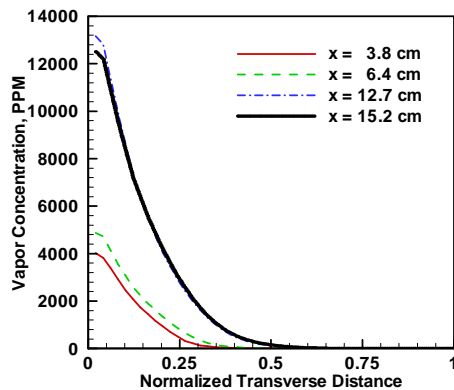


Fig. 9 Vapor concentration profiles at different axial locations (HS = 200 W, $T_i = 450$ K, $\phi = 0.42$, $t = 1000$ ms).

Temporal evolution of vapor concentration profiles is given in Fig. 10. Droplets need some time to travel through the domain and establish a vapor concentration pattern. This evolution process takes about 30 ms after injection and the vapor concentration is negligible during this period. Vapor concentration, then, starts to build up and establishes a pattern at about 200 ms. The unsteady effects are negligible and unique vapor concentration profiles could be seen beyond this time. Present study conducts the unsteady simulations upto 1000 ms in order to accurately capture vapor concentration profiles.

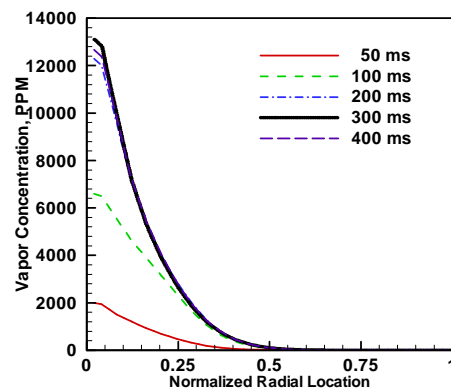


Fig. 10 Temporal evolution of vapor concentration profiles ($x = 12.7$ cm, HS = 200 W, $T_i = 450$ K, $\phi = 0.42$).

CONCLUSIONS

A computational model, which accounts for local thermal non-equilibrium between gas and liquid phases, has been developed in this study to predict the evaporation characteristics of liquid spray in porous media. The effects of local thermal non-equilibrium on vapor concentration were analyzed. Equilibrium models slightly underpredict the peak temperature of the porous medium (10 K for a heat input of 200 W, for instance) when compared to local thermal non-equilibrium models. Vapor concentration results show a strong dependence on porous medium temperature, which, in turn, depend on the strength of the heat source and the effectiveness of heat transfer between porous medium and coflow air.

REFERENCES

- [1] Hardesty, D. R., and Weinberg, F. J., 1974, "Burners Producing Large Excess Enthalpies," *Combustion Science and Technology*, Vol. 8, pp. 201-214.
- [2] Takeno, T., and Sato, K., 1979, "An Excess Enthalpy Flame Theory", *Combustion Science and Technology*, Vol. 20, pp. 73-84.
- [3] Howell, J. R., Hall, M. J., and Ellzey, J. L., 1996, "Combustion of Hydrocarbon Fuels Within Porous Inert Media," *Prog. Energy and Combustion Science*, Vol. 22 pp. 121-145.
- [4] Viskanta, R., 1995, "Interaction of Combustion and Heat Transfer in Porous Inert Media", in *Transport Phenomena in Combustion*, Ed. S. H. Chan, Taylor and Francis, pp. 64-87.
- [5] Bouma, P. H., and de Goey, L. P. H., 1999, "Premixed Combustion on Ceramic Foam Burners," *Combustion and Flame*, Vol. 119, pp. 133-143.
- [6] Henneke, M. R., and Ellzey, J. L., 1995, "Modeling of Filtration Combustion in a Packed Bed," *Combustion and Flame*, Vol. 117, pp. 832-840.
- [7] Leonardi, S. A., Viskanta, R., and Gore, J. P., 2003, "Analytical and Experimental Study of Combustion and Heat Transfer in Submerged Flame Metal Fiber Burners/Heaters," *J. Heat Transfer, Transactions of the ASME*, Vol. 125, pp. 118-125.
- [8] Sahraoui, M., and Kaviany, M., 1994, "Direct Simulation vs Volume-averaged Treatment of Adiabatic, Premixed Flame in a Porous Medium," *Int. J. Heat Mass Transfer*, Vol. 37, No. 18, pp. 2817-2834.
- [9] Rumminger, M. D., Dibble, R. W., Heberle, N. H., and Crosley, D. R., 1996, "Gas Temperature Above a Porous Radiant Burner: Comparison of Measurements and Model Predictions," *26th Symposium (International) on Combustion*, pp.1755-1762.
- [10] Alazmi, B., and Vafai, K., 2000, "Analysis of Variants Within the Porous Media Transport Models," *J. Heat Transfer, Transactions of the ASME*, Vol. 122, pp. 303-326.
- [11] Kuwahara, F., Shirota, M., and Nakayama, A., 2001, "A Numerical Study of Interfacial Convective Heat Transfer Coefficient in Two-energy Equation Model for Convection in Porous Media," *Int. J. Heat Mass Transfer*, Vol. 44, pp. 1153-1159.
- [12] Nakayama, A., Kuwahara, F., Sugiyama, M., and Xu, G., 2001, "A Two-energy Equation Model for Conduction and Convection in Porous Media," *Int. J. Heat Mass Transfer*, Vol. 44, pp. 4375-4379.
- [13] Dual, F., Fichot, F., and Quintard, M., 2004, "A Local Thermal Non-equilibrium Model for Two-phase Flows with Phase-change in Porous Media," *Int. J. Heat Mass Transfer*, Vol. 47, pp. 613-639.
- [14] Kaviany, M., 1995, *Principles of Heat Transfer in Porous Media*. Springer-Verlag, New York, Inc.
- [15] Wakao, N., and Kaguei, S., 1982, *Heat and Mass Transfer in Packed Beds*. Gordon and Breach Science Publishers, New York.
- [16] Jugjai, S., and Polmart, N., 2003, "Enhancement of Evaporation and Combustion of Liquid Fuels through Porous Media," *Experimental Thermal and Fluid Science*, Vol. 27, pp. 901-909.
- [17] Kaplan, M., and Hall, M. J., 1995, "The Combustion of Liquid Fuels Within a Porous Media Radiant Burner," *Experimental Thermal and Fluid Science*, Vol. 11, pp. 13-20.
- [18] Martynenko, V. V., Echigo, R., and Yoshida, H., 1998, "Mathematical Model of Self-sustaining Combustion in Inert Porous Medium with Phase Change under Complex Heat Transfer," *Int. J. Heat Mass Transfer*, Vol. 41, No. 1, pp. 117-126.
- [19] Tseng, C.-J., and Howell, J. R., 1996, "Combustion of Liquid Fuels in a Porous Radiant Burner," *Combustion Science and Technology*, Vol. 112, pp. 141-161.
- [20] Marbach, T. L., and Agrawal, A. K., 2003, "Fuel Vaporization and Combustion with the Use of Porous Inert Media," *39th AIAA/ASME/SAE/ASEE Joint Propulsion Conference*, July 20-23, 2003, Huntsville, Alabama.
- [21] Periasamy, C., Sankara Chinthamony, S. K., and Gollahalli, S. R., 2004, "Numerical Modeling of Evaporation Processes in Porous Media for Gas Turbine Applications," *AIAA-2004-139, 42nd AIAA Aerospace Sciences Meeting and Exhibit*, Reno, January 5-8, 2004.
- [22] Periasamy, C., Sankara Chinthamony, S. K., and Gollahalli, S. R., 2004, "A Computational Study of the Evaporation Characteristics of an Air-blast Atomized, Kerosene Spray in Porous Media," *PWR2004-52016, Proc. ASME Power*, Baltimore, MD, March 30 - April 1, 2004.

[23] Sankara Chinthamony, S. K., Periasamy, C., and Gollahalli, S. R., 2004, "Spray Impingement and Evaporation through Porous Media," GT2004-53391, *Proc. ASME Turbo Expo 2004*, June 14-17, Vienna, Austria (accepted for publication).

[24] Patankar, S. V., 1980, *Numerical Heat Transfer and Fluid Flow*. Hemisphere Publishing Corporation.

[25] Runge, T., Teske, M., and Polymeropoulos, C. E., 1998, "Low-temperature Vaporization of JP-4 and JP-8 Fuel Droplets," *Atomization and Sprays*, Vol. 8, pp. 25-44.

[26] Vafai, K., and Kim, S. J., 1989, "Forced Convection in a Channel Filled with a Porous Medium: An Exact Solution," *J. Heat Transfer*,

Transactions of the ASME, Vol. 111, pp. 1103-1106.

[27] Reitz, R. D., and Bracco, F. V., 1982, "Mechanism of Atomization of a Liquid Jet," *Physics of Fluids*, Vol. 25, No. 10, pp. 1730-1742.

ACKNOWLEDGEMENTS

This work was supported by the US Army Research Laboratory and the US Army Research Office (Contract Number: DAAD 190210082). The authors thank Mr. Benjamin Baird for his many useful suggestions during this work.

Appendix H

Effect of Coflow Air Turbulence

In previous simulations, the turbulence effects of the coflow air stream were neglected in the heat and mass transfer calculations of droplet stream with coflow air.

In this section, the effect of coflow air turbulence is considered using the Nusselt number (Nu) and Sherwood number (Sh) correlations, proposed by Birouk and Gökalp (2006) for droplet evaporation in turbulent flow. The correlations are given below:

$$\text{Nu} = A + B \text{Re}_d^{1/2} \text{Pr}^{1/3} (C_T)^n \quad (\text{H.1})$$

$$\text{Sh} = A + B \text{Re}_d^{1/2} \text{Sc}^{1/3} (C_T)^n \quad (\text{H.2})$$

where Re_d is the droplet Reynolds number and C_T is the turbulent coefficient. The constants A and B, and the turbulence coefficient are expressed as follows, for $0.01 < I < 0.15$ and $2 < \text{Re} < 1330000$:

Heat Transfer:

$$C_T = 0.538 + 0.1807d^{1/2} + 0.328I(I + 0.0405)\text{Re}_\infty^{1/2} \quad (\text{H.3})$$

$$A = 2.0; \quad B = 1; \quad n = 1.0$$

where I is $u'/U = 0.1$. For the maximum droplet diameter considered in this study (50 μm) and the maximum coflow air velocity of 2 m/s, the droplet Reynolds number is estimated to be 3 and the C_T is 0.884.

Mass Transfer:

$$C_T = 0.439 + 0.1807d^{1/2} + 0.234I(I + 0.05)\text{Re}_\infty^{1/2} \quad (\text{H.4})$$

$$A = 2.0; \quad B = 1; \quad n = 1.0$$

where I is $u'/U = 0.1$. For the maximum droplet diameter considered in this study (50 μm) and the maximum coflow air velocity of 2 m/s, the droplet Reynolds number is estimated to be 3 and the C_T is 0.703.

The FLUENTTM's internal vaporization model was modified to include the turbulence effects via a set of user-defined functions. Figure H.1 presents the transverse distribution of kerosene droplet diameter at 1.5 cm upstream of evaporation porous medium. The figure shows that the transverse droplet diameter profiles predicted by both the models follow similar trend and match well with experimental data. When the turbulence effects were not considered, the droplet diameter was overpredicted by 30% at the centerline, and underpredicted by 18% at the spray edges. From the droplet axial velocity profiles (Figure 4.34), at transverse locations of $r/R = 0.2$ to 0.3 , the change in velocity is less than 5%. This suggests the presence of the shear layer between vaporizing fuel spray and the coflow air in this region. When the spray

vaporizes, the turbulence levels are high in the shear layer. Hence, the droplet diameter predictions match well with the experimental data. Both at the spray core and edges, the turbulence levels depend on the fuel concentration and local density. This could lead to the differences in the predictions of droplet diameter. Further, surrounding the vaporizing droplet, usually the laminar flow conditions exist even if the droplets are moving in the turbulent flow field.

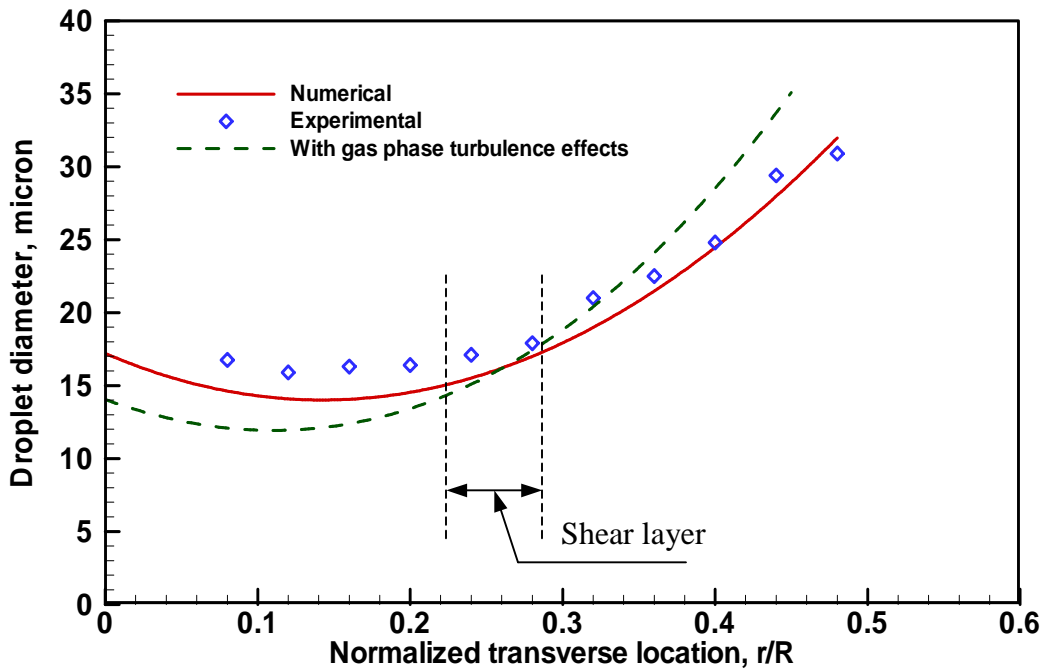


Figure H.1 Effect of coflow air turbulence on the transverse droplet diameter profiles of kerosene spray 1.5 cm upstream of the evaporation porous medium

Appendix I

List of Publications Based on this Work

Journal Paper:

1. Periasamy, C., Sankara Chinthamony, S. K., and Gollahalli, S. R. (2007), "An Experimental Evaluation of Evaporation Enhancement with Porous Media in Liquid-Fueled Burners," *Journal of Porous Media* Vol. 10, No. 2, pp. 137-150.

Peer-reviewed Conference Papers:

1. Periasamy, C., Saboonchi, A., and Gollahalli, S. R. (2007), "Numerical Prediction of Evaporation Processes in Porous Media Combustors," DETC2007-34672, ASME International Design Engineering Conference, Las Vegas, LV, Sept. 4-7, 2007 (Final paper submitted).
2. Periasamy, C., and Gollahalli, S. R. (2007), "Lean Extinction Characteristics of Kerosene Spray Flames in Porous Media," 5th International Energy Conversion Engineering Conference, St. Louis, MO, June 25-27, 2007 (Final paper submitted).
3. Periasamy, C., and Gollahalli, S. R. (2006), "A Parametric Simulation of the Evaporation in Liquid-Fueled Porous Burners," ASME Power 2006, PWR2006-88016, Atlanta, GA, May 2-4, 2006.
4. Periasamy, C., Sankara Chinthamony, S. K., and Gollahalli, S. R. (2005), "Experimental Determination of Minimum Heat Feedback for Complete Vaporization in Porous Media Burners," AIAA-2005-5525, 3rd International Energy Conversion Engineering Conference, San Francisco, CA, August 15-18, 2005.
5. Periasamy, C., Sankara Chinthamony, S. K., and Gollahalli, S. R. (2004), "Modeling Liquid Spray Evaporation in Heated Porous Media with a Local Thermal Non-equilibrium Model," IMECE2004-61300, 2004 ASME International Mechanical Engineering Congress, Anaheim, CA, November 13-19, 2004.
6. Sankara Chinthamony, S. K., Periasamy, C., and Gollahalli, S. R. (2004), "Spray Impingement and Evaporation through Porous Media," GT2004-53391, ASME Turbo Expo 2004, Vienna, Austria, June 14-17, 2004.

7. Periasamy, C., Sankara Chinthamony, S. K., and Gollahalli, S. R. (2004), "A Computational Study of the Evaporation Characteristics of an Air-blast Atomized, Kerosene Spray in Porous Media," PWR2004-52016, ASME Power, Baltimore, MD, March 30 - April 1, 2004.
8. Periasamy, C., Sankara Chinthamony, S. K., and Gollahalli, S. R. (2004), "Numerical Modeling of Evaporation Processes in Porous Media for Gas Turbine Applications," AIAA-2004-139, 42nd AIAA Aerospace Sciences Meeting and Exhibit, Reno, January 5-8, 2004.

Presentations at Regional Conferences:

1. Periasamy, C., Saboonchi, A, and Gollahalli, S. R. (2006), "Influence of Solid Radiation in the Evaporation Enhancement of Liquid Fuels in Porous Media," 26th Oklahoma AIAA/ASME Symposium, The University of Oklahoma, Norman, April 2006.
2. Periasamy, C., Sankara Chinthamony, S. K., and Gollahalli, S. R. (2005), "An Experimental Study on Evaporation Enhancement of Kerosene Spray in Porous Media Burners," 25th Oklahoma AIAA/ASME Symposium, Oklahoma State University, Stillwater, OK, February 2005.
3. Periasamy, C., Sankara Chinthamony, S. K., and Gollahalli, S. R. (2004), "A Two-energy Equation Model for Liquid Spray Evaporation in Heated Porous Media," 24th Oklahoma AIAA/ASME Symposium, Oklahoma Christian University, Oklahoma City, February 2004.
4. Periasamy, C., and Gollahalli, S. R. (2003), "Evaporation of Liquid Spray in Porous Media: A Numerical Study," 23rd Oklahoma AIAA/ASME Symposium, The University of Oklahoma, Norman, March 2003.